HOT FLOW ANOMALIES AT EARTH'S BOW SHOCK AND THEIR MAGNETOSPHERIC-IONOSPHERIC SIGNATURES

By

Christina Seiman Chu, A.S., B.S., M.Sc.

A Dissertation Submitted in Partial Fulfillment of the Requirements

for the Degree of

Doctor of Philosophy

in

Physics

University of Alaska Fairbanks

August 2017

APPROVED:

Hui Zhang, Committee Chair
Antonius Otto, Committee Member
Chung-Sang Ng, Committee Member
David Sibeck, Committee Member
Renate Wackerbauer, Chair
Department of Physics
Paul Layer, Dean
College of Natural Science and Mathematics
Michael Castellini, *Dean of the Graduate School*

Abstract

Hot flow anomalies (HFAs) are typically observed upstream of bow shocks. They are characterized by a significant increase in particle temperature and substantial flow deflection from the solar wind flow direction coinciding with a decrease in density.

HFAs are important to study and understand because they may play an important role in solar wind-magnetosphere coupling. They may drive magnetopause motion, boundary waves, and flux transfer events. They can excite ultra low frequency waves in the magnetosphere, drive magnetic impulse events in the ionosphere, and trigger aurora brightening or dimming. Studying HFAs will aid in the understanding of fundamental processes that operate throughout the heliosphere such as particle energization and shocks.

This dissertation presents statistical and case studies of hot flow anomalies identified in Time History of Events and Macroscale Interactions During Substorms (THEMIS) satellite data from 2007–2009. The characteristics and occurrence of HFAs, their dependence on solar wind/interplanetary magnetic field (IMF) conditions and location, and their magnetospheric-ionospheric signatures, have been investigated using in-situ spacecraft observations and ground based observations. THEMIS observations show that HFAs span a wide range of magnetic local times (MLTs) from approximately 7 to 16.5 MLT. HFAs were observed up to 6.3 Earth radii (R_E) upstream from the bow shock. It has been found that the HFA occurrence rate depends on solar wind and interplanetary magnetic field (IMF) conditions as well as distance from the bow shock. HFA occurrence decreases with distance upstream from the bow shock. HFAs are more prevalent when there is an approximately radial interplanetary magnetic field. No HFAs were observed when the Mach number was less than 5, suggesting there is a minimum threshold Mach number for HFAs to form. HFAs occur most preferentially for solar wind speeds from 550–600 km/s.

Multiple THEMIS spacecraft observations of the same HFA provide an excellent opportunity to perform a spatial and temporal analysis of an HFA. The leading edge, tangential discontinuity inside the HFA, and trailing shock boundaries for the event were identified. The boundaries' orientations and motion through space were characterized. The HFA expansion against the solar wind was 283 km/s. The spatial structure of the

HFA was deduced from multiple spacecraft observations. The HFA is thicker closer to the bow shock.

The magnetospheric-ionospheric signatures of an HFA have been investigated using in-situ spacecraft observations and ground based observations. Magnetic field perturbations were observed by three GOES spacecraft at geostationary orbit and high-latitude ground magnetometers in both hemispheres. Observations from magnetometers located at different MLTs showed that the perturbation propagates tailward at 0.32°/s or 9 km/s (1.27°/s or 21 km/s) for the northern (southern) hemisphere, which is consistent with an HFA propagating tailward along the dawn flank. SuperDARN radar observations showed a change in plasma velocity shortly after the HFA was observed by THEMIS.

Table of Contents

Page

Title Page . . . . . **i**

Abstract . . . . . **iii**

Table of Contents . . . . . **v**

List of Figures . . . . . **ix**

List of Tables . . . . . **xxiii**

List of Acronyms . . . . . **xxv**

Acknowledgements . . . . . **xxvii**

Chapter 1 Introduction **1**

1.1 Earth's Local Space Environment 1

1.2 Boundaries in Space 7

1.2.1 Rankine-Hugoniot Conditions 7

1.2.2 Tangential Discontinuity 10

1.2.3 Contact Discontinuity 10

1.2.4 Rotational Discontinuity 11

1.2.5 Shocks 11

1.3 Bow Shock 13

1.4 Foreshock 14

Chapter 2 Foreshock Transients **17**

2.1 Common Coordinate Systems of Space Physics 17

2.2 Overview of Foreshock Transients 17

2.2.1 Hot Flow Anomalies 17

2.2.2 Foreshock Bubbles 17

2.2.3 Foreshock Cavities 18

2.2.4 Foreshock Cavitons 18

2.2.5 Foreshock Compressional Boundaries 19

2.3 Properties of Hot Flow Anomalies 19

2.4 Hot Flow Anomaly Formation 23

2.5 Hot Flow Anomaly Location and Size 27

2.6 Waves and Energetic Particles in Hot Flow Anomalies 30

2.7 Magnetospheric and Ionospheric Effects of Hot Flow Anomalies 30

2.8 Hot Flow Anomalies Upstream of Non-Earth Bow Shocks 31
2.9 Motivation and Outline of this Dissertation 38
Chapter 3 Data Sources 41
3.1 Time History of Events and Macroscale Interactions During Substorms . 41
3.1.1 Spacecraft Orbit and Separation 41
3.1.2 THEMIS Spacecraft Instruments 41
3.2 Advanced Composition Explorer 46
3.3 Wind Spacecraft 47
3.4 OMNI 48
3.5 Geostationary Operational Environmental Satellite 49
3.6 Ground Based Observations 52
3.6.1 SuperMAG 52
3.6.2 SuperDARN 54
3.7 Chapter Summary 56
Chapter 4 Methodology 57
4.1 Hot Flow Anomaly Event Identification 57
4.2 Model Bow Shock 58
4.2.1 Geocentric Plasma Equatorial Coordinate System 58
4.2.2 Defining the Bow Shock Surface and Calculating Distance Upstream via Lagrange Multipliers Technique 59
4.2.3 Calculate Bow Shock Normal 62
4.3 Calculating Normals to Shocks and Discontinuities 63
4.3.1 Minimum Variance Analysis 63
4.3.2 Coplanarity Method 64
4.3.3 Time Delay Analysis (Timing Method) 65
4.3.4 Tangential Discontinuities 66
4.3.5 Boundary Normal Coordinates 66
4.3.6 Hodograms 67
4.4 Calculating Shock and Boundary Normal Speeds 67
4.4.1 Time Delay Analysis with Two Spacecraft 67
4.4.2 Mass Flux Algorithm 68
4.4.3 Continuity of the Tangential Electric Field 68
4.5 Normalization of Bar Plots 68

4.6 Magnetic Local Time of Ground Stations 69
4.7 Distance Between Two Latitude and Longitude Points 69
4.8 Chapter Summary 70
Chapter 5 Statistical Analysis of Hot Flow Anomalies at Earth 71
5.1 Introduction 71
5.2 Results 72
5.3 Conclusions 85
Chapter 6 Spatial-Temporal Analysis of a Hot Flow Anomaly 87
6.1 Introduction 87
6.2 Overview of an HFA Observed by Five THEMIS Spacecraft on 10 August 2007 88
6.3 HFA Boundary Speed 93
6.3.1 TD Speed 98
6.3.2 Shock Speed 98
6.4 HFA Spatial Structure 100
6.5 Conclusions 105
Chapter 7 Magnetospheric and Ground Signatures of a Hot Flow Anomaly . 107
7.1 Introduction 107
7.2 Case Study 108
7.2.1 Solar Wind and Magnetospheric Observations 108
7.2.2 Ground Observations 119
7.3 Conclusions 130
Chapter 8 Discussion and Conclusions 135
8.1 Statistical Analysis of Hot Flow Anomalies 135
8.2 Spatial and Temporal Analysis of Hot Flow Anomalies 138
8.3 Magnetospheric and Ground Signatures of Hot Flow Anomalies 139
8.4 HFAs Versus Other Foreshock Transients 141
References 143

List of Figures

Page

Figure 1.1 Earth's magnetosphere in the noon-midnight plane, artist's representation. 2

Figure 1.2 Loci of a succession of fluid parcels emitted at constant speed from a source rotating with the Sun [*Kivelson and Russell*, 1995]. 3

Figure 1.3 Artist representation of Parker spiral interplanetary magnetic field lines originating at the Sun [*"The Sun's Magnetic Field"*, 2012]. 3

Figure 1.4 The different layers of Earth's atmosphere are plotted. The temperatures of the neutral atmospheric layers is shown with the thin black curve labeled "temperature curve" and the axis on the bottom. The electron densities of the ionosphere layers is shown with the thick solid blue curve in the center of the plot and the axis at the top. Altitude above the ground is on the left axis, and pressure and molecular mean free path are the right axes. [*Yizengaw*, 2017] 6

Figure 1.5 Typical magnetic shock profiles [*Baumjohann and Treumann*, 1996] 13

Figure 1.6 Earth's foreshock in the equatorial plane, artist representation [*Balogh and Treumann*, 2013] 14

Figure 2.1 Observations of a HFA from *Schwartz et al.* [1985]. Data is from AMPTE-UKS on October 30 1984. From top to bottom, the parameters shown are magnetic field strength, latitude and azimuthal direction in geocentric solar ecliptic (GSE) coordinates (sunward direction is $\theta = 0$, $\phi = 0$ with $\theta = 90$ as northward and, $\phi = 270$ as dawn ward), electron number density, wave autocorrelator gain control level, ion flow velocity, flow latitudinal and azimuthal directions, and electron and ion temperatures. . . 20

Figure 2.2 A hybrid computer simulation of a hot flow anomaly (region inside red circle) at the bow shock of Earth's magnetic field. Green and red areas closer to Earth are hot plasmas trapped in the Earth's magnetic field. Source: N. Omidi 21

Figure 2.3 Ion velocity distribution plots and electron velocity distribution cut plots for mature and young HFAs observed by THEMIS C from *Zhang et al.* [2010]. The top row shows ion distributions inside a mature (a) and young (b) HFA. The second row shows electron distributions inside a mature (c) and young (d) HFA. The solid black line in figures (a)–(d) point toward the Sun. In the bottom row, (e) shows one dimensional cuts of electron distributions in the solar wind (black crosses), in the HFA sheath region (green crosses), and in the center of a mature HFA. (f) shows one dimensional cuts of the electron distribution of Figure 2.3(d), inside a young HFA. The black crosses and red triangles show the cut along the perpendicular and parallel velocity directions respectively. 22

Figure 2.4 Young HFA observed by THEMIS C on 19 August 2008 [*Zhang et al.*, 2010]. From top to bottom, the geocentric solar magnetic (GSM) parameters shown are the three magnetic field components, magnetic field strength, ion density, components of plasma flow, plasma ion spectrum, plasma electron spectrum, and the wavelet analysis result for the B_x component of magnetic field. The blue vertical dashed lines mark the edges of the HFA. The ion plasma frequency is over-plotted in Figure 2.4(c) and the right hand axis with a dashed blue line. The ion and electron temperatures are over-plotted in black dots and the right hand axes in Figure 2.4(e) and (f) respectively. 24

Figure 2.5 A proto-HFA (left) and corresponding mature HFA (right) observed by THEMIS B and C respectively on 19 August 2008 [*Zhang et al.*, 2010]. From top to bottom, the GSM parameters shown are the three magnetic field components, magnetic field strength, plasma density, components of ion flow, plasma ion spectrum, and plasma electron spectrum. The ion and electron temperature measured by THEMIS B are over-plotted in black dots and using the right hand axis in Figure 2.5e and f respectively. 26

Figure 2.6 The HFA size-γ functions based on the size estimation by Alfvén Mach velocity on the left and the transition speed on the right. The fixed solar wind speed was shown in Alfvén Mach number. (a) $\gamma = 60^\circ \pm 20^\circ$ and $M_A = 10 \pm 5$, (b) $\gamma = 60^\circ \pm 20^\circ$ and $M_A = 10 \pm 5$, (c) $\gamma = 100^\circ \pm 20^\circ$ and $M_A = 10 \pm 5$, (d) $\gamma = 100^\circ \pm 25^\circ$ and $M_A = 10 \pm 5$. All Alfvén Mach numbers were calculated from the actual Alfvén velocity. [*Facskó et al.*, 2009] . . . 28

Figure 2.7 The HFA size-$\Delta\Phi$ functions based on the size estimation by Alfvén Mach velocity on the left and the transition speed on the right. The fixed solar wind speed was shown in Alfvén Mach number. (a) $\Delta\Phi = 60^\circ \pm 20^\circ$ and $M_A = 10 \pm 10$, (b) $\Delta\Phi = 60^\circ \pm 20^\circ$ and $M_A = 13 \pm 2$, (c) $\Delta\Phi = 80^\circ \pm 10^\circ$ and $M_A = 16 \pm 4.5$, (d) $\Delta\Phi = 80^\circ \pm 15^\circ$ and $M_A = 12.5 \pm 2.5$. All Alfvén Mach numbers were calculated from the actual Alfvén velocity. [*Facskó et al.*, 2009] 29

Figure 2.8 The HFA size-velocity functions with Alfvén velocity calculated using ACE and crossing time measured by Cluster. The sizes were calculated using the method based on Alfvén speed (black) and the transition speed (red). The fixed solar wind speed was measured in units of Alfvén Mach number. $\gamma = 80^\circ \pm 10^\circ$ and $\Delta\Phi = 40^\circ \pm 20^\circ$. All Alfvén Mach numbers were calculated from the actual Alfvén velocity. [*Facskó et al.*, 2009] 29

Figure 2.9 Sketch of HFA upstream of the bow shock and a corresponding localized magnetopause deformation. Source: H. Zhang. 31

Figure 2.10 Simulation results of a HFA at the termination shock from *Giacalone and Burgess* [2010]. The angle between the current sheet and the shock normal is θ_{Cn}. The current sheets are indicated by the dashed lines. The color indicates the final value of the total plasma density at the end of the simulation. Blue corresponds to densities equal to the starting density whereas red indicates plasma density that is four times the starting density. The direction of the magnetic field is indicated by the "+" (out of the page) and "-" (into the page). 32

Figure 2.11 Observations of a hot flow anomaly at Mercury from MESSENGER on 16 April 2011 [*Uritsky et al.*, 2014]. The very top panel is $|B|$ on a long time scale. The following three panels from top to bottom are B_x, B_y. B_z, $|B|$. The bottommost panel is the tangential B_τ and normal B_N magnetic field in a current sheet coordinate system where the current sheet normal is the cross product between magnetic field before and after the event. . 33

Figure 2.12 Observations of two Venus hot flow anomalies from MESSENGER on 5 June 2007 from *Slavin et al.* [2009] shown in black. From top to bottom is B_x, B_y. B_z, and $|B|$. The observation of the bow shock is labeled as BS. Venus Express data is overlaid in red. 35

Figure 2.13 Observations of a Martian hot diamagnetic cavity by the Mars Global Surveyor on 22 July 1988 from *Øieroset et al.* [2001]. From top to bottom, the parameters shown are the electron energy spectrogram, electron density, electron temperature, magnetic field strength, and magnetic field ϕ and θ angles. The angles are defined as: $\phi = \arctan\frac{B_y}{B_x}$ and $\theta = \arcsin\frac{B_x}{|B|}$. 36

Figure 2.14 Observations of a Martian hot flow anomaly from MAVEN on 17 December 2014 from *Collinson et al.* [2015]. Panel A shows the region the spacecraft was observing where blue indicates the foreshock, purple are boundary compression regions, and yellow is the HFA core. In panel B, from top to bottom is $|B|$, B_x, B_y. B_z, and shock angle. Panel C shows the ion spectrometer observations with the time-energy spectrogram, density, temperature, and velocity. Panel D shows the electron spectrometer observations with the time-energy spectrogram and density and temperature. 37

Figure 2.15 Observations of a HFA at Saturn's bow shock by Cassini on 8 November 2004 from *Masters et al.* [2009]. From top to bottom, the parameters plotted are magnetic field strength, magnetic field θ and ϕ angles, electron and ion densities, components of the bulk flow velocity, and a time-energy spectrogram of electron count rate. θ is defined as the angle between the field vector and the xy plane and ϕ is the angle between the projection of the field vector into the xy plane and the negative x direction (anti-sunward). The data is in Kronocentric Solar Magnetospheric coordinates. 39

Figure 3.1 A photograph of all five THEMIS probes mounted to the probe launch carrier ["*THEMIS - eoPortal Directory - Satellite Missions*", 2017]. . 42
Figure 3.2 A photograph of a THEMIS FGM vector compensated fluxgate ring-core sensor ["*THEMIS - eoPortal Directory - Satellite Missions*", 2017]. . . . 42
Figure 3.3 A photograph of a THEMIS ESA instrument ["*THEMIS Electrostatic Analyzer*", 2017]. 45
Figure 3.4 A photograph of the ACE satellite ["*NASA's ACE Spacecraft*", 2017]. 46
Figure 3.5 A photograph of the Wind satellite ["*The WIND Spacecraft Experiment*", 2011]. 48
Figure 3.6 A photograph of the GOES-M probe ["*Kennedy Media Gallery*", 2017]. 50
Figure 3.7 A continuity timeline of GOES spacecraft 10, 11, and 12 from launch to decommissioning. 50
Figure 3.8 A photo of the Rankin Inlet SuperDARN radar. The main array and the seacan are in the left background. The UAV landing zone (plywood) can be seen on the left in the foreground ["*Maintenance trip to Rankin Inlet*", 2016]. 54

Figure 5.1 (a) The spatial location of all THEMIS C intervals in the interplanetary medium for 2007–2009 in GPE coordinates. The thick black curve is the *Merka et al.* [2005] bow shock for an Alfvén Mach number range of 2–20. (b) The spatial locations of HFAs and SHFAs identified in THEMIS C data, August 2007 to December 2009, are plotted in these figures in the XY, XZ, and YZ planes using GPE coordinates. The thick black curves are the *Merka et al.* [2005] bow shock for an Alfvén Mach number range of 2–20. Four symbols represent the four HFA categories: young HFA, mature HFA, young SHFA, and mature SHFA (open diamond, filled-in diamond, open circle, and filled in circle respectively). The color of each HFA or SHFA corresponds to the largest temperature measured inside each HFA. . . . 73

Figure 5.2 (a) and (b): The ratios of the minimum density of the HFA or SHFA core to the local solar wind density are plotted with respect to the events' magnetic local time (MLT). Panel (a) shows SHFAs and (b) shows HFAs. (c) and (d): Ratio of ion temperatures of HFAs or SHFAs to the local solar wind ion temperature are plotted with respect to the events' MLT. Panel (c) shows SHFAs and (d) shows HFAs. Four symbols represent the four HFA categories: young HFA, mature HFA, young SHFA, and mature SHFA (open diamond, filled-in diamond, open circle, and filled in circle respectively). SHFAs are shown in green, HFAs are shown in black. Red lines indicate the median value of data bins along the x axis. 75

Figure 5.3 HFAs and SHFAs identified in THEMIS C data, August 2007 to December 2009, plotted with respect to the events' distance upstream from the *Merka et al.* [2005] bow shock. Events have been separated into four categories: young HFA, mature HFA, young SHFA, and mature SHFA. Each bin has been normalized to the amount to time THEMIS spent upstream of the bow shock. THEMIS made observations up to 24.5 R_E upstream of the bow shock. 76

Figure 5.4 (a) and (b): The ratios of the minimum density of the HFA or SHFA core to the local solar wind density are plotted with respect to the events' distance upstream from the *Merka et al.* [2005] bow shock. Panel (a) shows SHFAs and (b) shows HFAs. (c) and (d): The ratios of the maximum event ion temperature to the events' average solar wind ion temperature, (T_{ihfa}/T_{isw}), are plotted in these figure with respect to the events' distance upstream from the *Merka et al.* [2005] bow shock. Panel (c) shows SHFAs and (d) shows HFAs. (e) and (f): The ratio of the events' maximum event ion temperature to the events' average solar wind ion temperature relative to the ratio of the events' maximum event electron temperature to the events' average solar wind electron temperature, $(T_{ihfa}/T_{isw})/(T_{ehfa}/T_{esw})$, are plotted in these figure with respect to the events' distance upstream from the *Merka et al.* [2005] bow shock. Panel (e) shows SHFAs and (f) shows HFAs. Four symbols represent the four HFA categories: young HFA, mature HFA, young SHFA, and mature SHFA (open diamond, filled-in diamond, open circle, and filled in circle respectively). SHFAs are shown in green, HFAs are shown in black. Red lines indicate the median value of data bins along the x axis. 78

Figure 5.5 Analysis of HFAs and SHFAs with respect to IMF cone angle. The 136 HFAs were separated into 4 categories (young HFA, mature HFA, young SHFA, and mature SHFA) and binned with respect to the average IMF cone angle in the local solar wind for each event. Each bin was normalized with respect to the amount of time that THEMIS C saw solar wind of that angle from 2007–2009. Color coded error bars for each HFA category are plotted. 80

Figure 5.6 Analysis of HFAs and SHFAs with respect to IMF spiral angle. The 136 HFAs were separated into 4 categories, young HFA, mature HFA, young SHFA, and mature SHFA and binned with respect to the average IMF spiral angle in the local solar wind for each event. Each bin was normalized with respect to the amount of time that THEMIS C saw solar wind of that angle from 2007-2009. Color coded error bars for each HFA category are plotted. The vertical axis has been clipped to 0.0025 because the error bars on any bars that extended above 0.0025 are large enough that those bars can be ignored in the analysis. 81

Figure 5.7 The number of HFAs in each solar wind speed bin is normalized by the amount of time there is solar wind of that speed. Four colors represent the four HFA categories: young HFA, mature HFA, young SHFA, and mature SHFA. Error bars for each of the 4 HFA categories are plotted. . . 82

Figure 5.8 This figure plots the thermal energy increase of each HFA or SHFA compared to its kinetic energy decrease (as compared to the solar wind). The HFAs and SHFAs are identified from THEMIS C data from 2008. The green and black symbols refer to SHFAs and HFAs respectively. Open and filled symbols refer to young and mature events respectively. Dotted black line on the plot is the one-to-one diagonal. Red horizontal lines mark the median value of data bins along the x axis. 84

Figure 6.1 The orbits of THEMIS A, B, C, D, and E on 10 August 2007 from 21:15 to 21:21 UT are shown as the short thick lines on the XY, XZ, and YZ GSM planes. The locations at time 21:15 UT are represented by the symbols as indicated in the legend. Yellow, green, cyan, blue, and purple correspond to THEMIS A, B, C, D, and E respectively. 89

Figure 6.2 From top to bottom, each row shows the on board moment parameters of the HFA as observed by THEMIS A on 10 August 2007: magnetic field components, total magnetic field, density, particle velocity components, ion temperature, and electron temperature. Figure shows 21:10 to 21:21 UT. Vertical orange line marks the leading edge of the HFA, vertical magenta line marks the TD, and the vertical blue line marks the shock. . 90

Figure 6.3 From top to bottom, each row shows the on board moment parameters of the HFA as observed by THEMIS B on 10 August 2007: magnetic field components, total magnetic field, density, particle velocity components, ion temperature, and electron temperature. Figure shows 21:10 to 21:21 UT. Vertical orange line marks the leading edge of the HFA, vertical magenta line marks the TD, and the vertical blue line marks the shock. . 90

Figure 6.4 From top to bottom, each row shows the on board moment parameters of the HFA as observed by THEMIS C on 10 August 2007: magnetic field components, total magnetic field, density, particle velocity components, ion temperature, and electron temperature. Figure shows 21:10 to 21:21 UT. Vertical orange line marks the leading edge of the HFA, vertical magenta line marks the TD, and the vertical blue line marks the shock. . 91

Figure 6.5 From top to bottom, each row shows the on board moment parameters of the HFA as observed by THEMIS D on 10 August 2007: magnetic field components, total magnetic field, density, particle velocity components, ion temperature, and electron temperature. Figure shows 21:10 to 21:21 UT. Vertical orange line marks the leading edge of the HFA, vertical magenta line marks the TD, and the vertical blue line marks the shock. . 91

Figure 6.6 From top to bottom, each row shows the on board moment parameters of the HFA as observed by THEMIS E on 10 August 2007: magnetic field components, total magnetic field, density, particle velocity components, ion temperature, and electron temperature. Figure shows 21:10 to 21:21 UT. Vertical orange line marks the leading edge of the HFA, vertical magenta line marks the TD, and the vertical blue line marks the shock. . 92

Figure 6.7 Each row shows the magnetic field as observed by ACE, Wind, and THEMIS C on 10 and 11 August 2007. THEMIS C data is shown in black, ACE is shown in red, and Wind is shown in purple. ACE and Wind have both been shifted forward in time. From top to bottom, the rows show B_x, B_y, and B_z in GSM, total magnetic field B_t, cone angle, and clock angle. Figure shows 21:00 UT on 10 August 2007 to 1:00 UT on 11 August 2007. 94

Figure 6.8 The orientation of representations of the HFA TD and shock in the XZ GSM plane. Yellow, green, cyan, blue, and purple correspond to THEMIS A, B, C, D, and E respectively. The colored arrows are along the TD normal directions for each THEMIS spacecraft. The symbols represent their positions from 21:15:54–21:17:47 UT on 10 August 2007. The boundary lines shown are the intersection line of the $y = y_{\text{spacecraft position}}$ plane and the planes perpendicular to the TD normal (dashed line) and shock normal (dot and dashes line). The direction of the TD normal at THEMIS B is labeled in green. The distance between THEMIS A and B is drawn as the dashed purple line. That distance projected onto the THEMIS B TD normal is the solid purple double headed arrow. 97

Figure 6.9 The orientation of representations of the HFA TD and shock in the XZ GSM plane. Yellow, green, cyan, blue, and purple correspond to THEMIS A, B, C, D, and E respectively. The colored arrows are along the shock normal directions for each THEMIS spacecraft. The symbols represent their positions from 21:15:54–21:18:36 UT on 10 August 2007. The boundary lines shown are the intersection line of the $y = y_{\text{spacecraft position}}$ plane and the planes perpendicular to the TD normal (dashed line) and shock normal (dot and dashes line). The direction of the TD normal at THEMIS B is labeled in green. The distance between THEMIS A and B is drawn as the dashed purple line. That distance projected onto the THEMIS B TD normal is the solid purple double headed arrow. 99

Figure 6.10 The boundaries of the HFA, the leading edge boundary, TD, and shock are plotted showing their locations at 21:15:54, 21:17:47, and 21:18:36 UT on 10 August 2007. The green planes represent the location of the leading edge boundary. The blue planes represent the locations of the TD. The red planes represent the locations of the shock. The symbols in the middle of the planes are the locations of the THEMIS satellites during its observation of the HFA. Yellow, green, cyan, blue, and purple symbols correspond to THEMIS A, B, C, D, and E respectively. 101

Figure 6.11 The orientation of the bow shock and representations of the HFA leading edge boundary, TD, and shock in the XZ GSM plane. The solid black curves are the *Merka et al.* [2005] model bow shock for Alfvén Mach number range of 2-20. Yellow, green, cyan, blue, and purple correspond to THEMIS A, B, C, D, and E respectively. The symbols represent their positions at 21:15:54, 21:17:47, and 21:18:36 UT on 10 August 2007. The boundary lines shown are the intersection line of the $y = y_{\text{spacecraft B position}}$ plane and the planes perpendicular to the leading edge normal (dotted line), TD normal (dashed line), and shock normal (dot and dashes line). 102

Figure 6.12 The orientation of the bow shock and representations of the HFA leading edge boundary, TD, and shock in the XZ GSM plane. The solid black curves are the *Merka et al.* [2005] model bow shock for Alfvén Mach number range of 2–20. Yellow, green, cyan, blue, and purple correspond to THEMIS A, B, C, D, and E respectively. The symbols represent their positions at 21:17:47 UT on 10 August 2007. The boundary lines shown are the intersection line of the $y = y_{\text{spacecraft position}}$ plane and the planes perpendicular to the leading edge normal (dotted line), TD normal (dashed line), and shock normal (dot and dashes line). The HFA dimensions as calculated for THEMIS B, C, D, and E are shown in pink. The HFA dimensions as calculated for THEMIS A are shown in red. 104

Figure 7.1 The locations of THEMIS A, B, C, D, and E, GOES 10, 11, and 12, ACE, and Wind are shown in the XY, XZ, and YZ planes using the GSM coordinate system on 22 August 2007. The colored lines indicate the spacecraft trajectory from 19:00–19:10 UT. The symbols associated with each spacecraft indicate the satellite locations at 19:00 UT. Each set of three plots in (a), (b), and (c) show the XY, XZ, and YZ planes with different axes ranges. The solid black curves are the *Merka et al.* [2005] model bow shock for Alfvén Mach number range of 2 to 20. 109

Figure 7.2 From top to bottom, each row shows the on board moment parameters of the HFA as observed by THEMIS A on 22 August 2007: magnetic field components, total magnetic field, density, particle velocity components, ion temperature, and electron temperature. Figure shows 19:04 to 19:08 UT. Vertical orange line marks the leading edge of the HFA. Vertical magenta line marks the trailing edge of the HFA. 110
Figure 7.3 From top to bottom, each row shows the on board moment parameters of the HFA as observed by THEMIS B on 22 August 2007: magnetic field components, total magnetic field, density, particle velocity components, ion temperature, and electron temperature. Figure shows 19:04 to 19:08 UT. Vertical orange line marks the leading edge of the HFA. Vertical magenta line marks the trailing edge of the HFA. 111
Figure 7.4 From top to bottom, each row shows the on board moment parameters of the HFA as observed by THEMIS C on 22 August 2007: magnetic field components, total magnetic field, density, particle velocity components, ion temperature, and electron temperature. Figure shows 19:04 to 19:08 UT. Vertical orange line marks the leading edge of the HFA. Vertical magenta line marks the trailing edge of the HFA. 111
Figure 7.5 From top to bottom, each row shows the on board moment parameters of the HFA as observed by THEMIS D on 22 August 2007: magnetic field components, total magnetic field, density, particle velocity components, ion temperature, and electron temperature. Figure shows 19:04 to 19:08 UT. Vertical orange line marks the leading edge of the HFA. Vertical magenta line marks the trailing edge of the HFA. 112
Figure 7.6 From top to bottom, each row shows the on board moment parameters of the HFA as observed by THEMIS E on 22 August 2007: magnetic field components, total magnetic field, density, particle velocity components, ion temperature, and electron temperature. Figure shows 19:04 to 19:08 UT. Vertical orange line marks the leading edge of the HFA. Vertical magenta line marks the trailing edge of the HFA. 112

Figure 7.7 Each row shows the magnetic field as observed by ACE, Wind, and THEMIS C on 22 August 2007. THEMIS C data is shown in black, ACE is shown in red, and Wind is shown in purple. ACE and Wind have both been shifted forward in time. From top to bottom, the rows show B_x, B_y, and B_z in GSM, total magnetic field B_t, cone angle, and clock angle. Figure shows 16:30 to 20:00 UT on 22 August 2007. 114
Figure 7.8 The detrended GOES 10 magnetic field data for 18.8 to 19.6 UT on 22 August 2007. The rows from top to bottom show the detrended B_x, detrended B_y, detrended B_z, and the magnetic field magnitude in the GSM coordinate system. The vertical line marks the time that the magnetic field perturbation was observed, 19:09:36UT. 115
Figure 7.9 The detrended GOES 11 magnetic field data for 18.8 to 19.6 UT on 22 August 2007. The rows from top to bottom show the detrended B_x, detrended B_y, detrended B_z, and the magnetic field magnitude in the GSM coordinate system. The vertical line marks the time that the magnetic field perturbation was observed, 19:02:24 UT. 116
Figure 7.10 The detrended GOES 12 magnetic field data for 18.8 to 19.6 UT on 22 August 2007. The rows from top to bottom show the detrended B_x, detrended B_y, detrended B_z, and the magnetic field magnitude in the GSM coordinate system. The vertical line marks the time that the magnetic field perturbation was observed, 19:06:36UT. 116
Figure 7.11 GOES 10, 11, and 12 magnetic footpoints in the northern geographical hemisphere on 22 August 2007 from 19:00–19:10 UT. Footpoints are determined by identifying region where the magnetic field line that passes through the spacecraft intersects the Earth's surface. Plot generated at `https://sscweb.gsfc.nasa.gov/` 117
Figure 7.12 GOES 10, 11, and 12 magnetic footpoints in the southern geographical hemisphere on 22 August 2007 from 19:00–19:10 UT. Footpoints are determined by identifying region where the magnetic field line that passes through the spacecraft intersects the Earth's surface. Plot generated at `https://sscweb.gsfc.nasa.gov/` 118
Figure 7.13 Rankin Inlet SuperDARN radar field of view outlined with the black solid line. The radar is located at the point labeled "RKN". 119

Figure 7.14 Rankin Inlet SuperDARN radar velocity observations made between 19:00–19:12 UT on 22 August 2007. Each scan is a sequence of all beam directions. The value of the velocity is then color-coded and overlaid on a map 120
Figure 7.15 SuperDARN radar large-scale convection maps made at (a) 19:04 and (b) 19:11 UT on 22 August 2007using polar and high latitude radars. The light gray dashed vertical line indicated the direction towards 12 MLT. Plots generated at VT SuperDARN website. 122
Figure 7.16 SuperMAG northern hemisphere ground magnetometer observations on 22 August 2007. Magnetometer stations 65 to 85 degrees magnetic latitude and 6–10 MLT are shown. Observations are shown in the local NEZ coordinate system at the individual magnetometer sites. 123
Figure 7.17 SuperMAG northern hemisphere ground magnetometer observations on 22 August 2007. Magnetometer stations 65 to 85 degrees magnetic latitude and 10–12 MLT are shown. Observations are shown in the local NEZ coordinate system at the individual magnetometer sites. 124
Figure 7.18 SuperMAG southern hemisphere ground magnetometer observations on 22 August 2007. Magnetometer stations -65 to -85 degrees magnetic latitude and 6–12 MLT are shown. Observations are shown in the local NEZ coordinate system at the individual magnetometer sites. . . . 125
Figure 7.19 SuperMAG ground magnetometer observations on 22 August 2007. 37 individual magnetometer sites in the northern hemisphere and 6 in the southern hemisphere. The E component perturbation amplitude of magnetometer data is plotted in the NEZ coordinate system. 128
Figure 7.20 Polar plots of ground level magnetic field perturbations from SuperMAG station data. Stations are plotted as green dots on the map. The maximum horizontal perturbation direction for each station is plotted with a green line. There is a plot for every minute from 19:06–19:11 UT. [Figure courtesy of SuperMAG website] 129

List of Tables

Page

Table 1.1 Typical Solar Wind Parameters at Earth [*Kivelson and Russell*, 1995] 4
Table 1.2 Typical Near Earth Plasma Parameters 5

Table 3.1 THEMIS Orbit Stages, 2007–2009 43
Table 3.2 History and Status of all GOES Satellites 51
Table 3.3 Ground Station Sites and Geomagnetic Locations 53

Table 4.1 Model Bow Shock Coefficients for GPE Coordinate System [*Merka et al.*, 2005] 61

Table 5.1 Percentage of HFAs with Radial IMF in Different Solar Wind Speed Ranges 83

Table 6.1 THEMIS Observations of the HFA Boundaries for Event on 10 August 2007 95

Table 7.1 THEMIS Observations of the HFA Boundaries for Event on 22 August 2007 110
Table 7.2 Time SuperMAG Ground Station Sites Observed Magnetometer Perturbation 127
Table 7.3 Summary of Times Perturbations Observed 22 August 2007 133

List of Acronyms

ACE	Advanced Composition Explorer
AMPTE-UKS	Active Magnetospheric Particle Tracer Explorer-UK Satellite
CSR	Coherent Scatter Radar
EFI	Electric Field Instruments
EM	Electromagnetic
ESA	Electrostatic Analyzers
EUV	Extreme Ultraviolet
FB	Foreshock Bubble
FCB	Foreshock Compressional Boundary
FGM	Fluxgate Magnetometer
GOES	Geostationary Operational Environmental Satellites
GPE	Geocentric Plasma Ecliptic [coordinate system]
GSE	Geocentric Solar Ecliptic [coordinate system]
GSM	Geocentric Solar Magnetic [coordinate system]
HFA	Hot Flow Anomaly
IMF	Interplanetary Magnetic Field
ISR	Incoherent Scatter Radar
MAVEN	Mars Atmosphere and Volatile EvolutioN spacecraft
MESSENGER	MErcury Surface, Space ENvironment, GEochemistry, and Ranging spacecraft
MFI	Magnetic Field Investigation
MHD	Magnetohydrodynamics

MIE	Magnetic Impulse Events
MLT	Magnetic Local Time
MSO	Mercury Solar Orbital [coordinate system]
MVA	Minimum Variance Analysis
RD	Rotational Discontinuity
R_E	Earth Radii
RH	Rankine-Hugoniot
SCM	Search Coil Magnetometers
SHFA	Spontaneous Hot Flow Anomaly
SST	Solid State Telescopes
SuperDARN	Super Dual Auroral Radar Network
TCV	Traveling Convection Vortex
TD	Tangential Discontinuity
THEMIS	Time History of Events and Macroscale Interactions During Substorms
ULF	Ultra-Low Frequency

Acknowledgements

A dissertation is the culmination of knowledge obtained in the course of completing a PhD, but hidden between the lines are the stories of support the student received along the way. First and foremost, I would like to thank my mother Mei and father Herbert for making the sacrifices they did so that I was able to have the opportunities, education, and successes they could not. Thank you to my sister Connie for being a pal to grow up alongside of, even through today.

Thank you to my committee chair and dissertation advisor, Dr. Hui Zhang, for her countless hours of hard work to get me to where I am today. The opportunities you have opened my life up to by accepting me as your student have allowed me to learn so much, to travel around the world, and to meet many incredible scientists. Thank you so much for your patience!

My dissertation committee have been instrumental to getting me though the PhD process; I'm so very appreciative!

- Thank you to Dr. David Sibeck for being an encouraging mentor, even when my progress seemed slow at NASA. Your suggestion to apply to the Jenkins Fellowship program led to experiences around the globe that I will never forget. Your endless suggestions for paper and dissertation modifications really lifted my spirits.

- Thank you to Dr. Antonius Otto for your many, many enlightening comments on my paper drafts and dissertation. The dissertation content benefited greatly from your input.

- Thank you to Dr. Chung Sang Ng for your insightful questions at every committee meeting.

I have a large list of friends who always believed in me, even when I did not. Although I am grateful for and truly believe I learned something for every interaction I had with my friends leading up to and during my PhD years, I want to offer a special thank you to certain people:

- Thomas, we've been friends since kindergarten and I have found it interesting that we talk more during my doctoral degree years than ever before. Thank you for your incredible support through my non-academic endeavors. Thank you for being there. I finally give you permission to call me Doc.

- Amber, thanks for being an anchor I could always turn to in Atlanta.
- Nhi, thanks for always being such a positive person! Thanks for giving me someone to send pictures of cute penguin stuff to.
- Jeff, you were amongst the first people in the world to call me "Dr. Chu". This incredible faith that I would make it really buoyed me up every time.
- Rachel, thanks for being so sweet, always (and for the crochet items!).
- Christy, thanks for finding time to join the group in our crazy antics. I know you are so incredibly busy with life and a demanding career.
- Doug! Thanks for the camaraderie, helping me get through the comps, and helping get through life in general. Times have been great, and I can't wait to see pictures of your post-graduate life. I hope I get to repay your kindness one day.
- Sun, thanks for being my officemate. It can't have been easy a lot of the time since I have my quirks. Thanks for being a friendly face while I was at Goddard! I really appreciate the dissertation template. I hope we get to find delicious food together in the future.
- Min-Shiu and Xuanye, thanks for being the people on the other side of the hall so I did not have to spend dozens of days at a time without speaking to another person. And thank you for sharing your office space when 708G was remodeled; it was nice to have a window for a few weeks.
- Leslie, thank you for dissertation formatting and SuperDARN assistance!
- Narges, thank you for being a no-nonsense source of strength at all the space physics conferences over the years.
- Katariina, thank you for taking me on as a masters degree student so long ago. You have continued to be a fantastic mentor who I really looked forward to seeing at every conference! Thank you for being a fantastic role model as a woman in space physics.
- Kersti, thank you for the many hours I got to relax with you both on the ski trails and at the flight school. They were a needed break from academic work!

- Tom, thanks for all the board games, grilled foods, and diving! Exactly what I needed so many times.

- Nicole, thanks for being a force of nature at the end of this dissertation process! You are awesome and I am really going to miss doing random things around town together.

I do not know what my future holds, but I believe I am a better person for having gone through the doctoral degree program at the University of Alaska Fairbanks. I would like to offer a hearty thank you to those people I have not listed here. There are many; you don't need your names on this page because I certainly remember how you've impacted my life.

I wish to thank the NASA Harriet G. Jenkins Graduate Fellowship Program for their support with grant NNX13AR91H. This work was partially supported by NSF grants AGS-1007449, AGS-1303689, AGU-1303596, and AGS-1352669.

I acknowledge NASA contract NAS5-02099 and V. Angelopoulos for use of data from the THEMIS Mission. Specifically: C. W. Carlson and J. P. McFadden for use of ESA data. K. H. Glassmeier, U. Auster and W. Baumjohann for the use of FGM data provided under the lead of the Technical University of Braunschweig and with financial support through the German Ministry for Economy and Technology and the German Center for Aviation and Space (DLR) under contract 50 OC 0302.

For the ground magnetometer data I gratefully acknowledge: Intermagnet; USGS, Jeffrey J. Love; CARISMA, PI Ian Mann; CANMOS; The S-RAMP Database, PI K. Yumoto and Dr. K. Shiokawa; The SPIDR database; AARI, PI Oleg Troshichev; The MACCS program, PI M. Engebretson, Geomagnetism Unit of the Geological Survey of Canada; GIMA; MEASURE, UCLA IGPP and Florida Institute of Technology; SAMBA, PI Eftyhia Zesta; 210 Chain, PI K. Yumoto; SAMNET, PI Farideh Honary; The institutes who maintain the IMAGE magnetometer array, PI Eija Tanskanen; PENGUIN; AUTUMN, PI Martin Connors; DTU Space, PI Dr. Rico Behlke; South Pole and McMurdo Magnetometer, PI's Louis J. Lanzarotti and Alan T. Weatherwax; ICESTAR; RAPIDMAG; PENGUIn; British Antarctic Survey; McMac, PI Dr. Peter Chi; BGS, PI Dr. Susan Macmillan; Pushkov Institute of Terrestrial Magnetism, Ionosphere and Radio Wave Propagation (IZMIRAN); GFZ, PI Dr. Juergen Matzka; MFGI, PI B. Heilig; IGFPAS, PI J. Reda; University of L'Aquila, PI M. Vellante; SuperMAG, PI Jesper W. Gjerloev.

Much appreciation to the SuperDARN team for making their data available.

Thank you to Barb Hameister for very throughly reviewing my thesis for the graduate school!

Christina Seiman Chu

August 2017

Chapter 1
Introduction

The goals of this dissertation are to present general background knowledge of the regions of space physics, to review properties of foreshock transients from published literature, to discuss the data sources used to perform the analysis in the chapters, to discuss data analysis methods used in this dissertation, present results from a statistical study of hot flow anomaly properties and their local solar wind environment, present an analysis of the spatial structure of a hot flow anomaly, and present an analysis of the magnetospheric and ionospheric signatures of a hot flow anomaly. To start, this chapter lays out an overall description of the physics that determines the interaction of the solar wind with Earth's magnetic environment.

1.1 Earth's Local Space Environment

Earth's local space environment can be described by the interaction of energetic charged particles with magnetic and electric fields. In the vicinity of our planet, the charged particles derive their energy from the Sun or from the solar wind's interactions with Earth's magnetosphere. The solar wind is the stream of charged particles that flow outwards from the Sun and permeates the solar system and interplanetary space. The Earth's magnetosphere is the region dominated by Earth's magnetic field.

The solar wind originates at the Sun, which is at the left of Figure 1.1, and blows outwards to Earth and its magnetosphere, shown on the right of the figure. The solar corona is the extended outer atmospheric layer of the Sun. It is a region where there are hot temperatures of approximately 1.6×10^6 K. The corona has temporal and spatially varying regions of open magnetic field lines called coronal holes. Coronal gas can leave the Sun through these holes to form the fast solar wind. Another source of fast solar wind may be quiet regions of the Sun [*Martens and Cauffman*, 2002]. Slow solar wind sources include the edges of coronal holes, transient reconnections in closed-field streamers, and active regions [*Martens and Cauffman*, 2002].

The solar wind carries with it a frozen-in interplanetary magnetic field (IMF). The magnetic field is considered to be frozen into the solar wind because the magnetic diffusion is negligible [*Baumjohann and Treumann*, 1996]. Assuming a fully ionized plasma, the only collision frequency of concern is the Coulomb collisions between protons and electrons. It takes approximately 3.5 days for solar wind with a typical velocity of 500 km/s to

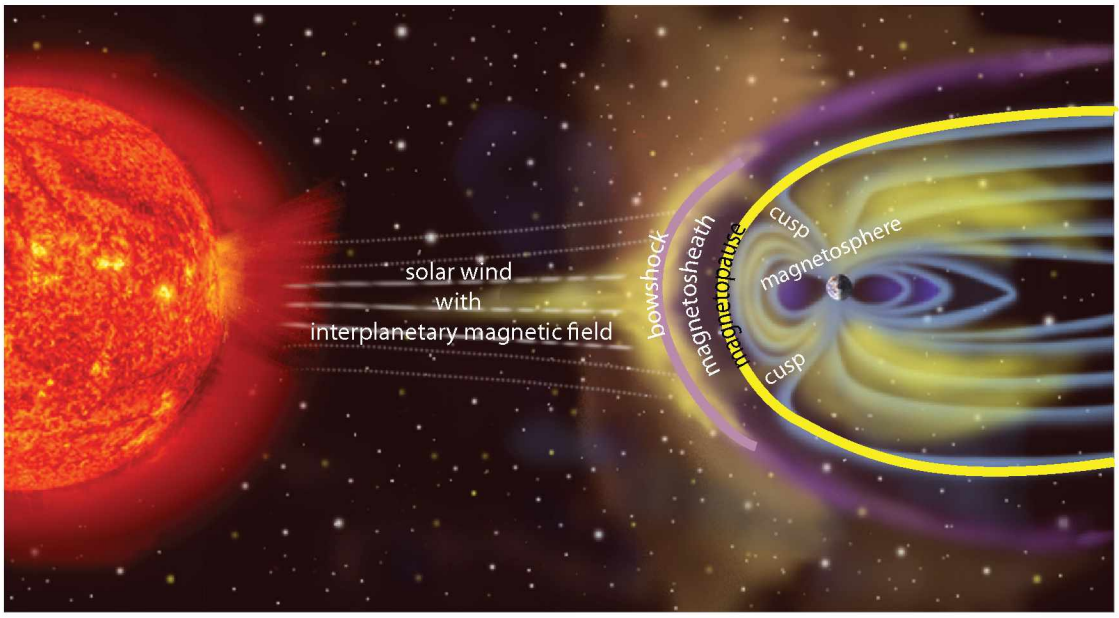

Figure 1.1. Earth's magnetosphere in the noon-midnight plane, artist's representation.

flow across the Sun-Earth distance. Using the magnetic diffusion time equation, one can calculate that the magnetic field only diffuses approximately 10^3 m in the time required for the solar wind to flow from the Sun to the Earth; that essentially makes the magnetic field frozen into the solar wind. According to the frozen-in condition, the magnetic field is carried along with the particle stream from the Sun.

The solar wind flows nearly radially outwards from the surface of the Sun, but at the same time, the solar surface also spins with a nominal 27 day period. This combined effect leads to a twisted interplanetary magnetic field orientation known as a Parker spiral and is represented in Figure 1.2. Figure 1.3 is an artist representation of the Parker spiral, which is also sometimes referred to as a "ballerina skirt", in three dimensions. The IMF orientation at Earth can be characterized with angles such as the spiral angle or cone angle. The spiral angle is the angle that the IMF vector, projected onto the ecliptic plane, makes relative to the Sun-Earth line. The cone angle is the angle between the IMF vector and the Sun-Earth line.

Typical solar wind parameters at Earth are summarized in Table 1.1 [*Kivelson and Russell*, 1995]. Here n is the plasma density, $|B|$ is the magnetic field magnitude, and plasma β is the ratio of thermal plasma pressure to magnetic pressure. As the solar wind moves towards the planet, the Earth's magnetic field acts as an obstacle and pressure increases in front of it. The pressure will distribute itself as a compressional, fast mode wave [*Schwartz*

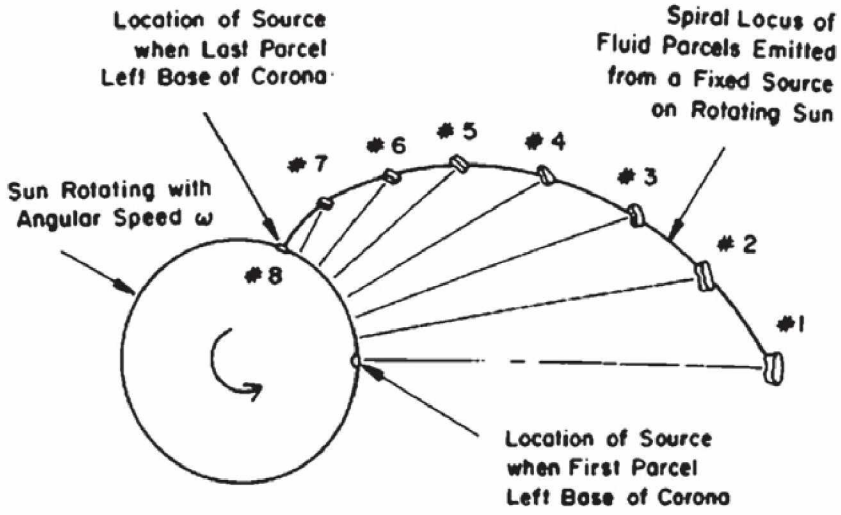

Figure 1.2. Loci of a succession of fluid parcels emitted at constant speed from a source rotating with the Sun [*Kivelson and Russell*, 1995].

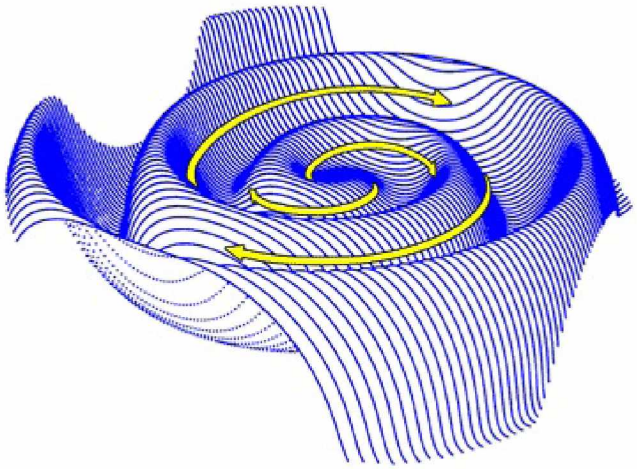

Figure 1.3. Artist representation of Parker spiral interplanetary magnetic field lines originating at the Sun [*"The Sun's Magnetic Field"*, 2012].

Table 1.1. Typical Solar Wind Parameters at Earth [*Kivelson and Russell*, 1995]

Parameter	*Value*	
Proton Density	6.6	cm^{-3}
Electron Density	7.1	cm^{-3}
He^{2+} Density	0.25	cm^{-3}
Flow Speed (radial)	450	km/s
Proton Temperature	1.2×10^5	K
Electron Temperature	1.2×10^5	K
Magnetic Field	7	nT

et al., 1996]. In the solar wind frame, the Earth is approaching faster than the speed of a fast mode wave, so a shock will form in front of the planet, similar to the shock formed in front of supersonic aircraft. This is called the bow shock and it is important because it slows, heats and deflects solar wind flow before it interacts with the Earth's magnetosphere. Bow shocks are further discussed in Section 1.3.

The magnetopause boundary is a sharp current layer separating the Earth's magnetic environment from the solar wind. Its distance from the surface of the Earth is defined by the pressure balance between the dynamic pressure of the solar wind (converted into an equivalent thermal and magnetic pressure applied to the magnetosphere) and the magnetic field pressure of the Earth.

The magnetosheath is the region of shocked, turbulent, subsonic plasma flow between the bow shock and magnetopause, and it may play an important role in the structure of the bow shock and the magnetopause. Its plasma is hotter and denser than the solar wind plasma and the magnetic field strength is also stronger. Magnetosheath material can enter the boundary layers of the magnetosphere through processes such as magnetic reconnection and viscous interactions. Reconnection is a physical process that reconfigures magnetic field topology. Plasma does not get evenly distributed, but forms regions of different temperatures and densities. Typical magnetosheath plasma properties are listed in Table 1.2.

Earth's magnetic environment is the magnetosphere and is the region shown filled with magnetic field lines (blue lines in Figure 1.1). Typical dayside magnetosphere properties are listed in Table 1.2. The magnetosphere is the region around a body dominated

Table 1.2. Typical Near Earth Plasma Parameters

Region	$n\left[\mathrm{cm}^{-3}\right]$	Thermal Energy [eV]	$\lvert B\rvert\,[nT]$	Plasma β
Solar Wind	3–20	∼10	1–30	∼10
Magnetosheath	3–20	∼ 100	∼15	1–10
Magnetosphere	0.1–1	∼ 1000	Varies with distance from planet	Varies with distance from planet
Mantle	0.01–1	100	∼20	0.0001–0.1
Tail Lobe	∼0.01	100	∼20	∼0.0001

by the body's magnetic field. An artistic depiction of Earth's magnetosphere is shown in Figure 1.1. The Sun (figure left) ejects solar wind, consisting of mostly protons and electrons, radially outwards due to the large pressure difference between the hot solar corona and the interstellar medium. The solar wind blows outwards away from the Sun and terminates in interstellar space after it interacts with the weakly ionized interstellar medium [*Baumjohann and Treumann*, 1996].

There are additional atmospheric layers inside of the magnetosphere, between the magnetopause and the ground on Earth. Starting on the ground and moving upwards, the layers stratified by temperature are the thermosphere, stratosphere, mesosphere, thermosphere, and exosphere. The approximate altitudes of the layers are shown in Figure 1.4.

Above the mesosphere and overlapping the thermosphere and exosphere, there is a layer where atmospheric atoms have been ionized to create a region called the ionosphere. This is a region approximately located between 80 and about 600 km above the surface of the Earth. It can be categorized into regions labeled the D (below 90 km), E (between 90 and 130 km), and F (above 130 km) regions. The F region can be subdivided into the F1 and F2 regions because of the ledge that sometimes forms in the electron density profile. In Figure 1.4, the approximate altitudes and electron densities of these layers is shown with the thick solid blue curve in the center of the plot and the axis at the top. Sources of ionization include photons which cause photoionoization and energetic particle precipitation which is also called impact ionization. Photons which cause photoionization, such as extreme ultraviolet (EUV) and x-ray radiation, primarily come from the Sun. Ionizing particles can come from the galaxy as galactic cosmic rays, the sun, the magnetosphere,

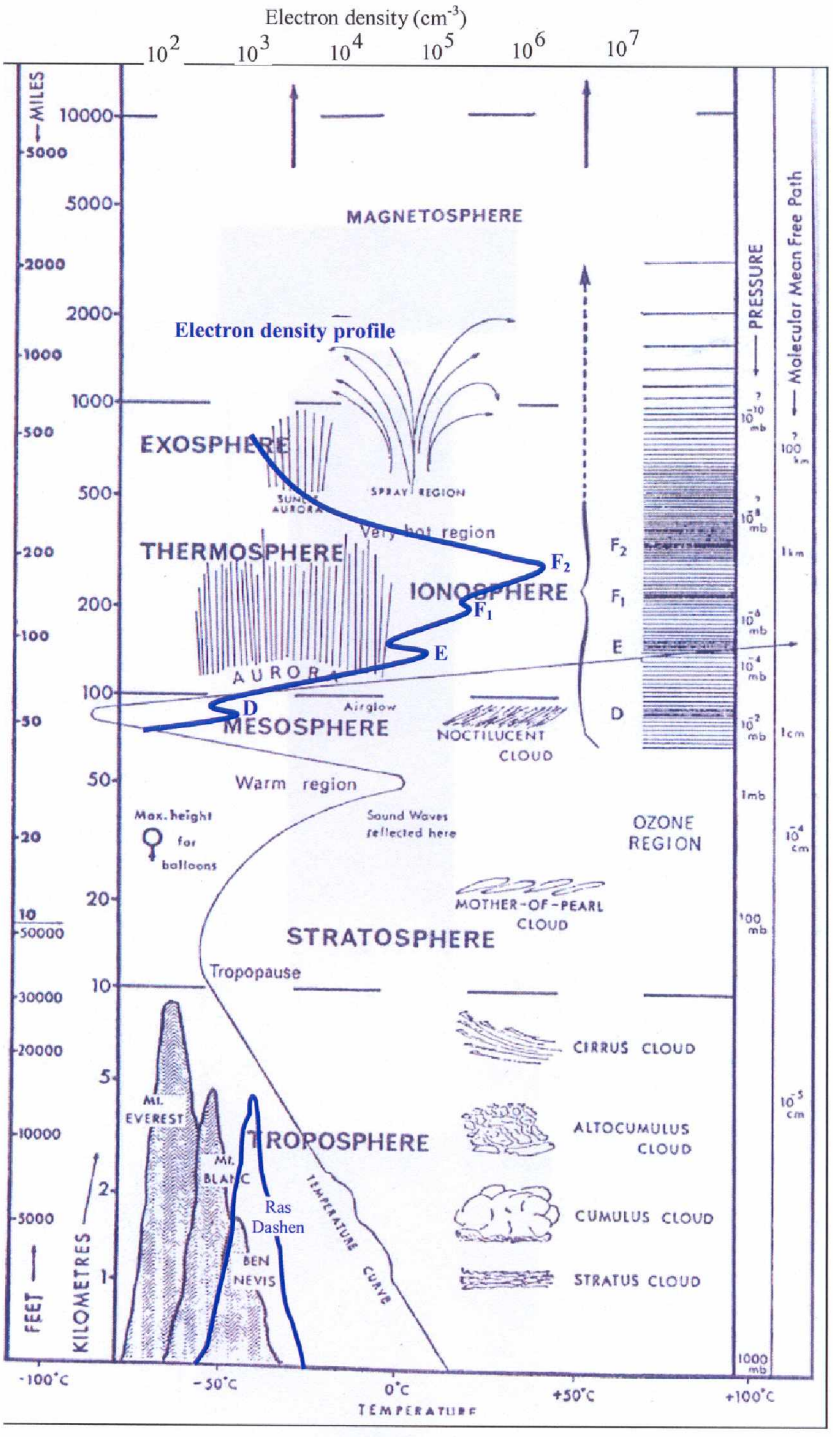

Figure 1.4. The different layers of Earth's atmosphere are plotted. The temperatures of the neutral atmospheric layers is shown with the thin black curve labeled "temperature curve" and the axis on the bottom. The electron densities of the ionosphere layers is shown with the thick solid blue curve in the center of the plot and the axis at the top. Altitude above the ground is on the left axis, and pressure and molecular mean free path are the right axes. [*Yizengaw*, 2017]

and the ionosphere itself if a process for local ion or electron acceleration is operating [*Kivelson and Russell*, 1995].

The ionosphere reflects and modifies radio waves used for communication and navigation. It is the region where aurora are excited in the atmosphere. It is also the region that absorbs the most energetic photons from the Sun and one that reflects radio waves which makes long-distance radio communication possible.

1.2 Boundaries in Space

A boundary in space is an interface that separates regions of space with different characteristics. They are sites for mass, momentum, and energy exchange in space plasmas. A large scale plasma boundary can be defined through discontinuous, macroscopic plasma parameters: density ρ, pressure p, bulk velocity $\mathbf{u}$, magnetic field $\mathbf{B}$, electric field $\mathbf{E}$, and current $\mathbf{j}$. The fields and plasma parameters are not independent across the discontinuity; they satisfy the conditions of Maxwell's equations as well as the conservation of mass, momentum, and energy.

Assuming a single fluid of electrically charged particles which is subject to internal magnetic fields is called magnetohydrodynamics (MHD). A special case of MHD, called ideal MHD, assumes the conditions of ideal Ohm's law

$$\mathbf{E} = -\mathbf{u} \times \mathbf{B} \tag{1.1}$$

and resistivity $\eta = 0$. The assumptions of ideal MHD can be used to derive expressions describing the how plasma parameters change across the boundary, which are known as boundary jump conditions. The transition from one side of the boundary to the other may require dissipation. The discontinuity represents a layer of transition and is a region where dissipation is concentrated. Dissipation is negligible on both sides of the discontinuity.

1.2.1 Rankine-Hugoniot Conditions

The Rankine-Hugoniot (RH) conditions are expressions for the conservation of mass, momentum, and energy across a one-dimensional stationary discontinuity, such as a shock front. There are five conditions which can be derived with the following five equations:

Continuity Equation:

$$\frac{\partial \rho}{\partial t} + \nabla \cdot (\rho \mathbf{u}) = 0 \tag{1.2}$$

Momentum Equation:

$$\rho \frac{\partial \mathbf{u}}{\partial t} + \rho (\mathbf{u} \cdot \nabla) \mathbf{u} = -\nabla p + \mathbf{j} \times \mathbf{B} \tag{1.3}$$

Energy Equation (assuming ideal MHD conditions):

$$\frac{\partial}{\partial t} \left(\frac{\rho u^2}{2} + \frac{p}{\gamma - 1} + \frac{B^2}{2\mu_0} \right) + \nabla \cdot \left(\frac{\rho u^2}{2} \mathbf{u} + \frac{\gamma}{\gamma - 1} p \mathbf{u} + \frac{\mathbf{E} \times \mathbf{B}}{\mu_0} \right) = 0 \tag{1.4}$$

where μ_0 is the vacuum permeability and γ is the polytropic index.

Two of Maxwell's Equations:

Faraday's Law:

$$\nabla \times \mathbf{E} = -\frac{\partial \mathbf{B}}{\partial t} \tag{1.5}$$

Gauss's Law for Magnetic Fields:

$$\nabla \cdot \mathbf{B} = 0 \tag{1.6}$$

A steady, thin, one-dimensional boundary is assumed with parameters $\rho_1, p_1, \mathbf{u}_1, \mathbf{B}_1$ on one side and $\rho_2, p_2, \mathbf{u}_2, \mathbf{B}_2$ on the other. The boundary normal, $\mathbf{n}$, points towards the side with ρ_1. For shocks, it is customary for the shock to point into the unshocked medium [*Schwartz*, 1998].

Since the boundary is steady, Equation 1.2 becomes

$$\nabla \cdot (\rho \mathbf{u}) = 0 \tag{1.7}$$

Equation 1.3 becomes

$$\rho (\mathbf{u} \cdot \nabla) \mathbf{u} = -\nabla p + \mathbf{j} \times \mathbf{B} = -\nabla \left(p + \frac{B^2}{2\mu_0} \right) + \frac{1}{\mu_0} (\mathbf{B} \cdot \nabla) \mathbf{B} \tag{1.8}$$

and Equation 1.4 becomes

$$\nabla \cdot \left(\frac{\rho u^2}{2} \mathbf{u} + \frac{\gamma}{\gamma - 1} p \mathbf{u} + \frac{\mathbf{E} \times \mathbf{B}}{\mu_0} \right) = 0 \tag{1.9}$$

Using Equation 1.1,

$$\mathbf{E} \times \mathbf{B} = (-\mathbf{u} \times \mathbf{B}) \times \mathbf{B} = B^2\mathbf{u} - (\mathbf{u} \cdot \mathbf{B})\,\mathbf{B} \tag{1.10}$$

That leads Equation 1.4 and 1.9 to further evaluate to

$$\nabla \cdot \left(\frac{\rho u^2}{2}\mathbf{u} + \frac{\gamma}{\gamma - 1} p\mathbf{u} + \frac{B^2\mathbf{u} - (\mathbf{u} \cdot \mathbf{B})\,\mathbf{B}}{\mu_0} \right) = 0 \tag{1.11}$$

With a steady boundary, Equation 1.5 becomes

$$\nabla \times \mathbf{E} = 0 \tag{1.12}$$

Using Equation 1.1 it becomes

$$\nabla \times (-\mathbf{u} \times \mathbf{B}) = 0 \tag{1.13}$$

The bracket notation, [ ], is used to indicate the difference of the enclosed quantity between the two sides of the discontinuity such that:

$$\nabla X = 0 \Rightarrow \hat{n}\,[X] = 0 \tag{1.14}$$

$$\nabla \cdot \mathbf{X} = 0 \Rightarrow \hat{\mathbf{n}} \cdot [X] = 0 \tag{1.15}$$

$$\nabla \times \mathbf{X} = 0 \Rightarrow \hat{\mathbf{n}} \times [X] = 0 \tag{1.16}$$

In combination with the bracket notation, the equations become the Rankine-Hugoniot or "jump" conditions:

$$[\rho u_n] = 0 \tag{1.17}$$

$$\left[\rho u_n \mathbf{u} + \left(p + \frac{B^2}{2\mu_0} \right) \hat{\mathbf{n}} - \frac{1}{\mu_0} B_n \mathbf{B} \right] = 0 \tag{1.18}$$

$$\left[u_n \left(\frac{\rho u^2}{2} + \left(\frac{\gamma}{\gamma - 1} \right) p + \frac{B^2}{\mu_0} \right) - \frac{B_n}{\mu_0} \mathbf{u} \cdot \mathbf{B} \right] = 0 \tag{1.19}$$

$$[u_n \mathbf{B_t} - B_n \mathbf{u_t}] = 0 \tag{1.20}$$

$$[B_n] = 0 \tag{1.21}$$

These general Rankine-Hugoniot equations lead to three different families of discontinuities with an explicit set of jump conditions. They are conditions with 1: zero normal

mass flow $v_n = 0$, 2: finite mass flow across the discontinuity but continuous normal flow direction $nv_n \neq 0$ and $[v_n] = 0$, and 3: non-vanishing normal fluxes $nv_n \neq 0$.

1.2.2 Tangential Discontinuity

For a zero normal mass flow and non-vanishing, continuous magnetic field normal to the discontinuity surface, the Rankine-Hugoniot conditions become:

$$u_n = 0 \tag{1.22}$$

$$B_n = 0 \tag{1.23}$$

$$\left[\hat{\mathbf{n}}\left(p + \frac{B^2}{2\mu_0}\right)\right] = 0 \tag{1.24}$$

which is called a tangential discontinuity. The flow is tangential to the boundary, the magnetic field is tangential to the boundary, and the pressure is the same on both sides. The tangential magnetic field and velocity vectors may have arbitrary changes in magnitudes and directions across the discontinuity. Tangential discontinuities are commonly observed in the solar wind. The percentage of TDs versus other types of discontinuities varies with different estimates. *Horbury et al.* [2001] observed that 77% of the discontinuities they analyzed were TDs but other studies have shown 10% to 50–60% were TDs.

1.2.3 Contact Discontinuity

For a zero normal mass flow and continuous tangential magnetic field across the discontinuity, the Rankine-Hugoniot conditions become:

$$u_n = 0 \tag{1.25}$$

$$B_n \neq 0 \tag{1.26}$$

$$[B_n] = 0 \tag{1.27}$$

$$[\mathbf{B_t}] = 0 \tag{1.28}$$

$$[\mathbf{u_t}] = 0 \tag{1.29}$$

$$[p] = 0 \tag{1.30}$$

which is called a contact discontinuity. The flow is tangential to the boundary and a normal component of the magnetic field exists. All plasma parameters except density and temperature are continuous across the contact discontinuity. Because the thermal pressure remains constant across the boundary, any changes in density must be compensated by a change in temperature. Any temperatures jumps are quickly dissipated by electron heat conduction. Contact discontinuities do not persist for very long times.

1.2.4 Rotational Discontinuity

For a finite mass flow across the discontinuity but continuous normal flow direction, the Rankine-Hugoniot conditions become:

$$u_n = \frac{B_n}{\sqrt{\mu_0 \rho}} \tag{1.31}$$

$$[\rho] = 0 \tag{1.32}$$

$$[p] = 0 \tag{1.33}$$

$$[B_n] = 0 \tag{1.34}$$

$$\left[B^2\right] = 0 \tag{1.35}$$

$$[u_n] = 0 \tag{1.36}$$

$$\left[\mathbf{u_t} - \frac{\mathbf{B_t}}{\sqrt{\mu_0 \rho}}\right] = 0 \tag{1.37}$$

which is called a rotational discontinuity. Across the boundary, there is a finite normal mass flow and continuous u_n which means there cannot be a jump in density. Because B_n and u_n are constant, the tangential components are required to rotate together across the boundary.

1.2.5 Shocks

For non-vanishing normal fluxes across a discontinuity, the Rankine-Hugoniot conditions describe shocks. Shocks are defined as nonlinear waves of plasma. They are places where plasma and fields go through abrupt changes in parameters including field strength, tem-

perature, density, and flow speed. A shock is an irreversible, entropy increasing, wave that causes a transition from supersonic to subsonic flow.

Shocks are characterized by a non-vanishing normal plasma flow, $u_n \neq 0$ accompanied by compression and dissipation. Shocks can be further divided into the categories of fast shocks or slow shocks. Fast shocks exhibit an increase in magnetic field magnitude and the field vector bends away from the shock normal. Kinetic energy is converted to thermal and magnetic energy. Slow shocks exhibit a decrease in magnetic field magnitude and the field vector bends towards the shock normal.

Shocks can be described with the parameter Mach number. The sonic Mach number of a shock is the ratio of the flow speed to the sound speed [*Kivelson and Russell*, 1995], specifically the ratio of the speed of the shock along the shock normal to the speed of sound in the medium upstream of the shock [*Schwartz*, 1998]. There are multiple Mach numbers which can be calculated. The fast and slow Mach numbers are the ratios of the normally incident flow speed to the fast and slow MHD wave speeds, respectively, in the upstream medium. Wave speeds depend on propagation direction because MHD modes are non-isotropic [*Schwartz*, 1998]. The Alfvén Mach number is often used to characterize a shock and is independent of the plasma propagation direction. It is written as

$$M_A = \frac{|\mathbf{V_u} \cdot \hat{\mathbf{n}}|}{|\mathbf{B_u}| \sqrt{\mu_0 \rho_u}} \tag{1.38}$$

where $\mathbf{V_u}$ is the velocity, $\mathbf{B_u}$ is the magnetic field, ρ_u is the density. The intermediate Mach number, $M_A \sec \theta_{Bnu}$, where θ_{Bnu} is the angle between the upstream magnetic field and the shock normal, is an upper limit to the slow Mach number. There is no upper limit to the fast Mach number. Above the critical shock number, simple resistivity cannot provide the total shock dissipation. The critical shock number is the value above which a shock is supercritical, below which a shock is subcritical. Supercritical shocks typically have reflected ions present due to the ion dynamics. Subcritical shocks typically only have reflected ions at low fractional densities. The Earth's bow shock is usually a supercritical one [*Kivelson and Russell*, 1995]. The critical Mach number is ~ 2.7 for $\theta_{Bnu} = 90^\circ$ and decreases as θ_{Bnu} decreases. The Earth's bow shock typically has a Mach number of 1.5–10. Shocks in space plasma are almost always collisionless shocks.

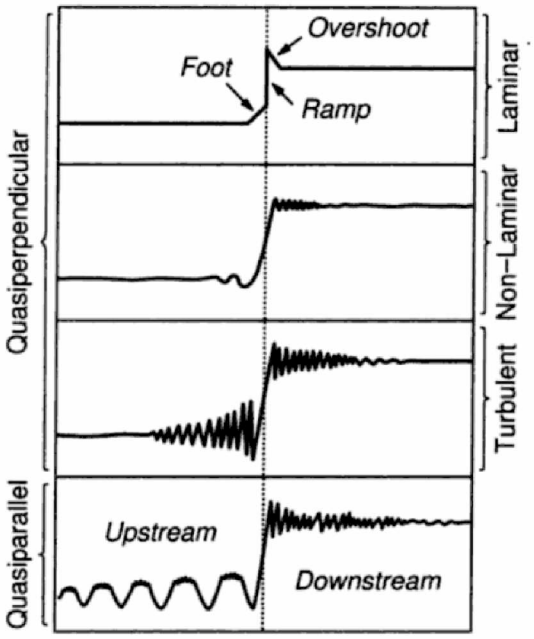

Figure 1.5. Typical magnetic shock profiles [*Baumjohann and Treumann*, 1996]

1.3 Bow Shock

Bow shocks may be characterized as quasi-parallel or quasi-perpendicular depending on how the upstream magnetic field vector is oriented relative to the shock normal where the field lines touch the bow shock. It should be noted that the properties described in this section are caused by kinetic physics and are not in the MHD description.

A quasi-parallel shock is a shock where the angle between the shock normal and the upstream magnetic field direction lies between 0° and 45°. These shocks allow a more efficient escape of energized particles than the quasi-perpendicular shock described below. Small variations in the upstream magnetic field orientation are amplified by the shock and will generate turbulence. A typical quasi-parallel shock is shown in the bottom panel of Figure 1.5.

A quasi-perpendicular shock is a shock where the angle between the shock normal and the upstream magnetic field direction is between 45° and 90°. Particles reflecting off this type of shock cannot travel far into the upstream region because the gyro motion brings them back into the shock. These shocks typically exhibit a shock foot where the magnetic field gradually increases in magnitude in front of the main shock. Behind the main ramp of the shock, the shock will show an overshoot in magnetic field magnitude.

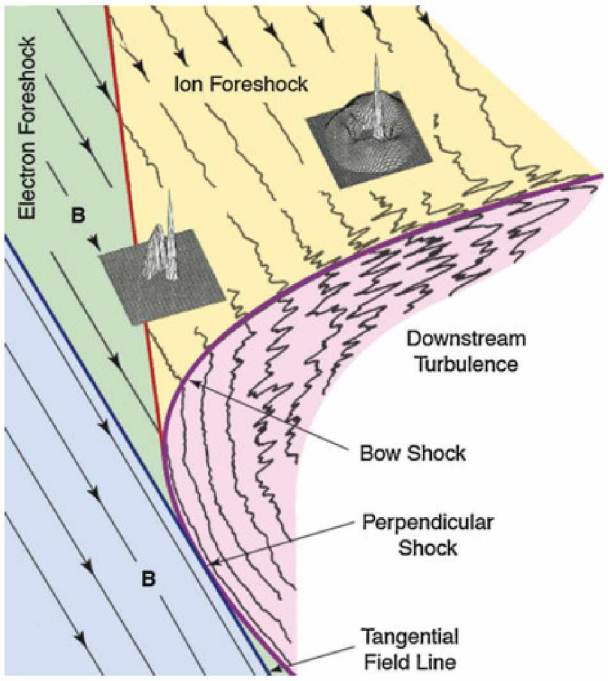

Figure 1.6. Earth's foreshock in the equatorial plane, artist representation [*Balogh and Treumann*, 2013]

The magnetic field magnitude is slightly larger than the asymptotic downstream values. Typical quasi-perpendicular shocks are shown in the top three panels of Figure 1.5.

1.4 Foreshock

Upstream of the bow shock is a very turbulent region called the foreshock [*Balogh and Treumann*, 2013]. This region contains particles and waves associated with the shock. This region is filled with reflected particles gyrating sunward along the magnetic field lines. There is both an ion and electron foreshock as shown in Figure 1.6 which are each filled with their respective particles. Electrons have significantly less mass than ions so the electron foreshock extends further upstream than the ion foreshock because reflected electrons can travel further upstream. The IMF orientation is important for determining the location of the foreshock. Figure 1.6 shows a Parker spiral orientation with IMF approximately 45° to the Sun-Earth line. If the IMF were aligned approximately 0°, radially along the Sun-Earth line, the foreshock would not be limited to the dawn side location as shown in the figure, but the foreshock would encompass the entire dayside [*Blanco-Cano et al.*, 2009].

There are many types of transient phenomena upstream of the bow shock which look similar in satellite data. The next chapter will discuss hot flow anomalies (HFAs), foreshock bubbles, foreshock cavities, foreshock cavitons, and foreshock compressional boundaries.

Chapter 2
Foreshock Transients

This chapter discusses different types of foreshock transients identified in spacecraft data. Hot flow anomalies are introduced and the importance of studying them is discussed. This chapter concludes with a discussion of how this dissertation is organized.

2.1 Common Coordinate Systems of Space Physics

Two common coordinate systems used in space physics are the Geocentric Solar Ecliptic (GSE) and Geocentric Solar Magnetic (GSM) coordinate systems. Both systems have their origin at the center of the Earth. In the GSE coordinate system, the x axis points from Earth to the Sun, y axis is in the ecliptic plane pointing towards dusk (direction opposing planetary motion), and the z axis is parallel to ecliptic pole in addition to being orthogonal to x and y. In the GSM coordinate system, the x axis points from Earth to the Sun, the z axis is the projection of the dipole axis on the GSE YZ plane, and the y axis is orthogonal to both the x and z components.

2.2 Overview of Foreshock Transients

2.2.1 Hot Flow Anomalies

Hot flow anomalies are kinetic plasma phenomena that can be observed outside of a bow shock. HFAs were first observed in in-situ satellite data near the Earth's bow shock. They are characterized by a significant increase in particle temperature and substantial flow deflection from the solar wind flow direction corresponding to a decrease in density. HFA formation is typically associated with the interaction of a tangential discontinuity with the back-streaming ions reflected from the bow shock. HFAs are discussed in more detail starting with Section 2.3.

2.2.2 Foreshock Bubbles

It has been suggested that foreshock bubbles (FBs) are formed via the interaction of some rotational discontinuities with the ions back-streaming from the bow shock [*Omidi et al.*, 2010]. The core of the structure has decreased magnetic field magnitude and density from solar wind values. The trailing edge has a fast magnetosonic shock. Although foreshock bubbles are mostly associated with rotational discontinuities, *Liu et al.* [2015] reported

observations of foreshock bubbles formed with tangential discontinuities. *Turner et al.* [2013] reported that some key differences between HFAs and foreshock bubbles include the following:

1. HFAs formation requires an IMF discontinuity to intersect the bow shock while FB formation does not,
2. HFAs are typically a few Earth radii (R_E) in width normal to the discontinuity and form at the bow shock whereas FBs can be larger than 10 R_E in width and form far upstream of the bow shock,
3. HFAs move along the bow shock with the discontinuity intersection but FBs convect with the solar wind,
4. Foreshock bubbles may accelerate electrons to higher energies than HFAs,
5. HFAs require the electric field on one or both sides of the discontinuity to be pointed back into it but FBs do not.

The work does not provide a broad look at accelerated electron energies to distinguish FBs from HFAs. All the points listed in *Turner et al.* [2013] are not universally agreed upon and that will be discussed in Chapter 8.

2.2.3 Foreshock Cavities

Foreshock cavities are narrow regions of density and magnetic field decreased from that of the solar wind which are bounded by enhanced density and magnetic field [*Sibeck et al.*, 2002]. The bulk flow within foreshock cavities is slightly less than that of the solar wind. Temperature and pressure inside are slightly greater than that in the solar wind [*Omidi et al.*, 2013a].

2.2.4 Foreshock Cavitons

Foreshock cavitons are non-linear structures similar to foreshock cavities but are observed in a sea of ultra-low frequency waves (ULF) [*Blanco-Cano et al.*, 2009]. They are structures with large depressions in density and magnetic field magnitude near the bow shock bounded by enhanced magnetic fields. Hot diffuse ions are observed in the core of the structures. They are presumedly formed by the nonlinear interaction of foreshock waves.

2.2.5 Foreshock Compressional Boundaries

Foreshock compressional boundaries (FCB) were first reported in hybrid simulations [*Sibeck et al.*, 2008]. Hybrid simulations treat ions as kinetic particles and electrons as a massless fluid. Foreshock compressional boundaries form on the edges of the foreshock in response to plasma heating and expansion within the foreshock resulting from strong wave-particle interactions. They are associated with strong compressions of density and magnetic field followed by decreases in both parameters below solar wind levels. The core is filled with suprathermal particles. *Omidi et al.* [2009] used hybrid simulations to show that the formation and strength of a foreshock compressional boundary depends on the generation and nonlinear evolution of ULF waves which were produced by the interaction of back-streaming foreshock ions with the solar wind. With global hybrid models, *Omidi et al.* [2013a] generated FCBs that are part of a foreshock cavity structure. *Omidi et al.* [2009] show that the plasma and magnetic field perturbations associated with FCBs increase with increasing Mach number. FCBs exhibit a steepened, shock-like structure at large Mach numbers [*Omidi et al.*, 2009].

This structure is a transition region separating highly disturbed foreshock plasma from the solar wind. [*Rojas-Castillo et al.*, 2013] examined foreshock compressional boundaries observed by the Cluster satellite mission. They observed that there are FCBs that are a transition region from pristine solar wind to the foreshock plasma. There are also FCBs that separate regions of large amplitude waves from regions of high frequency small amplitude waves. FCBs were observed for different solar wind conditions like cone angle and velocity. They also had decelerated and deflected solar wind flow.

2.3 Properties of Hot Flow Anomalies

Schwartz et al. [1985] first reported HFAs as "an active current sheet in the solar wind." *Thomsen et al.* [1986] called HFAs "hot diamagnetic cavities" in their concurrent independent identification and analysis of these events using ISEE satellite data. The *Schwartz et al.* [1985] observations by Active Magnetospheric Particle Tracer Explorer-UK Satellite (AMPTE-UKS) on 30 October 1984 are shown in Figure 2.1. As a spacecraft travels through an HFA, it will see heated plasma bounded by regions of enhanced and variable magnetic field magnitude and density corresponding to a deflection in the flow speed and increase in temperature. The vertical dotted lines in Figure 2.1 at 12:21:00 and 12:23:00

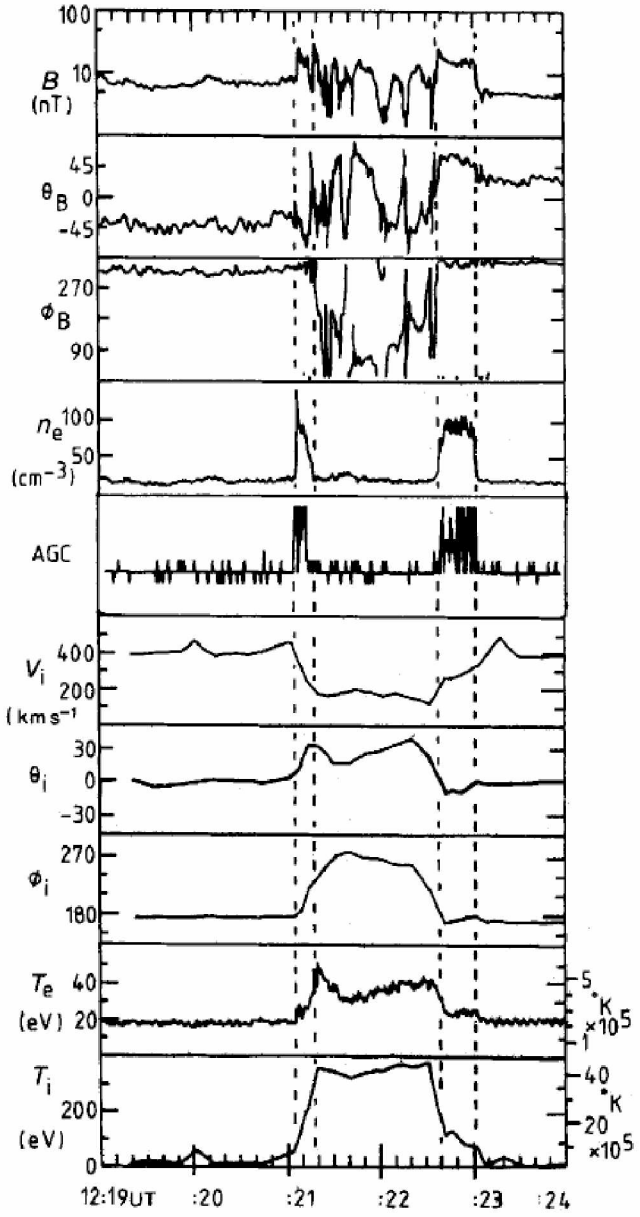

Figure 2.1. Observations of a HFA from *Schwartz et al.* [1985]. Data is from AMPTE-UKS on October 30 1984. From top to bottom, the parameters shown are magnetic field strength, latitude and azimuthal direction in geocentric solar ecliptic (GSE) coordinates (sunward direction is $\theta = 0$, $\phi = 0$ with $\theta = 90$ as northward and, $\phi = 270$ as dawn ward), electron number density, wave autocorrelator gain control level, ion flow velocity, flow latitudinal and azimuthal directions, and electron and ion temperatures.

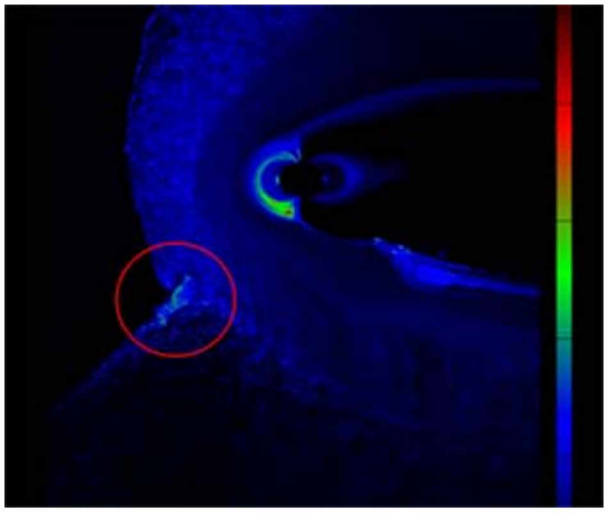

Figure 2.2. A hybrid computer simulation of a hot flow anomaly (region inside red circle) at the bow shock of Earth's magnetic field. Green and red areas closer to Earth are hot plasmas trapped in the Earth's magnetic field. Source: N. Omidi

mark fast shocks on both edges of the HFA. The vertical dotted lines at 12:21:20 and 12:22:40 mark the tangential discontinuities which separate the dense HFA sheath population from the tenuous plasma at the center of an HFA (the sheath is observed between both 12:21:00–12:21:20 and 12:22:40–12:23:00). The ion temperature inside a HFA is typically on the order of magnitude above the electron temperature ($T_i \sim 10^7$ K and $T_e \sim 10^6$ K) and the plasma flow speed typically ranges from about 20% to 50% of the solar wind speed [*Onsager et al.*, 1990].

Figure 2.2 shows a hybrid computer simulation of a hot flow anomaly, which is circled in red. Most notably, this simulation shows a structure extending out into the solar wind from the bow shock region. The colors represent temperature.

Two distinct types of HFAs have been identified, "young" and "mature" [*Thomsen et al.*, 1986; *Lucek et al.*, 2004; *Zhang et al.*, 2010]. Figure 2.3 shows the ion and electron velocity distributions for both mature and young HFAs. HFA observations with two distinct ion populations, both a solar wind and reflected component, have been interpreted as the signatures of an early stage of development (Figure 2.3b), a young HFA. HFA observations with a single hot ion population have been interpreted as the signature of the later stages of a HFA (Figure 2.3a), a mature HFA [*Zhang et al.*, 2010]. Electron distributions are very different for mature and young HFAs. As seen in Figure 2.3e, the solar wind electron distribution is nearly Maxwellian at lower energies. For the mature HFA, the sheath

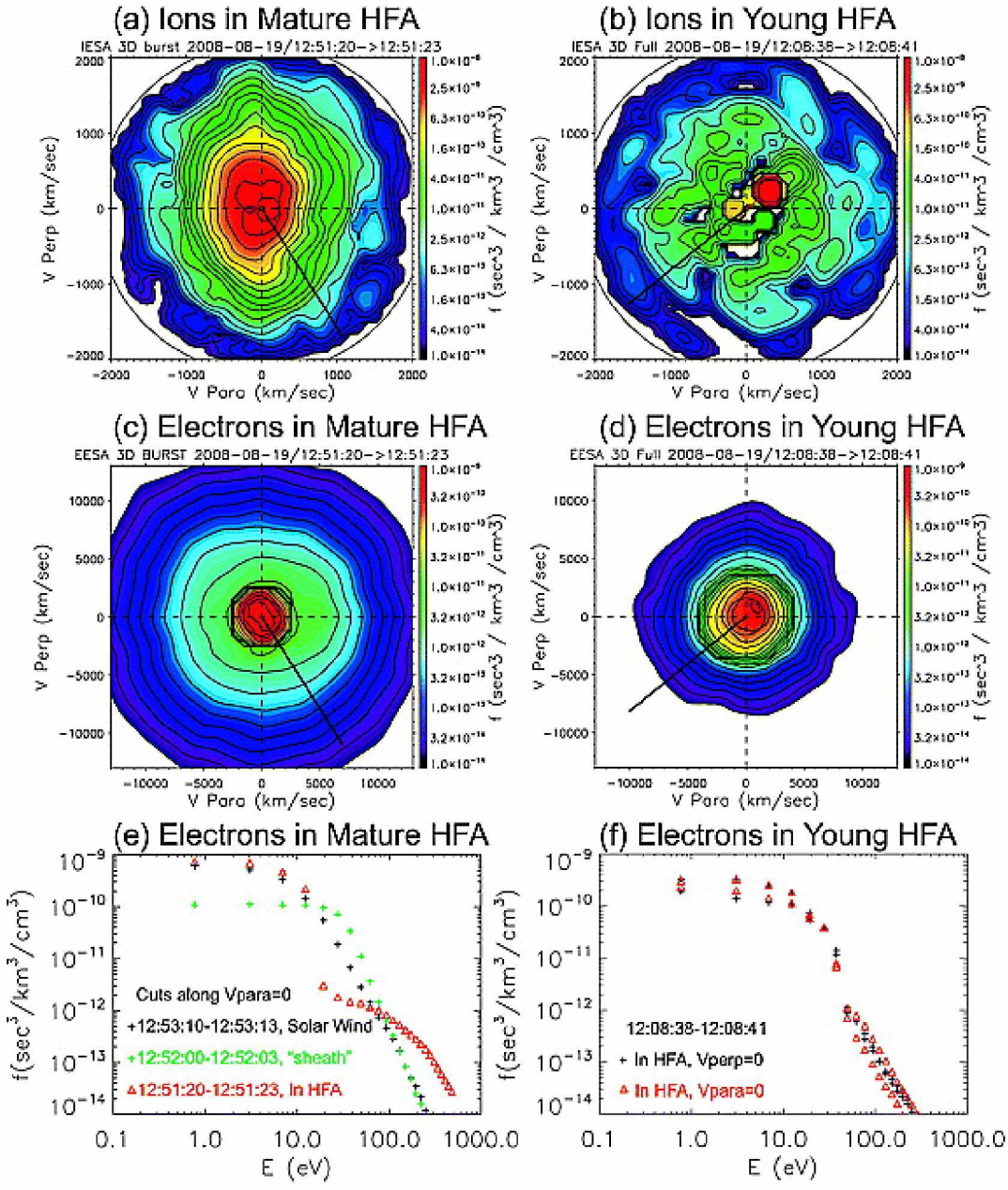

Figure 2.3. Ion velocity distribution plots and electron velocity distribution cut plots for mature and young HFAs observed by THEMIS C from *Zhang et al.* [2010]. The top row shows ion distributions inside a mature (a) and young (b) HFA. The second row shows electron distributions inside a mature (c) and young (d) HFA. The solid black line in figures (a)–(d) point toward the Sun. In the bottom row, (e) shows one dimensional cuts of electron distributions in the solar wind (black crosses), in the HFA sheath region (green crosses), and in the center of a mature HFA. (f) shows one dimensional cuts of the electron distribution of Figure 2.3(d), inside a young HFA. The black crosses and red triangles show the cut along the perpendicular and parallel velocity directions respectively.

shows a flat top spectra, characteristic of Earth's magnetosheath [e.g. *Feldman et al.* 1983]. At the center of both the mature and young HFAs, there is a rounded 's' shape above 10 eV but below 10 eV, the original solar wind shape is maintained [*Thomsen et al.*, 1988; *Zhang et al.*, 2010]. *Eastwood et al.* [2008] has suggested that the electron firehose instability is important for creating isotropic distributions in HFAs.

Figure 2.1 shows the plasma parameters of a mature HFA. Not all mature HFAs show magnetic field and density enhancements on both edges of the event. *Schwartz* [1995] reported that some HFAs show enhancements only on the trailing edge. Figure 2.4 shows the parameters of a young HFA. The young HFA is not characterized by strongly enhanced magnetic field or density. Figure 2.4 shows that young HFAs typically exhibit just a decrease in magnetic field strength and density. They do show a strong deflection in the flow speed like mature HFAs though. *Kecskeméty et al.* [2006] noted that the solar wind is higher on the leading edge of the HFAs observed.

Vaisberg et al. [2016] analyzed the back-streaming ions within a young hot flow anomaly. They examined plasma number density, ion temperature, and ion spectrum and concluded that the reflected beam forms due to the escape of magnetosheath ions. Those ions entered the region where the interplanetary current sheet crosses the bow shock.

Spontaneous hot flow anomalies (SHFAs) were described by *Zhang et al.* [2013]; *Omidi et al.* [2013b] in satellite data and simulations. They are characterized by significantly heated and deflected solar wind plasma, but these are structures that form without the IMF discontinuity usually invoked to explain the existence of a traditional HFA. *Zhang et al.* [2013] reported that one early stage SHFA was characterized by enhanced magnetic field strengths and densities which bound regions of decreased magnetic field strength and density, little evidence of heating or significant flow deflections, and the absence of interplanetary discontinuities. The event evolved to have characteristics of classic HFAs, including depletions in the plasma density and magnetic field strength, suprathermal core temperatures, and highly deflected flows.

2.4 Hot Flow Anomaly Formation

Preceding the observation of an HFA, measurements may show that the solar wind is disturbed with the presence of back-streaming ion beams and/or diffuse ions, indicating a solar wind magnetic connection to the bow shock [*Schwartz et al.*, 1985]. Ions reflected from the bow shock are energized and thought to be trapped in the vicinity of the shock

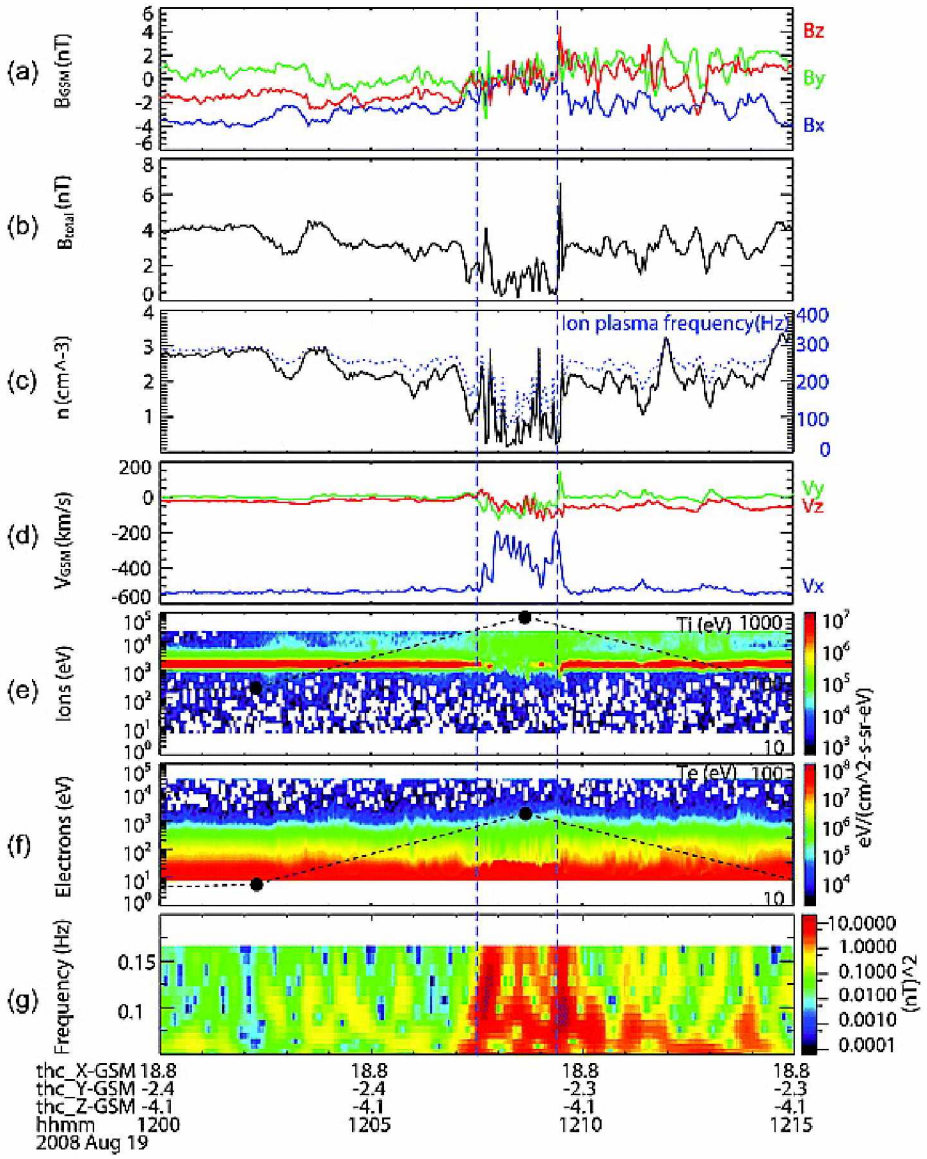

Figure 2.4. Young HFA observed by THEMIS C on 19 August 2008 [*Zhang et al.*, 2010]. From top to bottom, the geocentric solar magnetic (GSM) parameters shown are the three magnetic field components, magnetic field strength, ion density, components of plasma flow, plasma ion spectrum, plasma electron spectrum, and the wavelet analysis result for the B_x component of magnetic field. The blue vertical dashed lines mark the edges of the HFA. The ion plasma frequency is over-plotted in Figure 2.4(c) and the right hand axis with a dashed blue line. The ion and electron temperatures are over-plotted in black dots and the right hand axes in Figure 2.4(e) and (f) respectively.

by tangential discontinuities when the motional electric fields point toward the discontinuity at least on one side [*Thomsen et al.*, 1986]. *Zhao et al.* [2017] found that HFA's are more likely to form when the reflected flow from the bow shock is along the discontinuity. The ions are then thermalized by encounters with the bow shock, creating a high pressure plasma near the intersection of the bow shock and current sheet. The regions of increased temperature then expand against its surrounding medium which leads to a low density and magnetic field strength core flanked by enhanced magnetic field strength and density [*Zhang et al.*, 2010]. Tangential discontinuities in the solar wind have been shown to interact with the bow shock in simulations to generate HFAs [*Thomas et al.*, 1991; *Lin*, 2002]. Magnetic signatures of the tangential discontinuities have often been seen by *Facskó et al.* [2009] in their statistical analysis of 124 HFAs observed by the Cluster spacecraft. Rotational discontinuities have also been cited in the formation of HFAs [*Paschmann et al.*, 1988; *Øieroset et al.*, 2001] although most papers cite tangential discontinuities because that theory is motivated by simulation results [*Thomas et al.*, 1991]. In either case, the discontinuities associated with HFAs can sweep along the bow shock surface rather slowly, allowing time for HFA development [*Schwartz et al.*, 2000].

Zhang et al. [2010] used two spacecraft to study the evolution of a HFA. The plasma parameters for the event are shown in Figure 2.5. THEMIS B was further upstream than THEMIS C for that event. THEMIS B did not observe any flow deflection during the interval but it did observe density and magnetic field decreases (Figure 2.5(b) and (c) respectively) and electron heating (Figure 2.5(e)). Because of the spacecraft location and the typical signatures of HFAs seen, it was proposed that THEMIS B observed a structure which evolved into the typical mature HFA seen by THEMIS C. Analysis of the ion distribution of the proto-HFA showed two major ion populations, a solar wind beam and a beam of ions reflected from the bow shock, consistent with *Thomsen et al.* [1988]'s hypothesis for an HFA's early stages. Their theory goes on to say that strong coupling of the two ion populations converts the relative streaming energy of the two populations to the thermal energy of a single, hot, thermalized ion population [*Thomsen et al.*, 1988].

Schwartz et al. [2000] calculated the HFA occurrence rate at Earth to be about three a day. *Facskó et al.* [2009] suggested that more HFAs occur at high solar wind velocities. Observations indicate that HFAs sometimes exhibit a tendency to form in chains, such as the seven HFAs reported by *Zhang et al.* [2010] within a 12 hour window. The solar wind speed was high for that day ($\sim$600 km/s) which is consistent with *Facskó et al.* [2009]. The

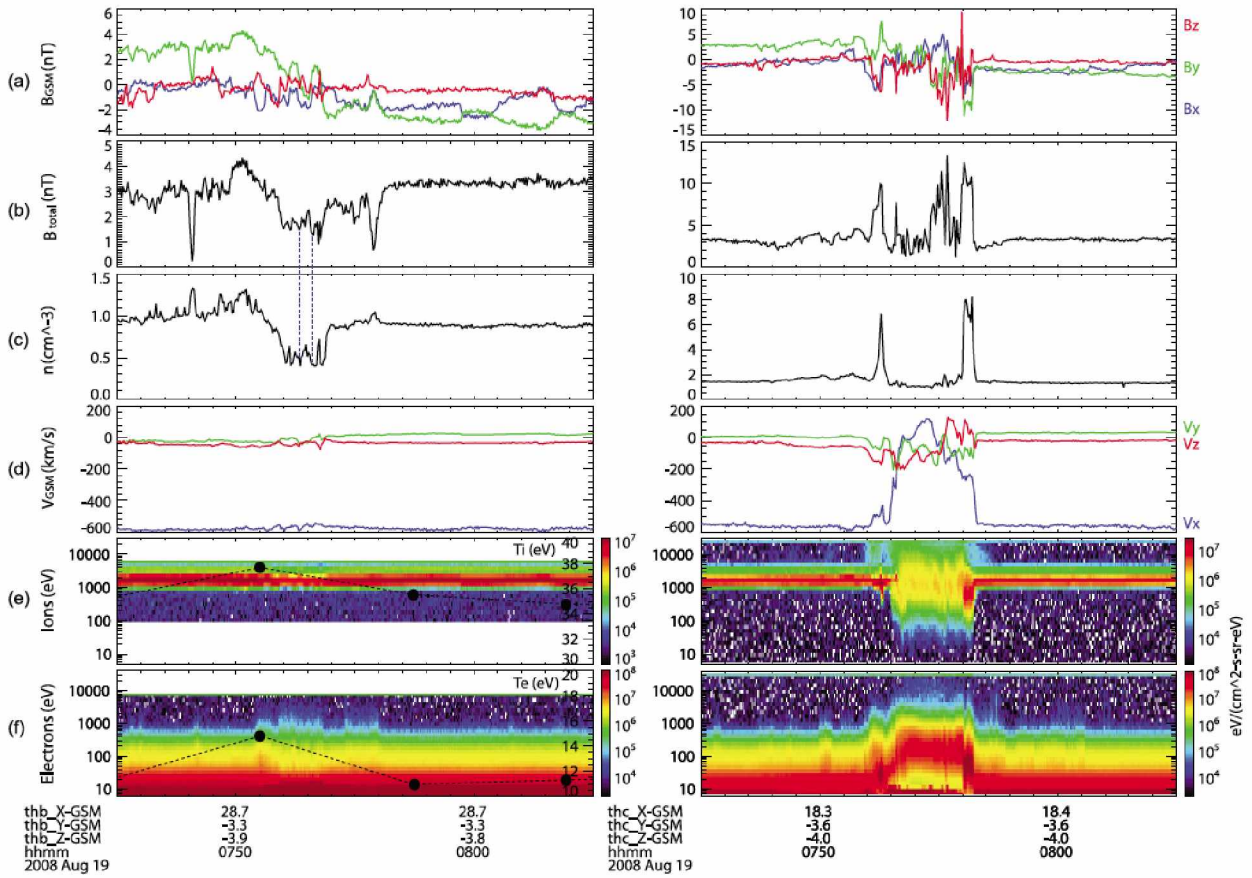

Figure 2.5. A proto-HFA (left) and corresponding mature HFA (right) observed by THEMIS B and C respectively on 19 August 2008 [*Zhang et al.*, 2010]. From top to bottom, the GSM parameters shown are the three magnetic field components, magnetic field strength, plasma density, components of ion flow, plasma ion spectrum, and plasma electron spectrum. The ion and electron temperature measured by THEMIS B are over-plotted in black dots and using the right hand axis in Figure 2.5e and f respectively.

frequency of fast solar wind in the ecliptic plane depends on the solar cycle so the number of HFAs formed is also thought to depend on the solar cycle [*Facskó et al.*, 2009].

2.5 Hot Flow Anomaly Location and Size

An unanswered question about HFAs is what influences where they can be observed. There are HFA events reported that are not embedded in the solar wind, but instead occur between the solar wind and the magnetosheath [*Paschmann et al.*, 1988]. From simulations, *Lin* [2002] showed that the structure of a magnetosheath HFA is similar to a HFA upstream of the bow shock, but the magnetosheath HFA exhibits lower pressures compared to the perpendicular pressure on its boundaries. *Schwartz et al.* [1988] reported that magnetosheath events (as seen by AMPTE UKS) do show strongly deflected flows and hot plasma but do not typically show the edge compressions of plasma and the magnetic field which are observed for events in the solar wind.

Simulations and observations provide conflicting results on whether HFAs occur at quasi-parallel or quasi-perpendicular shocks. *Lin* [2002] showed HFAs forming in the quasi-perpendicular shock region with a global hybrid simulation. *Omidi and Sibeck* [2007] showed HFAs forming in the quasi-parallel shock region with a global hybrid simulation, but not in the quasi-perpendicular region. From a study of 124 HFAs identified using Cluster data from 2003, 2006, and 2007, *Facskó et al.* [2009] found that more than half, ~66%, were found in the quasi-parallel region. *Wang et al.* [2013a] also reported observations of HFAs at both both quasi-parallel and quasi-perpendicular shocks using Cluster data. They found that HFAs with both edges at quasi-perpendicular shocks were closer to the bow shock than HFAs with both edges at quasi-parallel shocks. *Facskó et al.* [2009] also found that HFAs could be identified at greater than 19 R_E from Earth. *Wang et al.* [2013a] reported that HFAs observed with Cluster were observed from 0.57 to 2.82 R_E upstream from the bow shock.

Schwartz et al. [1985] estimated a typical HFA thickness of 15,000 km through ion velocities and a minimum variance analysis to identify the normal direction. *Facskó et al.* [2009] calculated HFA sizes using two different methods. They are described below:

One method used the calculated Alfvén speed. HFAs form through accelerated particle beams that share energy through the electromagnetic ion-ion beam instability. This beam creates Alfvén waves that carry away 1/3 of the energy, meaning only 2/3 of the energy heats the plasma [*Thomas and Brecht*, 1988; *Thomas*, 1989]. The propagation velocity

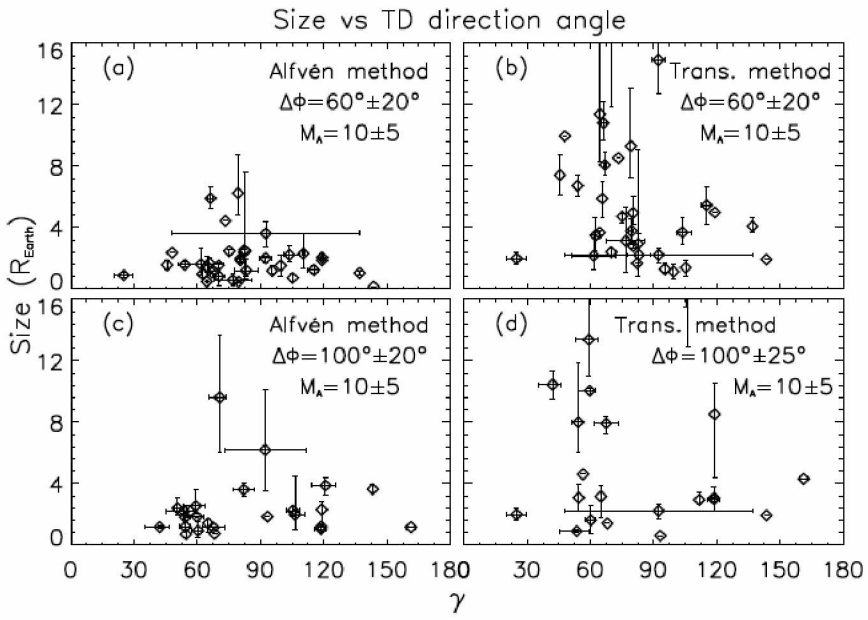

Figure 2.6. The HFA size-γ functions based on the size estimation by Alfvén Mach velocity on the left and the transition speed on the right. The fixed solar wind speed was shown in Alfvén Mach number. (a) $\gamma = 60^\circ \pm 20^\circ$ and $M_A = 10 \pm 5$, (b) $\gamma = 60^\circ \pm 20^\circ$ and $M_A = 10 \pm 5$, (c) $\gamma = 100^\circ \pm 20^\circ$ and $M_A = 10 \pm 5$, (d) $\gamma = 100^\circ \pm 25^\circ$ and $M_A = 10 \pm 5$. All Alfvén Mach numbers were calculated from the actual Alfvén velocity. [*Facskó et al.*, 2009]

of the waves does not exceed the Alfvén velocity, so twice the Alfvén speed multiplied by the time of existence was used to give a lower limit of HFA size. The second method uses the transit velocity of the tangential discontinuity across the surface of the bow shock. Method one yielded a size of 2–3 R_E while the other mostly gave sizes as being on the order of 1 R_E. Discrepancies in the calculations were attributed to the sensitivity of the methods to the accuracy of the data used.

The angle between the tangential discontinuity normal and the Earth-Sun direction was defined as γ by *Lin* [2002]; *Facskó et al.* [2009]. *Lin* [2002] predicted the largest HFA size to be at $\gamma = 80^\circ$ through HFA simulations. *Facskó et al.* [2009] found that the maximum size occurred close to that γ as shown in Figure 2.6. *Lin* [2002]; *Facskó et al.* [2009] defined $\Delta\Phi$ as the change in angle of the magnetic field direction across a tangential discontinuity. *Facskó et al.* [2009] showed that the size of HFAs increased with $\Delta\Phi$, which was consistent with *Lin* [2002] as shown in Figure 2.7. Faster mach numbers corresponded to larger HFA sizes as shown in Figure 2.8.

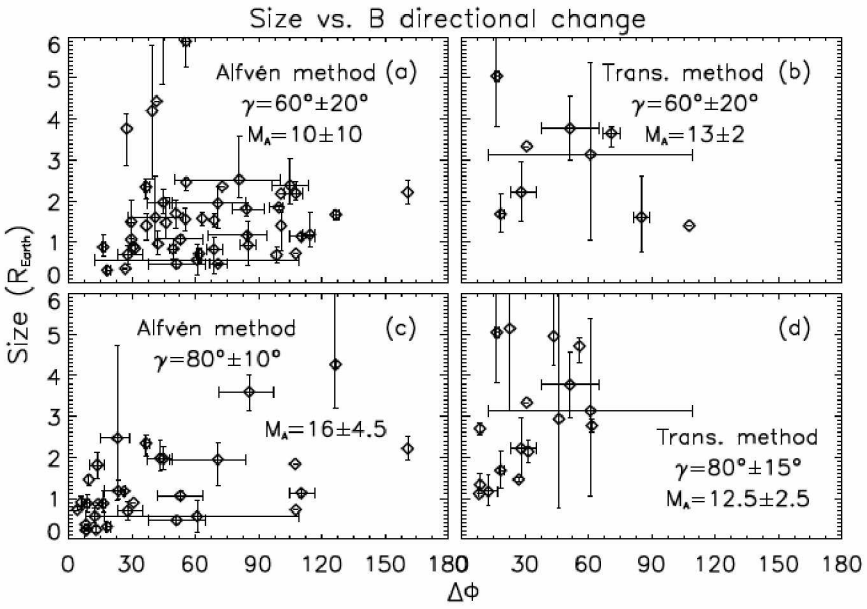

Figure 2.7. The HFA size-$\Delta\Phi$ functions based on the size estimation by Alfvén Mach velocity on the left and the transition speed on the right. The fixed solar wind speed was shown in Alfvén Mach number. (a) $\Delta\Phi = 60^\circ \pm 20^\circ$ and $M_A = 10 \pm 10$, (b) $\Delta\Phi = 60^\circ \pm 20^\circ$ and $M_A = 13 \pm 2$, (c) $\Delta\Phi = 80^\circ \pm 10^\circ$ and $M_A = 16 \pm 4.5$, (d) $\Delta\Phi = 80^\circ \pm 15^\circ$ and $M_A = 12.5 \pm 2.5$. All Alfvén Mach numbers were calculated from the actual Alfvén velocity. [*Facskó et al.*, 2009]

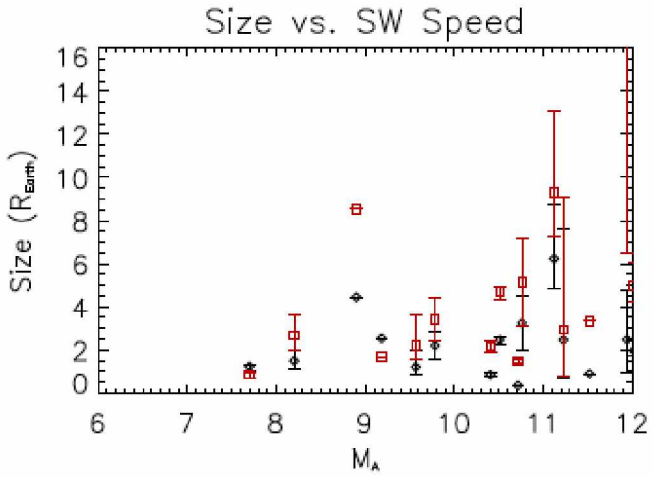

Figure 2.8. The HFA size-velocity functions with Alfvén velocity calculated using ACE and crossing time measured by Cluster. The sizes were calculated using the method based on Alfvén speed (black) and the transition speed (red). The fixed solar wind speed was measured in units of Alfvén Mach number. $\gamma = 80^\circ \pm 10^\circ$ and $\Delta\Phi = 40^\circ \pm 20^\circ$. All Alfvén Mach numbers were calculated from the actual Alfvén velocity. [*Facskó et al.*, 2009]

2.6 Waves and Energetic Particles in Hot Flow Anomalies

HFAs are associated with waves. Low frequency electrostatic waves have been observed outside of events [*Woolliscroft et al.*, 1986; *Fuselier et al.*, 1987]. These waves were interpreted as ion acoustic waves. *Zhang et al.* [2010] reported that both young and mature HFAs are associated with strong electromagnetic waves near the lower hybrid frequency. They suggested that electromagnetic right-hand resonant ion beam instabilities heat ions inside HFAs. It was also suggested that lower hybrid waves are the likely source of electron heating inside HFAs. Other types of waves present in young and mature HFAs may also have a role in particle heating. *Woolliscroft et al.* [1986]; *Fuselier et al.* [1987] found little plasma wave activity inside of HFAs. Wave activity reported with mature HFAs occurs in the HFA boundary layer and could be associated with fast shocks on at least one edge of the structure *[communication with H. Zhang]*.

There are often, but not always, energetic particles present in HFAs [*Hasegawa et al.*, 2012]. Energetic particles have been observed to have been accelerated by a well-defined dispersion structure [*Louarn et al.*, 2003], but without more statistics, it is difficult to know if this is typical HFA behavior *[communication with H. Zhang]*. The frequency of the existence of energetic particles in HFAs and the environmental conditions related to their presence (or lack thereof) is a topic that still needs to be examined.

2.7 Magnetospheric and Ionospheric Effects of Hot Flow Anomalies

HFAs are structures formed from a connection to the bow shock. The core pressure of an HFA is lower than that of the local solar wind and that causes the magnetopause to bulge outwards locally as shown in Figure 2.9. The deformation can generate field-aligned currents into the auroral ionosphere where the signature is measured as magnetic impulse events (MIE) or traveling convection vortices (TCV) [*Sibeck et al.*, 1999; *Eastwood et al.*, 2008; *Jacobsen et al.*, 2009].

Sunward magnetopause motion of 3 R_E due to HFAs in simulations was reported by *Lin* [2002]. *Sibeck et al.* [1999] reported the observation of a 5 R_E sunward magnetopause movement related to HFA passage. *Jacobsen et al.* [2009] reported a 4.8 R_E magnetopause deformation, with flow speeds in the magnetopause normal direction of 800 km/s, driven by a hot flow anomaly upstream of the bow shock. The analysis of more HFA events will quantify if magnetopause motion is typical and how large that motion may be.

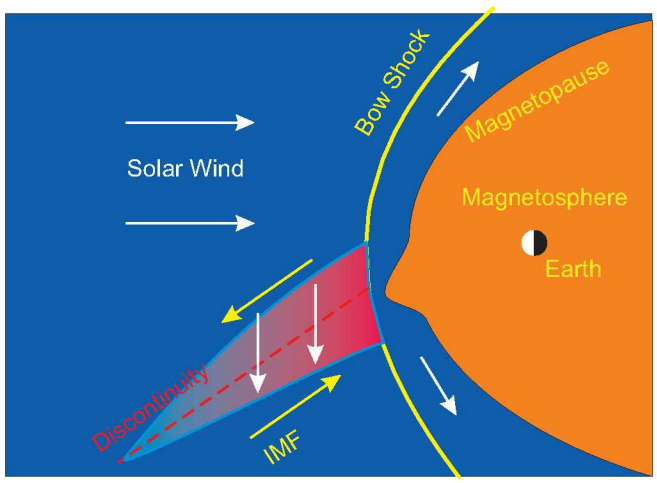

Figure 2.9. Sketch of HFA upstream of the bow shock and a corresponding localized magnetopause deformation. Source: H. Zhang.

The auroral response to HFAs was investigated by *Fillingim et al.* [2011]. The dynamic pressure decrease associated with an HFA causes the magnetopause to deform and that deformation should propagate anti-sunward. Sometimes, brightening of the dayside aurora is observed coincident with HFA or TCV signatures. *Fillingim et al.* [2011]'s survey of 34 HFAs showed that about 60% of events correspond to an increase in auroral brightness. For the events that have clear auroral signatures, the regions of auroral emission are either stationary or slow moving - much slower than the expected MIE or TCV propagation velocity.

Hasegawa et al. [2012] described flux rope signatures in some HFAs which indicate that magnetic reconnection can occur in HFAs. Reconnection may have a large effect on the magnetosphere by controlling plasma entry.

2.8 Hot Flow Anomalies Upstream of Non-Earth Bow Shocks

There has been evidence to suggest that hot flow anomalies are not just events that are observed at Earth's bow shock, but rather, a universal property of shocks. Possible HFAs have also been reported in Mercury [*Uritsky et al.*, 2014], Venus [*Slavin et al.*, 2009; *Collinson et al.*, 2012, 2014], Mars [*Øieroset et al.*, 2001; *Collinson et al.*, 2015], and Saturn [*Masters et al.*, 2009] orbiting satellite's data. Simulations of the boundary of the heliosphere have also shown evidence of HFA formation.

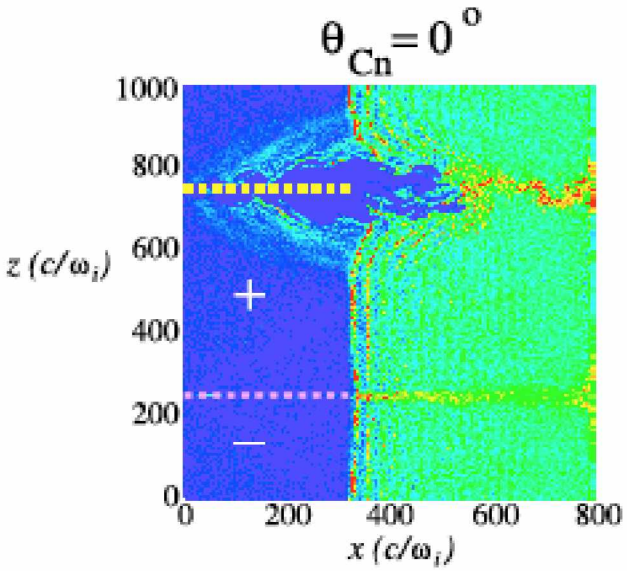

Figure 2.10. Simulation results of a HFA at the termination shock from *Giacalone and Burgess* [2010]. The angle between the current sheet and the shock normal is θ_{Cn}. The current sheets are indicated by the dashed lines. The color indicates the final value of the total plasma density at the end of the simulation. Blue corresponds to densities equal to the starting density whereas red indicates plasma density that is four times the starting density. The direction of the magnetic field is indicated by the "+" (out of the page) and "-" (into the page).

Heliosphere Termination Shock

Giacalone and Burgess [2010] reported the hybrid simulation results in Figure 2.10 showing an HFA at the termination shock of the heliosphere. It is similar to previously reported HFAs except it is dominated by pickup ions rather than specularly reflected ions.

Mercury

Uritsky et al. [2014] presented MErcury Surface, Space ENvironment, GEochemistry, and Ranging satellite (MESSENGER) observations of HFA-like magnetic field depressions upstream of Mercury. This included an observation of signatures of a ULF wave packet during a quasi-parallel shock configuration which was concluded to likely be triggered by an HFA. They concluded that HFA-like events occurred more often on the dawn-side than dusk and that HFAs observed at Mercury had smaller linear sizes than HFAs observed at other planets. Figure 2.11 is an example of a Mercury HFA plasma parameters in MSO coordinates. The Mercury Solar Orbital (MSO) coordinate system defines x from the center

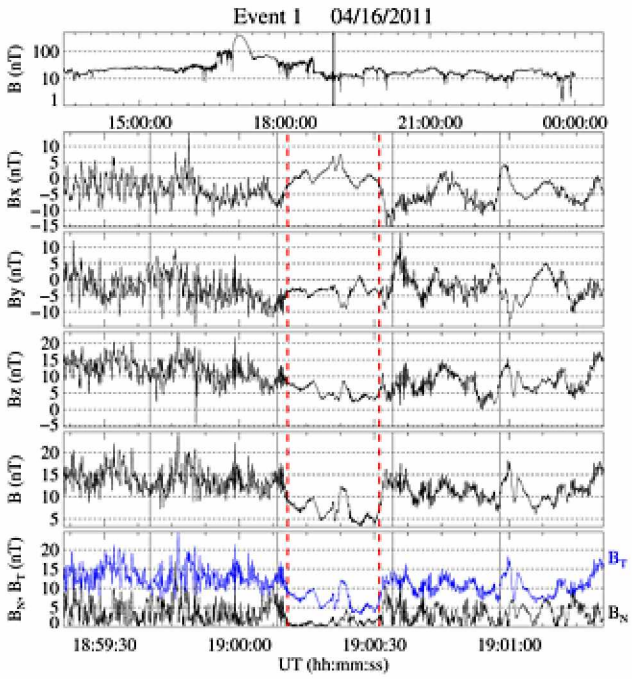

Figure 2.11. Observations of a hot flow anomaly at Mercury from MESSENGER on 16 April 2011 [*Uritsky et al.*, 2014]. The very top panel is $|B|$ on a long time scale. The following three panels from top to bottom are B_x, B_y. B_z, $|B|$. The bottommost panel is the tangential B_τ and normal B_N magnetic field in a current sheet coordinate system where the current sheet normal is the cross product between magnetic field before and after the event.

of the planet toward the Sun, z as the axis perpendicular to Mercury's orbital plane and pointing toward the north celestial pole, and y completing the right-handed coordinate system.

Venus

Slavin et al. [2009] presented MESSENGER spacecraft observations of two hot flow anomalies upstream of the Venusian bow shock on 5 July 2007. Two of the HFAs observed are presented in Figure 2.12. [*Collinson et al.*, 2012] presented Venus Express spacecraft observations of an HFA on 22 March 2008. *Collinson et al.* [2014] presented a study of seven Venus HFAs. The solar wind directly interacts with Venus's ionosphere and upper atmosphere because Venus has no measurable intrinsic magnetic field to shield it from solar plasma, but properties of Venus HFAs are still consistent with HFAs observed at other solar system bodies. *Collinson et al.* [2014] calculated an occurrence frequency of 1.2 ± 0.8 HFA events per day at Venus' bow shock.

Mars

A candidate for the existence of martian HFAs is shown in Figure 2.13. It shows observations from Mars Global Surveyor on 22 July 1988. *Øieroset et al.* [2001] referred to these events as "hot diamagnetic cavities" because unfortunately, no flow information was available to confirm the flow deflection required to classify these events conclusively as HFAs. There was also no ion data to show ion temperatures. If these events were HFAs however, it would seem to suggest that HFA formation does not happen at Earth's magnetopause because Mars does not have a magnetopause/magnetosphere. Earth HFAs upstream of the bow shock are typically reported near the sub-solar point but this martian event was observed near the dawn flank and near the terminator. If this were a HFA, it would show that HFAs may form at the flank of the bow shock where the shock is weaker.

Collinson et al. [2015] presented an HFA observation from the NASA Mars Atmosphere and Volatile EvolutioN (MAVEN) spacecraft on 17 December 2014. MAVEN, unlike Mars Global Surveyor used by *Øieroset et al.* [2001], did make ion observations of the HFA using the Solar Wind Electron Analyzer instrument. They concluded that the ion perturbations that drive the Martian HFA were weaker than those driving HFAs at magnetized planets.

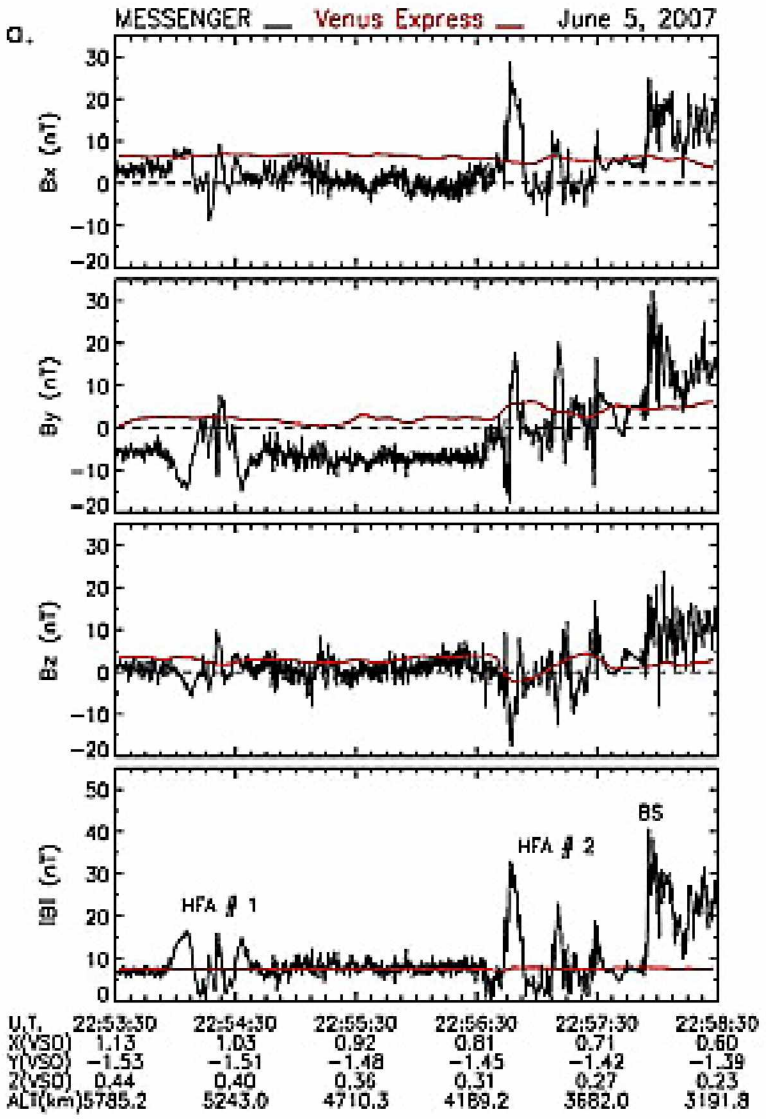

Figure 2.12. Observations of two Venus hot flow anomalies from MESSENGER on 5 June 2007 from *Slavin et al.* [2009] shown in black. From top to bottom is B_x, B_y. B_z, and $|B|$. The observation of the bow shock is labeled as BS. Venus Express data is overlaid in red.

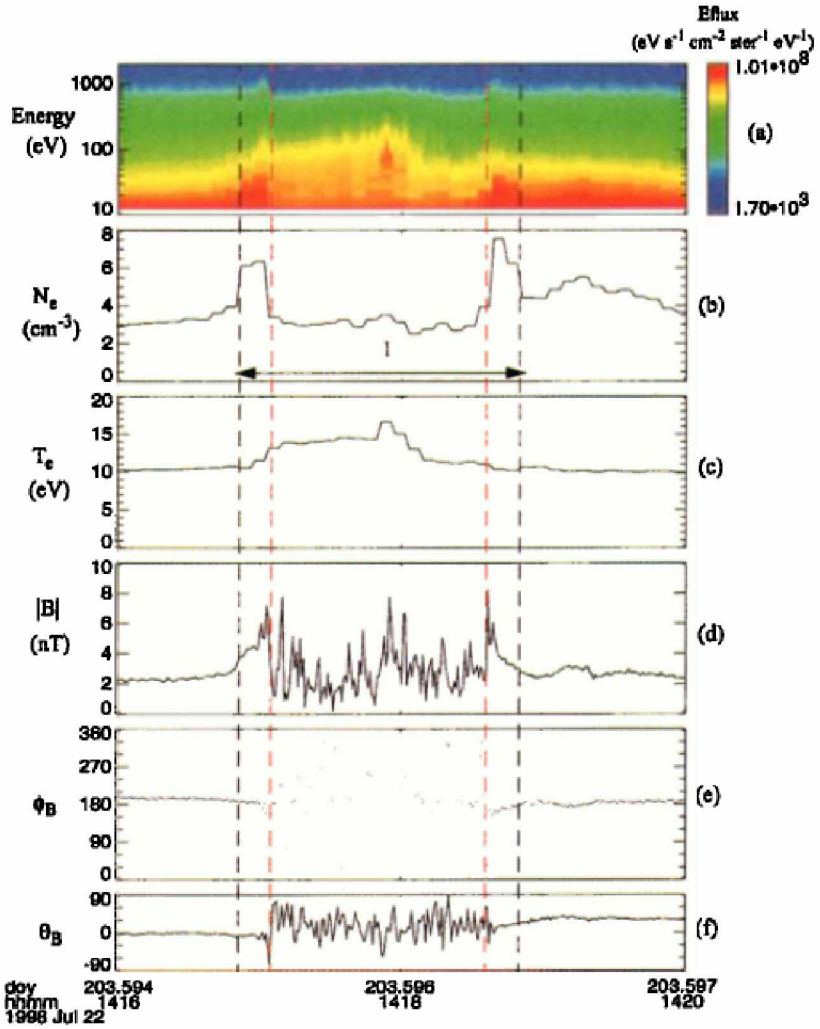

Figure 2.13. Observations of a Martian hot diamagnetic cavity by the Mars Global Surveyor on 22 July 1988 from *Øieroset et al.* [2001]. From top to bottom, the parameters shown are the electron energy spectrogram, electron density, electron temperature, magnetic field strength, and magnetic field ϕ and θ angles. The angles are defined as: $\phi = \arctan\frac{B_y}{B_x}$ and $\theta = \arcsin\frac{B_x}{|B|}$.

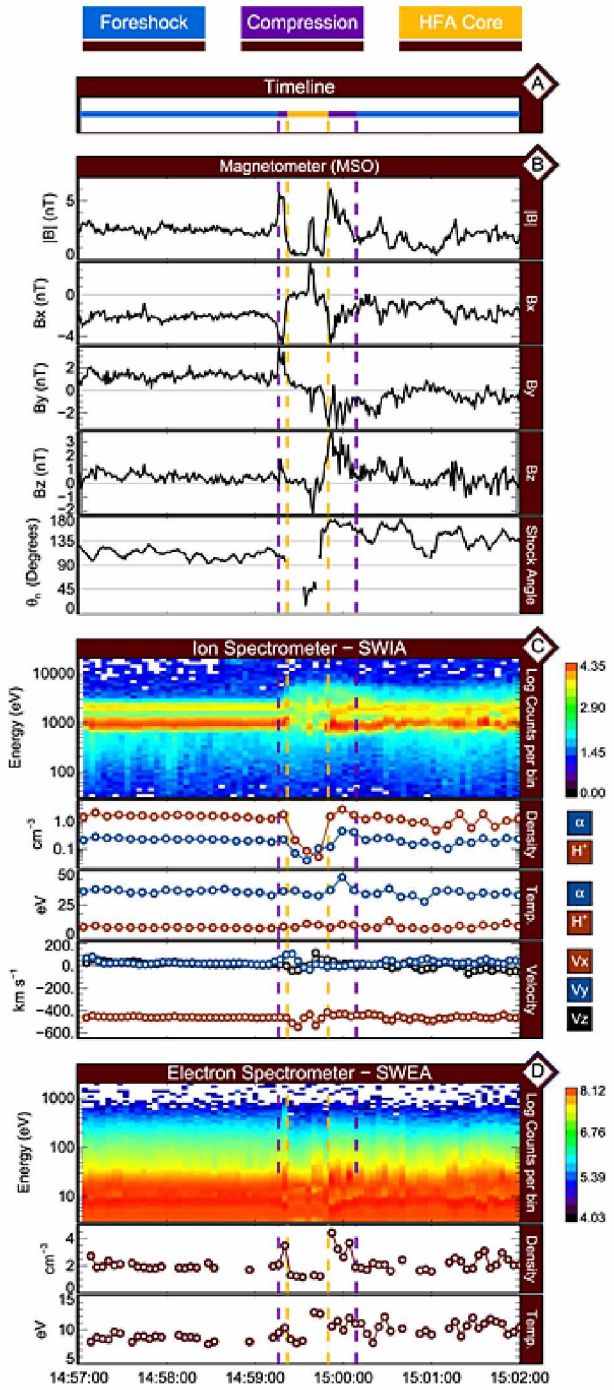

Figure 2.14. Observations of a Martian hot flow anomaly from MAVEN on 17 December 2014 from *Collinson et al.* [2015]. Panel A shows the region the spacecraft was observing where blue indicates the foreshock, purple are boundary compression regions, and yellow is the HFA core. In panel B, from top to bottom is $|B|$, B_x, B_y. B_z, and shock angle. Panel C shows the ion spectrometer observations with the time-energy spectrogram, density, temperature, and velocity. Panel D shows the electron spectrometer observations with the time-energy spectrogram and density and temperature.

The event was 0.66 Martian radii across, where a Martian radius is 3,390 km. The MAVEN observations are shown in Figure 2.14.

Saturn

Kronian data from Cassini shows HFA events such as in Figure 2.15 from *Masters et al.* [2009]. The figure shows the typical HFA signatures of magnetic field strength compressions flanking a hot ion and electron core. The region of field depression corresponds to the cavity of heated plasma. A flow deflection was observed and it was likely along the current sheet. This case was the first confirmed HFA at a bow shock other than Earth's and suggests that HFAs may indeed be found throughout the solar system. A lower limit of Kronian HFA occurrence is one event every 15 days. The actual number may be higher because we are limited by the limited spatial sampling of the spacecraft.

2.9 Motivation and Outline of this Dissertation

This dissertation addresses hot flow anomalies at Earth's bow shock. Hot flow anomalies are important to study and understand because of the coupled nature of the geospace region. They could drive magnetopause motion, boundary waves, and flux transfer events. They may also excite ultra low frequency (ULF) waves in the magnetosphere, drive magnetic impulse events in the ionosphere, and trigger aurora brightening or dimming [*Sibeck et al.*, 1999; *Eastwood et al.*, 2008; *Jacobsen et al.*, 2009; *Fillingim et al.*, 2011]. Some open questions about hot flow anomalies addressed in this dissertation include: How far HFAs extend upstream from the bow shock and how HFA characteristics and occurrence depend on solar wind/IMF conditions and location. There is also an analysis of HFA spatial structure and how it evolves with time. How HFAs can impact the magnetosphere and ionosphere is examined.

This dissertation is organized as follows: The next chapter, Chapter 3, discusses data sources for the HFA studies presented in this dissertation. This includes various satellite and ground based missions and instruments. Chapter 4 discusses some of the methodology used to perform the analysis in later chapters. This includes a discussion on the identification of hot flow anomalies, the mathematical representation of the model bow shock used, a discussion on magnetic local time, and a discussion on the normalization of bar plots in later chapters.

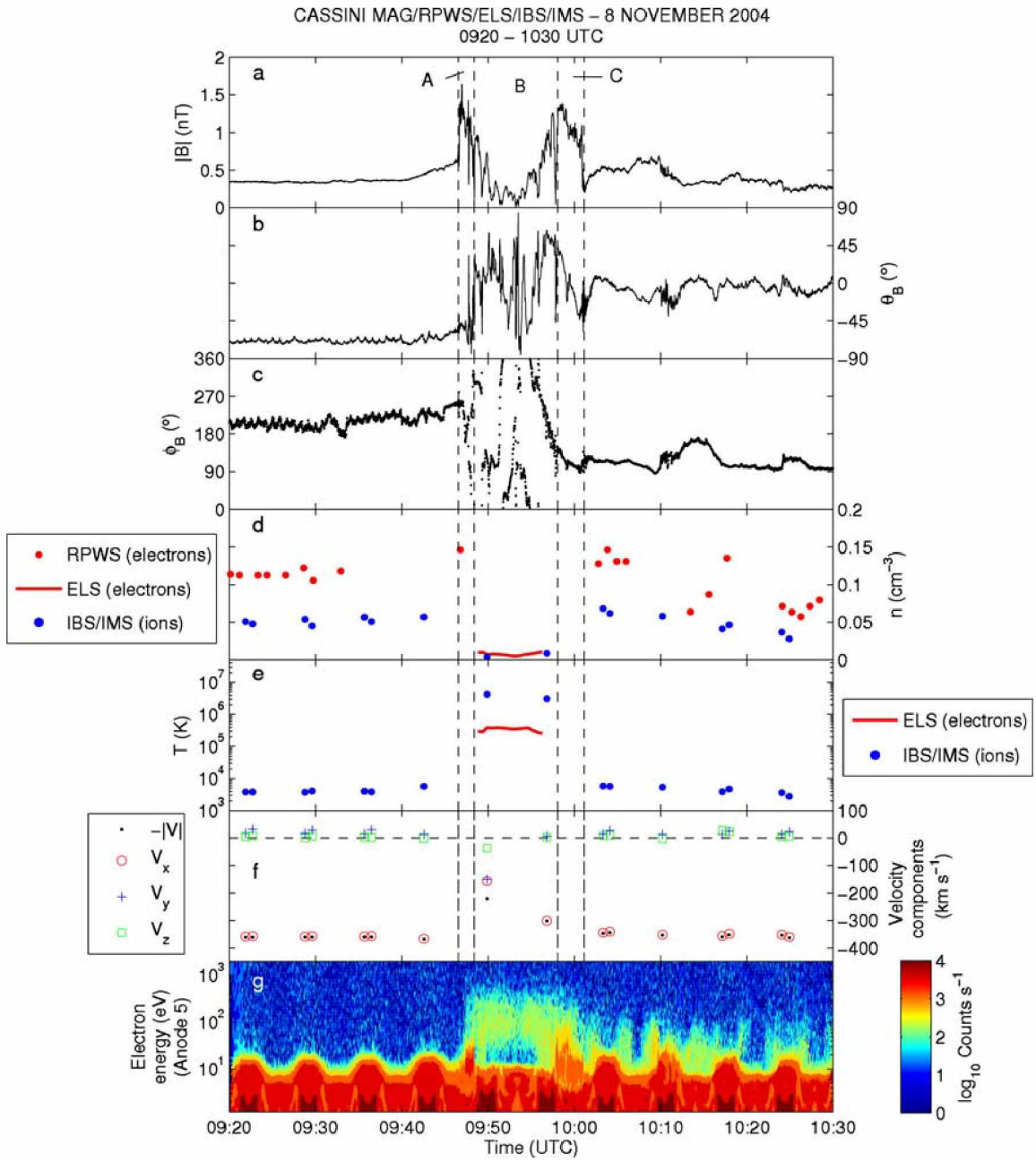

Figure 2.15. Observations of a HFA at Saturn's bow shock by Cassini on 8 November 2004 from *Masters et al.* [2009]. From top to bottom, the parameters plotted are magnetic field strength, magnetic field θ and ϕ angles, electron and ion densities, components of the bulk flow velocity, and a time-energy spectrogram of electron count rate. θ is defined as the angle between the field vector and the xy plane and ϕ is the angle between the projection of the field vector into the xy plane and the negative x direction (anti-sunward). The data is in Kronocentric Solar Magnetospheric coordinates.

Results for HFA location and distance upstream of the bow shock are discussed in Chapter 5. That chapter also discusses kinetic and thermal energies of HFAs. Chapter 6 discusses the temporal and spatial evolution of an HFA observed by multiple satellites. HFAs impacts on the magnetosphere and ionosphere are discussed in Chapter 7. Chapter 8 is a summary of all conclusions of this dissertation.

Chapter 3
Data Sources

This dissertation utilized many data sources to perform different analysis of hot flow anomalies. It includes in-situ space missions and ground based measurements from a distance. This chapter presents general information on the missions and instrumentation that provided data.

3.1 Time History of Events and Macroscale Interactions During Substorms

Data for the structures analyzed in this dissertation came from the Time History of Events and Macroscale Interactions During Substorms (THEMIS) satellites [*Angelopoulos*, 2008]. THEMIS consists of a five satellite constellation launched into Earth orbit on February 17, 2007 and an array of ground observatories located in Canada and the United States. The spacecraft, labeled A through E, were launched at Cape Canaveral Air Force Station Space Launch Complex 17 aboard a Delta II rocket. An image of the probes is shown in Figure 3.1. Each THEMIS probe had a mass of 126 kg which included 49 kg of fuel. THEMIS satellites are spin stabilized spacecraft with three second spin periods.

3.1.1 Spacecraft Orbit and Separation

The THEMIS satellites orbit Earth in different trajectories which are varied to accomplish different mission objectives. The orbits also naturally precess over time. This dissertation analyzed THEMIS data from 14 July 2008 to 5 December 2009. This time period covers THEMIS orbit stages 1–10 which are detailed in Table 3.1. Probe 1 is called THEMIS B, probe 2 is THEMIS C, probe 3 is THEMIS D, probe 4 is THEMIS E, and probe 5 is THEMIS A.

3.1.2 THEMIS Spacecraft Instruments

Each of the five THEMIS satellites were identically instrumented with electric field instruments (EFI), electrostatic analyzers (ESA), fluxgate magnetometers (FGM), search coil magnetometers (SCM), and solid state telescopes (SST). This section will briefly discuss the instruments that provided the data used in the analysis in this dissertation.

Figure 3.1. A photograph of all five THEMIS probes mounted to the probe launch carrier [*"THEMIS - eoPortal Directory - Satellite Missions"*, 2017].

Figure 3.2. A photograph of a THEMIS FGM vector compensated fluxgate ringcore sensor [*"THEMIS - eoPortal Directory - Satellite Missions"*, 2017].

Table 3.1. THEMIS Orbit Stages, 2007–2009

Sample Orbit	Stage	Dates	Notes
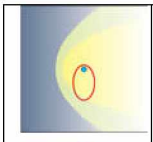	Stage 1: Injection or "Coast" Phase	02/15/07 - 09/15/07	Right after launch all spacecraft are lined up in the same orbit with a 15.4 R_E apogee.
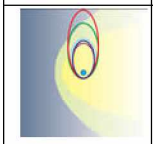	Stage 2: Orbit Placement Phase	09/15/07 - 12/15/07	Phase is also called "Dawn phase" because apogee of orbits are on dawn side of the magnetosphere. Probe 1 apogee is at 30 R_E, Probe 2 at 20 R_E, Probes 3 and 4 at 12 R_E, and Probe 5 at 10 R_E.
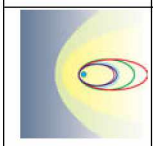	Stage 3: Tail Science Phase	12/15/07 – 04/15/08	In the tail science phase the apogee of the orbits are in the magnetotail. Probe 1 apogee is at 30 R_E, Probe 2 at 20 R_E, Probes 3 and 4 at 12 R_E, and Probe 5 at 10 R_E.
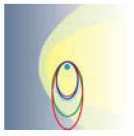	Stage 4: Radiation Belt Science Phase	04/15/08 - 06/15/08	The radiation belt science phase is also called the "Dusk phase" because the apogee of the orbits are on the dusk side of the magnetosphere. Probe 1 apogee is at 30 R_E, Probe 2 at 20 R_E, Probes 3 and 4 at 12 R_E, and Probe 5 at 10 R_E.
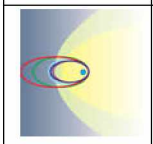	Stage 5: Dayside Science Phase	06/15/08 - 10/15/08	In the dayside science phase the apogee of the orbits are on the dayside of the magnetosphere. Probe 1 apogee is at 30 R_E, Probe 2 at 20 R_E, Probes 3 and 4 at 12 R_E, and Probe 5 at 10 R_E.
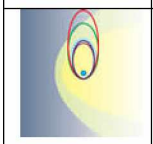	Stage 6: Dawn Phase	10/15/08 - 12/15/08	The apogee of the orbits is on the dawn side of the magnetosphere. Probe 1 apogee is at 30 R_E, Probe 2 at 20 R_E, Probes 3, 4, and 5 at 12 R_E.
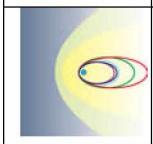	Stage 7: Tail Science Phase	12/15/08 – 04/15/09	In the tail science phase the apogee of the orbits are in the magnetotail. Probe 1 apogee is at 30 R_E, Probe 2 at 20 R_E, Probes 3, 4, and 5 at 12 R_E.
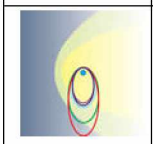	Stage 8: Radiation Belt Science Phase	04/15/09 - 06/15/09	Phase is also called the "Dusk phase" because the apogee of the orbits are on the dusk side of the magnetosphere. Probe 1 apogee is at 30 R_E, Probe 2 at 20 R_E, Probes 3, 4, and 5 at 12 R_E.
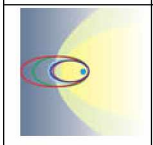	Stage 9: Dayside Science Phase	06/15/09 - 09/30/09	In the dayside science phase the apogee of the orbits are on the dayside of the magnetosphere. Probe 1 apogee is at 30 R_E, Probe 2 at 20 R_E, Probes 3 and 4 at 12 R_E, and Probe 5 at 13 R_E.
	Stage 10: Dawn Phase	12/29/09 - 03/01/10	Apogee of the P3, P4, and P5 orbits are on the dawn-side of the magnetosphere. Probes 3 and 4 have apogees at 12 R_E, and Probe 5 has an apogee at 13 R_E. P1 and P2 have now become ARTEMIS.

Fluxgate Magnetometer (FGM)

A fluxgate magnetometer (FGM) is used to measure background magnetic fields in the near Earth environment [*Auster et al.*, 2008]. Each THEMIS FGM, pictured in Figure 3.2, is capable of measuring low frequency fluctuations up to 64 Hz and capable of detecting variations of the magnetic field with amplitudes of 0.01 nT. Measurement ranges of $\pm$ 25,000 nT were capable with a noise of $\frac{10pT}{\sqrt{Hz}}$ at 1 Hz. The instrument onboard each THEMIS spacecraft consists of a vector compensated three axis fluxgate sensor unit and digital electronics on a single printed circuit board. The FGM board area is about 120 cm^2, the power consumption is 800 mW, and the mass of its electronics 150 g. The sensor is 75 g and the harness is 150 g. The stability of the instrument was proven to be better than 0.5 nT during the first 18 months of operation.

THEMIS FGM data is available at different resolutions: high telemetry, low telemetry, and spin resolution [*Auster et al.*, 2008]. The high telemetry channel permanently provides 128 Hz samples and the low telemetry channel can be commanded to provide transmission rates between 4 and 128 Hz. The lower time resolution data are calculated by filtering the raw data with a non-overlapping arithmetic averaging filter, by data decimation or a combination of both. Spin resolution data has a data point approximately every three seconds. High resolution data was the first data choice to use in this dissertation if available, followed by low resolution, and then by spin resolution.

Electrostatic Analyzer (ESA)

The electrostatic analyzer (ESA) [*McFadden et al.*, 2008], pictured in Figure 3.3, provides plasma data on both ions and electrons. The hardware is a pair of "top hat" electrostatic analyzers. They have common 180° by 6° fields of view that sweep out 4π steradians each spin period. In the 3 second spin of the satellite, the ESA instrument measures the three dimensional ion and electron distributions. The ion energy ranges from a few eV up to 25 keV and the electron energy ranges from a few eV up to 30 keV. The moment data includes density, velocity and temperatures for both ions and electrons.

Data modes include full mode, burst mode, reduced mode, and on board moments. Full and reduced modes can both be further divided into Fast-Survey Spacecraft-Mode or Slow-Survey Spacecraft-Mode.

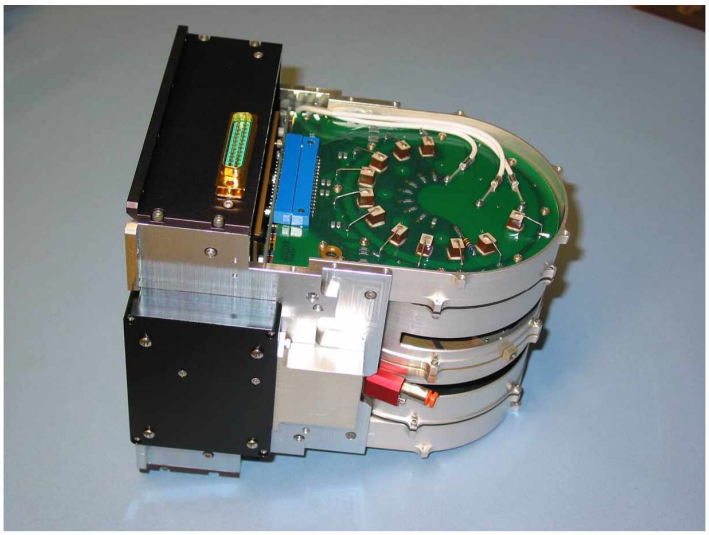

Figure 3.3. A photograph of a THEMIS ESA instrument [*"THEMIS Electrostatic Analyzer"*, 2017].

Full mode packets are low time resolution observations. They usually preserve all 32 energies sampled and contain data from the 88 solid angles the the field of view is divided into. The data packets come in one of two modes: Fast-Survey mode has 32 spins per packet and Slow-Survey mode has 128 spins per packet. Full mode packets are used in creating summary plots, in validating the calculated on-board moment data, and to generate distribution functions [*McFadden et al.*, 2008]. Full mode packets are also called survey mode packets.

Burst mode packets are high resolution three dimensional plasma distribution functions that have a spin-period time resolution. The burst mode packet format is typically the same as full mode data format, with 32 energies and 88 solid angles. Burst mode is usually limited to a few five minute intervals for each orbit because of telemetry limitations. The burst mode time intervals are selected by a ground command or by on-board software triggers. Burst data provide high resolution measurements used to determine boundary crossings at areas including the magnetotail neutral sheet, plasma sheet boundary layer, magnetopause, and bow shock [*McFadden et al.*, 2008].

Reduced mode packets are 1-spin time resolution plasma distributions with continuous sampling of limited solid angles and/or energies. In Fast-Survey mode, the typical ion reduced mode packet contains a 24-energy, 50-solid angle distribution, while the electron reduced mode packet contains a 32-energy, 6-solid-angle distribution. In Slow-Survey mode, reduced mode packets typically contain 32-energy omni-directional spec-

Figure 3.4. A photograph of the ACE satellite ["*NASA's ACE Spacecraft*", 2017].

tra. Data collected in the Slow-Survey mode can be used to produce energy-time spectrograms that match the time cadence of the on-board moment data [*McFadden et al.*, 2008].

On-board moment data are spin resolution on-board computations of the plasma density, three components of flux (note velocity=flux/density), six components of the pressure tensor, and three components of heat flux. THEMIS on-board moment calculations include corrections for spacecraft charging [*McFadden et al.*, 2008].

For dayside solar wind intervals from 2007-2009, the years of data used in the analysis of this dissertation, there were no burst mode intervals for the observed hot flow anomaly intervals. Full mode data has too low time resolution to analyze the THEMIS observed HFAs. Reduced mode data has limited energy and solid angle coverage and therefore cannot be used to calculate the moment data. For these reasons, on-board moment data was used in this dissertation.

3.2 Advanced Composition Explorer

The Advanced Composition Explorer (ACE) [*Chiu et al.*, 1998; *Stone et al.*, 1998] satellite was launched on a McDonnell-Douglas Delta II 7920 launch vehicle on August 25, 1997 from the Kennedy Space Center in Florida. Figure 3.4 is a photograph of the satellite. It is a commonly referenced solar wind monitor for Earth that follows a halo Lissajous orbit around the L1 Lagrange point. ACE currently stays roughly 38 R_E from the Sun-Earth line in its orbit, but its Lissajous orbit is expanding.

Lagrange points are positions where the combined gravitational forces of two large masses equal the centrifugal force felt by a much smaller third body. The interaction of the forces creates a point of equilibrium where a spacecraft may be "parked" to make observations.The L1 point is the location of Earth-Sun gravitational equilibrium which is about 1.5 million km from Earth (approximately at 230 R_E) and 148.5 million km from the Sun.

As of 2015, ACE was projected to have enough propellant on board to maintain an orbit at L1 until approximately 2024. The fuel is used on orbit maneuvers to keep the spacecraft bound to the L1 point and on attitude maneuvers to maintain the high gain antenna constraint met. The spacecraft spins at 5 rotations per minute with the spin axis generally pointed along the Sun-Earth line and most of the scientific instruments on the top, sunward face. Types of plasma measurements onboard include: isotope spectrums in the MeV range and fluxes (including H, He, C, O, N, Ne, Mg, Si, Fe), magnetic field, density, velocity, and temperature.

The plasma structures observed by ACE can impact the bow shock and magnetosphere if they have the right direction of travel. The interval of time between an observation of a feature at ACE and then the interaction of the same feature with the bow shock and magnetosphere depends on the velocity of the feature.

3.3 Wind Spacecraft

The Wind satellite [*Ogilvie et al.*, 1995; *Lin et al.*, 1995; *Lepping et al.*, 1995] pictured in Figure 3.5 was launched on November 1, 1994. It is a commonly referenced solar wind monitor for Earth that currently follows a halo orbit about L1 in its extended mission phase. The orbit is nominally 235 to 265 R_E diameter. Types of plasma measurements include: Fluxes (proton, ion, electron, alpha), energy-angle distributions, magnetic field, density, velocity, and temperature. Magnetic fields are measured with the Magnetic Field Investigation (MFI) instrument which is composed of two fluxgate magnetometers. They are located both 2/3 of the way out and at the end of a 12 m boom mounted to the spacecraft.

Plasma observations at Wind, similar to ACE, need to take the plasma velocity into consideration when determining whether and when something observed in the solar wind may interact with the bow shock and magnetopause. IMF observations taken at large off axis separations from the Sun-Earth line do not always correlate well with ob-

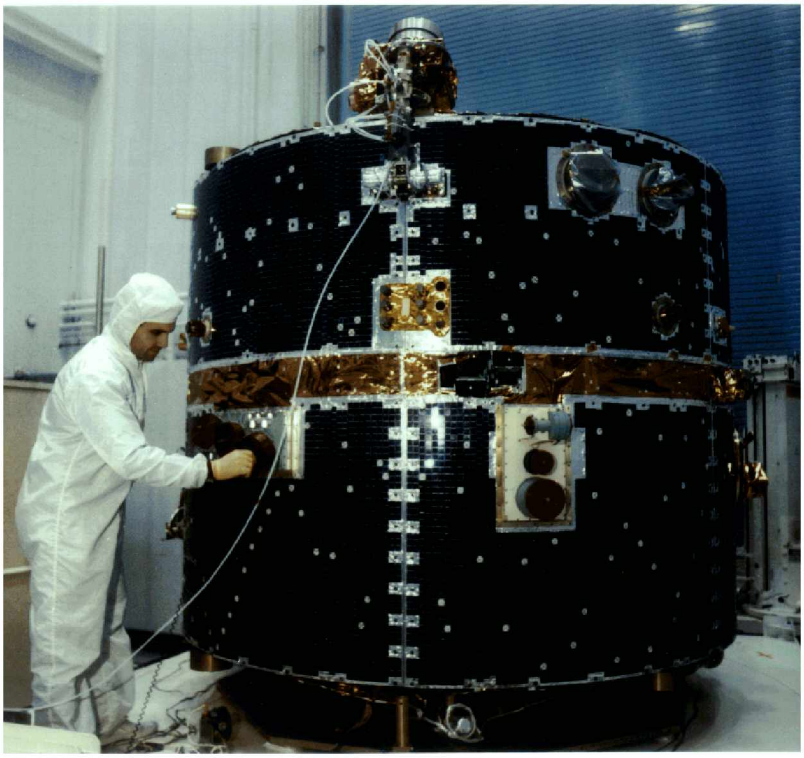

Figure 3.5. A photograph of the Wind satellite [*"The WIND Spacecraft Experiment"*, 2011].

servations made by near-Earth solar wind monitors. This effect can be more exaggerated for Wind than for ACE since Wind's orbit is larger than ACE's.

3.4 OMNI

OMNI 2 (here-afterwards referred to as OMNI) is a dataset of hourly-averaged near-Earth solar wind magnetic field and plasma parameters from many spacecraft in geocentric orbits and in orbits about the L1 Lagrange point which is approximately 225 R_E sunwards from Earth along the Sun-Earth line. It is a successor to the original OMNI dataset created and maintained at the National Space Science Data Center in the mid-1970's [*"OMNI2"*, 2015]. The dataset also includes hourly fluxes of energetic protons, geomagnetic activity indices and sunspot numbers. The data from different spacecraft have been extensively cross compared, and for some spacecraft and parameters, cross-normalized. Only data taken beyond the Earth's bow shock have been included. The dataset currently includes dates from 1963 up through the current date and can be accessed through the website `http://omniweb.gsfc.nasa.gov/`.

One can access low resolution or high resolution OMNI data. For low resolution hourly data, time-shifts of higher resolution data to expected magnetosphere-arrival times are done for data from spacecraft in L1 orbits (ISEE 3, Wind, ACE), prior to taking hourly averages. *King and Papitashvili* [2005] noted that "the time shift assumed that variation phase fronts share an orientation normal to the ecliptic and intercepting that plane midway between the Parker IMF spiral angle and the normal to the Sun-Earth line". Low resolution OMNI data are made available at hourly, daily, and 27-day resolutions. The high resolution OMNI dataset includes 1-min and 5-min bow-shock-nose-shifted solar wind magnetic field and plasma data from the IMP 8, Geotail, Wind and ACE spacecraft [*"Omni, About the Data"*, 2015].

3.5 Geostationary Operational Environmental Satellite

On October 16, 1975, the first of the Geostationary Operational Environmental Satellites (GOES) [*Singer et al.*, 1996] was launched into geostationary orbit around Earth. GOES is a series of satellites used to provide continuous imagery and data on Earth atmospheric conditions and solar activity. An image of the GOES-M probe is shown in Figure 3.6. To ensure continual coverage, new satellites with improved instrumentation are launched prior to decommissioning old satellites. GOES satellites are designated with a letter prior to launch. Once a satellite has achieved orbit, it is assigned a number. Table 3.2 shows the history and status of all GOES satellites [*"GOES History"*, 2015]. Figure 3.7 shows a graphical timeline of GOES 10, 11, and 12 from launch to decommissioning.

A geostationary orbit is a circular orbit in Earth's equatorial plane with a speed matching the Earth's rotation so the satellite maintains a fixed position in the sky, remaining stationary with respect to a point on the ground. The geostationary orbit's distance from the center of the Earth is 6.6 R_E. The satellites continually view the continental United States, Atlantic and Pacific Oceans, Southern Canada, and Central and South America. GOES operates in two primary locations: GOES East is located at 75° W and provides most of the U.S. weather information. GOES West is located at 135° W over the Pacific Ocean. An on-orbit spare GOES satellite is maintained in a storage position in the event of an anomaly or failure of GOES East or GOES West. The storage position is at 105° W.

The analysis in this dissertation utilized data from GOES 10, 11, and 12. The magnetometers on the three-axis stabilized GOES I–M (called GOES 8–12 after launch) are three-axis fluxgate magnetometers. The magnetometer electronics are inside the space-

Figure 3.6. A photograph of the GOES-M probe [*"Kennedy Media Gallery"*, 2017].

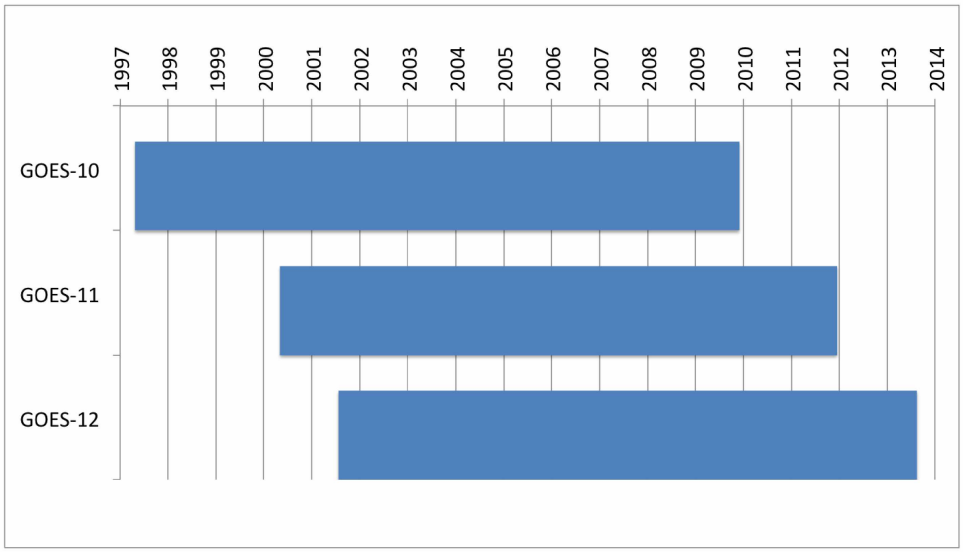

Figure 3.7. A continuity timeline of GOES spacecraft 10, 11, and 12 from launch to decommissioning.

Table 3.2. History and Status of all GOES Satellites

Designation		Launch Date	Status
Launch	*Operational*		
GOES-A	GOES 1	16 October 1975	Decommissioned 1985
GOES-B	GOES 2	16 June 1977	Decommissioned 1993, reactivated 1995, deactivated 2001
GOES-C	GOES 3	16 June 1978	Used as a communications relay for South Pole research station
GOES-D	GOES 4	9 September 1980	Decommissioned 1988
GOES-E	GOES 5	22 May 1981	Decommissioned 1990
GOES-F	GOES 6	28 April 1983	Decommissioned 1992
GOES-G	N/A	3 May 1986	Failed to orbit
GOES-H	GOES 7	26 February 1987	Retired 1996; Reactivated as comsat in 1999; Decommissioned 2012
GOES-I	GOES 8	13 April 1994	Decommissioned 2004
GOES-J	GOES 9	23 May 1995	Decommissioned 2007
GOES-K	GOES 10	25 April 1997	Decommissioned 2009
GOES-L	GOES 11	3 May 2000	Decommissioned 2011
GOES-M	GOES 12	23 July 2001	Decommissioned 2013
GOES-N	GOES 13	24 May 2006	In operation as GOES East
GOES-O	GOES 14	27 June 2009	In on-orbit storage
GOES-P	GOES 15	4 March 2010	In operation as GOES West
GOES-R	GOES 16	19 November 2016	At checkout orbit in validation phase
GOES-S	-	-	Scheduled for launch in 3Q FY 2017

craft while the sensors are mounted on a three-meter boom attached at the north west corner of the anti-Earth panel. On the boom, the primary sensor is at the end and a second redundant sensor is located 0.3 meters inboard of the primary. Only one magnetometer may be operated at a time. Each magnetometer axis is measured once a telemetry frame (0.512 seconds), with a 42 millisecond delay between the sampling of successive axes. The magnetometer range is $\pm$ 1000 nT with accuracy of 1 nT [*Singer et al.*, 1996].

The magnetic field measured by GOES is used to detect geosynchronous orbit magnetopause crossings and shocks in the solar wind, to assist forecasters in qualitatively assessing the level of geomagnetic disturbance, to interpret changes in energetic particle measurements, to provide data to the National Geophysical Data Center, to support in real-time scientific activities such as rocket launches, and to conduct research for a better understanding of the space environment.

3.6 Ground Based Observations

The magnetosphere is coupled to the ionosphere so structures and perturbations in the magnetosphere will cause observable perturbations in the ionosphere. Ionospheric changes may be measured with low Earth orbit satellites, rockets, and ground based instruments. In this dissertation, data from several different ground stations were analyzed to determine whether a HFA observed at Earth's bow shock could cause perturbations observable on the ground. These stations were chosen from the many hundreds that exist because the data was easy to access and the stations were located in the areas where effects from a HFA would be expected. The following subsections describe the location of the stations and instruments which provided the data used. Table 3.3 lists the geomagnetic latitude and longitude locations of the stations whose data is utilized in this dissertation.

3.6.1 SuperMAG

SuperMAG is comprised of worldwide collaborators whose purpose is to gather ground magnetometer data into an easily accessible database at `http://supermag.jhuapl.edu/mag/` [*Gjerloev*, 2009]. There are observations from over 300 ground based magnetometers in the database. SuperMAG provides validated ground magnetic field perturbations in a common coordinate system, time resolution, and with a common baseline removal method.

Table 3.3. Ground Station Sites and Geomagnetic Locations

Station Name		Geographic		Geomagnetic	
Abbreviation	Name	Longitude	Latitude	Longitude	Latitude
RES	Resolute Bay	265.11	74.69	-38.41	83.02
CBB	Cambridge Bay	255.00	69.10	-49.81	77.01
RKN	Rankin Inlet	266.89	62.82	-26.40	72.60
T34	Ekati	249.30	64.70	-54.76	72.12
INK	Inuvik	226.70	68.25	-84.75	71.21
KAV	Kaktovik	216.63	70.07	-95.96	71.11
BRW	Barrow	203.25	71.30	-107.98	70.15
YKC	Yellowknife	245.52	62.48	-58.50	69.35
ARC	Arctic Village	214.43	68.13	-95.88	68.80
SMI	Fort Smith	248.05	60.02	-53.86	67.44
FSP	Fort Simpson	238.77	61.76	-66.49	67.34
FYU	Fort Yukon	214.70	66.57	-94.30	67.29
RAL	Rabbit Lake	256.32	58.22	-41.58	67.06
DAW	Dawson City	220.89	64.05	-86.84	65.95
PKR	Poker Flat	212.74	65.08	-94.86	65.42
T41	Kiana	199.60	67.00	-106.83	65.18
CMO	College	212.14	64.87	-95.22	65.10
SBA	Scott Base	166.78	-77.85	-32.76	-79.89
MCM	McMurdo Station	166.67	-77.85	-32.77	-79.92
DRV	Dumont Durville	140.01	-66.67	-124.02	-80.51

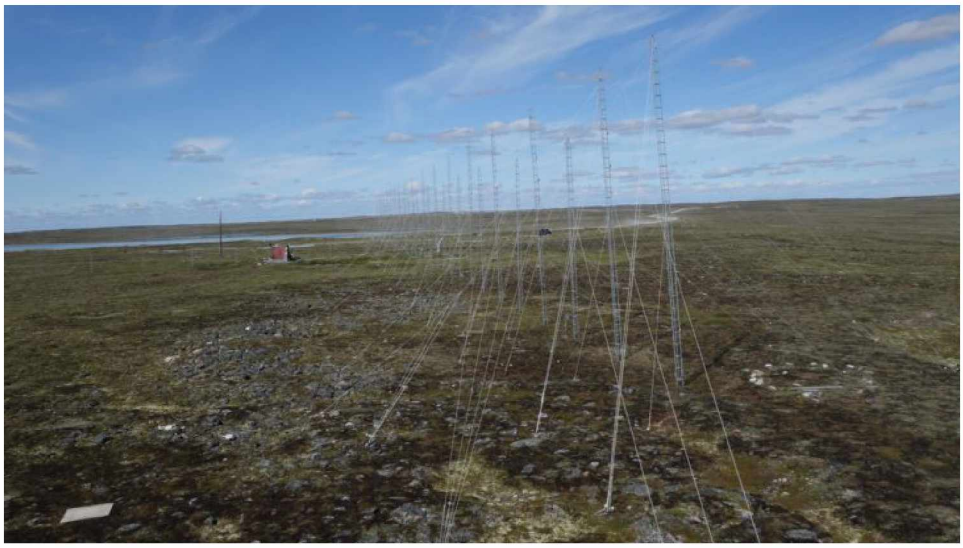

Figure 3.8. A photo of the Rankin Inlet SuperDARN radar. The main array and the seacan are in the left background. The UAV landing zone (plywood) can be seen on the left in the foreground [*"Maintenance trip to Rankin Inlet"*, 2016].

3.6.2 SuperDARN

Super Dual Auroral Radar Network (SuperDARN) [*Greenwald et al.*, 1995] is a worldwide network of over 30 low power, high frequency (HF) radars that probe Earth's ionosphere from mid-latitudes to polar latitudes. SuperDARN data presented in this dissertation are figures generated at `http://vt.superdarn.org/tiki-index.php`. Each radar in the network is of similar design and uses the same operating software. An image of the Rankin Inlet SuperDARN is shown in Figure 3.8. SuperDARN radars are continually operated pulsed radars which transmit a peak power of 9600 W. The pulsed radars transmit an electromagnetic pulse by modulating the amplitude of a radio frequency signal with a rectangular function.

The radar uses radiation of EM signals for the detection and location of a target. The SuperDARN targets are magnetic field aligned plasma density irregularities in the E and F regions of the ionosphere. Plasma density irregularities tend to diffuse along magnetic field lines. Plasma irregularities are only detected if they are perpendicular to the radial component of the impinging radar signal. Reflections off of plasma density irregularities are specular. Specular reflection is the reflection of a wave from a surface where the angle of incidence equals the angle of reflection.

Two types of radar scatter which can occur are coherent scatter and incoherent scatter. Coherent scatter is scatter from a target with some degree of spatial and temporal coherence (correlation over distance and time). Incoherent scatter is scatter from a target with a minimal amount of spatial coherence. SuperDARN is comprised of coherent scatter radars. Incoherent scatter radars (ISR) have more power than coherent scatter radars (CSR) (Mw vs Kw) and also tend to work at higher frequencies. Echoes for both types of radars come from collective scattering, or plasma irregularities. ISRs observe weak ion-acoustic structures in any direction. CSRs only observe large amplitude structures aligned with the magnetic field.

The primary parameters from a radar are range, echo power, doppler shift, and spectral width (velocity). Range is calculated by measuring the time delay between the transmission of an electromagnetic signal and the reception of its echo. Echo power is the power of the received signal at the time an echo is observed. Doppler shift is the difference in frequency between the transmitted and received signal.

The operation frequencies are in the HF band, 8–20 MHz. These frequencies are used because ionospheric refraction causes the radar signals to become orthogonal to the Earth's magnetic field lines. At high latitudes, the magnetic field lines are nearly vertical to the ground. If there are echoes, they are directed back towards the radar. The amount of ionospheric refraction depends on the plasma electron density. This density varies diurnally, annually, and with geomagnetic activity, so the radars must be capable of operation over an extended HF frequency range.

The radars have overlapping fields of view and combine to cover large surface regions of Earth. A single radar can give the line of sight velocity, which is the velocity of a target in the direction towards or away from a radar. It is the projection of the velocity along a line of sight. With overlapping radar field of views and overlapping observations, a pair of linearly independent line of sight velocities can be combined to form the vector velocity of a target. That vector velocity is the actual direction a target is moving. Bulk plasma flow in the ionosphere's E and F regions is obtained by mapping multiple vector velocities.

3.7 Chapter Summary

This chapter presented all the data sources used in the dissertation. The next chapter will begin to discuss how the data from these sources was used. It will also present details on some mathematical calculations performed.

Chapter 4
Methodology

This dissertation analyzes hot flow anomalies identified from THEMIS data. This chapter presents details on how events were identified. It will discuss details of the empirical bow shock model used in this dissertation. It also presents details of mathematical methods used.

4.1 Hot Flow Anomaly Event Identification

THEMIS data were analyzed in both the Geocentric Solar Ecliptic (GSE) and Geocentric Solar Magnetic (GSM) coordinate systems. The statistical study of hot flow anomalies in this dissertation utilized 136 HFAs identified in THEMIS C data from 2007 to 2009. The database of HFAs was created by looking for event signatures in the data one hour at a time.

The largest component of the solar wind flow was along the Sun-Earth line (GSM or GSE coordinate systems). The slowest solar wind speeds observed during the years examined was on the order of 300 km/s. A well defined flow deflection should be at least 10% higher than the slowest observed solar wind (more than 30 km/s higher). If a flow deflection in the x direction of more than 35 km/s above the solar wind speed was detected, a concurrent increase in ion temperature and decrease in plasma density was also looked for. If the event ion temperature was more than 10^6 K above the average solar wind ion temperature, the plasma density was examined. In the time interval where there was a flow deflection, the minimum density was compared to the average solar wind in the identified solar wind intervals before and after each event. For an observation period to be labeled an HFA, the solar wind density was required to be larger than the minimum HFA core density.

HFAs have been delineated into the category of non-spontaneous (or "regular" HFAs) or spontaneous. To make the classification, the following steps were performed: First, solar wind intervals immediately before and after each HFA were identified. These intervals are typically 10 minutes long and did not include any non-nominal solar wind. There were times when THEMIS crossed the bow shock into the magnetosheath within 10 minutes of the hot flow anomaly boundaries. In those cases, solar wind intervals shorter than 10 minutes were selected. The angle between the magnetic field of the first solar wind interval and the second solar wind interval was calculated. If that angle is below

30°, the HFA was classified as spontaneous (SHFA) otherwise the HFA was classified as a "regular" or non-spontaneous HFA.

4.2 Model Bow Shock

4.2.1 Geocentric Plasma Equatorial Coordinate System

Solar wind flow directions vary over time which causes the bow shock and magnetosphere to be blown in different directions like a wind sock. This can make comparisons of non-simultaneous bow shock observations questionable with traditional coordinate systems. *Merka et al.* [2005] described a geocentric plasma ecliptic (GPE) coordinate system to allow comparison of events occurring at different bow shock crossings. GPE is a rotation of the GSE coordinate system. In GPE, the x axis is antiparallel to the solar wind flow, the ecliptic north is in the XZ plane, and y is orthogonal to x and z. GPE coordinates were used in this study to determine the distance each event occurred from the bow shock.

Rotate from GSE to GPE

To rotate from GSE to GPE, first define the vector going from the GSE origin (the center of the Earth) to the HFA, $\langle x_H, y_H, z_H \rangle$. Rotate that vector about the GSE z axis, then about the GPE y axis. To accomplish the rotations, we did the following steps in this subsection.

All vectors given are in GSE coordinates unless otherwise indicated. We know the solar wind vector in the GSE coordinate system is given by $\mathbf{v} = \langle x_1, y_1, z_1 \rangle$ (note that x_1 is a negative number since the solar wind flows away from the Sun). Therefore, the x axis of the GPE system is $\mathbf{x}' = \langle -x_1, -y_1, -z_1 \rangle$. If we project $\mathbf{x}'$ onto the GSE xy plane, we get $\mathbf{x}'' = \langle -x_1, -y_1, 0 \rangle$. Defining θ as the angle between $\hat{\mathbf{x}} = \langle 1, 0, 0 \rangle$ and $\mathbf{x}''$, $\theta = \arccos\left(\frac{-x_1}{\sqrt{x_1^2+y_1^2}}\right)$ where if $-y_1$ is negative, θ will be negative and if $-y_1$ is positive, θ will be positive. Given the HFA location as $\mathbf{P} = \langle x_H, y_H, z_H \rangle$, the rotation of that vector about the z GSE axis, $\langle 0, 0, 1 \rangle$, by angle θ is given by

$$\mathbf{HFA_R} = \begin{bmatrix} \cos\theta & -\sin\theta & 0 \\ \sin\theta & \cos\theta & 0 \\ 0 & 0 & 1 \end{bmatrix} \cdot \begin{bmatrix} x_H \\ y_H \\ z_H \end{bmatrix} = \begin{bmatrix} x_H\cos\theta - y_H\sin\theta \\ x_H\sin\theta + y_H\cos\theta \\ z_H \end{bmatrix} \tag{4.1}$$

To rotate $\mathbf{HFA_R}$ about the GPE y axis $\mathbf{y}'$, we first need to define the vector $\mathbf{y}'$. Define GSE coordinate system points $A\,(0,0,0)$, $C\left(-x_1,-y_1,-z_1\right)$, $D\,(0,0,1)$ and vectors $\mathbf{AC} = \langle -x_1,-y_1,-z_1\rangle = \mathbf{x}'$ and $\mathbf{AD} = \langle 0,0,1\rangle$. $\mathbf{AD}$ is the GSE coordinate's z axis; it is parallel to ecliptic pole and will lie in the GPE's xz plane. Therefore, we can calculate $\mathbf{AD}\times\mathbf{AC}$ to find the GPE y axis, $\mathbf{y}'$. $\mathbf{AD}\times\mathbf{AC} = \begin{vmatrix} \hat{\mathbf{i}} & \hat{\mathbf{j}} & \hat{\mathbf{k}} \\ 0 & 0 & 1 \\ -x_1 & -y_1 & -z_1 \end{vmatrix} = \langle y_1,-x_1,0\rangle = \mathbf{y}'$. The unit vector of $\mathbf{y}'$ is $\hat{\mathbf{y}}' = \left\langle \frac{y_1}{\sqrt{x_1^2+y_1^2}}, \frac{-x_1}{\sqrt{x_1^2+y_1^2}}, 0 \right\rangle$.

Given an arbitrary unit vector $\hat{\mathbf{u}} = \langle u_x,u_y,u_z\rangle$, the matrix for a rotation by an angle of ϕ about an axis in the direction of $\hat{\mathbf{u}}$ is

$$R = \begin{bmatrix} \cos\phi + u_x^2(1-\cos\phi) & u_xu_y(1-\cos\phi) - u_z\sin\phi & u_xu_z(1-\cos\phi) + u_y\sin\phi \\ u_xu_y(1-\cos\phi) + u_z\sin\phi & \cos\phi + u_y^2(1-\cos\phi) & u_yu_z(1-\cos\phi) - u_x\sin\phi \\ u_xu_z(1-\cos\phi) - u_y\sin\phi & u_zu_y(1-\cos\phi) + u_x\sin\phi & \cos\phi + u_z^2(1-\cos\phi) \end{bmatrix} \tag{4.2}$$

For the rotation about $\hat{\mathbf{y}}'$, define ϕ as the angle between $\mathbf{x}''$ and $\mathbf{x}'$. That means $\phi = \arccos\left(\frac{x_1^2+y_1^2}{\sqrt{x_1^2+y_1^2}\sqrt{x_1^2+y_1^2+z_1^2}}\right)$ where if $-z_1$ is negative, ϕ will be positive and if $-z_1$ is positive, θ will be negative. Therefore,

$$R = \begin{bmatrix} \cos\phi + \frac{y_1^2}{x_1^2+y_1^2}(1-\cos\phi) & -\frac{x_1y_1}{x_1^2+y_1^2}(1-\cos\phi) & -\frac{x_1}{\sqrt{x_1^2+y_1^2}}\sin\phi \\ -\frac{x_1y_1}{x_1^2+y_1^2}(1-\cos\phi) & \cos\phi + \frac{x_1^2}{x_1^2+y_1^2}(1-\cos\phi) & -\frac{y_1}{\sqrt{x_1^2+y_1^2}}\sin\phi \\ \frac{x1}{\sqrt{x_1^2+y_1^2}}\sin\phi & \frac{y_1}{\sqrt{x_1^2+y_1^2}}\sin\phi & \cos\phi \end{bmatrix} \tag{4.3}$$

$R\cdot\mathbf{HFA_R}$ will yield the HFA position in GPE coordinates.

4.2.2 Defining the Bow Shock Surface and Calculating Distance Upstream via Lagrange Multipliers Technique

In this dissertation, we wanted to calculate the distance that each HFA was upstream from the bow shock. Keeping in mind that the bow shock is a curved surface, we therefore want to find the minimum distance between an HFA observed by a spacecraft and some point

on the bow shock surface. The following points and surfaces are in the GPE coordinate system.

The bow shock surface for this study was defined by *Merka et al.* [2005] as the equation

$$g(x,y,z) = a_1x^2 + y^2 + a_3z^2 + 2a_4xy + 2a_7x + 2a_8y + a_{10} = 0 \tag{4.4}$$

where the a_n coefficients have been determined empirically by analyzing approximately 550 bow shock crossings provided by 17 distinct spacecraft from the years 1963 - 1980. There are five sets of coefficients, which were determined by satellite bow shock crossings for five different Alfvén mach number ranges, given in Table 4.1.

The distance squared between the HFA at (x_H, y_H, z_H) and a point on the bow shock surface, (x,y,z), is given by

$$f(x,y,z) = (x - x_H)^2 + (y - y_H)^2 + (z - z_H)^2 \tag{4.5}$$

We will find the minimum distance using the method of Lagrange multipliers.

First, let

$$L(x,y,z,\lambda) = f(x,y,z) + \lambda g(x,y,z) \tag{4.6}$$

using the f and g defined above. Because we are essentially adding zero to $f(x,y,z)$, we are not changing the original function f provided the constraint is met. Substitute f and g into L:

$$L = (x - x_H)^2 + (y - y_H)^2 + (z - z_H)^2 + \lambda a_1x^2 + \lambda y^2 + \lambda a_3z^2 + \lambda 2a_4xy + \lambda 2a_7x + \lambda 2a_8y + \lambda a_{10} \tag{4.7}$$

Expand the expressions to get

$$L = \begin{array}{l} x^2 - 2xx_H + x_H^2 + y^2 - 2yy_H + y_H^2 + z^2 - 2zz_H + z_H^2 + \\ \lambda a_1x^2 + \lambda y^2 + \lambda a_3z^2 + \lambda 2a_4xy + \lambda 2a_7x + \lambda 2a_8y + \lambda a_{10} \end{array} \tag{4.8}$$

Minimization by Lagrange multipliers dictates that we want the three conditions of Equations 4.9, 4.10, and 4.11:

$$\frac{\partial L}{\partial x} = 0 = 2x - 2x_H + 2\lambda a_1x + 2\lambda a_4y + 2\lambda a_7 \tag{4.9}$$

Table 4.1. Model Bow Shock Coefficients for GPE Coordinate System [*Merka et al.*, 2005]

M_A	a_1	a_3	a_4	a_7	a_8	a_{10}
2 - 5	-0.12292±0.57716	0.81092±0.11429	-0.20902±0.14660	28.270±2.966	-0.75985±0.96604	-649.29±36.19
5 - 8	-0.02996±0.05664	0.93743±0.05399	0.00227±0.02399	21.196±0.697	-0.57751±0.30654	-536.81±18.35
8 - 13	-0.21644±0.09335	0.91729±0.05016	0.01680±0.03805	19.570±0.914	0.02222±0.28772	-471.21±21.97
13 - 20	0.04615±0.19012	1.00468±0.08448	0.01286±0.06630	20.280±1.200	-0.03024±0.46548	-512.18±27.12
2 - 20	-0.04766±0.04981	0.94784±0.03655	0.00761±0.01723	21.034±0.553	-0.31152±0.20116	-524.03±14.65

$$\frac{\partial L}{\partial y} = 0 = 2y - 2y_H + 2\lambda y + 2\lambda a_4 x + 2\lambda a_8 \tag{4.10}$$

$$\frac{\partial L}{\partial z} = 0 = 2z - 2z_H + 2\lambda a_3 z \tag{4.11}$$

Now we have a system of four equations (Equations 4.4, 4.9, 4.10, and 4.11) and four variables (x, y, z, and λ). We can numerically solve the system to find x, y, z, and λ. Afterwards, we can check the Hessian to determine whether the solution, point (x,y,z), is a minima, maxima, or saddle point. In this dissertation, solving the system was done numerically in IDL.

4.2.3 Calculate Bow Shock Normal

Given that $g(x,y,z)$ of Equation 4.4 is the bow shock surface, and defining the calculated point (x,y,z) from Section 4.2.2 be $P_0(x_0,y_0,z_0)$, the normal line of the surface at P_0 is the line through P_0 parallel to $\nabla g\big|_{P_0}$.

Using Equation 4.4, $\frac{\partial g}{\partial x} = 2a_1x + 2a_4y + 2a_7$, $\frac{\partial g}{\partial y} = 2y + 2a_4x + 2a_8$, and $\frac{\partial g}{\partial z} = 2a_3z$.

The line normal to the surface $g(x,y,z)$ at point P_0 is given by $x = x_0 + \left[\frac{\partial g}{\partial x}\right]_{P_0} t$, $y = y_0 + \left[\frac{\partial g}{\partial y}\right]_{P_0} t$, and $z = z_0 + \left[\frac{\partial g}{\partial z}\right]_{P_0} t$ with parameter t such that $-\infty \leqq t \leqq \infty$. Evaluating with g, the line normal to the bow shock is:

$$x = x_0 + \left(2a_1x_0 + 2a_4y_0 + 2a_7\right) t \tag{4.12}$$

$$y = y_0 + \left(2y_0 + 2a_4x_0 + 2a_8\right) t \tag{4.13}$$

$$z = z_0 + (2a_8z_0)\, t \tag{4.14}$$

The bow shock normal vector at $P_0(x_0,y_0,z_0)$ is

$$\left(2a_1x_0 + 2a_4y_0 + 2a_7\right)\hat{\mathbf{i}} + \left(2y_0 + 2a_4x_0 + 2a_8\right)\hat{\mathbf{j}} + (2a_8z_0)\,\hat{\mathbf{k}}$$

4.3 Calculating Normals to Shocks and Discontinuities

4.3.1 Minimum Variance Analysis

The minimum variance analysis (MVA) method for magnetic fields [*Sonnerup and Cahill*, 1967; *Sonnerup and Scheible*, 1998] can be used to calculate the normal to discontinuities, a transition layer. For situations where all waves were propagating parallel to the shock normal, the MVA method could be use to calculate the direction of shock normals, but this condition is only met for waves in a limited region of parameter space. The MVA method makes use of the fact that magnetic fields are divergenceless. That divergenceless requires that the change in the normal component of the magnetic field on both sides of any shock or discontinuity to be zero, $B_{n1} = B_{n2}$. The MVA method determines the normal direction to be the one along which the magnetic field has the minimum variance. The variance is defined as

$$\sigma = \sqrt{\sum_{m=1}^{N} \frac{|(\mathbf{B_m} - \langle \mathbf{B} \rangle) \cdot \mathbf{n}|^2}{N}} \tag{4.15}$$

where N is the total number of data points selected for this analysis that bracket the discontinuity, $\mathbf{B_m}$ is a data point of the magnetic field set, $\langle \mathbf{B} \rangle$ is the vector average of all $\mathbf{B}$ data points defined as $\langle \mathbf{B} \rangle = \frac{1}{N} \sum_{m=1}^{N} \mathbf{B_m}$, and $\mathbf{n}$ is the normal vector of the discontinuity. The MVA method determines the normal $\mathbf{n}$ by minimizing σ. Ideally, the minimum variance along the normal direction is zero, but the calculated normal via MVA is only the most probable normal direction.

Eigenvalues from this method arise from the Lagrange multiplier technique used to minimize σ. The eigenvalues are all real and their corresponding eigenvectors are orthogonal. Placing the three eigenvalues in order of decreasing magnitude, $\lambda_1, \lambda_2, \lambda_3$, the corresponding eigenvectors, $\mathbf{x_1}, \mathbf{x_2}, \mathbf{x_3}$, represent directions of maximum, intermediate, and minimum variance of the field component along each vector. The eigenvector, $\mathbf{x_3}$, which corresponds to the smallest eigenvalue, λ_3, is used as an estimate the vector normal to the transition layer being examined. That smallest eigenvalue is the variance of the magnetic field component along the estimated normal. The eigenvectors corresponding to maximum and intermediate variance are tangential to the transition layer [*Sonnerup and Scheible*, 1998].

Calculation of the minimum-to-intermediate eigenvalue ratio will allow a comparison of the chosen minimum variance direction as compared to the variance along other direc-

tions. For example, a ratio of 0.1 means that the minimum variance is 10% or less of the variance along other directions. The eigenvalue ratio is important to calculate because when two eigenvalues are nearly the same, the uncertainty in the corresponding eigenvectors is large with respect to rotation about the remaining eigenvector. For example, if λ_2 and λ_3 are approximately the same, their ratio will be close to unity. The uncertainty of the corresponding eigenvectors is large with respect to rotation about $\mathbf{x_1}$. In extreme cases, the calculated intermediate and minimum variance directions, $\mathbf{x_2}$ and $\mathbf{x_3}$, could be rotated 90° from their actual directions. This means the normal vector produced cannot be trusted.

Three types of degeneracy are possible for the eigenvalues. First is $\lambda_1 \simeq \lambda_2$. This case does not limit MVA analysis for determining normal vectors provided that $\lambda_3 \ll \lambda_2 \simeq \lambda_1$. A second type of degeneracy is $\lambda_2 \simeq \lambda_3$. In this case, there is no valid normal vector calculated. $\mathbf{x_1}$ is still a valid tangential direction to the layer if $\lambda_1 \ll \lambda_2 \simeq \lambda_3$. The third type of degeneracy is where $\lambda_1 \simeq \lambda_2 \simeq \lambda_3$. For this case, no information about the normal or tangential directions to the layer is obtained [*Sonnerup and Scheible*, 1998].

This method fails when there is a systematic temporal change in the normal direction [*Sonnerup and Scheible*, 1998]. This can happen where there is a zero-level offset of the magnetometer measuring the field component along the spacecraft spin axis. When using MVA, care should also be taken to require that the minimum variance direction results do not change appreciably when one varies the selected range of magnetic field vector input data.

4.3.2 Coplanarity Method

The coplanarity method is used to calculate shock normals. The Coplanarity Theorem states that for compressive shocks, the magnetic field on both sides of the shock and the shock normal all lie in the same plane. Define $\triangle\mathbf{B}$ as the downstream magnetic field $\mathbf{B_d}$ minus the upstream magnetic field $\mathbf{B_u}$ and $\triangle\mathbf{V}$ is the downstream velocity $\mathbf{V_d}$ minus the upstream velocity $\mathbf{V_u}$. With magnetic coplanarity, the normal is defined as

$$\hat{\mathbf{n}} = \pm \frac{(\mathbf{B_d} \times \mathbf{B_u}) \times \triangle\mathbf{B}}{|(\mathbf{B_d} \times \mathbf{B_u}) \times \triangle\mathbf{B}|} \tag{4.16}$$

This method will fail if the angle between the upstream magnetic field and the shock normal is 0° or 90°.

If the magnetic field on both sides of a shock and shock normal all lie in the same plane, the only tangential stresses are from magnetic tension so that the velocity jump across the shock also must lie in same plane [*Schwartz*, 1998]. This allows for the calculation of mixed mode normal vectors. Three common mixed mode normals are

$$\hat{\mathbf{n}} = \pm \frac{(\mathbf{B_u} \times \triangle \mathbf{V}) \times \triangle \mathbf{B}}{|(\mathbf{B_u} \times \triangle \mathbf{V}) \times \triangle \mathbf{B}|} \tag{4.17}$$

$$\hat{\mathbf{n}} = \pm \frac{(\mathbf{B_d} \times \triangle \mathbf{V}) \times \triangle \mathbf{B}}{|(\mathbf{B_d} \times \triangle \mathbf{V}) \times \triangle \mathbf{B}|} \tag{4.18}$$

and

$$\hat{\mathbf{n}} = \pm \frac{(\triangle \mathbf{B} \times \triangle \mathbf{V}) \times \triangle \mathbf{B}}{|(\triangle \mathbf{B} \times \triangle \mathbf{V}) \times \triangle \mathbf{B}|} \tag{4.19}$$

The velocity in these equations can be measured in any frame and does not need to be in a shock rest frame. This method assumes that there are a sufficiently large number of data points upstream and downstream of the shock [*Schwartz*, 1998].

4.3.3 Time Delay Analysis (Timing Method)

The timing method is used to calculate the boundary normal and normal propagation speed using the two assumptions that discontinuities, shocks, or compressional boundaries are planar and that they move at a constant speed. This method utilizes the relative positions and timings of multiple spacecraft that observe the same boundary. This method requires the solving of a system of equations in the form of

$$\left(\mathbf{V_s} t_{\alpha\beta}\right) \cdot \hat{\mathbf{n}} = \mathbf{r}_{\alpha\beta} \cdot \hat{\mathbf{n}} \tag{4.20}$$

where $\mathbf{r}_{\alpha\beta}$ is the relative separation vector between any spacecraft pair and $t_{\alpha\beta}$ is the corresponding time difference for when they observed a particular boundary [*Schwartz*, 1998]. The velocity in these equations can be measured in any frame and does not need to be in a shock rest frame.

For time delay analysis with four spacecraft, there are three independent equations:

$$\frac{\left(\triangle x_{1i} \cdot n_x + \triangle y_{1i} \cdot n_y + \triangle z_{1i} \cdot n_z\right)}{V_n} = \triangle t_{1i} \tag{4.21}$$

where i=2,3,4. $\triangle x_{1i}$, $\triangle y_{1i}$, and $\triangle z_{1i}$ are the separations between spacecraft 1 and spacecraft 2,3,4 respectively. $\triangle t_{1i}$ is the time delay between when spacecraft 1 observed the boundary and when spacecraft 2,3, and 4 observed the boundary. The three components of the normal vector divided by the normal speed is calculated by solving the linear equations. Calculating the components of the normal vector and the normal propagation velocity, $V_s = \mathbf{V_s} \cdot \hat{\mathbf{n}}$, are obtained by using the constraint that $n_x^2 + n_y^2 + n_z^2 = 1$.

This method fails when the four spacecraft are coplanar or nearly coplanar. If the separation of the spacecraft are large, the planarity assumption may break down. Care should also be taken to complete the numerical analysis with data in a coordinate system that is stationary (unlike the common GSE with a moving origin) or using spacecraft positions in a common coordinate system [*Schwartz*, 1998].

4.3.4 Tangential Discontinuities

For tangential discontinuities, the upstream and downstream magnetic field vectors are parallel to the shock plane and are generally not parallel to one another [*Schwartz*, 1998]. With this, the normal is given by

$$\hat{\mathbf{n}} = \pm \frac{\mathbf{B_u} \times \mathbf{B_d}}{|\mathbf{B_u} \times \mathbf{B_d}|} \tag{4.22}$$

4.3.5 Boundary Normal Coordinates

Boundary normal coordinates, commonly referred to as the LMN coordinate system, are coordinate axes defined relative to a boundary such as a shock. The L and M axes lie in a plane tangential to the boundary. The N axis is normal to the boundary. There is not a universal convention for defining the directions of the L and M axes. The method used in this work is to take the largest eigenvalue from the MVA analysis and let the associated eigenvector be the L axis. The M direction is defined so LMN is a right handed Cartesian system. It is customary to ensure that the N points away from the object, such as a planet or comet for example, supporting the boundary. If not, the signs of all components of N can be reversed to achieve this condition.

4.3.6 Hodograms

A magnetic hodograph is a curve created by drawing a series of measured magnetic field vectors and connecting the arrowheads of the vectors with line segments. The line segments are connected following the time sequence of when they were measured. A hodograph displayed in two directions is called a hodogram. As an example, a projection onto a plane that is tangential to the layer is a plot of $B_1 = \mathbf{B_m} \cdot \mathbf{x_1}$ versus $B_2 = \mathbf{B_m} \cdot \mathbf{x_2}$ where $\mathbf{x_1}$ and $\mathbf{x_2}$ are the eigenvectors as defined in Section 4.3.1. $\mathbf{B_m}$ is a data point from the magnetic field dataset. A projection of B_1 or B_2 against $B_3 = \mathbf{B_m} \cdot \mathbf{x_3}$ is a plot versus the normal field component ($\mathbf{x_3}$ defined in Section 4.3.1).

4.4 Calculating Shock and Boundary Normal Speeds

After calculating a shock normal vector, the shock normal speed in the Earth rest frame can be obtained. Relevant frames of reference include the solar wind frame, the spacecraft rest frame, and Earth rest frame. The spacecraft and Earth rest frames are nearly identical and will be considered the same in this dissertation. In addition to the method for calculating the discontinuity speed in Section 4.3.3, there are three other methods discussed below.

4.4.1 Time Delay Analysis with Two Spacecraft

The shock normal speed in the solar wind frame is equal to the shock normal speed in the rest frame minus the solar wind speed along the shock normal direction. The shock normal speed in the rest frame can be obtained from multiple spacecrafts' data. The velocity of the shock is equal to the distance between the locations where the spacecrafts each respectively observed the shock divided by the time difference between each spacecraft's observation of the shock. This method assumes that the shock normal is along the line connecting the two spacecraft. This is not generally true so we project the distance between observations along the shock normal to make the time delay calculation. This method also assumes the shock is moving at a constant speed.

4.4.2 Mass Flux Algorithm

Shock normal speed in the solar wind frame can be calculated using the mass flux conservation equation which yields this equation:

$$V_s = \frac{\rho_u \mathbf{V_u} - \rho_d \mathbf{V_d}}{\rho_u - \rho_d} \cdot \hat{\mathbf{n}} \tag{4.23}$$

where ρ_u and ρ_d are the density upstream and downstream of the shock respectively [*Schwartz*, 1998]. $\mathbf{V_u}$ and $\mathbf{V_d}$ are the velocity downstream and upstream of the shock respectively. The velocity here can be measured in any frame and does not need to be in a shock rest frame. $\hat{\mathbf{n}}$ is the shock normal unit vector. This method requires there to be enough points in the upstream and downstream regions.

4.4.3 Continuity of the Tangential Electric Field

Shock normal speed in the solar wind frame can be calculated using the RH condition representing the continuity of the tangential electric field [*Smith and Burton*, 1988]. This method does not require an explicit calculation of the shock normal. The shock speed is calculated using the equation

$$V_s = \frac{|\triangle \mathbf{V} \times \mathbf{B_d}|}{|\triangle \mathbf{B}|} \tag{4.24}$$

where $\triangle \mathbf{V}$ is the upstream velocity minus the downstream velocity, $\mathbf{B_d}$ is the downstream magnetic field vector, and $\triangle \mathbf{B}$ is the upstream magnetic field vector minus the downstream magnetic field vector. The velocity here can be measured in any frame and does not need to be in a shock rest frame. This method requires there to be enough points in the upstream and downstream regions. This method breaks down for parallel acoustic shocks because $B_d = B_u$ [*Schwartz*, 1998].

4.5 Normalization of Bar Plots

Let the total number of events in a particular bin be N. The total number of measurements the THEMIS satellite made which fit the parameters of that particular bin is represented by n. The normalized value for each bin is

$$N_0 = \frac{N}{n} = \frac{\text{number of events}}{\text{total number of measurements}} \tag{4.25}$$

The Poisson error for a counted number of events N is $\sqrt{N}$. Similarly, the Poisson error for the total number of measurements n is $\sqrt{n}$. From a propagation of errors analysis using average deviations, the uncertainty for each normalized value calculated is

$$\Delta N_0 = N_0 \sqrt{\left(\frac{\sqrt{N}}{N}\right)^2 + \left(\frac{\sqrt{n}}{n}\right)^2} = N_0 \sqrt{\frac{1}{N} + \frac{1}{n}} \tag{4.26}$$

4.6 Magnetic Local Time of Ground Stations

For a given observation by a ground station (given in universal time), the magnetic local time (MLT) of that observation can be calculated if one knows the station's magnetic longitude using the equation

$$MLT = UT + \left(\frac{m_{longitude} - 71}{15}\right) \tag{4.27}$$

MLT in the equation denotes the magnetic local time of the station during the observation, *UT* is the universal time during the observation, and $m_{longitude}$ is the magnetic longitude of the station. MLT is independent of latitude. It is a basic way to describe where an observation was made relative to the Earth and Sun.

4.7 Distance Between Two Latitude and Longitude Points

A great circle is the shortest distance over the Earth's surface and ignores things like hills and terrain. In this dissertation, the great circle distance between two points is calculated assuming a spherical Earth meaning ellipsoidal effects are ignored. The distance between two locations on a planet can be calculated many ways including use of the haversine formula, spherical law of cosines, and Pythagoras' theorem applied to an equirectangular approximation.

This dissertation uses the haversine formula. The haversine is defined as

$$a = \sin^2\left(\frac{\varphi_2 - \varphi_1}{2}\right) + \cos\varphi_1 \cdot \cos\varphi_2 \cdot \sin^2\left(\frac{\lambda_2 - \lambda_1}{2}\right) \tag{4.28}$$

where φ is the latitude and λ is the longitude. Latitude and longitude are in radians in the equation [*Calculate distance, bearing and more between Latitude/Longitude points*, 2017].

The great circle distance, d is calculated with

$$d = R \cdot c \tag{4.29}$$

where R is the Earth's radius and c is calculated with

$$c = 2 \cdot \arcsin\left(\text{minimum}\left(1, \sqrt{a}\right)\right) \tag{4.30}$$

c is the angular distance in radians, and a is the square of half the chord length between the points.

4.8 Chapter Summary

This chapter discussed general analysis techniques applied to the data analysis chapters of this dissertation. The next chapter analyzes the database of HFAs created using the techniques in Section 4.1. That chapter is a statistical study of HFAs. Future chapters will examine individual HFAs in-depth.

Chapter 5
Statistical Analysis of Hot Flow Anomalies at Earth

This chapter presents a statistical analysis of HFAs identified in THEMIS data from 2007 to 2009. The study focuses on HFA properties in relation to local solar wind properties near each event.

5.1 Introduction

Hot flow anomaly location results have been reported in past literature. *Facskó et al.* [2009] found that HFAs could be identified at distances from Earth greater than 19 R_E. Using a model bow shock and accounting for the local solar wind, they observed HFAs greater than 4 R_E upstream from the bow shock. Determining the typical locations of HFA observations will further our fundamental understanding of where conditions favor HFA existence.

HFA properties that may evolve with time include flow velocities, density, temperature, magnetic field strength, and size. *Zhang et al.* [2010] showed observations of a proto-HFA (with decreases from solar wind levels in magnetic field strength and plasma density) and then observations of a mature HFA with the same satellite constellation 110 seconds later (hot core flanked by enhanced magnetic field strength and plasma density).

Spontaneous HFAs (SHFA) were described by *Zhang et al.* [2013]; *Omidi et al.* [2013b]. SHFAs exhibit the same deflected solar wind plasma velocities and plasma heating used to classify events as HFAs, but they are observed without the solar wind discontinuities that are thought to generate HFAs. *Omidi et al.* [2014] showed that SHFAs in hybrid code simulations may form at all cone angles and form more frequently at higher Alfvén Mach numbers.

HFA or SHFA formation requires kinetic energy from the solar wind to be converted into thermal energy inside the event. This suggests that young HFAs or SHFAs should exhibit a smaller increase in thermal energy than mature HFAs or SHFAs. *Wang et al.* [2013b] analyzed HFAs observed by Cluster to conclude that part of the solar wind kinetic energy is converted to thermal energy inside HFAs via heating processes.

This study compares the characteristics, such as density depletion and temperature increase, of four categories of HFAs: young spontaneous, young non-spontaneous, mature spontaneous, and mature non-spontaneous. We also examine the occurrence rate of

HFAs and their dependence on solar wind/IMF conditions and distance from the bow shock.

We expect that the HFA core density and temperatures may exhibit weak dependancies on both the distance the HFA is observed from the bow shock and its magnetic local time. From conclusions drawn by *Facskó et al.* [2009], we expect that the THEMIS observed HFAs in this study will have an occurrence rate that increases for fast solar wind speeds. Physically, at the bow shock, solar wind particles are reflected back towards the foreshock region at the solar wind speed. It is presumed that the interaction of the reflected and incoming solar wind is what forms the HFA. Higher solar wind speeds therefore mean the reflected beam has higher energy and an increased chance that an HFA could form. We expect the occurrence rate of HFAs to decrease with increasing distance upstream from the bow shock. We expect that the highest occurrence rates of HFAs will occur near the more radial IMF orientations because at those configurations, the particles reflected off of the bow shock are able to travel further upstream into the foreshock region and interact with the solar wind particles.

5.2 Results

The results and conclusions text of this chapter are presented in *Chu et al.* [2017]. Figure 5.1(a) shows the locations where THEMIS C made observations in the solar wind from 2007–2009 in the XY, XZ, and YZ plane of the GPE coordinate system. Figure 5.1(b) shows the location of 136 hot flow anomalies in the XY, XZ, and YZ plane using GPE coordinates. Four symbols represent the four HFA categories: young HFA, mature HFA, young SHFA, and mature SHFA (open diamond, filled-in diamond, open circle, and filled in circle respectively). The color of each HFA or SHFA corresponds to the maximum ion temperature observed in the core of each HFA. In this study, the observed ion temperature inside an HFA ranged from 3 to 97 times above the electron temperature. The drawn bow shocks are model surfaces using coefficients from the *Merka et al.* [2005] bow shock model for an Alfvén Mach number range of 2–20. *Merka et al.* [2005] specifies empirically calculated bow shocks for five individual Alfvén Mach number ranges of 2–5, 5–8, 8–13, 13–20, and 2–20. The average bow shock derived from data with the widest Mach number range, 2–20, was chosen for the figures instead of a bow shock derived with Mach number ranges 2–5, 5–8, 8–13, or 13–20 so that a comparison of HFAs and SHFAs at all Mach numbers could be performed against each other. The HFAs were first divided into groups

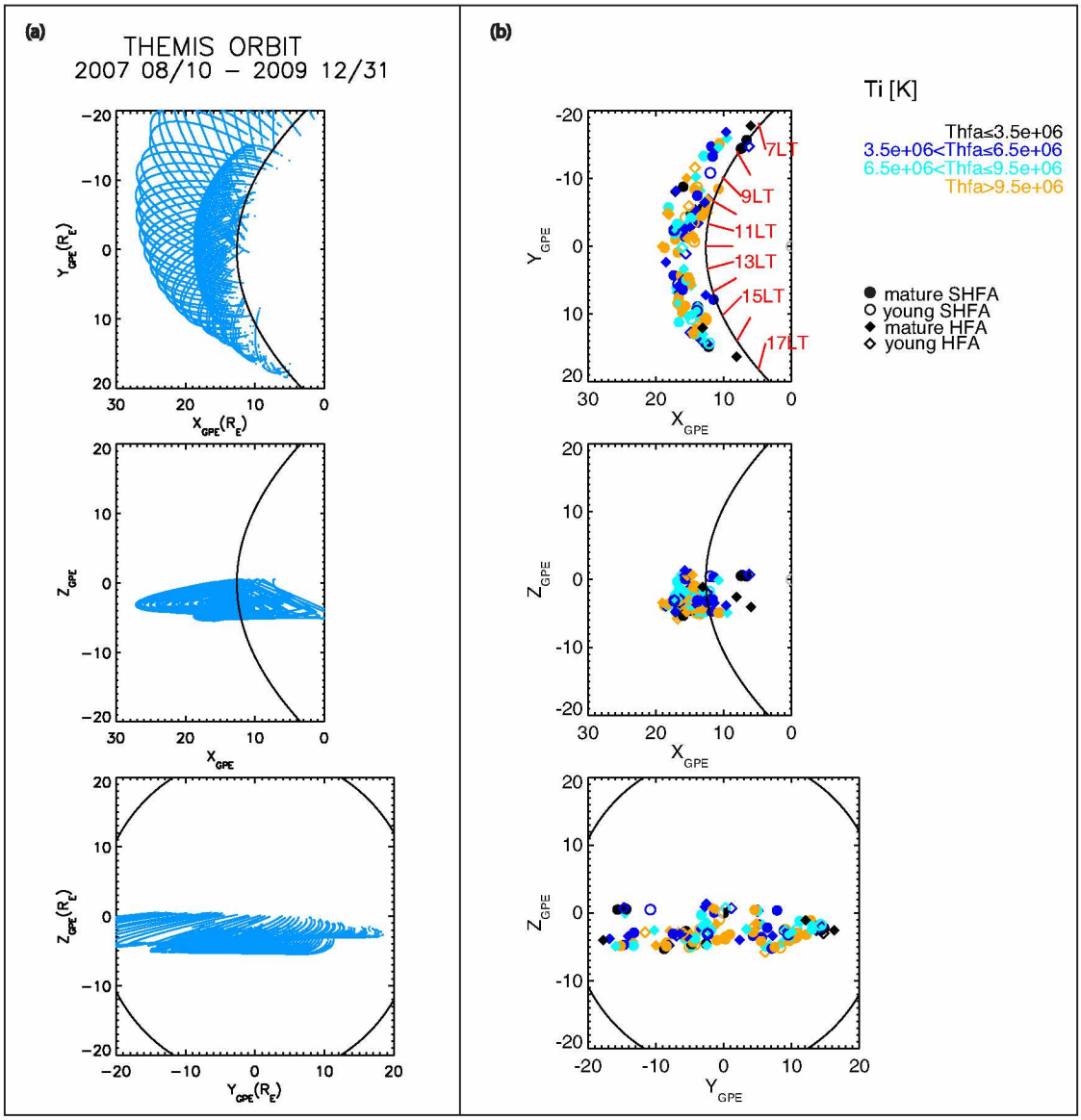

Figure 5.1. (a) The spatial location of all THEMIS C intervals in the interplanetary medium for 2007–2009 in GPE coordinates. The thick black curve is the *Merka et al.* [2005] bow shock for an Alfvén Mach number range of 2–20. (b) The spatial locations of HFAs and SHFAs identified in THEMIS C data, August 2007 to December 2009, are plotted in these figures in the XY, XZ, and YZ planes using GPE coordinates. The thick black curves are the *Merka et al.* [2005] bow shock for an Alfvén Mach number range of 2–20. Four symbols represent the four HFA categories: young HFA, mature HFA, young SHFA, and mature SHFA (open diamond, filled-in diamond, open circle, and filled in circle respectively). The color of each HFA or SHFA corresponds to the largest temperature measured inside each HFA.

based on their local solar wind Mach number (Mach 2–5, 5–8, 8–13, and 13–20). For each Mach number range, the distance of the HFA from the corresponding model bow shock was calculated. The plotted HFA positions relative to the 2–20 Mach number model bow shock were scaled so that all HFAs are located upstream of the bow shock.

In Figure 5.1b, the top plot with the XY plane shows that HFAs were observed over the range of magnetic local times (MLT) from approximately 7 to 16.5 MLT. The colors of Figure 5.1b show the ion temperatures of the HFA cores, T_i. On the XY plane of Figure 5.1(b), we see that the hottest ion temperatures at the core of the HFAs, shown in red, are seen within approximately 8–15 MLT and not seen at the far dawn and dusk flanks outside the 8–15 MLT range.

Figure 5.2(a) shows n_{HFA}/n_{sw} with respect to MLT for young and mature SHFAs, and Figure 5.2(b) shows that for young and mature regular HFAs. n_{HFA} is the minimum density value observed for each HFA event. The red horizontal lines represent the median value of the HFAs' n_{HFA}/n_{sw} in the MLT range spanned by each red line. n_{HFA}/n_{sw} does not seem to show a dependance on MLT.

Figure 5.2(c) shows the ratio of the hottest measured ion temperature of each HFA to the average local solar wind ion temperature plotted with respect to MLT for young and mature SHFAs, while Figure 5.2(d) shows the HFA to local solar wind ion temperature ratio for young and mature regular HFAs plotted against MLT. The red horizontal lines represent the median value of the HFA to local solar wind ion temperature ratio in the MLT range spanned by each red line. HFAs with high event core ion temperatures or large ratio values were not seen at the dawn and dusk flanks. This may suggest that HFAs cool as they convect with the solar wind towards the flanks. It may also suggest that HFAs form with lower core temperatures away from the subsolar region.

Figure 5.3 shows the HFAs of the dataset binned by distance upstream from the *Merka et al.* [2005] model bow shock, where the distance was measured along the normal to the bow shock. These distances are calculated using the model bow shock coefficients that correspond to the Alfvén Mach number ranges 2–5, 5–8, 8–13, or 13–20. The bins are normalized by the amount of time that THEMIS C spent in the respective bin's range from 2007–2009. HFAs and SHFAs were observed up to 6.3 R_E and 6.1 R_E upstream from the bow shock respectively. It is possible that proto-HFAs were present even further upstream from the bow shock but they did not exhibit large enough plasma parameter deflections

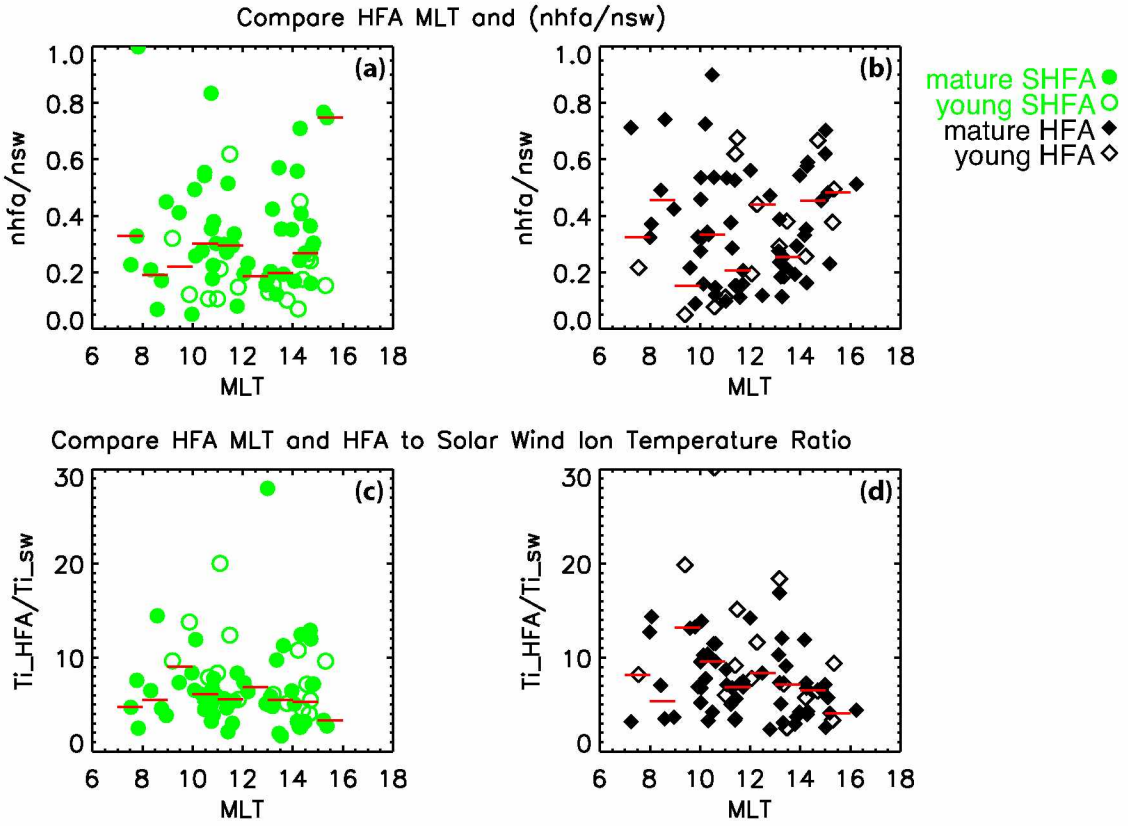

Figure 5.2. (a) and (b): The ratios of the minimum density of the HFA or SHFA core to the local solar wind density are plotted with respect to the events' magnetic local time (MLT). Panel (a) shows SHFAs and (b) shows HFAs. (c) and (d): Ratio of ion temperatures of HFAs or SHFAs to the local solar wind ion temperature are plotted with respect to the events' MLT. Panel (c) shows SHFAs and (d) shows HFAs. Four symbols represent the four HFA categories: young HFA, mature HFA, young SHFA, and mature SHFA (open diamond, filled-in diamond, open circle, and filled in circle respectively). SHFAs are shown in green, HFAs are shown in black. Red lines indicate the median value of data bins along the x axis.

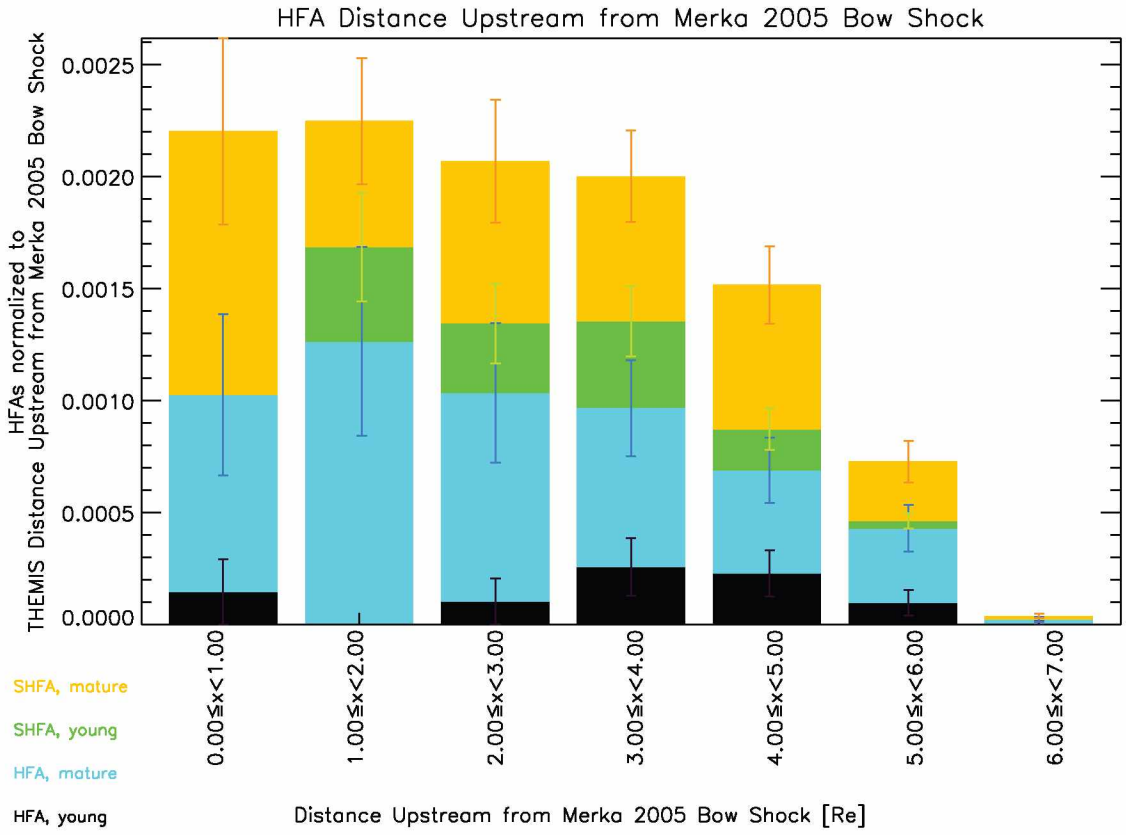

Figure 5.3. HFAs and SHFAs identified in THEMIS C data, August 2007 to December 2009, plotted with respect to the events' distance upstream from the *Merka et al.* [2005] bow shock. Events have been separated into four categories: young HFA, mature HFA, young SHFA, and mature SHFA. Each bin has been normalized to the amount to time THEMIS spent upstream of the bow shock. THEMIS made observations up to 24.5 R_E upstream of the bow shock.

for identification as an HFA or SHFA. HFAs and SHFAs both show similar trends where the occurrence decreases with increasing distance upstream from the bow shock.

Figures 5.4(a) and (b) shows n_{HFA}/n_{sw} with respect to each event's distance from the *Merka et al.* [2005] model bow shock for young and mature SHFAs (a) and young and mature regular HFAs (b). The red horizontal lines represent the median value of n_{HFA}/n_{sw} in the bow shock distance range spanned by each red line. The median values of n_{HFA}/n_{sw} generally decreases with distance from the bow shock for SHFAs from 0 R_E to 4 R_E upstream from the bow shock but over all distances does not show a clear trend. For the HFA dataset in this study, when an HFA forms near the bow shock, its core density has a median ratio of approximately 0.4 to the nearby solar wind's density. As an HFA's distance upstream from the bow shock increases, the core density to solar wind density ratio decreases.

Figures 5.4(c) and (d) plots the ratio of the hottest ion temperature observed in each HFA to the average solar wind temperature, T_{ihfa}/T_{isw}, against the HFA's distance from the *Merka et al.* [2005] bow shock. Young and mature SHFAs are shown in Figure 5.4(c) and young and mature regular HFAs are shown in Figure 5.4(d). The red horizontal lines represent the median value of T_{ihfa}/T_{isw} in the bow shock distance range spanned by each red line. The absolute hottest ion heating for both SHFAs and HFAs is located at around 4 R_E. Examining the red median lines, the conclusion is that there was no clear relationship between the HFA to solar wind temperature ratio and distance a HFA was observed upstream from the bow shock.

Figures 5.4(e) and (f) examine how much the ion temperature increased inside each HFA compared to how much the electron temperature increased inside the HFA $((T_{ihfa}/T_{isw})/(T_{ehfa}/T_{esw}))$ and plots that against distance from the *Merka et al.* [2005] bow shock. Young and mature SHFAs are shown in Figure 5.4(e) and young and mature regular HFAs are shown in Figure 5.4(f). The red horizontal lines represent the median value of $((T_{ihfa}/T_{isw})/(T_{ehfa}/T_{esw}))$ in the bow shock distance range spanned by each red line. Significant differences between the ion and electron heating ratios was not expected. The ion heating relative to the electron heating was highest between 2 and 6 R_E for both SHFAs and HFAs, but this was only a slight increase in heating from HFAs in the other distance bins.

In Figure 5.4(e), examining the red median lines for the SHFAs reveals that $((T_{ihfa}/T_{isw})/(T_{ehfa}/T_{esw}))$ generally increased with distance from the bow shock. For HFAs

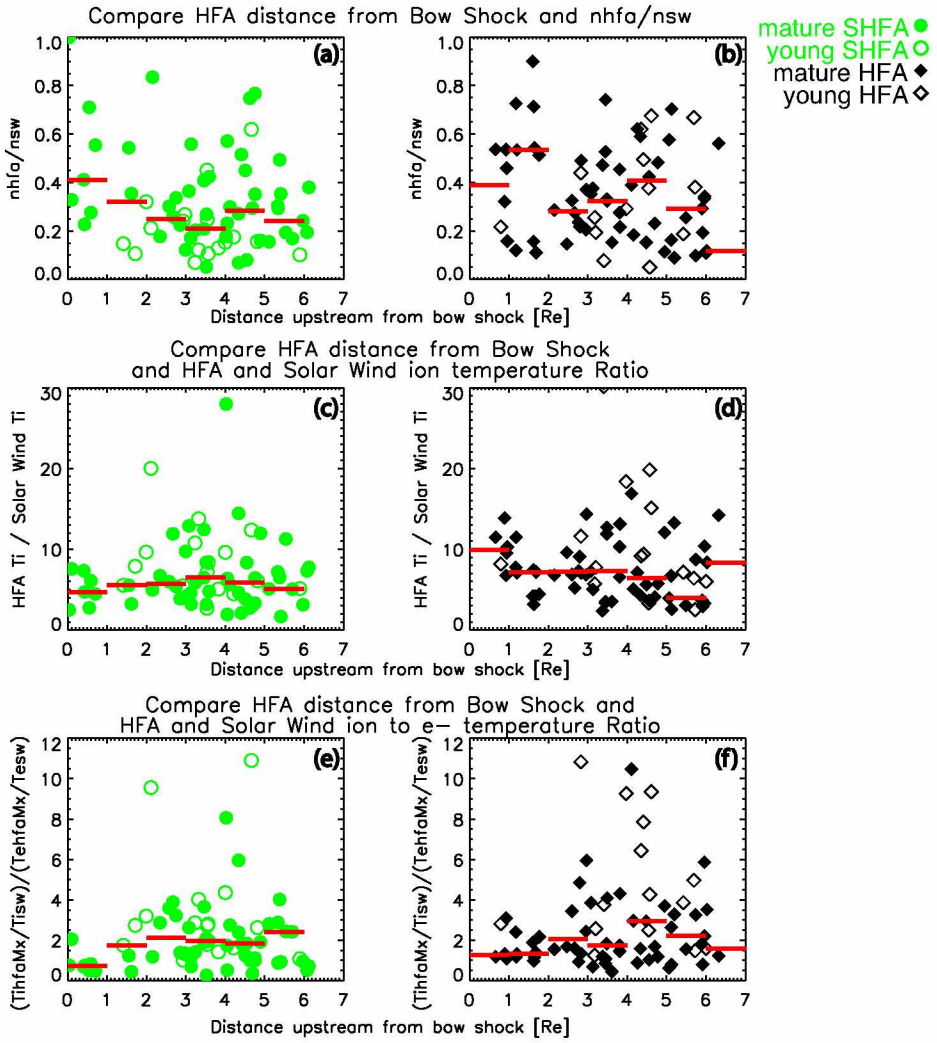

Figure 5.4. (a) and (b): The ratios of the minimum density of the HFA or SHFA core to the local solar wind density are plotted with respect to the events' distance upstream from the *Merka et al.* [2005] bow shock. Panel (a) shows SHFAs and (b) shows HFAs. (c) and (d): The ratios of the maximum event ion temperature to the events' average solar wind ion temperature, (T_{ihfa}/T_{isw}), are plotted in these figure with respect to the events' distance upstream from the *Merka et al.* [2005] bow shock. Panel (c) shows SHFAs and (d) shows HFAs. (e) and (f): The ratio of the events' maximum event ion temperature to the events' average solar wind ion temperature relative to the ratio of the events' maximum event electron temperature to the events' average solar wind electron temperature, $(T_{ihfa}/T_{isw})/(T_{ehfa}/T_{esw})$, are plotted in these figure with respect to the events' distance upstream from the *Merka et al.* [2005] bow shock. Panel (e) shows SHFAs and (f) shows HFAs. Four symbols represent the four HFA categories: young HFA, mature HFA, young SHFA, and mature SHFA (open diamond, filled-in diamond, open circle, and filled in circle respectively). SHFAs are shown in green, HFAs are shown in black. Red lines indicate the median value of data bins along the x axis.

in Figure 5.4(f), $((T_{ihfa}/T_{isw})/(T_{ehfa}/T_{esw}))$ generally increased with distance from the bow shock until about 5 R_E and then decreased. For SHFAs, the factor that ions were heated by, (T_{ihfa}/T_{isw}), approximately equaled the factor that electrons were heated by, (T_{ehfa}/T_{esw}), for 0–1 R_E so that $((T_{ihfa}/T_{isw})/(T_{ehfa}/T_{esw}))$ was about equal to 1. As HFAs were observed further from the bow shock, the factor that ions were heated by was greater than the factor that electrons were heated by.

For both SHFAs and HFAs, from 0 to 2 R_E, the median value of the ratio $((T_{ihfa}/T_{isw})/(T_{ehfa}/T_{esw}))$ is slightly lower than for 2–7 R_E. From approximately 0 to 1 R_E upstream of the bow shock, the amount of ion heating, (T_{ihfa}/T_{isw}), is the same as the electron heating, (T_{ehfa}/T_{esw}). From 1 to 7 R_E, the electron heating ratio, (T_{ehfa}/T_{esw}), was lower than the ion heating ratio, (T_{ihfa}/T_{isw}), so that $((T_{ihfa}/T_{isw})/(T_{ehfa}/T_{esw}))$ was greater than 1.

Figure 5.5 examines the relationship between both HFAs and SHFAs and the IMF cone angle (cone angle is the angle between the Sun–Earth line and B_{IMF}). Cone angle θ is defined as $\theta = \cos^{-1}\left(\frac{b_x}{\sqrt{b_x^2+b_y^2+b_z^2}}\right)$. THEMIS C observed solar wind intervals both before and after each HFA so two different cone angles could be calculated for each event, one averaging the solar wind before observing the HFA and one after. To create this figure, both angles were calculated and the most radial cone angle was chosen as the sole solar wind cone angle value for the particular HFA (the angle closest to 0° or 180° was chosen). The highest normalized occurrence rates of HFAs and SHFAs are for cone angles between 0° and 40° and from 160° to 180°. This figure shows that HFAs form more preferentially for more radial IMF configurations and 0° and 180° correspond to radial IMF conditions.

Figure 5.6 examines the relationship between HFAs and SHFAs and their corresponding average solar wind IMF orientation. In our analysis, 0° and 180° corresponds to radial IMF where 0° is along the positive x GSM direction. Spiral angle is the angle between the IMF projected into the solar equatorial plane and the sun-earth line. THEMIS C observed solar wind intervals both before and after observing each HFA so two different spiral angles could be calculated for each event, one averaging the solar wind before observing the HFA and one after. To create this figure, both angles were calculated and the most radial angle was chosen as the sole solar wind spiral angle value for the particular HFA (the angle closest to -180°, 0°, or 180° was chosen). HFAs and SHFAs are most prevalent for more radial IMF angles. For radial IMF, the incoming solar wind particles can interact

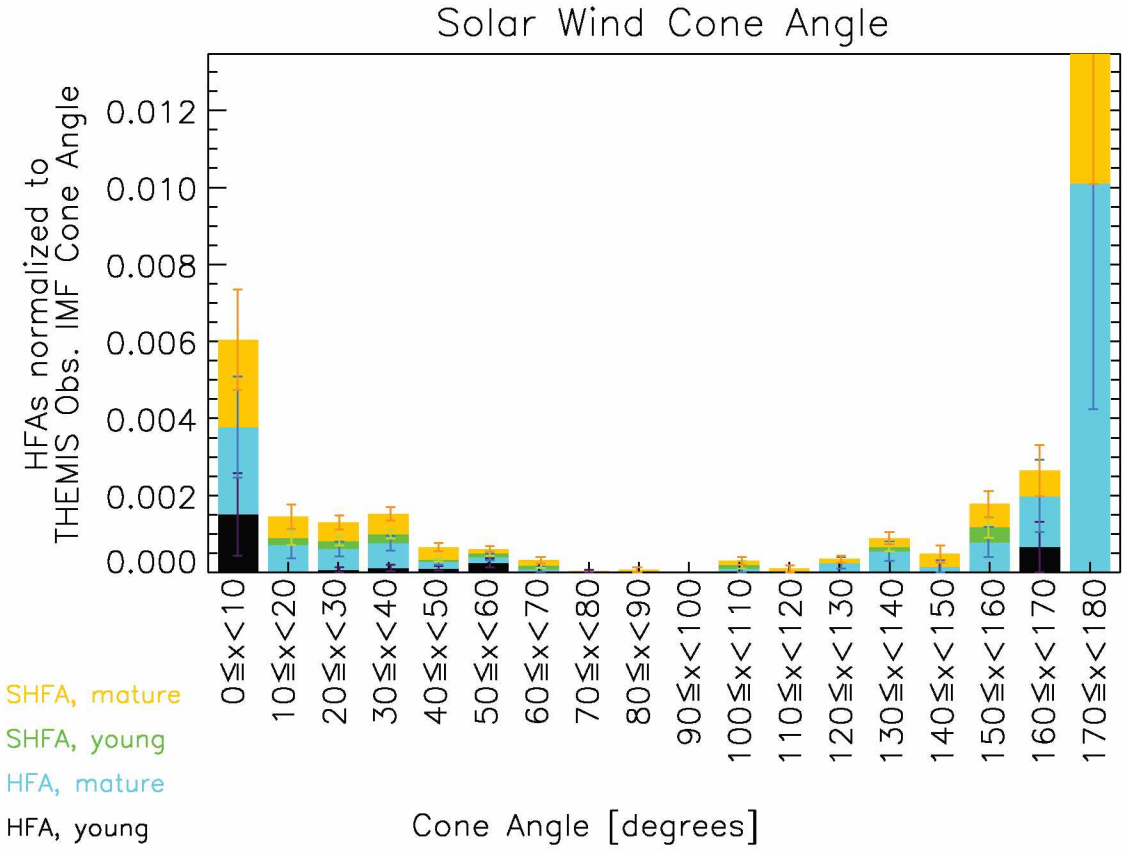

Figure 5.5. Analysis of HFAs and SHFAs with respect to IMF cone angle. The 136 HFAs were separated into 4 categories (young HFA, mature HFA, young SHFA, and mature SHFA) and binned with respect to the average IMF cone angle in the local solar wind for each event. Each bin was normalized with respect to the amount of time that THEMIS C saw solar wind of that angle from 2007–2009. Color coded error bars for each HFA category are plotted.

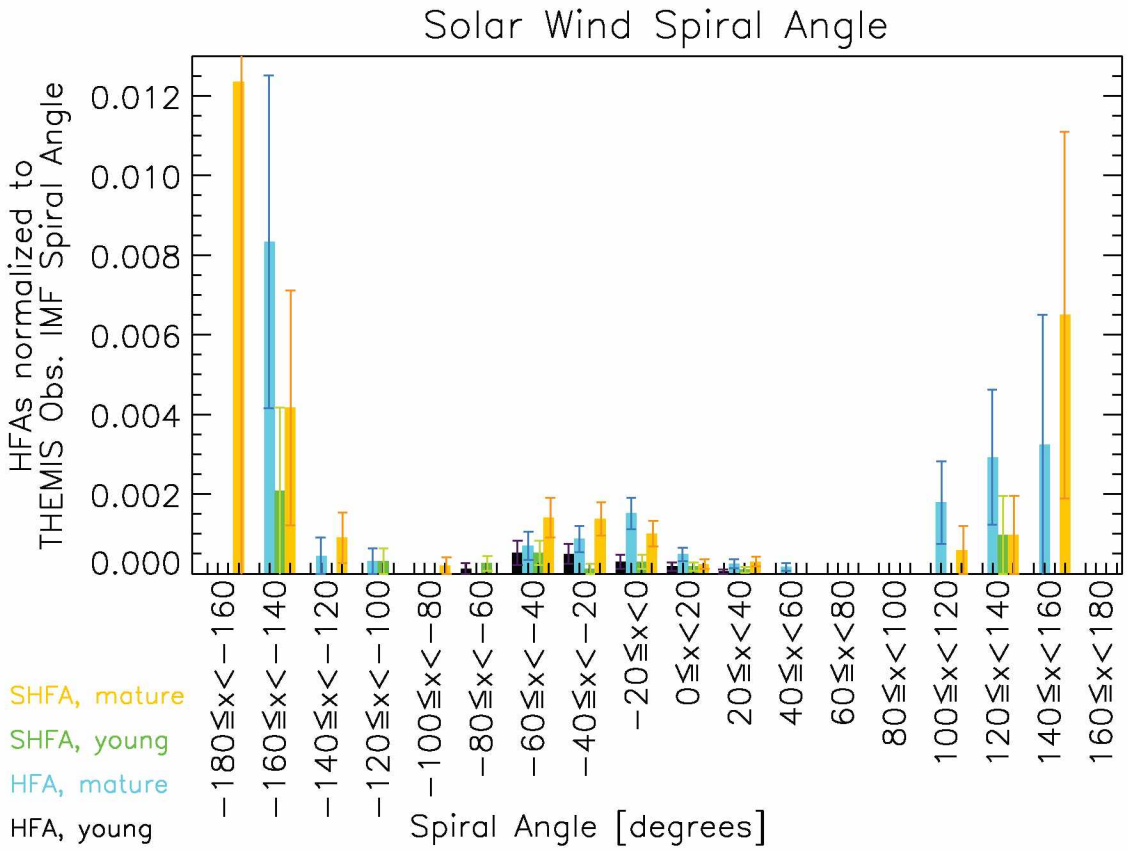

Figure 5.6. Analysis of HFAs and SHFAs with respect to IMF spiral angle. The 136 HFAs were separated into 4 categories, young HFA, mature HFA, young SHFA, and mature SHFA and binned with respect to the average IMF spiral angle in the local solar wind for each event. Each bin was normalized with respect to the amount of time that THEMIS C saw solar wind of that angle from 2007-2009. Color coded error bars for each HFA category are plotted. The vertical axis has been clipped to 0.0025 because the error bars on any bars that extended above 0.0025 are large enough that those bars can be ignored in the analysis.

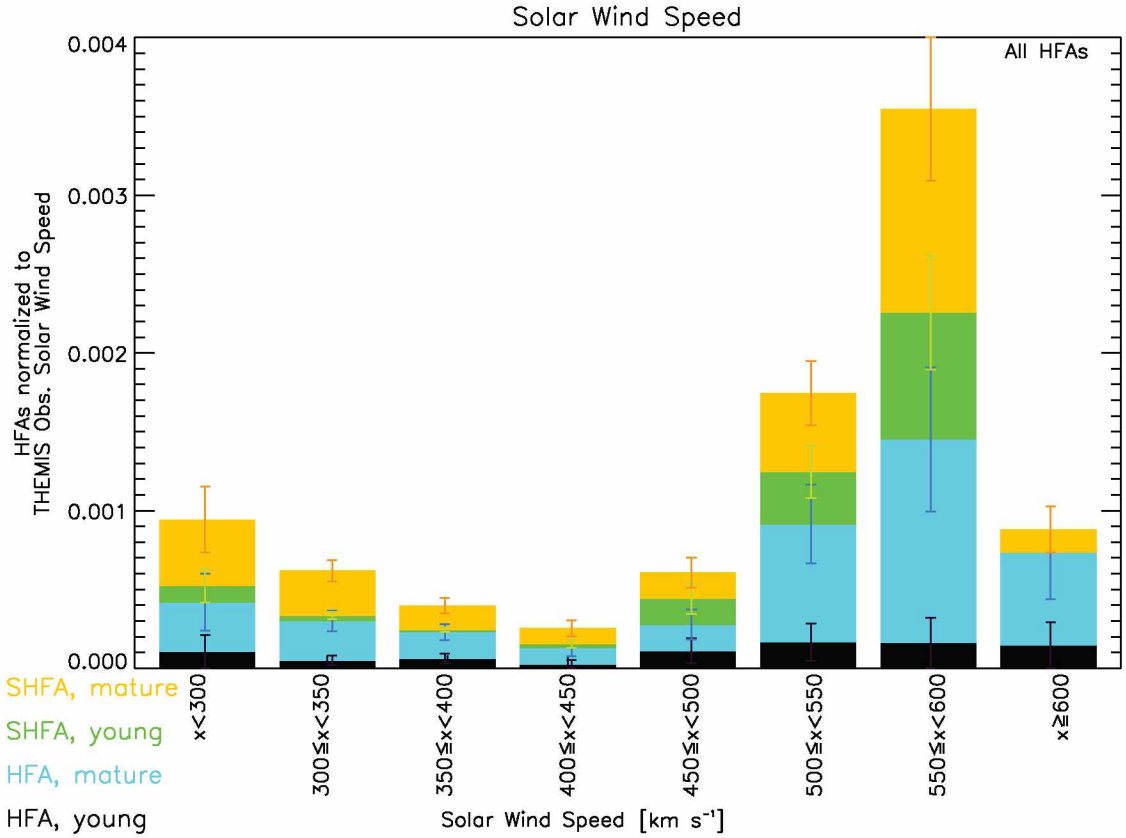

Figure 5.7. The number of HFAs in each solar wind speed bin is normalized by the amount of time there is solar wind of that speed. Four colors represent the four HFA categories: young HFA, mature HFA, young SHFA, and mature SHFA. Error bars for each of the 4 HFA categories are plotted.

with particles being reflected from the bow shock most effectively in the thermalization process which create HFAs. Taking the error bars into account, the greatest number of HFAs and SHFAs occur between spiral angles of -160° to -140°, -60° to -0°, and 120° to 160°.

Figure 5.7 shows HFA occurrence normalized to solar wind speeds. First, the number of HFAs were binned according to the local solar wind speed near HFA observations. The local solar wind speed was calculated using an average of solar wind intervals before and after each event. Then the number of events in each bin was normalized by the total amount of time that THEMIS C observed solar wind of that speed during the years of 2007–2009. The peak normalized occurrence rate of HFAs and SHFAs occurs for solar wind speed of 550–600 km s^{-1}. *Facskó et al.* [2009] noted in their study that HFA formation

Table 5.1. Percentage of HFAs with Radial IMF in Different Solar Wind Speed Ranges

Solar Wind Speed	Percentage of HFAs with Radial IMF
$x < 300$ km/s	0%
300 km/s $\leq x <$ 350 km/s	14%
350 km/s $\leq x <$ 400 km/s	12%
400 km/s $\leq x <$ 450 km/s	10%
450 km/s $\leq x <$ 500 km/s	18%
500 km/s $\leq x <$ 550 km/s	5%
550 km/s $\leq x <$ 600 km/s	22%
$x \geq 600$ km/s	40%

is more prevalent for faster solar wind speeds, a point which this dataset agrees with for 400–600 km s^{-1}.

In Figure 5.7, the HFA occurrence rate decreases with increasing solar wind speeds from 0–400 km s^{-1}. To explain this observation, we performed an analysis to separate the IMF orientation effect on occurrence rates from the effects of solar wind speed. From Figure 5.6 and 5.5, we observed that HFAs occur preferentially when the IMF is radial. Radial IMF was defined as times when the IMF had a cone angle between 0° and 15° or 165° and 180°. For each solar wind speed bin of Figure 5.7, we calculated the percentage of HFAs in that bin that had radial IMF. Results are listed in Table 5.1. In Table 5.1, x is defined as each event's solar wind speed. The bins of $x < 300$ km s^{-1} and $x \geq 600$ km s^{-1} have too few events in them to be statistically significant and were ignored. We observed decreasing occurrence rates from 300–450 km s^{-1} in Figure 5.7 which corresponds to rows 300–350 km s^{-1}, 350–400 km s^{-1}, and 400–450 km s^{-1} in Table 5.1. The percentage of HFAs with radial IMF in these bins decreases as solar wind speed increases (14%, 12%, 10%). The decrease in the HFA occurrence rate with increasing solar wind speed in the range of 300-450 km $s^{-}1$ comes from a decrease in the number of radial IMF HFAs at those solar wind speeds. For speeds between 400–600 km s^{-1}, the percentages in the table do not follow their respective bins in Figure 5.7. We put forth that HFA occurrence rate is not as highly related to IMF orientation at fast solar wind speeds because fast solar wind creates other favorable HFA formation conditions. The speed of backstreaming particles is faster for faster solar wind speeds. The thermal energy in HFAs mainly comes from the

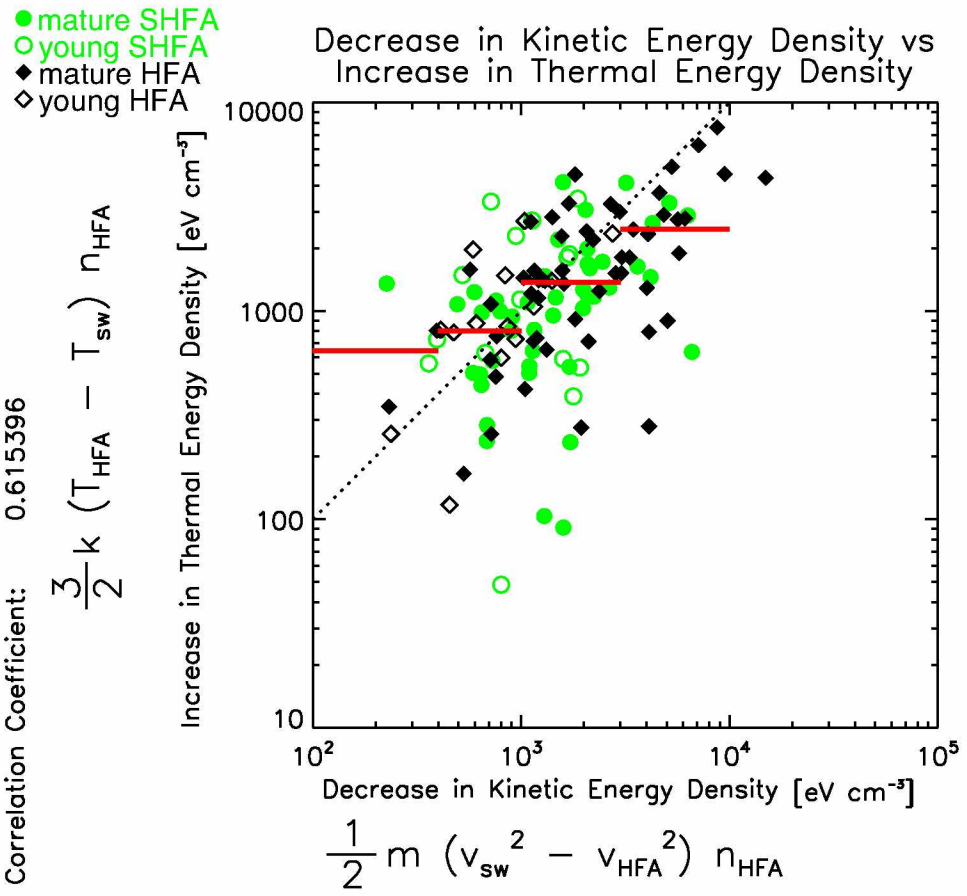

Figure 5.8. This figure plots the thermal energy increase of each HFA or SHFA compared to its kinetic energy decrease (as compared to the solar wind). The HFAs and SHFAs are identified from THEMIS C data from 2008. The green and black symbols refer to SHFAs and HFAs respectively. Open and filled symbols refer to young and mature events respectively. Dotted black line on the plot is the one-to-one diagonal. Red horizontal lines mark the median value of data bins along the x axis.

coupling between the reflected beam and the original solar wind beam. This causes the relative speed between the two beams to be crucial for HFA formation.

Figure 5.8 plots the thermal energy density increase within each HFA and SHFA versus the corresponding kinetic energy density decrease (as compared to the solar wind in both cases). The correlation coefficient is 0.62. The HFAs kinetic and thermal energy are both calculated at the time when the flow deflection inside the HFA is the strongest. The green and black symbols refer to SHFAs and HFAs, respectively. Open and filled symbols refer to young and mature events, respectively. The black dotted line in the plot is the one-to-one diagonal. Red lines indicate the median value of data bins along the x axis. Some young HFAs and SHFAs have a smaller increase in thermal energy than ma-

ture HFAs and SHFAs, but this is not seen for all cases in this figure. This leads to the hypothesis that some of the mature HFAs and SHFAs in our study are events that have existed for a while and have therefore cooled through some mechanism such as adiabatic expansion. HFAs expand when the internal pressure is high. When they cool down, the internal pressure decreases. SHFAs and HFAs do not show differences in this analysis of an event's kinetic and thermal energies relative to the local medium.

5.3 Conclusions

In this study, 136 HFAs (104 mature, 32 young; 66 spontaneous, 70 regular) have been identified from THEMIS C data from August 2007 to December 2009. The dataset has 17 young SHFAs, 49 mature SHFAs, 15 young HFAs, 55 mature HFAs. They span a wide range of MLTs. In this study, HFAs and SHFAs were observed up to 6.3 R_E and 6.1 R_E upstream from the bow shock, respectively. Particles reflected from the bow shock have a limited distance that they can travel sunward because of the impinging background flow and that limits how far HFAs and SHFAs can be observed upstream from the bow shock. HFA and SHFA occurrence decreases with distance upstream from the bow shock, which has not been reported in previous literature. HFAs with the highest event core ion temperatures were not seen at the flanks. The ratio of HFA ion temperature increase to HFA electron temperature increase is highest around 12 MLT and slightly duskward. Both mature and young HFAs are slightly more prevalent when there is an approximately radial interplanetary magnetic field (Figure 5.6 and 5.5). HFAs occur most preferentially for solar wind speeds from 550–600 km s^{-1}. n_{HFA}/n_{sw} shows no clear trend with distance from the bow shock. By examining the thermal and kinetic energy of the events, it is hypothesized that some of the mature HFAs and SHFAs in our study are most likely events that have existed for a while before observation by THEMIS, and have therefore cooled through some mechanism such as adiabatic expansion. SHFAs and HFAs do not show major differences in this study.

Now having a general picture of how HFAs are related to solar wind properties, it is useful to examine the spatial structure of an HFA. That is the subject of the next chapter.

Chapter 6

Spatial-Temporal Analysis of a Hot Flow Anomaly

THEMIS as a five satellite constellation made it an ideal mission to study the spatial structure of HFAs. In 2007, THEMIS orbited Earth in a pearls-on-a-string configuration and HFAs with multiple spacecraft observations of them were identified. An analysis of one of those HFAs is presented in this chapter.

6.1 Introduction

Hot flow anomalies are three dimensional structures usually reported upstream of a bow shock. Space plasma structures like HFAs can have both temporal and spatial features. However, spatial and temporal effects are difficult to distinguish using single point spacecraft measurements. Multipoint observations are the best datasets to use for this work. HFA properties that may evolve through time include flow velocities, density, temperature, and size. Temporal effects in the data can be distinguished from spatial effects through the following: when multiple (relatively close) satellites observe HFA signatures during the exact same short time interval, there is a high probability that the same HFA is being measured and so the data will not have significant temporal effects, only spatial. When the spacecraft that observe the same plasma structure are spread further apart, concurrent observations will provide information on how the the structure differs in along the lines of separation of the spacecraft.

The five spacecraft of the THEMIS mission are traveling at different radial distances during certain mission phases. Using multipoint measurements from this mission, it is possible to resolve spatial and temporal features of HFAs. The following considerations will allow for the analysis of both temporal and spatial HFA variations.

HFA widths have typically been reported in the literature as 1–3 R_E [*Schwartz et al.*, 1988; *Facskó et al.*, 2009] so the THEMIS separation of 100's of km to dozens of R_E over the mission lifetime are appropriate for this study. In 2007, the THEMIS satellites were 100's of km apart in a pearls-on-a-string configuration. Because of the satellites' proximity, the multi-spacecraft-HFA's data may not resolve all spatial effects present. If multiple spacecraft detect HFA signatures in quick succession, and the HFA shocks (boundaries) move approximately in the direction along which the spacecraft are aligned, we can assume all spacecraft traveled through approximately the same points of a single HFA and draw conclusions about temporal changes.

6.2 Overview of an HFA Observed by Five THEMIS Spacecraft on 10 August 2007

To study how HFAs evolve over time, 10 HFAs which had multiple spacecraft pass through almost simultaneously were identified. Of these events, plasma parameters, distribution functions, pitch angles distributions, and particle energies of the upstream/downstream HFA signatures were compared. A case study analysis of an HFA observed by all five THEMIS satellites on 10 August 2007 is presented in this chapter. Figure 6.1 shows the locations of THEMIS during the 21:15 to 21:21 UT interval in the XY, XZ, and YZ GSM planes. Figure 6.2 shows the observations of THEMIS A, Figure 6.3 shows THEMIS B, Figure 6.4 shows THEMIS C, Figure 6.5 shows THEMIS D, and Figure 6.6 shows THEMIS E. Figures 6.2–6.6 each show the magnetic field components in GSM coordinates, the magnetic field magnitude, plasma density, velocity components in GSM coordinates, ion temperatures, and electron temperatures observed by their respective satellites.

This structure was categorized as an HFA because it had all the defining characteristics of an HFA as detailed in *Schwartz et al.* [1985] and many other journal articles. There was a significant flow deflection from the solar wind flow that was concurrent with a temperature increase. In Figures 6.2–6.6, the leading edges are marked with vertical orange lines. *Schwartz et al.* [1985]; *Paschmann et al.* [1988] observed that when a spacecraft traversed an HFA, they observed two tangential discontinuities bracketing the HFA core. Those tangential discontinuities were bracketed by two sheaths, and those sheaths were bracketed by two shocks.

Determining the boundaries on the leading edge of this event was complicated because there was not a strong HFA sheath on the leading edge. The leading edge of the HFA was observed at approximately 21:16 UT for each spacecraft. The exact times are shown in Table 6.1. The exact time used as the observation of the leading edge in this study was selected by examining the magnetic field magnitude during the time interval approximately a minute before the temperature increase and velocity deflection. In that interval, the time where the maximum magnetic field magnitude was observed was selected as the time of the leading edge. Because pronounced sheaths were not observed, the point of largest magnetic field magnitude was used as a proxy for the sheath boundary. It was not straightforward to identify both a leading edge TD and leading edge shock, so only one boundary was identified. The HFA trailing edge boundaries which are tangential discontinuities are marked in Figures 6.2–6.6 with magenta vertical lines. The trailing edge shock boundaries in those figures are marked with blue vertical lines. The

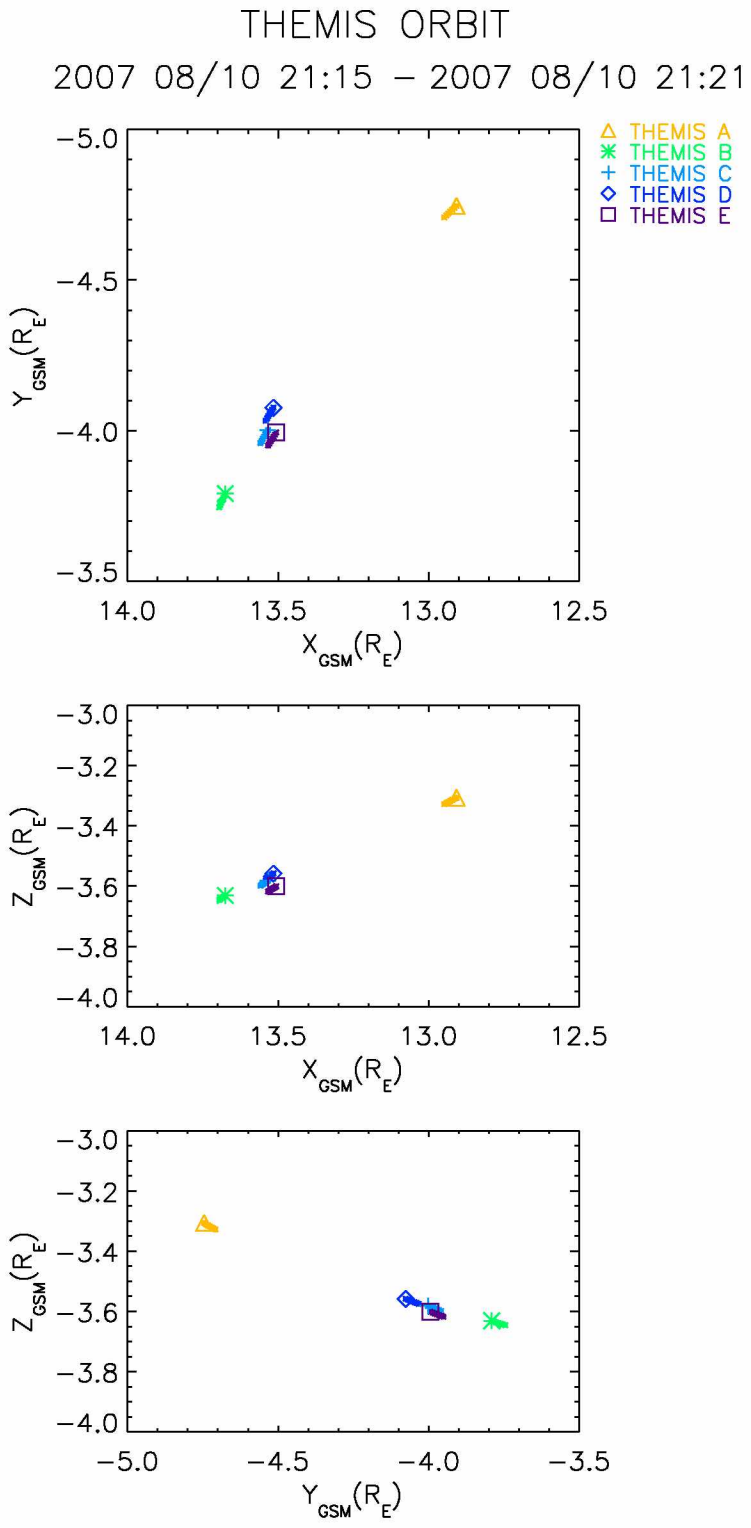

Figure 6.1. The orbits of THEMIS A, B, C, D, and E on 10 August 2007 from 21:15 to 21:21 UT are shown as the short thick lines on the XY, XZ, and YZ GSM planes. The locations at time 21:15 UT are represented by the symbols as indicated in the legend. Yellow, green, cyan, blue, and purple correspond to THEMIS A, B, C, D, and E respectively.

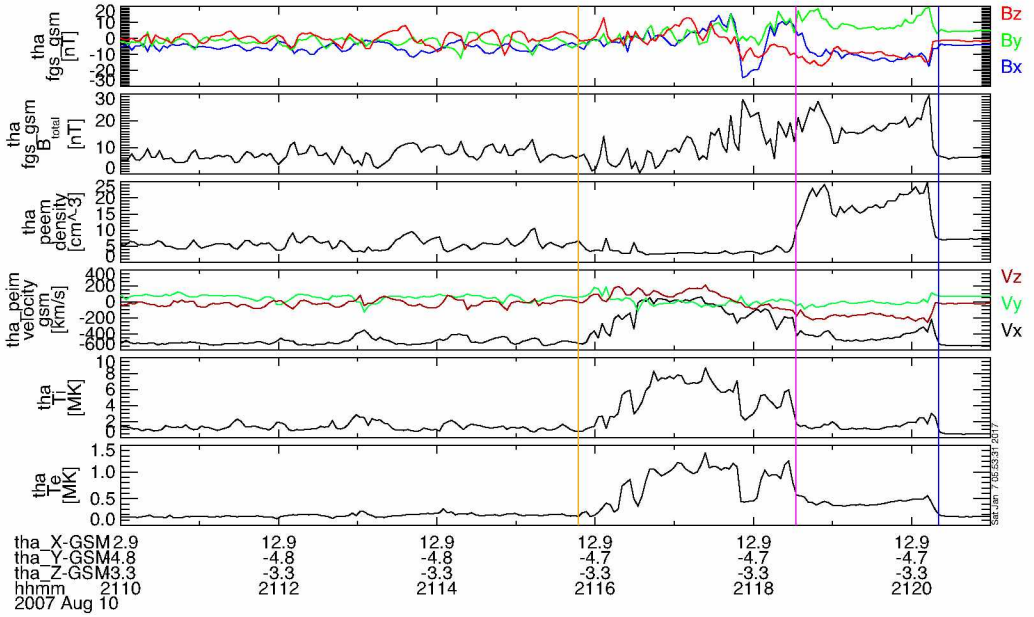

Figure 6.2. From top to bottom, each row shows the on board moment parameters of the HFA as observed by THEMIS A on 10 August 2007: magnetic field components, total magnetic field, density, particle velocity components, ion temperature, and electron temperature. Figure shows 21:10 to 21:21 UT. Vertical orange line marks the leading edge of the HFA, vertical magenta line marks the TD, and the vertical blue line marks the shock.

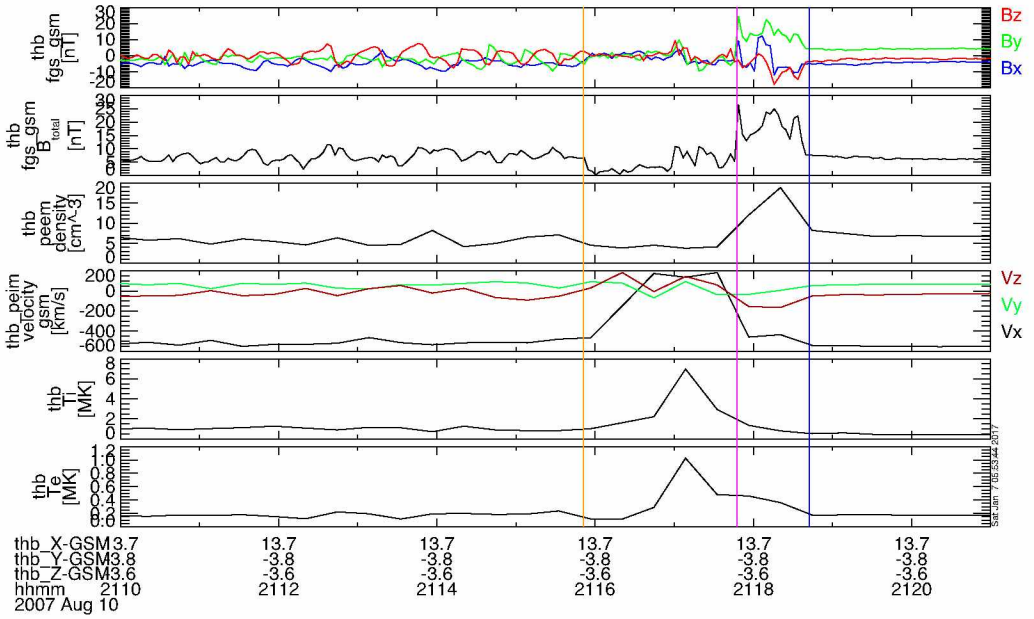

Figure 6.3. From top to bottom, each row shows the on board moment parameters of the HFA as observed by THEMIS B on 10 August 2007: magnetic field components, total magnetic field, density, particle velocity components, ion temperature, and electron temperature. Figure shows 21:10 to 21:21 UT. Vertical orange line marks the leading edge of the HFA, vertical magenta line marks the TD, and the vertical blue line marks the shock.

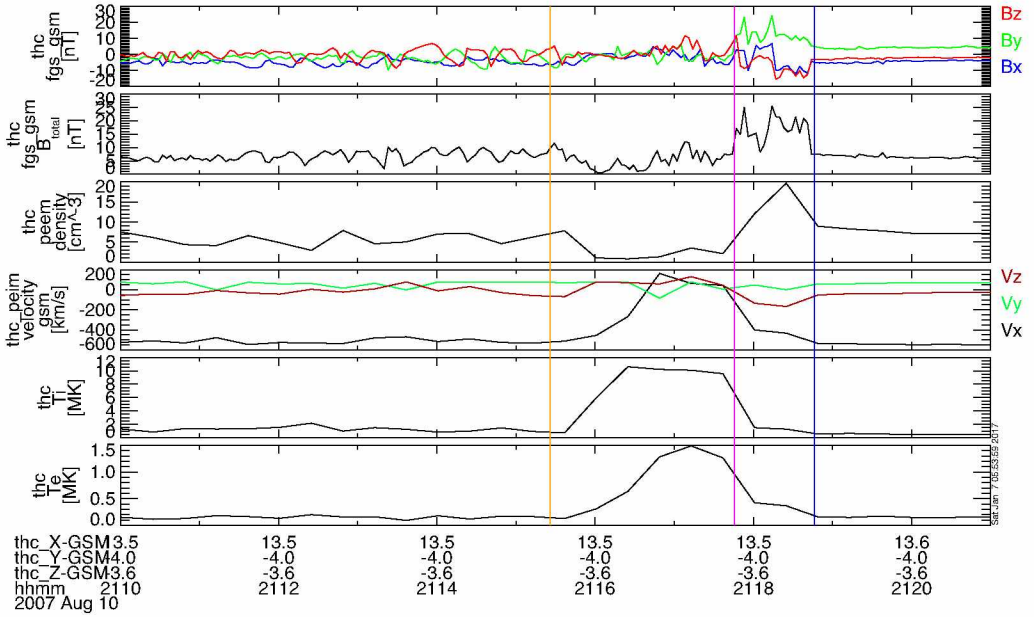

Figure 6.4. From top to bottom, each row shows the on board moment parameters of the HFA as observed by THEMIS C on 10 August 2007: magnetic field components, total magnetic field, density, particle velocity components, ion temperature, and electron temperature. Figure shows 21:10 to 21:21 UT. Vertical orange line marks the leading edge of the HFA, vertical magenta line marks the TD, and the vertical blue line marks the shock.

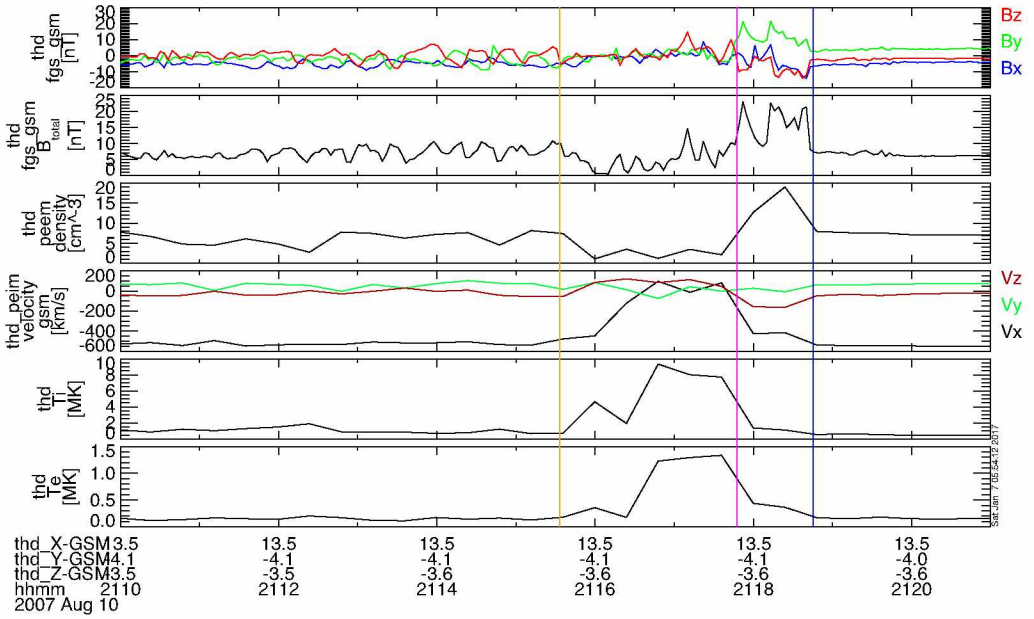

Figure 6.5. From top to bottom, each row shows the on board moment parameters of the HFA as observed by THEMIS D on 10 August 2007: magnetic field components, total magnetic field, density, particle velocity components, ion temperature, and electron temperature. Figure shows 21:10 to 21:21 UT. Vertical orange line marks the leading edge of the HFA, vertical magenta line marks the TD, and the vertical blue line marks the shock.

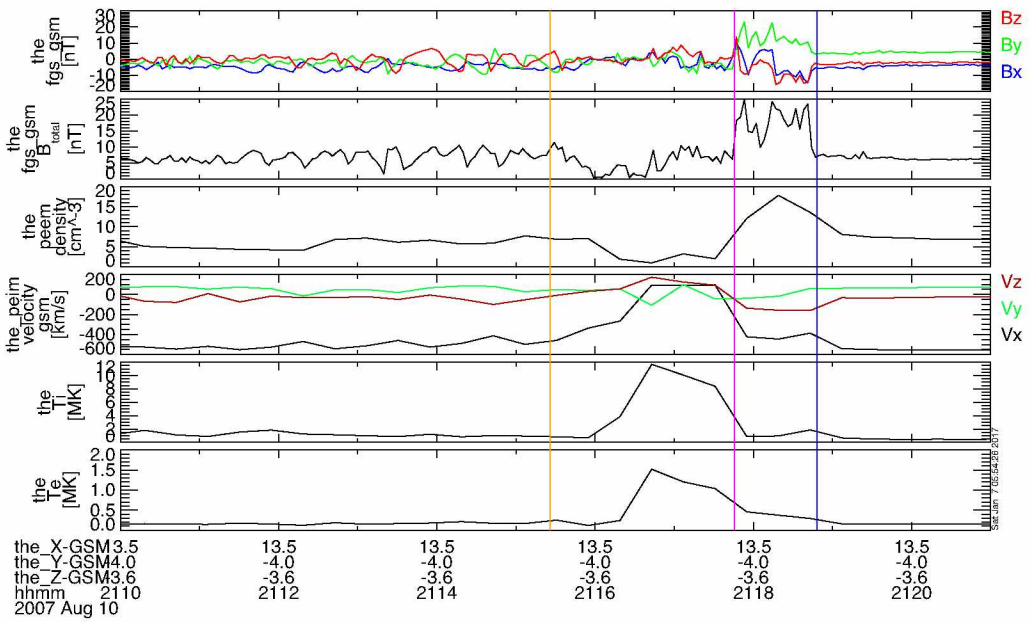

Figure 6.6. From top to bottom, each row shows the on board moment parameters of the HFA as observed by THEMIS E on 10 August 2007: magnetic field components, total magnetic field, density, particle velocity components, ion temperature, and electron temperature. Figure shows 21:10 to 21:21 UT. Vertical orange line marks the leading edge of the HFA, vertical magenta line marks the TD, and the vertical blue line marks the shock.

analysis of the plasma data from each spacecraft showed there was both a well defined tangential discontinuity and a shock on the trailing edge but not the leading edge.

It was determined that the magenta marked boundaries in Figures 6.2–6.6 were tangential discontinuities and not shocks by comparing the plasma and magnetic field on either side of the discontinuity with the tangential discontinuity Rankine-Hugoniot conditions from Section 1.2.2. The flow was tangential to the boundary, the magnetic field is tangential to the boundary, and the scalar pressure is the same on both sides of the boundary. For example, the deflected flow in the HFA core was calculated to be approximately 92° to the TD normal direction. This is relatively parallel to the TD boundary plane, as expected. Use of the MVA method allowed production of a hodogram in the LMN coordinate system with $\mathbf{B_N}$ versus $\mathbf{B_L}$ for each discontinuity. The normal field component fluctuates around an average value that is near zero. Recall from Section 1.2.2 that $B_N = 0$ for TDs. Internal 2-D or 3-D substructures produce fluctuations in the normal component so B_N is not always exactly zero as the spacecraft passes over the TD.

MVA analysis of the leading edge did not produce a normal with B_N approximately equal to zero. It is unreasonable to confidently call the leading edge boundary a TD.

Coplanarity did not produce consistent normal vectors for all five spacecraft. That would have required the boundary, if it were a shock, to have significantly different orientations in a relatively small space. Further analysis of why it is unclear whether the leading edge is a TD or shock is done in the later sections of this chapter.

Upstream solar wind monitors during the THEMIS observations of the HFA were ACE and Wind. Their time shifted magnetic field observations are shown plotted on top of THEMIS C observations in Figure 6.7. The time shifts involved checking the cone and clock angle changes, in addition to the magnetic field, for all three spacecraft examined and aligning the perturbations observed. During the HFA interval, THEMIS C was nominally located at $(13, -3.5, -4)$ R_E, ACE was at $(228, 29, 10)$ R_E and Wind was at $(224, -100, 0.8)$ R_E. By locating an interval where ACE and Wind observed a deflection in B_x, B_y, and B_z in GSM, cone angle, and clock angle that was similar to observations at THEMIS C, ACE data was shifted forward by 37 minutes and Wind data was shifted forward by 44 minutes. These satellite's magnetic field components, cone angle, and clock angle deflections were similar to deflections observed by THEMIS C near 0:20 UT. THEMIS C nominally observed the HFA at 21:15 UT. After analyzing Figure 6.7, we conclude that neither ACE nor Wind observed the discontinuity associated with the creation of the HFA.

6.3 HFA Boundary Speed

All five THEMIS spacecraft observed both the HFA's tangential discontinuity and trailing edge (upstream) shock. Table 6.1 shows the times that those HFA boundaries were observed by the individual spacecraft. Table 6.1 also shows the leading edge and discontinuity normals calculated via the MVA method outlined in Section 4.3.1 and shock normals calculated via the coplanarity method outlined in Section 4.3.2. The boundary normals are similar to the normals presented in *Liu et al.* [2016] in their analysis of this same event.

Possible causes for the small variations in all calculated boundary normals from spacecraft to spacecraft include changes to the orientation of the boundary in space, a boundary that is not completely planar, and uncertainties in spacecraft measurements. Because the spacecraft are relatively spatially close together and the measurements are fairly consistent across five separate spacecraft, it is most likely that these variations do not affect the results of this dissertation.

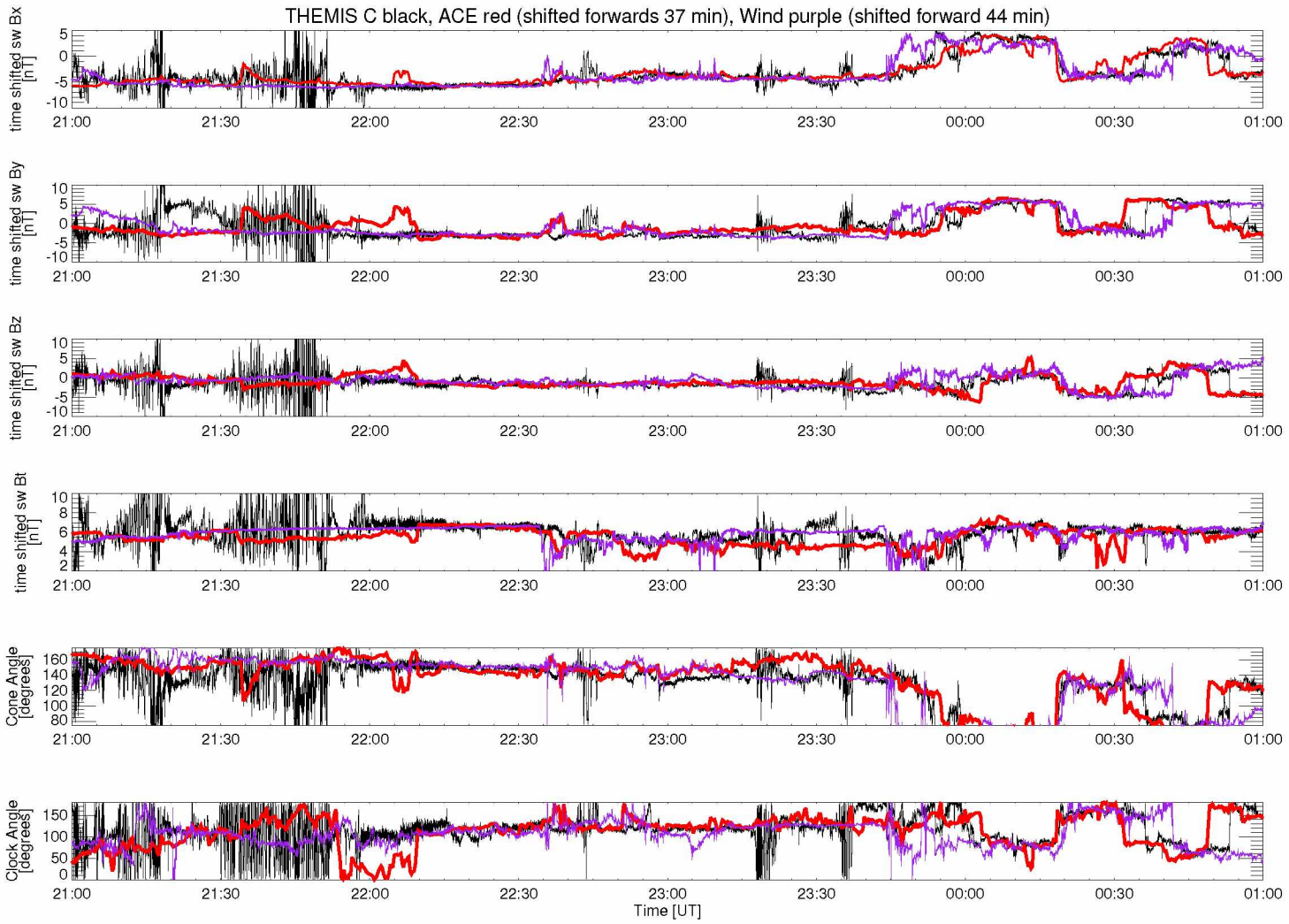

Figure 6.7. Each row shows the magnetic field as observed by ACE, Wind, and THEMIS C on 10 and 11 August 2007. THEMIS C data is shown in black, ACE is shown in red, and Wind is shown in purple. ACE and Wind have both been shifted forward in time. From top to bottom, the rows show B_x, B_y, and B_z in GSM, total magnetic field B_t, cone angle, and clock angle. Figure shows 21:00 UT on 10 August 2007 to 1:00 UT on 11 August 2007.

Table 6.1. THEMIS Observations of the HFA Boundaries for Event on 10 August 2007

THEMIS Spacecraft	Time Leading Edge Observed [UT]	Leading Edge Normal	Time Tangential Discontinuity Observed [UT]	Discontinuity Normal	Time Shock Observed (HFA trailing edge) [UT]	Shock Normal
A	21:15:54	$(0.61, -0.64, 0.46)$	21:18:17	$(0.44, -0.32, -0.84)$	21:20:15	$(0.61, -0.22, -0.76)$
B	21:15:54	$(0.38, -0.59, 0.71)$	21:17:47	$(0.64, -0.25, -0.73)$	21:18:36	$(0.76, -0.11, -0.64)$
C	21:15:34	$(0.38, -0.27, 0.89)$	21:17:48	$(0.78, -0.42, -0.46)$	21:18:41	$(0.77, -0.27, -0.58)$
D	21:15:35	$(0.23, -0.20, 0.95)$	21:17:47	$(0.86, -0.35, -0.36)$	21:18:40	$(0.62, -0.42, -0.66)$
E	21:15:28	$(0.29, -0.34, 0.89)$	21:17:48	$(0.80, -0.22, -0.56)$	21:18:42	$(0.80, -0.21, -0.56)$

As shown on Table 6.1, the leading edge boundary normal was in a similar direction for all spacecraft. The normal referenced in this study has the values of $\langle 0.38, -0.27, 0.89 \rangle$ which is from analysis of THEMIS C data. Although a consistent normal direction was calculated for all spacecraft, B_N was not close to zero for all spacecraft so the identified leading edge was not labeled a TD. The small difference between the TD normal at THEMIS A and the other spacecraft could be caused because the TD surface was physically bent. The difference could also be from inherent errors in the identification of the THEMIS A leading edge boundary time. The boundary normal was very similar for THEMIS B, C, D, and E so a normal from this group, THEIMS C, was used in the following geometrical analysis of the HFA structure. The leading edge was assumed to move along the leading edge normal. The solar wind projected onto the leading edge normal is $(81, -58, 192)$ km/s.

The intermediate to minimum eigenvalue ratio, λ_2/λ_3, from MVA on the TD was similar for all spacecraft. e.g at THEMIS C, $\lambda_2/\lambda_3 = 12.1$. This follows the rule of thumb from *Sonnerup and Scheible* [1998] where a good application of MVA to a relatively small dataset should have $\lambda_2/\lambda_3 \leq 10$. This means the calculated normal vectors in Table 6.1 is reliable. Its speed is calculated later in this section.

Boundary normals in Table 6.1 were calculated using magnetic coplanarity. Similar normals were also obtained with the three mixed mode normal techniques described in Section 4.3.2. Obtaining similar normals with the mixed-mode normal techniques validates the coplanarity normal directions shown. Its speed is calculated later in this section.

We assumed the HFA boundaries expanded over time because the total pressure at the HFA center was higher than in the sheath and in the solar wind. The boundary speed was calculated using the two spacecraft timing method described in Section 4.4.1. Shock normals were calculated using the coplanarity method described in Section 4.3.2 and normals for each spacecraft are listed in Table 6.1.

We assumed the shock boundary at THEMIS B was parallel to that at THEMIS A and computed the separation along the shock normal direction. This assumption can be made because the shock normals calculated at each spacecraft location were approximately the same.

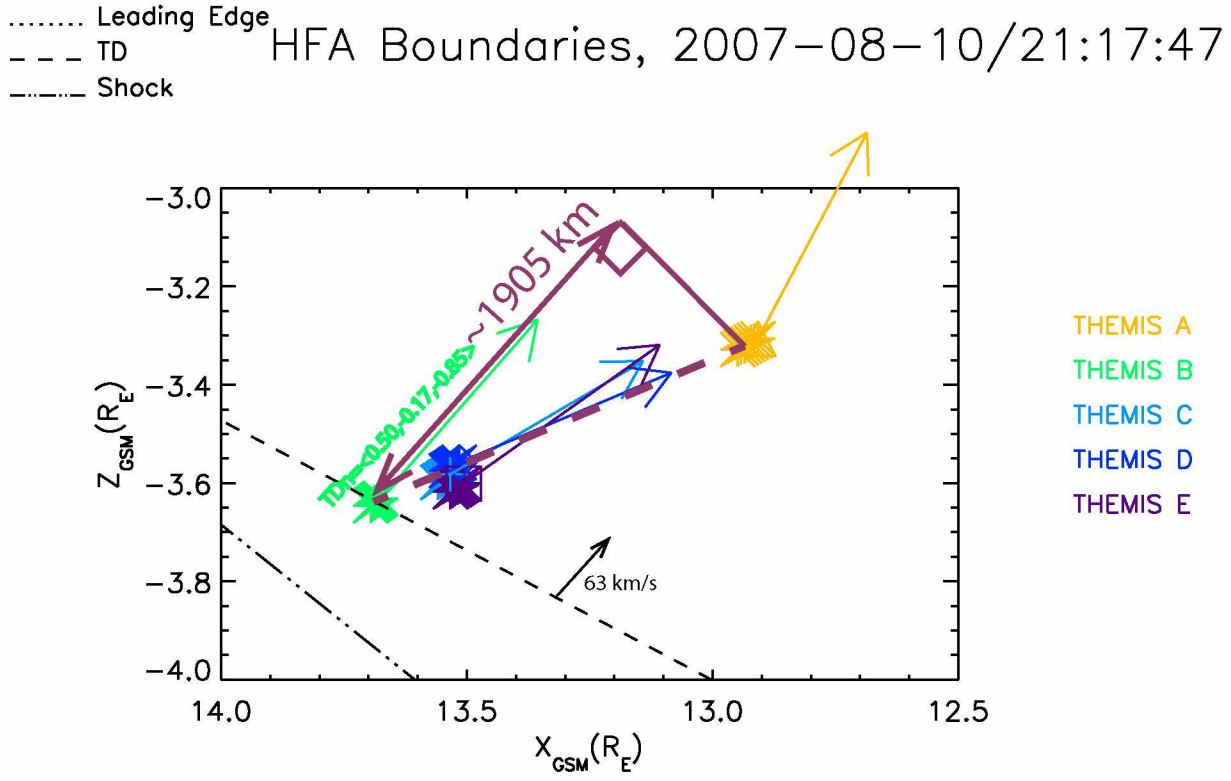

Figure 6.8. The orientation of representations of the HFA TD and shock in the XZ GSM plane. Yellow, green, cyan, blue, and purple correspond to THEMIS A, B, C, D, and E respectively. The colored arrows are along the TD normal directions for each THEMIS spacecraft. The symbols represent their positions from 21:15:54–21:17:47 UT on 10 August 2007. The boundary lines shown are the intersection line of the $y = y_{\text{spacecraft position}}$ plane and the planes perpendicular to the TD normal (dashed line) and shock normal (dot and dashes line). The direction of the TD normal at THEMIS B is labeled in green. The distance between THEMIS A and B is drawn as the dashed purple line. That distance projected onto the THEMIS B TD normal is the solid purple double headed arrow.

6.3.1 TD Speed

Using the discontinuity normal calculated at THEMIS A, the distance between THEMIS B and A at the times each observed the TD (distance projected along the TD normal) was 1905 km. Figure 6.8 illustrates the basic geometry of the structure and this projection of the distance. The time elapsed between observation of the TD at THEMIS B and A was 30 $\pm$ 0.125 s. That leads to a calculated TD speed along the TD normal of 63 km/s in the Earth rest frame as the TD went from THEMIS B to A. The average local solar wind speed was $(-512, 53, -12)$ km/s in GSM coordinates and the solar wind speed along the TD normal was $(-104, 74, 196)$ km/s with a magnitude of 234 km/s. By the two spacecraft timing method, the TD speed in the solar wind frame is 170 km/s in the TD normal direction. Repeating the same calculation but using the discontinuity normal calculated at THEMIS B, the TD speed in the solar wind frame is 230 km/s.

Tangential discontinuities are frozen in to the plasma they occur in. A TD frozen in to the solar wind plasma would experience no speed in the solar wind frame. The TD discussed in this section is not the TD in the unperturbed solar wind that created the HFA formation conditions. For the TD identified in Figures 6.2–6.6, either the pre-existing TD is strongly modified or the observed TD within the HFA is newly formed by the physics of the HFA. There is no requirement for this TD identified in the HFA to be frozen into the solar wind or to have a near zero velocity in the solar wind frame. The TD normal calculated using the solar wind magnetic field before and after the HFA was calculated using Equation 4.22 as $(0.14, -0.27, -0.95)$. This is different than the TD normal observed in the HFA, nominally $(0.64, -0.25, -0.73)$ at THEMIS B.

6.3.2 Shock Speed

The distance between THEMIS B and A at the times each observed the shock (distance projected along the shock normal) was 3070 km. Figure 6.9 illustrates the basic geometry of the structure and this projection of the distance. The time elapsed between observation of the shock at THEMIS B and A was 99 $\pm$ 0.125 s. That leads to a calculated shock speed along the shock normal of 31 km/s in the Earth rest frame as the shock went from THEMIS B to A. The average local solar wind speed was $(-512, 53, -12)$ km/s in GSM coordinates and the solar wind speed along the shock normal was $(-191, 70, 239)$ km/s with a magnitude of 314 km/s. By the two spacecraft timing method, the shock speed

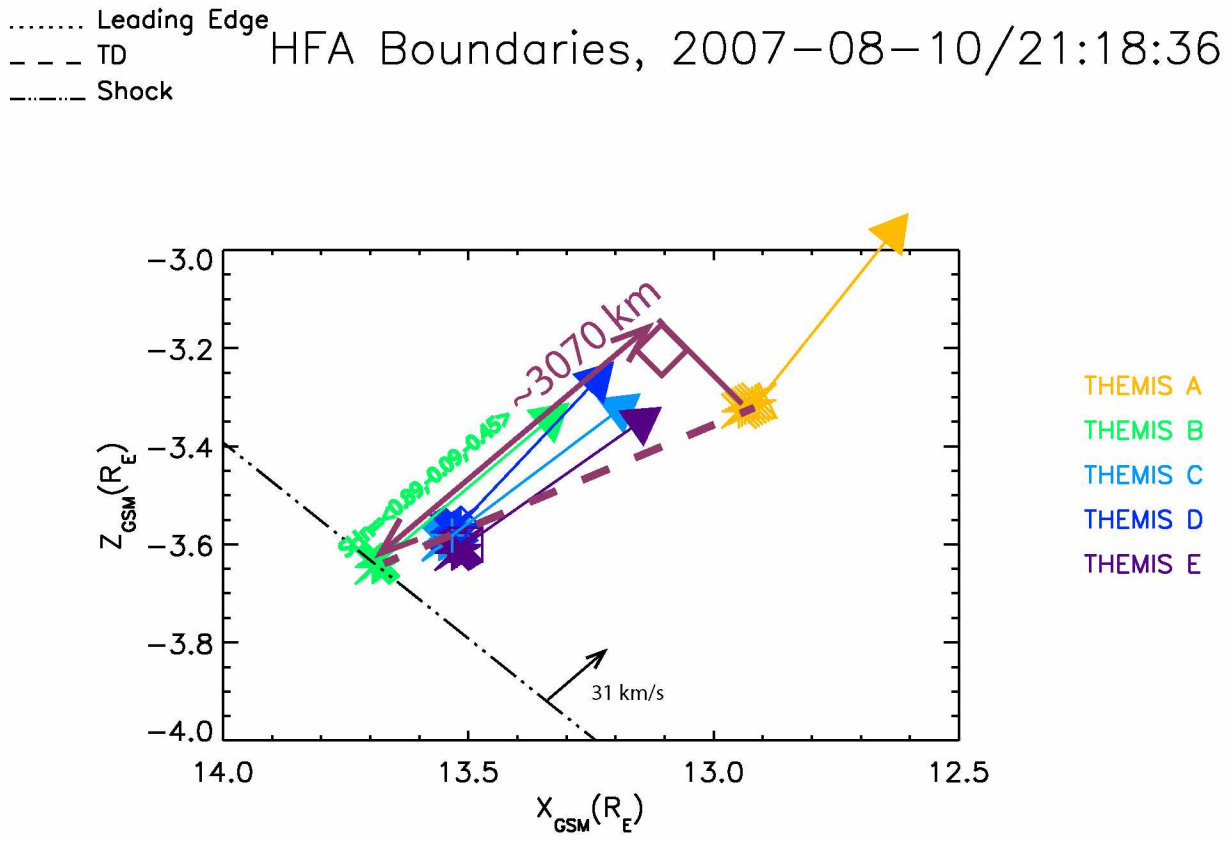

Figure 6.9. The orientation of representations of the HFA TD and shock in the XZ GSM plane. Yellow, green, cyan, blue, and purple correspond to THEMIS A, B, C, D, and E respectively. The colored arrows are along the shock normal directions for each THEMIS spacecraft. The symbols represent their positions from 21:15:54–21:18:36 UT on 10 August 2007. The boundary lines shown are the intersection line of the $y = y_{\text{spacecraft position}}$ plane and the planes perpendicular to the TD normal (dashed line) and shock normal (dot and dashes line). The direction of the TD normal at THEMIS B is labeled in green. The distance between THEMIS A and B is drawn as the dashed purple line. That distance projected onto the THEMIS B TD normal is the solid purple double headed arrow.

in the solar frame is 283 km/s. This is the speed at which the HFA expanded against the solar wind.

6.4 HFA Spatial Structure

THEMIS B, C, D, and E observed the HFA tangential discontinuity at times which were very close together. The on-board moment data resolution does not allow us to determine the order which the discontinuity passed spacecrafts C, D, and E. Because THEMIS B was furthest in space from this set of satellites, it is simplest to assume that the discontinuity passed THEMIS B first. From the plasma parameters, we note that the tangential discontinuity passed THEMIS A last. The same logic can be applied to the HFA's trailing shock so we can say the shock passed THEMIS B first and THEMIS A last.

Figure 6.10 shows the boundaries of the HFA. The calculated locations of the leading edge boundary, TD, and shock are each plotted for 21:15:54, 21:17:47, and 21:18:36 UT. 21:15:54 UT is the time when THEMIS B observed the HFA's leading edge boundary. 21:17:47 UT is when THEMIS B observed the TD. 21:18:36 UT is when THEMIS B observed the HFA's trailing edge shock boundary. The symbols in the middle of the planes, near X_{GSM}=15 R_E, mark the location of the THEMIS constellation. The spacecraft do not move very much during the HFA observation interval, but rather the HFA convects over satellites. While Figure 6.10 shows the boundaries in three dimensions, Figure 6.11 shows the bow shock and boundaries in the two dimensional XZ GSM plane.

Figure 6.11 is a two dimensional cut showing the $y = y_{\text{spacecraft B position}}$ plane. Due to projection effects when going from 3D to 2D, it can appear that from 21:15:54 UT to 21:18:36 UT, the TD and shock moved closer together from 21:15:54–21:17:47 UT and then further apart from 21:17:47–21:18:36 UT, but this is not what the boundaries actually did. Examining the boundaries in three dimensions (Figure 6.10), the distance between the TD and shock did increase over time.

As shown in Table 6.1, all five THEMIS spacecraft observed the leading edge of the HFA from times 21:15:28 UT to 21:15:54 UT, which is similar enough to approximate that all spacecraft observed the leading edge at the same time. This allows us to plot five points on the leading edge of the HFA as simply the spacecraft locations at 21:15:54 UT nominally in Figure 6.11. The THEMIS spacecraft did not all observe the trailing edge the same time. THEMIS A observed the trailing edge discontinuity and shock last and approximately a minute and a minute and a half, respectively, after the other four THEMIS

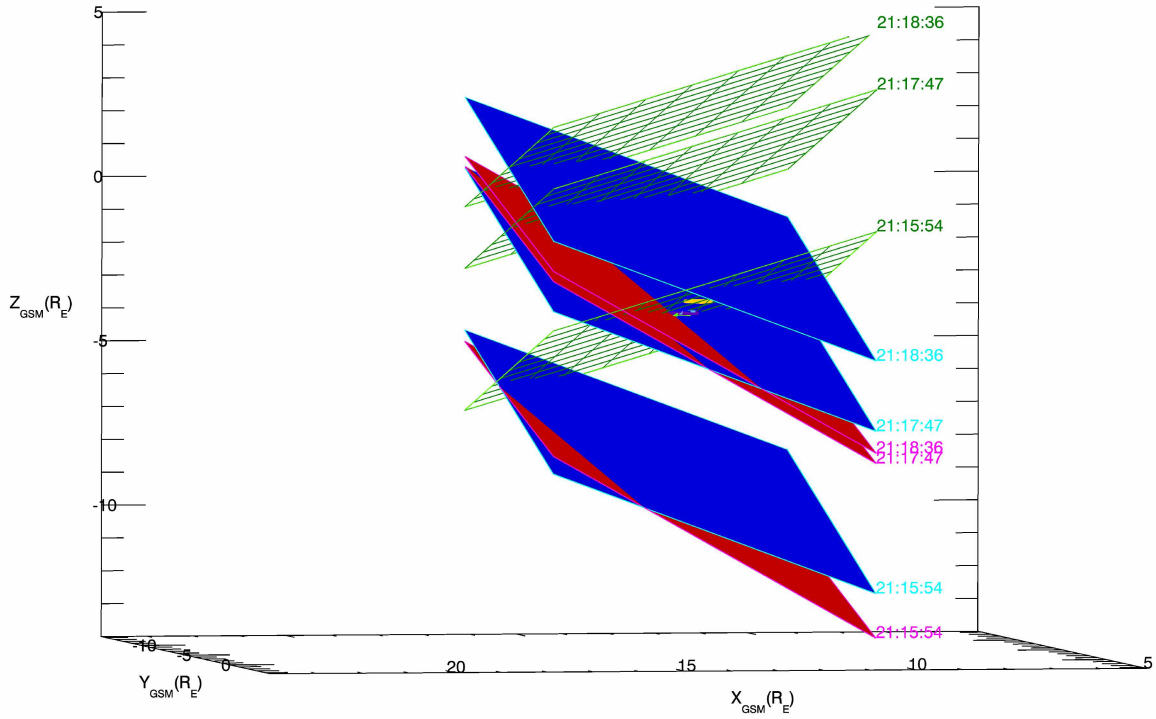

Figure 6.10. The boundaries of the HFA, the leading edge boundary, TD, and shock are plotted showing their locations at 21:15:54, 21:17:47, and 21:18:36 UT on 10 August 2007. The green planes represent the location of the leading edge boundary. The blue planes represent the locations of the TD. The red planes represent the locations of the shock. The symbols in the middle of the planes are the locations of the THEMIS satellites during its observation of the HFA. Yellow, green, cyan, blue, and purple symbols correspond to THEMIS A, B, C, D, and E respectively.

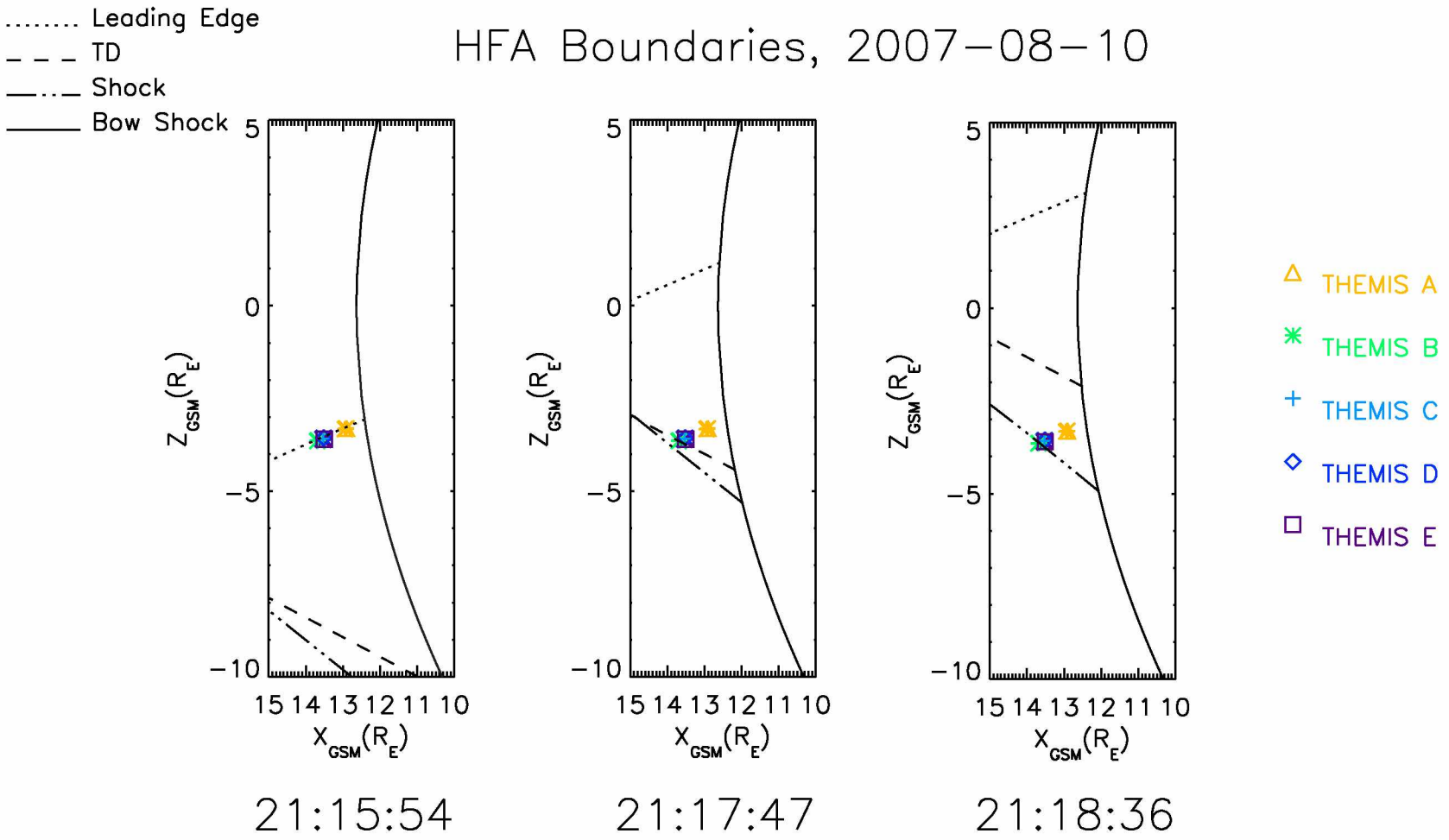

Figure 6.11. The orientation of the bow shock and representations of the HFA leading edge boundary, TD, and shock in the XZ GSM plane. The solid black curves are the *Merka et al.* [2005] model bow shock for Alfvén Mach number range of 2-20. Yellow, green, cyan, blue, and purple correspond to THEMIS A, B, C, D, and E respectively. The symbols represent their positions at 21:15:54, 21:17:47, and 21:18:36 UT on 10 August 2007. The boundary lines shown are the intersection line of the $y = y_{\text{spacecraft B position}}$ plane and the planes perpendicular to the leading edge normal (dotted line), TD normal (dashed line), and shock normal (dot and dashes line).

observed them. Also, at the time THEMIS A observed the TD, other spacecraft were observing the trailing edge shock (there is an approximately 25 second difference between THEMIS B-E's observation of the trailing shock and THEMIS A's observation of the TD, but the times are similar enough that we say these events were all concurrent).

From this, we can draw three different conclusions. One is that the trailing edge sheath grew thicker at THEMIS A's location than at the other spacecrafts' locations. This sheath thickened after the trailing edge passed THEMIS B–E. The second possible explanation is that the HFA sheath was thicker closer to the bow shock at the THEMIS A location when it was formed. A third possibility is a combination of the first two options. The most probable situation is the third option. Reasons that the trailing HFA sheath grew thicker include: 1. the thermal pressure is highest at the center of the HFA, and 2. the speed of the shock is larger than that of the TD so the distance between the two boundaries grow with time (the TD and shock are both moving away from the HFA core in nominally the same direction). Based on the orientation of the TD and shock in Figure 6.11, if the boundaries stayed approximately planar as the HFA matured and expanded, then the figure shows that the HFA sheath was thicker closer to the bow shock when it was formed. With the calculated boundary planes and boundary speeds, one could determine the line of intersection of the TD and shock planes. Provided that everything is planar and steady state, that line of intersection moved away from the bow shock over time.

The distances between the boundaries can be estimated. The results are summarized in Figure 6.12. First, the distance between the leading edge boundary and the TD can be estimated.

First, another look at the nature of the leading edge. At the leading edge, the local velocity is close to the unperturbed solar wind. If this were a boundary structure such as a TD that is frozen to the local solar wind plasma flow, it should move into the direction opposite of what was indicated in Figure 6.11. When examining the entropy at the leading edge (not shown in this dissertation), the entropy increases across the leading edge. If this boundary were a shock, the density and entropy should both increase when crossing the boundary, which does not happen. Perhaps the leading edge observation is a combination of nonlinear waves and discontinuities.

From Section 6.3, the solar wind speed projected along the TD normal was $(-104, 74, 196)$ km/s. The approximate time interval between the observation of the leading edge and TD by THEMIS B is 113 seconds. This leads to a leading edge to TD distance of ap-

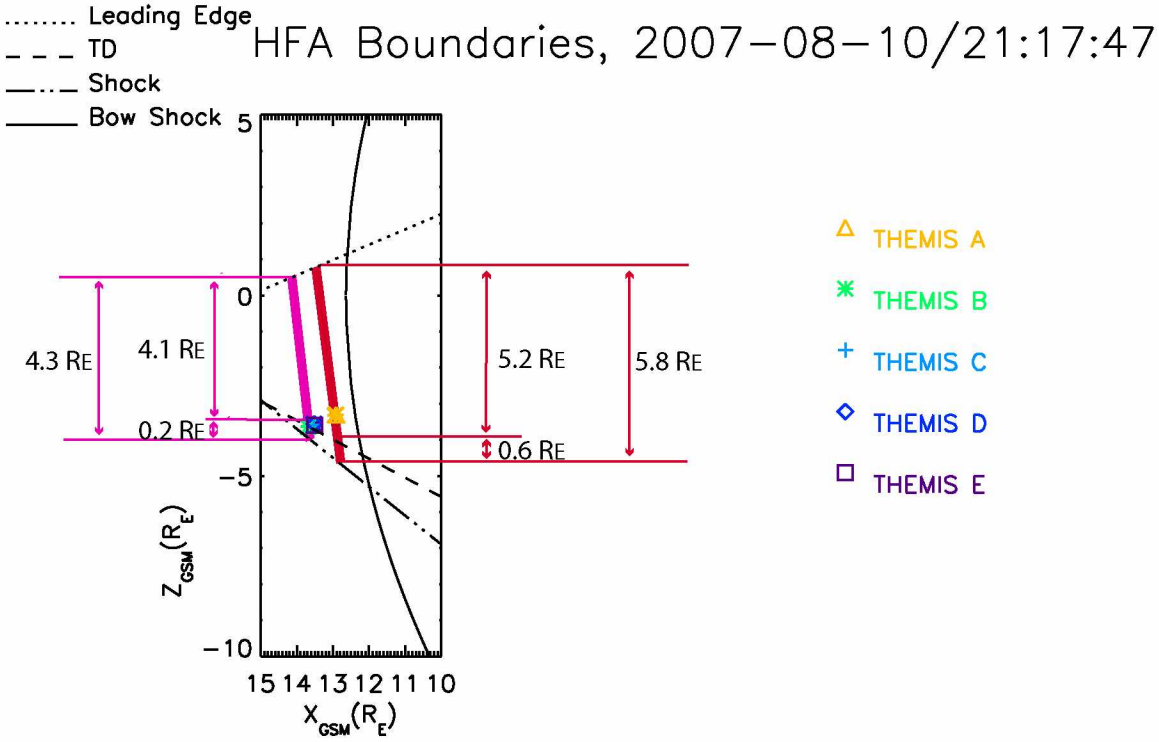

Figure 6.12. The orientation of the bow shock and representations of the HFA leading edge boundary, TD, and shock in the XZ GSM plane. The solid black curves are the *Merka et al.* [2005] model bow shock for Alfvén Mach number range of 2–20. Yellow, green, cyan, blue, and purple correspond to THEMIS A, B, C, D, and E respectively. The symbols represent their positions at 21:17:47 UT on 10 August 2007. The boundary lines shown are the intersection line of the $y = y_{\text{spacecraft position}}$ plane and the planes perpendicular to the leading edge normal (dotted line), TD normal (dashed line), and shock normal (dot and dashes line). The HFA dimensions as calculated for THEMIS B, C, D, and E are shown in pink. The HFA dimensions as calculated for THEMIS A are shown in red.

proximately 26,427.93 $\pm$ 0.04 km (approximately 4.1 R_E) for THEMIS B. The approximate time interval between the observation of the leading edge and TD by THEMIS A is 143 seconds. This leads to a leading edge to TD distance of approximately 33,444.19 $\pm$ 0.02 km (approximately 5.2 R_E) for THEMIS A. The HFA is thicker closer to the bow shock at the THEMIS A location. The approximate leading edge to TD observation interval for THEMIS C, D, and E was 134 seconds. Because these three spacecraft were located close to THEMIS B, it is assumed the HFA thickness observed by the spacecraft is similar to THEMIS B.

The distance between the TD and the shock can be estimated. We calculate the speed of the shock along the shock normal as it travels between THEMIS B and A with the following steps. First, calculate the distance between the two spacecraft projected along the shock normal, $(-0.29, 0.11, 0.37)$ R_E, divided by the time interval between shock observations at the spacecraft, 99 seconds. The speed of the shock between THEMIS B and A is $(-18, 7, 23)$ km/s. The approximate time interval between the observation of the TD and shock by THEMIS B (similar to THEMIS C, D, and E) is 49 seconds. This leads to a TD to shock distance of approximately 1524.11 $\pm$ 0.03 km (approximately 0.2 R_E) for THEMIS B, C, D, and E. The approximate time interval between the observation of the TD and shock by THEMIS A is 118 seconds. This leads to a TD to shock distance of approximately 3670.308 $\pm$ 0.004 km (approximately 0.6 R_E) for THEMIS A.

An estimate for the thickness of the HFA from the leading edge to the trailing shock can be obtained by combing the above results.THEMIS B, C, D, and E observations yield an HFA thickness of approximately 4.3 R_E. The observations from THEMIS A yield an HFA thickness of approximately 5.8 R_E.

6.5 Conclusions

An analysis of an HFA observed by all five THEMIS satellites at approximately 21:15 UT on 10 August 2007 was performed. The TD associated with the HFA was not observed by the upstream, solar wind monitoring satellites. We characterized HFA evolution after it had already reached the mature state. The total pressure at the HFA center was observed to be higher than that in the sheath and solar wind, so the HFA boundaries should be expanding. We calculated HFA expansion against the solar wind of nearly 300 km/s.

Using the conclusion that THEMIS B observed both the tangential discontinuity and shock boundaries before THEMIS A, that means that the THEMIS A observations are

of an HFA that has evolved further in time than that observed by THEMIS B. From the observations, the HFA sheath was thicker closer to the bow shock (near at the THEMIS A location) when the HFA was formed, and it grew thicker as the HFA matured. The leading edge boundary to TD distance was 4.1 R_E for THEMIS B, C, D, and E and 5.2 R_E for THEMIS A. The TD to trailing shock distance was 0.2 R_E for THEMIS B, C, D, and E and 0.6 R_E for THEMIS A. This leads to total HFA thicknesses of 4.3 R_E for THEMIS B, C, D, and E and 5.8 R_E for THEMIS A.

The normal velocities of the TD and shock in the Earth rest frame are relatively small. For example, for the TD to propagate 10 R_E, it would take approximately 1000 seconds. In that time, the trailing edge sheath would have expanded 5 R_E from the starting point. It is possible that this extrapolation is a limited one because there could be time dependence and curvature of the discontinuities and normal velocities.

HFAs are not just isolated structures in the solar wind. They are connected to the bow shock during their formation and perhaps longer. The decreased density in an HFA core can affect the magnetopause and therefore the magnetosphere and ionosphere. These effects are discussed in the next chapter.

Chapter 7

Magnetospheric and Ground Signatures of a Hot Flow Anomaly

Hot flow anomalies occur upstream of bow shocks. Their structure can affect the magnetopause and therefore the magnetosphere and ionosphere because these are all coupled regions. This chapter presents magnetospheric and ionospheric perturbations observed as a result of a HFA.

7.1 Introduction

An HFA upstream of the bow shock may produce effects that can be measured by spacecraft traversing the magnetosheath and magnetosphere. Simulations have shown sunward magnetopause displacements of 3 R_E due to HFAs. A 5 R_E sunward magnetopause displacement related to HFA passage has been observed with Interball and Magion satellite data [*Sibeck et al.*, 1999; *Koval et al.*, 2005]. The analysis of HFA events observed by THEMIS can quantify if this magnetopause motion is typical and determine how large that motion may be.

This study used ground and satellite observations to determine HFA impact on magnetosphere and ionosphere conditions. HFA induced magnetopause deformation may generate field-aligned currents into the ionosphere, which may be measured on the ground as magnetic impulse events or traveling convection vortices. These deformations can be magnetically mapped to magnetosphere/ionosphere disturbances with models such as that of *Tsyganenko and Stern* [1996]. HFA-induced effects may also include aurora brightening [*Sibeck et al.*, 1999]/dimming, magnetopause motion, boundary waves, FTEs, and the excitation of ULF waves. For example, *Eastwood et al.* [2011] analyzed a region with transient Pc3 pulsations in the magnetosphere generated by a hot flow anomaly. A corresponding enhancement of blue wavelength auroral emissions would indicate the presence of energetic electrons whereas an enhancement in red auroral emissions would indicate the precipitation of soft electrons.

Sitar et al. [1998] presented ionospheric signatures of an HFA observed on 24 July 1996. The interaction of an HFA with the magnetopause intensified a traveling convection vortex measured by ground magnetometers and produced HFA associated auroral brightening. Ionospheric TCVs are short duration spatially localized dayside phenomena. If the ground magnetometer data used covers a wide range of longitudes, some magnetometers (on the dayside) may observe a TCVs while other magnetometers (on the flanks or

night side) do not observe the TCVs, then the lifetime of the HFA can be estimated. By quantifying the duration of a TCV and its propagation velocity, one can obtain the size of the TCV in the ionosphere.

7.2 Case Study

7.2.1 Solar Wind and Magnetospheric Observations

THEMIS

A case study analysis of an HFA observed by all five THEMIS satellites on 22 August 2007 is presented in this chapter. Figure 7.1 shows the locations of THEMIS from 19:00 to 19:10 UT on 22 August 2007 in the XY, XZ, and YZ GSM planes. Figure 7.2 shows the observations of THEMIS A, Figure 7.3 shows THEMIS B, Figure 7.4 shows THEMIS C, Figure 7.5 shows THEMIS D, and Figure 7.6 shows THEMIS E. Figures 7.2–7.6 each show the magnetic field components in GSM coordinates, the magnetic field magnitude, plasma density, velocity components in GSM coordinates, ion pressure tensor components, and electron pressure tensor components observed by their respective satellites. The HFA plasma parameters for all satellites were very similar. THEMIS C is used as the reference spacecraft for the constellation in this study. THEMIS C made the HFA observation while it was at 10.4 MLT.

From the observations shown in Figure 7.4, THEMIS C observed a flow deflection in the dominant V_x component starting near 19:05:10 UT. The x component went from -281.88 km/s in the solar wind to -75.68 km/s in the HFA. The There was a near concurrent increase in the ion and electron temperatures during the time interval that the flow deflection was observed. The ion(electron) temperature increased from an average 6.1 $\times 10^5$ (9.2 $\times 10^4$) K in the solar wind to a maximum of 2.7$\times 10^6$ (4.1 $\times 10^5$) K in the HFA. The density decreased from 10.3 particles/cm^3 to a minimum of 5.5 particles/cm^3 in the HFA. These plasma observations met the criteria used to identify HFAs established in Section 4.1.

The leading edge boundary was selected by identifying the time when THEMIS observed the largest magnetic field magnitude before the largest flow deflection change in the HFA core. The largest field magnitude was used as a proxy for a leading edge compressed sheath. A similar proxy to a trailing edge sheath was used to identify the trailing edge boundaries. The time that the largest magnetic field magnitude was observed, be-

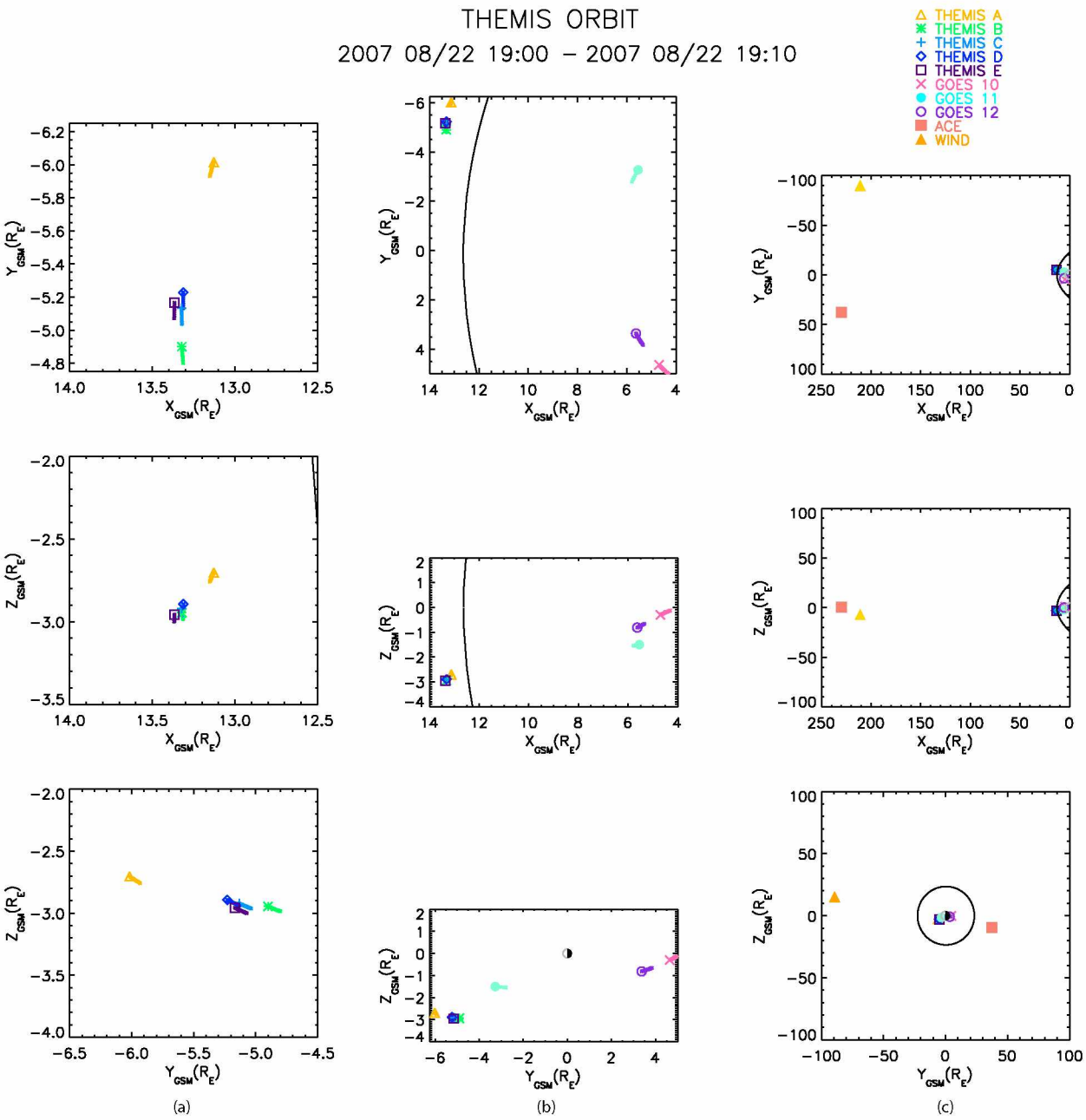

Figure 7.1. The locations of THEMIS A, B, C, D, and E, GOES 10, 11, and 12, ACE, and Wind are shown in the XY, XZ, and YZ planes using the GSM coordinate system on 22 August 2007. The colored lines indicate the spacecraft trajectory from 19:00–19:10 UT. The symbols associated with each spacecraft indicate the satellite locations at 19:00 UT. Each set of three plots in (a), (b), and (c) show the XY, XZ, and YZ planes with different axes ranges. The solid black curves are the *Merka et al.* [2005] model bow shock for Alfvén Mach number range of 2 to 20.

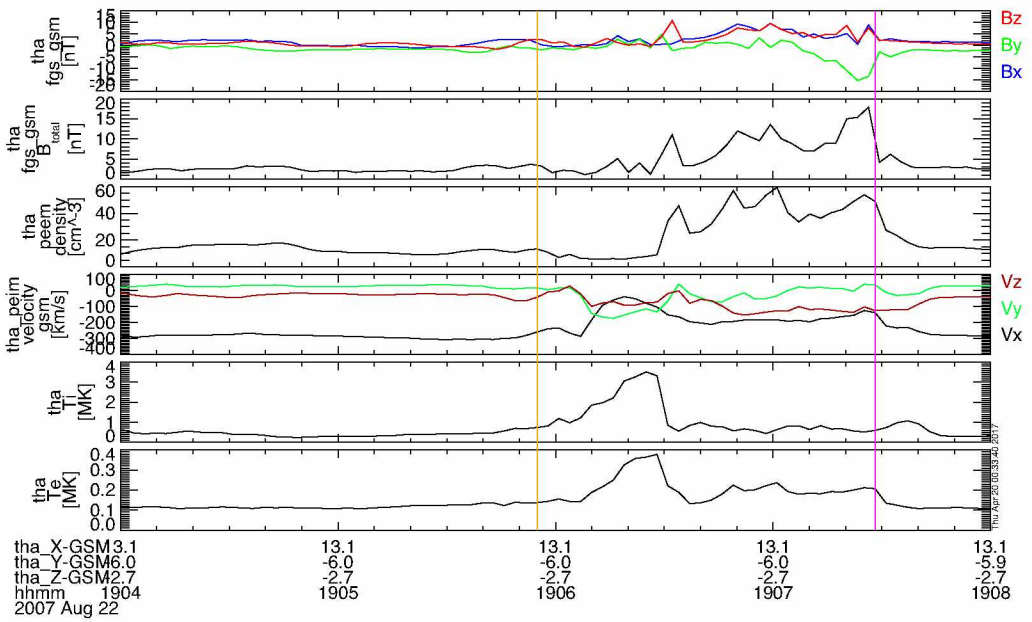

Figure 7.2. From top to bottom, each row shows the on board moment parameters of the HFA as observed by THEMIS A on 22 August 2007: magnetic field components, total magnetic field, density, particle velocity components, ion temperature, and electron temperature. Figure shows 19:04 to 19:08 UT. Vertical orange line marks the leading edge of the HFA. Vertical magenta line marks the trailing edge of the HFA.

fore density and ion and electron temperature returned to average solar wind values, was selected as the trailing edge boundary. The times selected as the boundaries are listed in Table 7.1.

Table 7.1. THEMIS Observations of the HFA Boundaries for Event on 22 August 2007

THEMIS Spacecraft	Leading Edge Observed [UT]	Trailing Edge Observed [UT]
A	19:05:55	19:07:27
B	19:05:24	19:46:43
C	19:05:20	19:06:40
D	19:05:21	19:06:46
E	19:05:18	19:06:36

During the HFA interval, the five THEMIS spacecraft were outside of the magnetosphere. Therefore, they do not have directly estimable magnetic footpoints on the ground. Being upstream of the bow shock, the HFA may affect a localized region of the magnetopause and in turn, the magnetosphere and magnetic field on the ground. This effect will be examined in later sections.

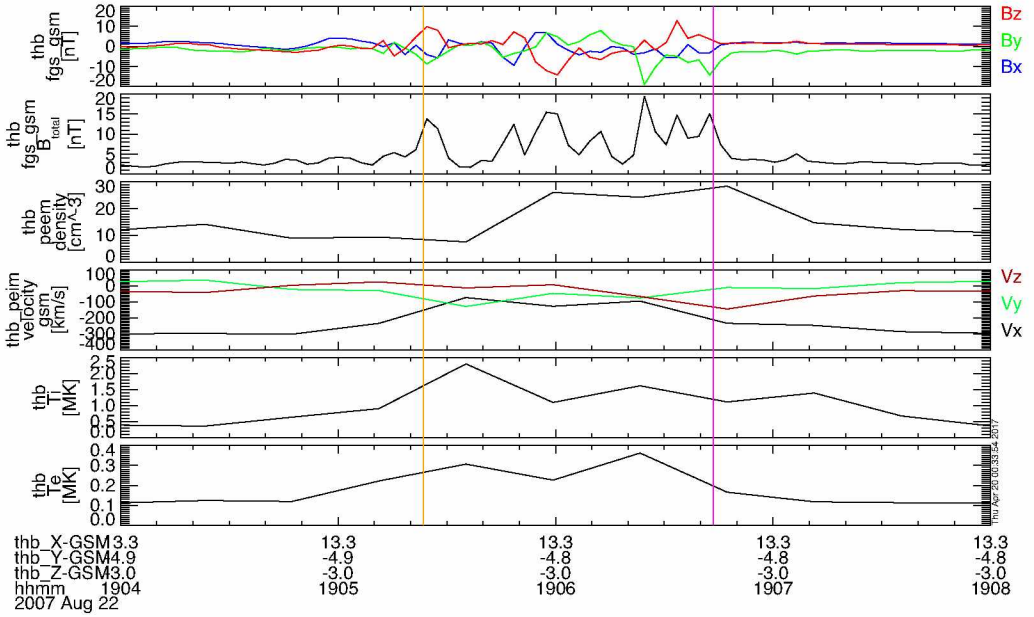

Figure 7.3. From top to bottom, each row shows the on board moment parameters of the HFA as observed by THEMIS B on 22 August 2007: magnetic field components, total magnetic field, density, particle velocity components, ion temperature, and electron temperature. Figure shows 19:04 to 19:08 UT. Vertical orange line marks the leading edge of the HFA. Vertical magenta line marks the trailing edge of the HFA.

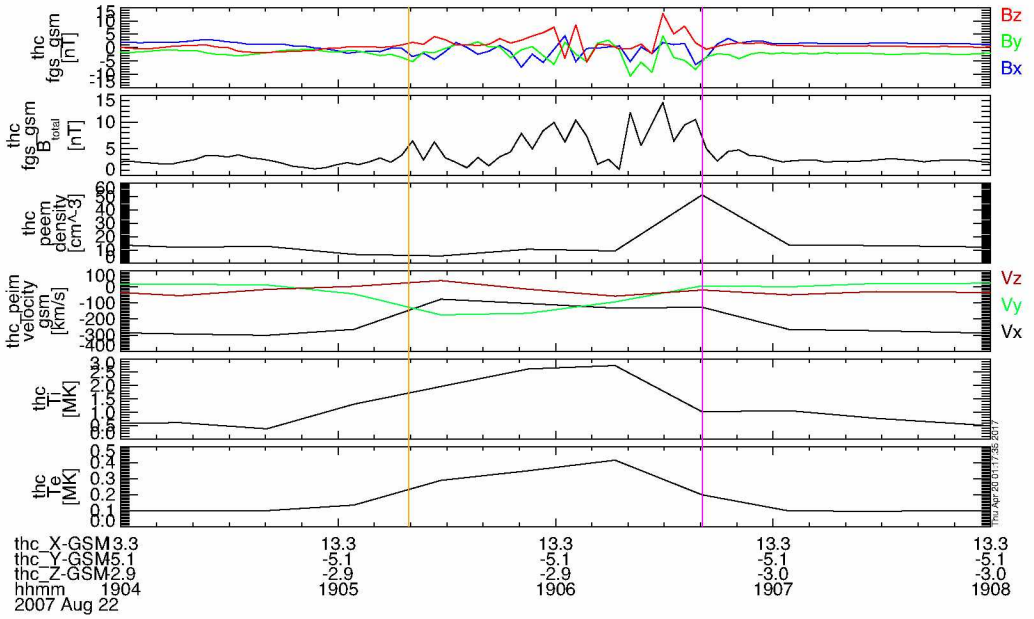

Figure 7.4. From top to bottom, each row shows the on board moment parameters of the HFA as observed by THEMIS C on 22 August 2007: magnetic field components, total magnetic field, density, particle velocity components, ion temperature, and electron temperature. Figure shows 19:04 to 19:08 UT. Vertical orange line marks the leading edge of the HFA. Vertical magenta line marks the trailing edge of the HFA.

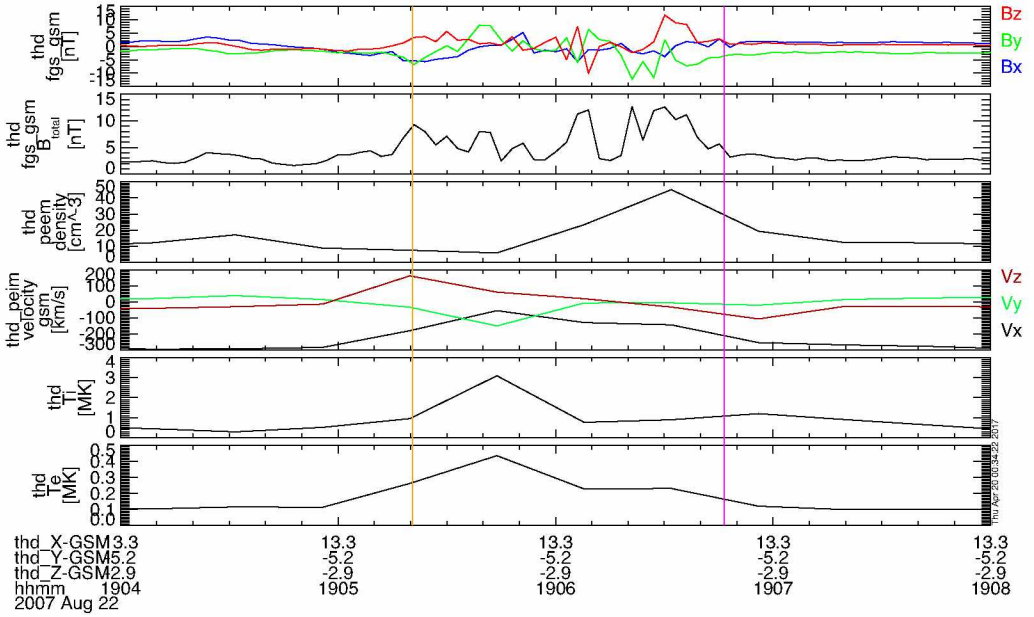

Figure 7.5. From top to bottom, each row shows the on board moment parameters of the HFA as observed by THEMIS D on 22 August 2007: magnetic field components, total magnetic field, density, particle velocity components, ion temperature, and electron temperature. Figure shows 19:04 to 19:08 UT. Vertical orange line marks the leading edge of the HFA. Vertical magenta line marks the trailing edge of the HFA.

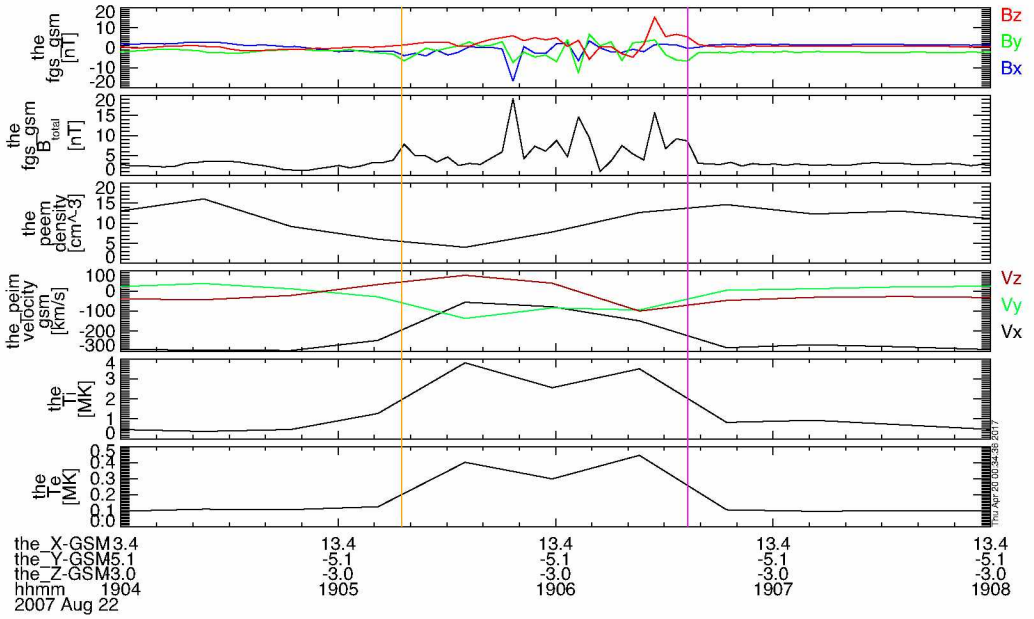

Figure 7.6. From top to bottom, each row shows the on board moment parameters of the HFA as observed by THEMIS E on 22 August 2007: magnetic field components, total magnetic field, density, particle velocity components, ion temperature, and electron temperature. Figure shows 19:04 to 19:08 UT. Vertical orange line marks the leading edge of the HFA. Vertical magenta line marks the trailing edge of the HFA.

Solar Wind Monitors

Upstream solar wind monitors during the THEMIS observations of the HFA were ACE and Wind. Their time shifted magnetic field observations are plotted on top of THEMIS C observations in Figure 7.7. The time shifts involved checking the cone and clock angle changes, in addition to the magnetic field, for all three spacecraft examined and aligning the perturbations observed. During the HFA interval, THEMIS C was nominally located at $(12.9, -5.4, -4.2)$ R_E, ACE was at $(230, 38, 0.3)$ R_E and Wind was at $(211, -90, -7)$ R_E. Their locations are plotted in Figure 7.1(c). By locating an interval where ACE and Wind observed a deflection in B_y that was similar to observations at THEMIS C, ACE data was shifted forward 70 minutes and Wind data was shifted forward by 65 minutes. An ACE and Wind B_y deflection was similar to a B_y deflection observed by THEMIS just before 17:00 UT. THEMIS C nominally observed the HFA at 19:05 UT. From examining the data in Figure 7.7, neither ACE nor Wind observed a discontinuity associated with the HFA.

GOES

During the hour immediately preceding and following the HFA observation by THEMIS, GOES 10, 11, and 12 also recorded observations. During the HFA interval, GOES 10 was nominally located at $(4.695, 4.643, -0.299)$ R_E, GOES 11 was at $(5.543, -3.272, -1.504)$ R_E and GOES 12 was at $(5.629, 3.366, 0.815)$ R_E. Figures 7.8, 7.9, and 7.10 each respectively show the detrended GOES 10, 11, and 12 magnetic field observations of an HFA on 22 August 2007. The detrending process removed the daily baseline from the dataset. The GOES locations relative to THEMIS are shown in Figure 7.1(b). GOES 11 was closest to the THEMIS constellation, followed by GOES 12 and then GOES 10.

All three GOES observed an approximately 1 to 2 nT perturbation in the magnetic field. The perturbations were first observed by the GOES closest to THEMIS (GOES 11), then GOES 12, and finally GOES 10. GOES 11 first observed the perturbation at 19:02:24 UT, GOES 12 observed it at 19:06:36 UT, and GOES 10 observed it at 19:09:36 UT. Using the GOES locations, the perturbation moved 178 km/s from GOES 11 to GOES 12 and 69 km/s from GOES 12 to GOES 10. The perturbation observed moved from the dawn-side magnetosphere to the dusk side. It is reasonable that magnetospheric signature of the HFA first arrives at a location that is closest to the instantaneous THEMIS location because the HFA will first perturb the magnetopause at a location close to it. The result-

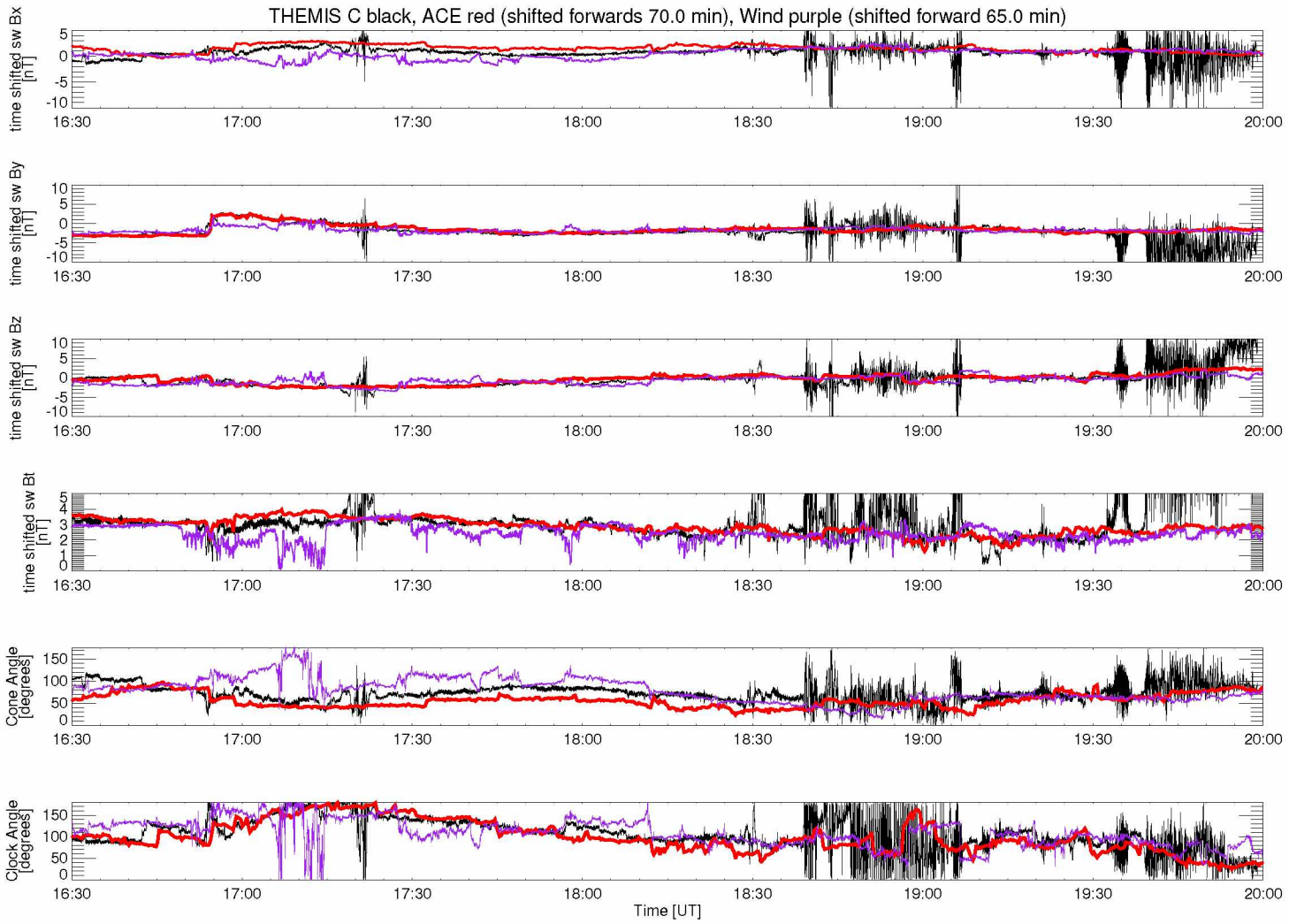

Figure 7.7. Each row shows the magnetic field as observed by ACE, Wind, and THEMIS C on 22 August 2007. THEMIS C data is shown in black, ACE is shown in red, and Wind is shown in purple. ACE and Wind have both been shifted forward in time. From top to bottom, the rows show B_x, B_y, and B_z in GSM, total magnetic field B_t, cone angle, and clock angle. Figure shows 16:30 to 20:00 UT on 22 August 2007.

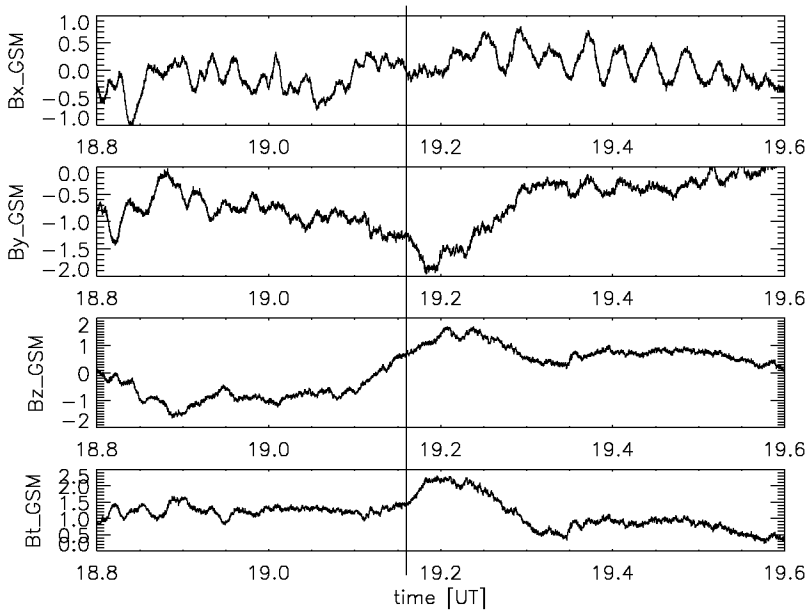

Figure 7.8. The detrended GOES 10 magnetic field data for 18.8 to 19.6 UT on 22 August 2007. The rows from top to bottom show the detrended B_x, detrended B_y, detrended B_z, and the magnetic field magnitude in the GSM coordinate system. The vertical line marks the time that the magnetic field perturbation was observed, 19:09:36UT.

ing magnetospheric perturbation can be expected to be a compression because the HFA sheath is a compressed region of plasma. That perturbation will then move outwards from the initial location, as observed.

Each magnetic field line in the magnetosphere has two footpoints. One is in the northern geomagnetic hemisphere and the other is in the southern hemisphere. Figure 7.11 shows the GOES 10, 11, and 12 footpoints on Earth's northern geographical hemisphere on 22 August 2007 from 19:00–19:10 UT. Footpoints are mapped using a magnetic field model generated using data from *Fairfield et al.* [1994] at `https://sscweb.gsfc.nasa.gov/`. Figure 7.12 shows the GOES 10, 11, and 12 footpoints on Earth's southern geographical hemisphere with the same magnetic field model. Footpoints are determined by identifying region where the magnetic field line that passes through the spacecraft intersects the Earth's surface. In the northern hemisphere, the footpoint falls near the 60° latitude area in North America. In the southern hemisphere, two footpoints are near 80° latitude and one is near 65°. Because perturbations were observed by GOES, it is probable that the regions near the GOES footpoints also observed perturbations. That is examined in the next two sections.

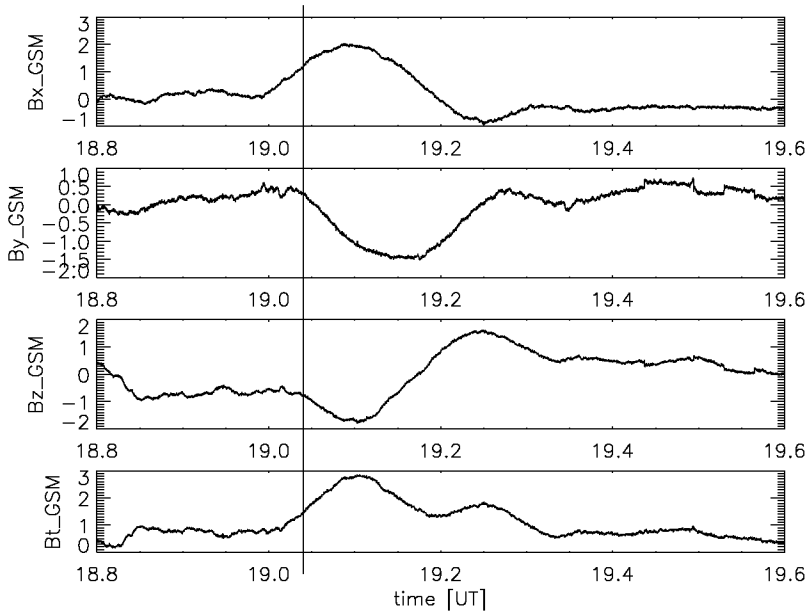

Figure 7.9. The detrended GOES 11 magnetic field data for 18.8 to 19.6 UT on 22 August 2007. The rows from top to bottom show the detrended B_x, detrended B_y, detrended B_z, and the magnetic field magnitude in the GSM coordinate system. The vertical line marks the time that the magnetic field perturbation was observed, 19:02:24 UT.

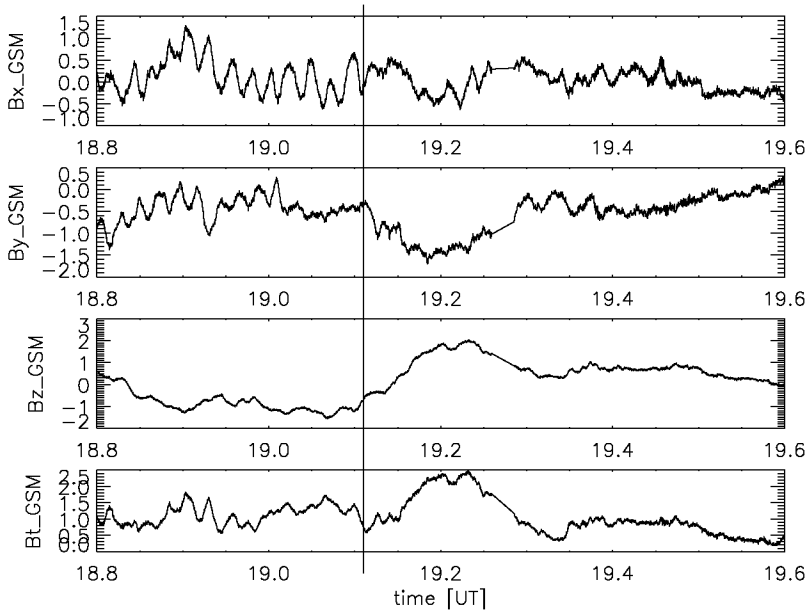

Figure 7.10. The detrended GOES 12 magnetic field data for 18.8 to 19.6 UT on 22 August 2007. The rows from top to bottom show the detrended B_x, detrended B_y, detrended B_z, and the magnetic field magnitude in the GSM coordinate system. The vertical line marks the time that the magnetic field perturbation was observed, 19:06:36UT.

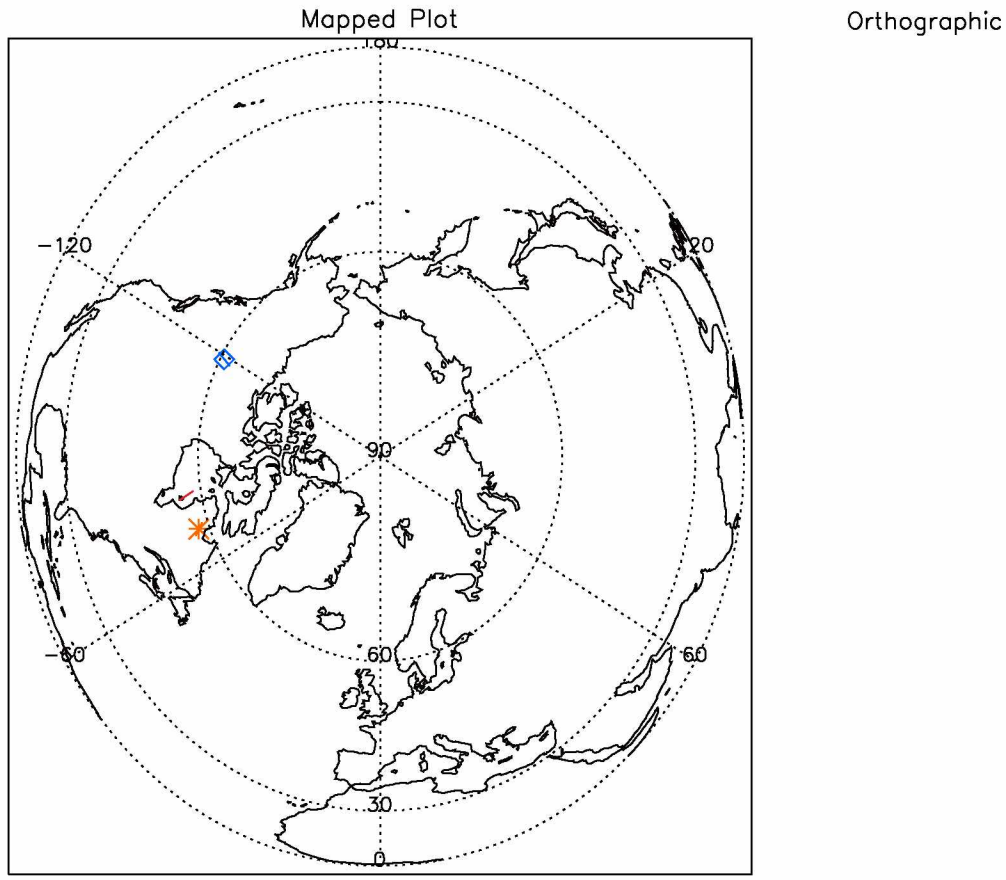

Figure 7.11. GOES 10, 11, and 12 magnetic footpoints in the northern geographical hemisphere on 22 August 2007 from 19:00–19:10 UT. Footpoints are determined by identifying region where the magnetic field line that passes through the spacecraft intersects the Earth's surface. Plot generated at `https://sscweb.gsfc.nasa.gov/`

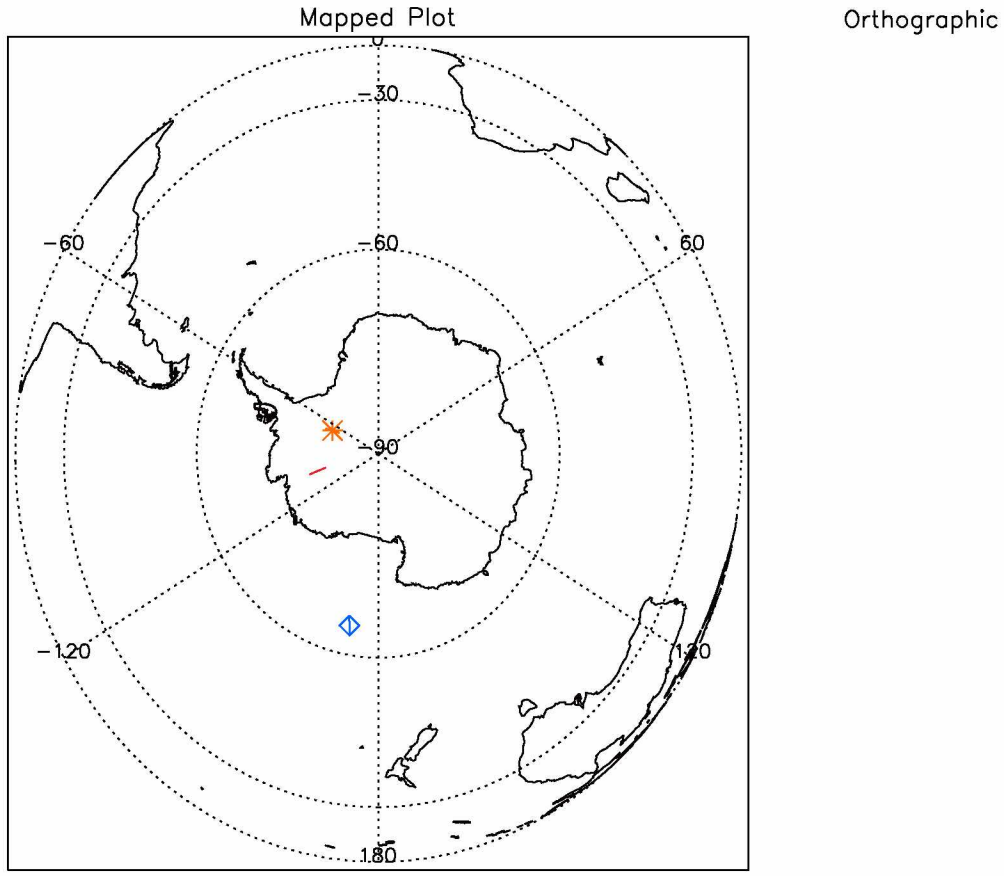

Figure 7.12. GOES 10, 11, and 12 magnetic footpoints in the southern geographical hemisphere on 22 August 2007 from 19:00–19:10 UT. Footpoints are determined by identifying region where the magnetic field line that passes through the spacecraft intersects the Earth's surface. Plot generated at `https://sscweb.gsfc.nasa.gov/`

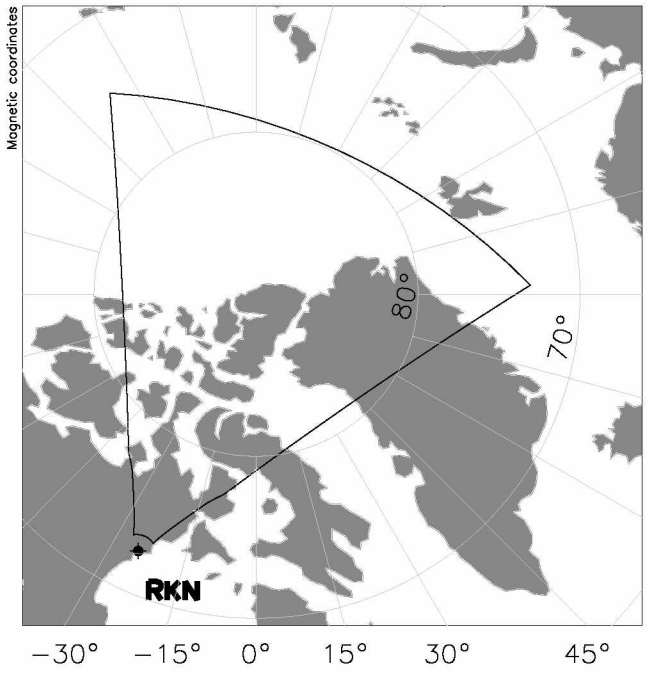

Figure 7.13. Rankin Inlet SuperDARN radar field of view outlined with the black solid line. The radar is located at the point labeled "RKN".

7.2.2 Ground Observations

SuperDARN

In 2007, the one SuperDARN radar making observations of the polar cap was the Rankin Inlet radar which observed the northern geographical hemisphere. There were no SuperDARN radars making observations of the southern polar cap. Figure 7.13 shows the field of view of the Rankin Inlet radar outlined in black. The boundary of the Rankin Inlet SuperDARN field of view is where perturbations of the magnetopause caused by the HFA in this case study would map down to the surface of the Earth. Because there is only one superDARN radar, there is only information on the line of sight velocity which is the velocity of plasma density irregularities towards or away from the radar, not necessarily the actual direction any plasma density irregularities are actually moving.

Figure 7.14 shows the Rankin Inlet SuperDARN radar velocity observations made before, during, and after the interval of the HFA shown in Figures 7.2–7.6. THEMIS observed the HFA from approximately 19:05 to 19:08 UT on 22 August 2007. From 19:01 to 19:08 UT, the Rankin Inlet radar observed negative velocity plasma movement. From 19:09 to 19:12 UT, positive velocities were observed by the radar. The shift in velocities

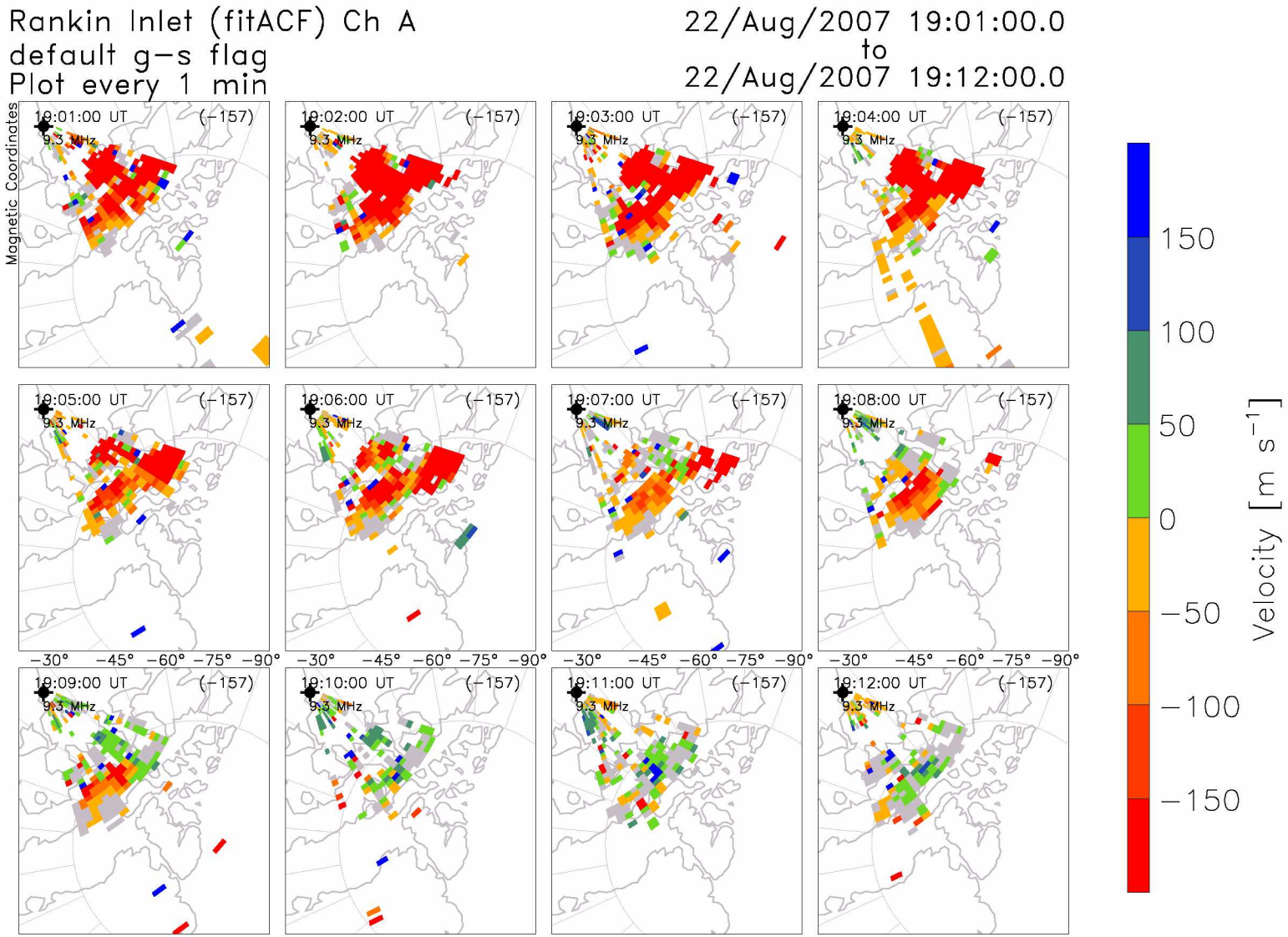

Figure 7.14. Rankin Inlet SuperDARN radar velocity observations made between 19:00–19:12 UT on 22 August 2007. Each scan is a sequence of all beam directions. The value of the velocity is then color-coded and overlaid on a map

observed could be caused by a pressure perturbation from the HFA impacting the magnetopause. Positive velocity corresponds to sunwards convection.

Figure 7.15 shows velocities generated by SuperDARN radar observations in the Northern hemisphere at (a) 19:04 UT and (b) 19:12 UT. Velocities are fitted using the method of *Ruohoniemi and Baker* [1998]. Figure 7.15(a) is representative of the interval 19:00–19:06 UT and (b) is representative of 19:09–19:12 UT. For the points colored in for both figures, there is a shift from red or $\geq$ -250 to -500 m/s in (a) to green or $\leq$ 12 to 125 m/s in (b). There is strong antisunwards convection before and during interval (a) and it seems to disappear in interval (b).

SuperMAG Observations

Magnetometer data in this dissertation is reported in the NEZ coordinate system, a local magnetic coordinate system for each magnetometer. The origin is the location of the magnetometer. N is the northwards component. The N direction points along the horizontal direction of the magnetic field for SuperMAG. Z points along the vertical direction and down towards the ground. E points towards along the $Z \times N$ direction. In this dissertation, N is plotted in black, E in red, and Z in blue. The data presented has 1 second time resolution.

Figures 7.16 and 7.17 shows the northern hemisphere SuperMAG magnetometer database observations for 22 August 2007 and Figure 7.18 shows the stations of the southern hemisphere. The figures show 65 to 85 degrees magnetic latitude and -65 to -85 degrees magnetic latitude respectively. The station names, associated site name abbreviation, and geographic and geomagnetic coordinates are listed in Table 3.3. Figure 7.16 shows stations from 6–10 MLT and Figure 7.17 shows 10–12 MLT. Figure 7.18 shows stations from 6–12 MLT.

Examining the southern hemisphere data in Figure 7.18, a minimum in the E component from 6–8 MLT is marked with vertical orange line b. The corresponding increase from 10–12 MLT is marked with light blue vertical line a. The E component decrease occurred at an earlier time for the noonward MLTs than dawnward MLTs and we can conclude a tailward perturbation propagation along the dawn flank. The specific times the perturbation was observed are listed in Table 7.2.

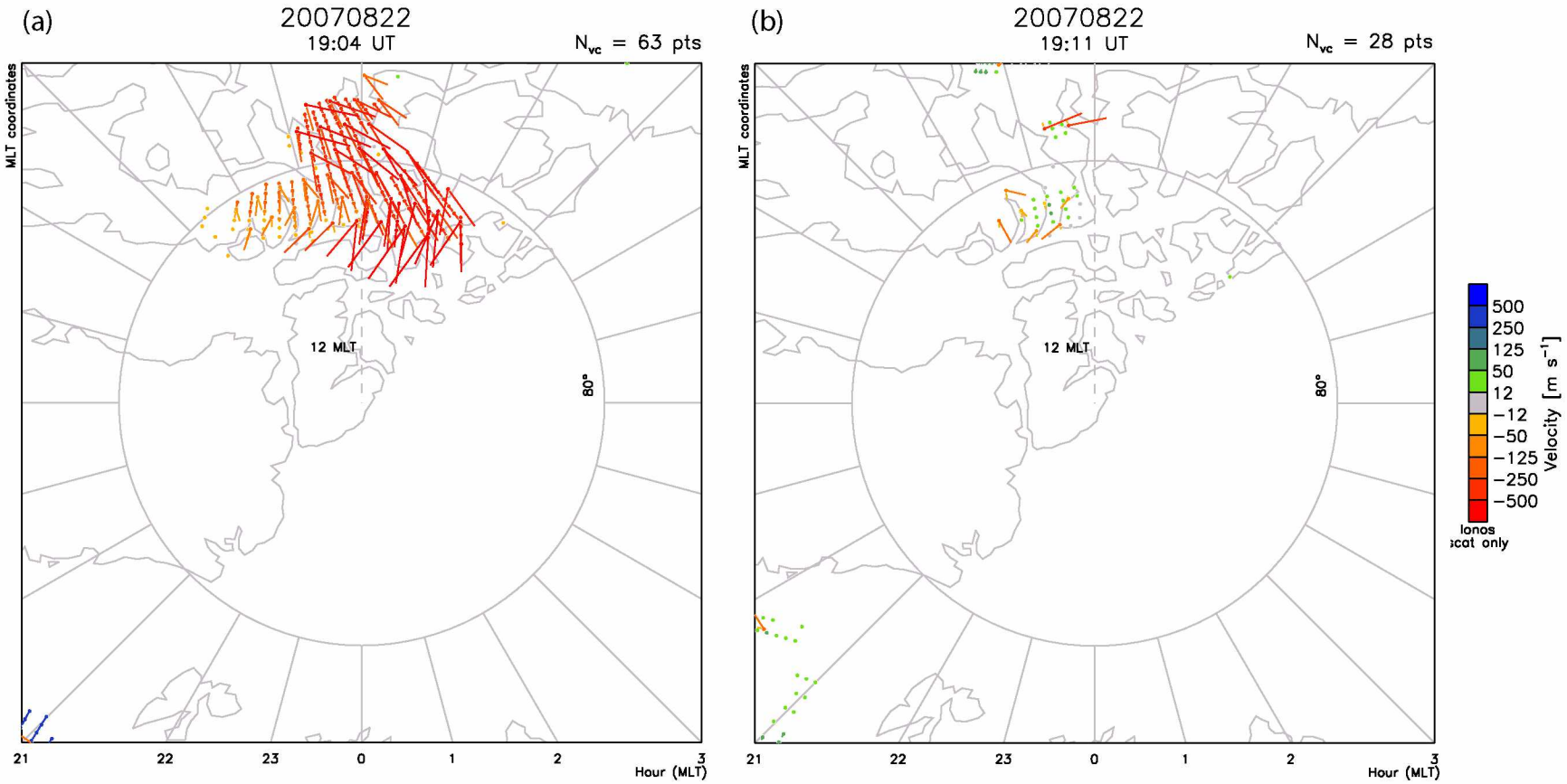

Figure 7.15. SuperDARN radar large-scale convection maps made at (a) 19:04 and (b) 19:11 UT on 22 August 2007using polar and high latitude radars. The light gray dashed vertical line indicated the direction towards 12 MLT. Plots generated at VT SuperDARN website.

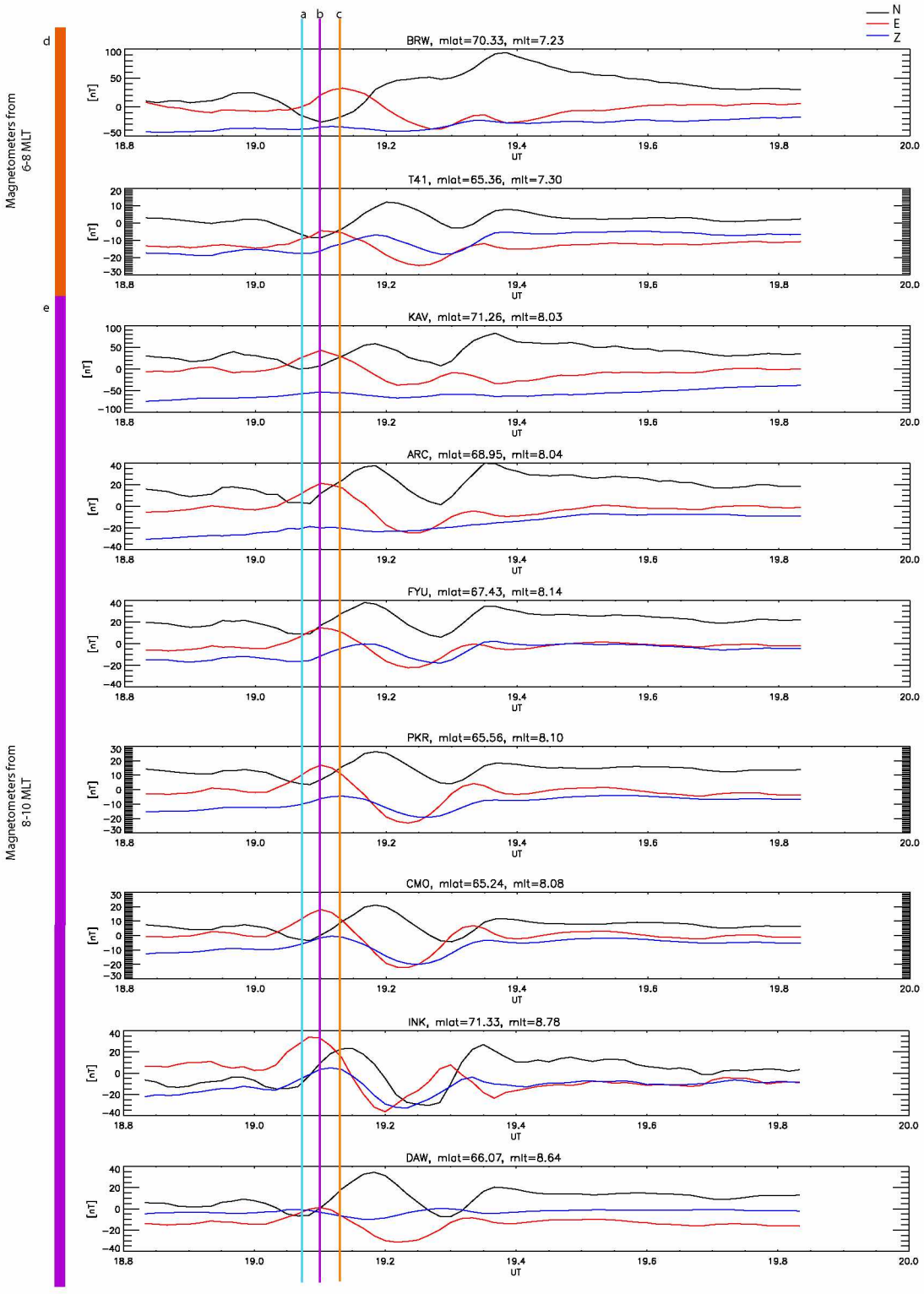

Figure 7.16. SuperMAG northern hemisphere ground magnetometer observations on 22 August 2007. Magnetometer stations 65 to 85 degrees magnetic latitude and 6–10 MLT are shown. Observations are shown in the local NEZ coordinate system at the individual magnetometer sites.

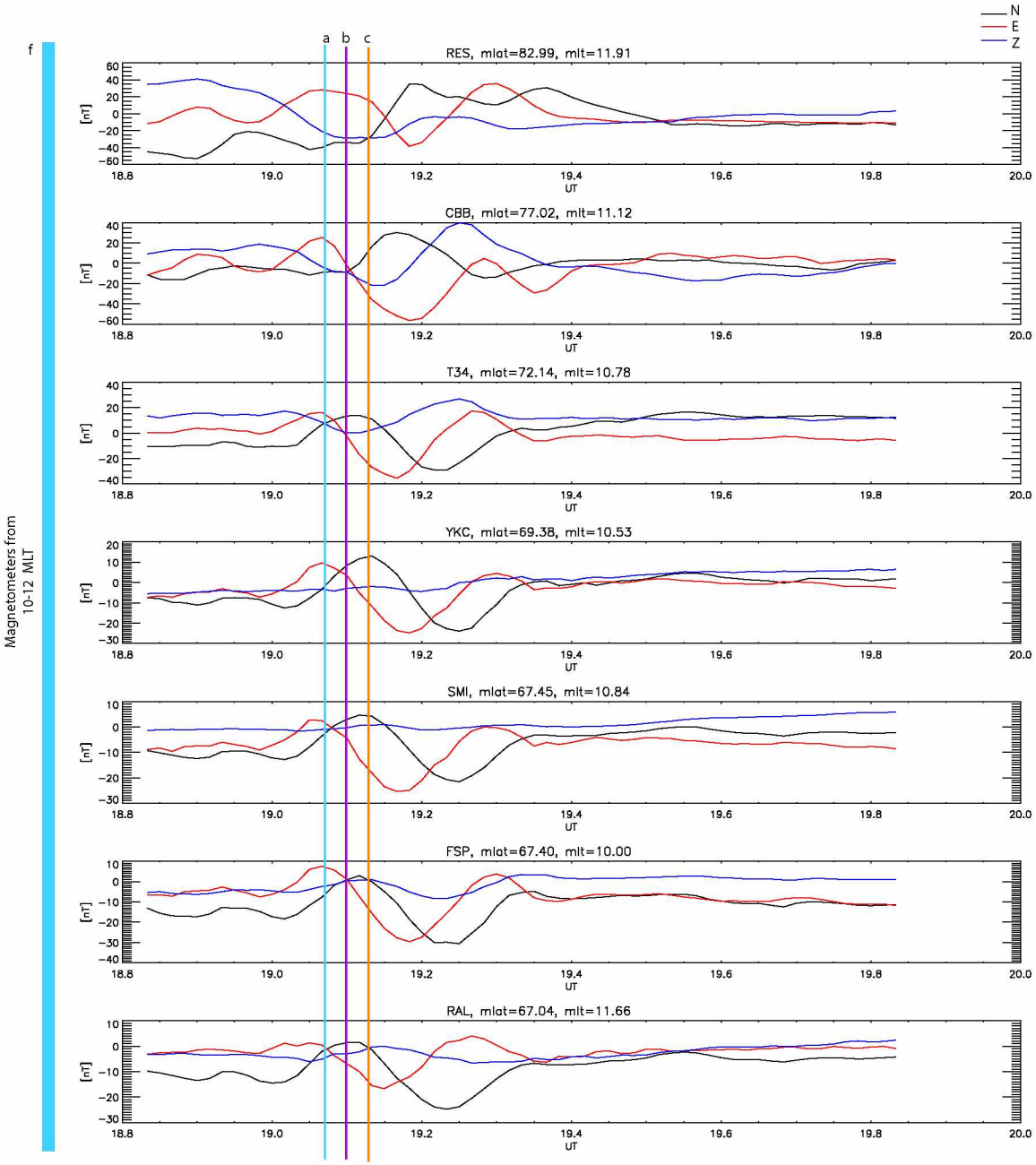

Figure 7.17. SuperMAG northern hemisphere ground magnetometer observations on 22 August 2007. Magnetometer stations 65 to 85 degrees magnetic latitude and 10–12 MLT are shown. Observations are shown in the local NEZ coordinate system at the individual magnetometer sites.

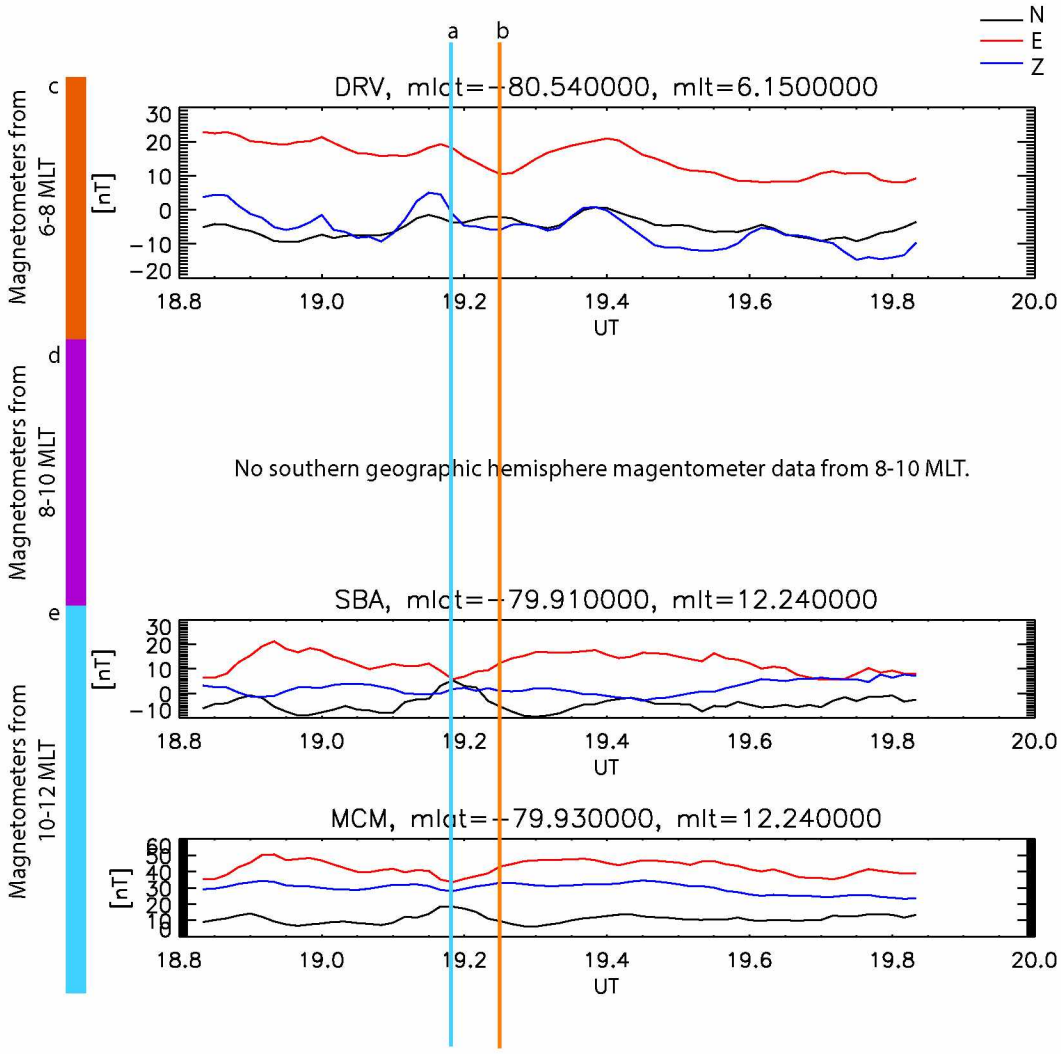

Figure 7.18. SuperMAG southern hemisphere ground magnetometer observations on 22 August 2007. Magnetometer stations -65 to -85 degrees magnetic latitude and 6–12 MLT are shown. Observations are shown in the local NEZ coordinate system at the individual magnetometer sites.

Similarly for the northern hemisphere, in Figures 7.16 and 7.17, an increase in the E component from 10–12 MLT is marked with vertical light blue line a. The same increase from 8–10 MLT is marked with purple vertical line b. The increase from 6–8 MLT is marked with orange vertical line c. The specific times the perturbation was observed are listed in Table 7.2. The E component decrease occurred at an earlier time for the larger MLTs than smaller MLTs, which is consistent with an HFA propagating tailward along the dawn flank.

Using the times the perturbation was observed at each station and the stations' geographic and geomagnetic separation, a maximum perturbation propagation velocity of 0.32°/s across geomagnetic longitude lines was calculated with the data from the northern hemisphere, Figures 7.16 and 7.17 and Table 7.2. The distance between the stations was calculated with the haversine formula given in Equation 4.28. This leads to a calculated velocity of approximately 9 km/s.

A maximum perturbation propagation velocity of 1.27°/s was calculated using the data from the southern hemisphere, Figure 7.18 and Table 7.2. The stations involved were approximately 80° S magnetic latitude. The velocity is approximately 21 km/s.

Figure 7.19 plots the E component perturbation amplitude against station magnetic latitude. This figure shows data from the northern and southern hemispheres. The largest amplitude of the perturbations is at 77° latitude in the northern hemisphere and 79.9° latitude in the southern hemisphere. Perturbation amplitude decreases at more equatorial latitudes. The perturbation amplitude curve flattens out below 65° latitude in both hemispheres. The perturbation amplitudes were larger in the northern hemisphere than the southern for any given latitude. This analysis was repeated for the N component of magnetic field and yielded similar results. We conclude that the magnetic field perturbation induced by the HFA was largest at high latitudes, on or near magnetic field lines affected by the HFA structure as expected. At lower latitudes, the field lines map to lower L shells in the magnetosphere. An L shell is the surface of rotation of a field line about the magnetic dipole axis. The perturbation is not as visible at lower latitudes and therefore would not be very large at low L shells in the magnetosphere.

Figure 7.20 shows polar plots of ground level magnetic field perturbations from SuperMAG station data. The maximum horizontal perturbation direction for each station is plotted with a green line. There is a plot for every minute from 19:06–19:11 UT. Plots of 19:04 UT and 19:05 UT look similar to that in 19:06 UT. Plots from 19:12 UT to 19:14 UT

Table 7.2. Time SuperMAG Ground Station Sites Observed Magnetometer Perturbation

Station Name		Time Perturbation Observed [UT]	Magnetic latitude	MLT
Abbreviation	Full Name			
BRW	Barrow	19:07:48	70.15	7.23
T41	Kiana	19:07:12	65.18	7.30
KAV	Kaktovik	19:06:00	71.11	8.03
ARC	Arctic Village	19:06:54	68.80	8.04
FYU	Fort Yukon	19:06:00	67.29	8.14
PKR	Poker Flat	19:06:00	65.42	8.10
CMO	College	19:06:00	65.10	8.08
INK	Inuvik	19:06:24	71.21	8.78
DAW	Dawson City	19:06:00	65.95	8.64
RES	Resolute Bay	19:04:12	83.02	11.91
CBB	Cambridge Bay	19:03:57	77.01	11.12
T34	Ekati	19:03:54	72.12	10.78
YKC	Yellowknife	19:04:12	69.35	10.53
SMI	Fort Smith	19:03:36	67.44	10.84
FSP	Fort Simpson	19:04:12	67.34	10.00
RAL	Rabbit Lake	19:03:36	67.06	11.68
SBA	Scott Base	19:09:00	-79.89	12.24
MCM	McMurdo Station	19:09:00	-79.92	12.24
DRV	Dumont Durville	19:10:12	-80.51	6.15

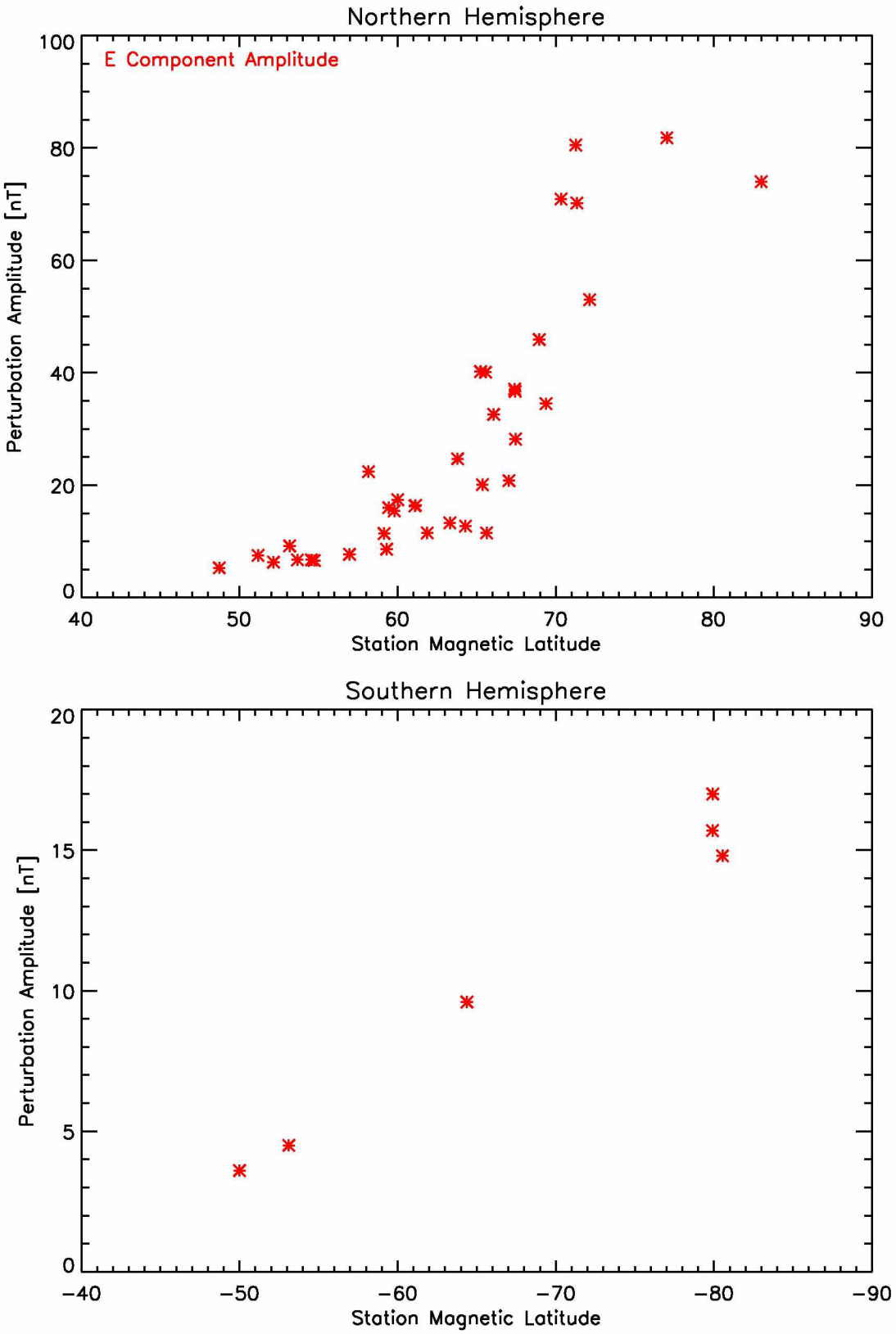

Figure 7.19. SuperMAG ground magnetometer observations on 22 August 2007. 37 individual magnetometer sites in the northern hemisphere and 6 in the southern hemisphere. The E component perturbation amplitude of magnetometer data is plotted in the NEZ coordinate system.

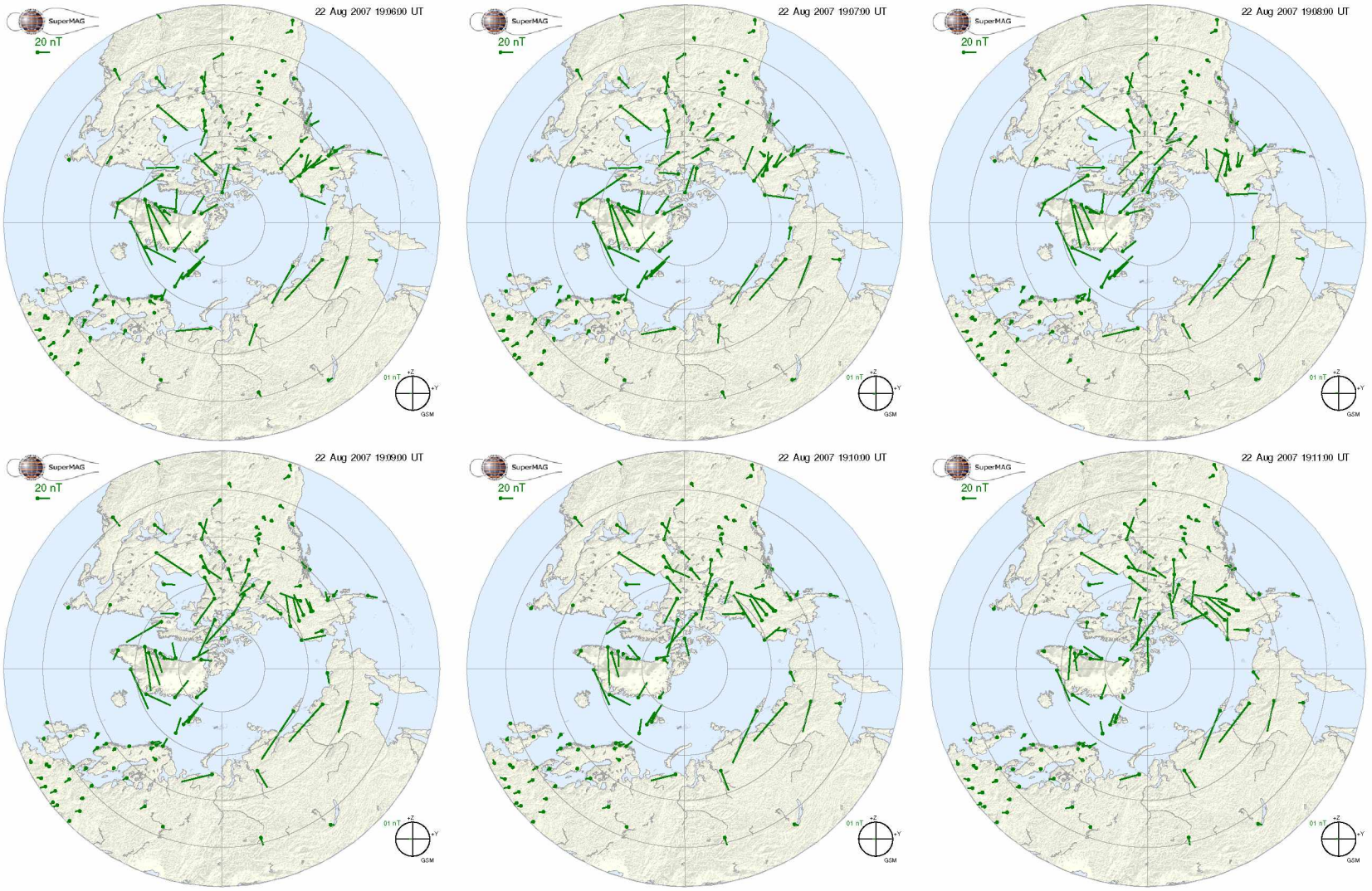

Figure 7.20. Polar plots of ground level magnetic field perturbations from SuperMAG station data. Stations are plotted as green dots on the map. The maximum horizontal perturbation direction for each station is plotted with a green line. There is a plot for every minute from 19:06–19:11 UT. [Figure courtesy of SuperMAG website]

look similar to that in 19:11 UT. The stations at the northwestern-most region of Greenland are closest to where perturbations from the HFA are expected to map down to Earth's surface. From 19:06 UT to 19:11 UT, the horizontal perturbation direction rotates from pointing towards the upper right of the figure to lower left.

7.3 Conclusions

An analysis of an HFA observed by all five THEMIS satellites at approximately 19:05 UT on 22 August 2007 was performed. The TD associated with the HFA was not observed in upstream, solar wind monitoring satellites.

In the magnetosphere, GOES magnetometers observed magnetic field perturbations. The HFA at the bow shock had a lower total core pressure than the solar wind which probably caused the magnetopause and magnetosphere to locally bulge outwards, accounting for the magnetic field perturbations observed. GOES observed compressions followed by slight decreases in magnetic field strength. It is possible that the HFA's compressed trailing edge sheath is what caused this signature in GOES. This magnetic field increase is also possible if there is an expansion wave (outward velocity and inward gradient of the magnetic field strength).

The perturbation amplitude was largest at GOES 11 (roughly 2 nT), the closest magnetospheric spacecraft to the location where THEMIS observed the HFA. The next largest amplitude was roughly 1.5 nT at GOES 12 and GOES 10. GOES 12 and GOES 10 are further from the HFA location observed by THEMIS. They were located on the dusk flank whereas THEMIS was on the dawn side.

The magnetospheric field lines affected by the HFA's core pressure decrease, relative to the solar wind, map to both the northern and southern hemispheres. Magnetic perturbations on the ground are caused by Alfvénic perturbations and there could be mode coupling to the Alfvén waves in the magnetosphere. If there is an expansion wave, one should expect that the amplitude of the expansion wave is strongest where the negative pressure pulse hits the magnetopause. The maximum of the azimuthal magnetic perturbations should be largest at some distance from this region. A direct change of azimuthal convection either through a modulation of the dayside reconnection rate or through a change of the sheath velocity around the magnetosphere (and on reconnected field lines) could also create an Alfvénic perturbation. These different coupling processes have different propagation time scales.

In the northern hemisphere, a SuperDARN radar observed a change in plasma velocity shortly after the HFA was observed by THEMIS at the bow shock. These observations were used in the creation of ionospheric convection maps. The maps showed a shift from strong antisunwards convection to an interval of low convection.

Ground magnetometers in both the northern and southern hemispheres observed perturbations. Magnetometers near noon MLTs, ie those closest to the HFA observed ground magnetometer perturbations first. Then stations at lower (more dawnward) MLT and further from the HFA observed the perturbations. The largest perturbation amplitude was near $\pm 80^{\circ}$ magnetic latitude for both hemispheres. There was a very clear decrease in amplitude observed by stations at more equatorial latitudes. The largest perturbation amplitude was near 8 MLT in the northern hemisphere and 6 MLT in the southern hemisphere. The amplitude decreased at more dawnwards MLTs.

Ground magnetometer data also showed the maximum horizontal component rotates near the time that the HFA was observed upstream of the bow shock. It is possible that this is a traveling convection vortex. Typical TCVs have tailwards propagation velocities between 4–6 km/s but the perturbation propagation velocity in this event was faster than this range. By identifying a peak ground magnetic field perturbation amplitude and the corresponding station magnetic latitude, a TCV would be expected to have its center near 77° in the northern hemisphere.

Kozlovsky et al. [2005] presented observations of the effects of a solar wind dynamic pressure pulse on the ionosphere. The observations led to the proposed scenario that the disturbance propagates along the magnetopause away from the sector where the pulse encountered the magnetosphere. Each point along the magnetopause where the disturbance arrived was a source of magnetosonic, fast Alfvén mode waves. In the magnetosphere, the total disturbance was a superposition of all waves reaching the point of observation at the time of interest. At every moment, there is a boundary which separates the magnetosphere where the magnetic field has already increased and where the changes have not become large yet. Behind the pressure pulse, the magnetic field increases and that means the contours of constant magnetic field strength move away from Earth. The magnetospheric plasma moves towards Earth. The changing angle between the plasma boundaries and the constant magnetic field contours leads to a pair of field aligned currents and the generation of a curl-free electric field behind the propagating front. The electric field will cause poleward plasma drift on closed magnetic field lines.

The poleward velocity conclusion was supported by global convection maps generated from SuperDARN HF radars. HFAs upstream of the bow shock are expected to produce observations similar to that of a solar wind dynamic pressure pulse.

From GOES 11 to GOES 12, the perturbation moved 178 km/s. From GOES 12 to GOES 10, the perturbation moved 69 km/s. The difference in speeds at these different parts of the magnetosphere could result from the relative separation of GOES and the nature of the propagation of the disturbance on the magnetopause. Perhaps the disturbance did not propagate symmetrically. Using the magnetometers, a perturbation propagation velocity across lines of longitude was calculated as 0.32°/s (9 km/s) for the northern hemisphere and 1.27°/s (21 km/s) for the southern hemisphere. Reasons for the difference between the northern and southern hemisphere could be because of uncertainty in the perturbation timing since there were fewer magnetometer stations in the southern hemisphere. The perturbation propagation velocity was faster in the magnetosphere than on the ground. The calculated azimuthal speeds could be determined by convection or by wave propagation in the azimuthal direction.

Table 7.3 is a summary of all the times that satellites and ground instruments observed a perturbation related to the HFA examined in this chapter. Events are listed with the earliest UTs at the top and later UTs at the bottom. GOES 11 made the first perturbation observations of all the satellites and ground stations surveyed at 19:02:24 UT. GOES 11 was in the magnetosphere at 9.96 MLT. First, examine the stations in the table from Fort Smith to Fort Simpson. FSP and RAL observe the perturbation concurrently. These stations are at nearly the same magnetic latitude and separated in MLT. The perturbation then moves to smaller (dawnwards) MLTs and higher latitudes (T34 to RES). YKC and SMI observations are likely because of pressure wavefronts from FSP and RAL. Following SMI in UT are the THEMIS and GOES 12 observations. Stations KAV to DAW essentially observe the perturbation at the same time. It covers roughly 5 degrees in latitude and half a MLT range. Using INK, ARC, and T41 data, the perturbation moves to lower (dawnwards) MLT and lower latitude though time. Because of a similarity in magnetic latitude, the perturbation at BRW could arrive from INK. The SuperDARN radar at Rankin Inlet was the last northern hemisphere ground station to observe a perturbation. This is reasonable because it should take time for the ionospheric convection change after a perturbation is observed upstream of the bow shock [*Kozlovsky et al.*, 2005]. DRV was the the last station in this analysis to observe a perturbation. This is reasonable because the station has the

Table 7.3. Summary of Times Perturbations Observed 22 August 2007

Satellite/Station Name	Time Perturbation Observed [UT]	MLT	Magnetic Latitude
GOES 11	19:02:24	9.96	–
FSP - Fort Smith	19:03:36	10.74	67.44
RAL - Rabbit Lake	19:03:36	11.55	67.06
T34 - Ekati	19:03:54	10.68	72.12
CBB - Cambridge Bay	19:03:57	11.01	77.01
RES - Resolute Bay	19:04:12	11.78	83.02
YKC - Yellowknife	19:04:12	10.44	69.35
SMI - Fort Simpson	19:04:12	9.90	67.34
THEMIS E	19:05:18	10.60	–
THEMIS C	19:05:20	10.60	–
THEMIS D	19:05:21	10.60	–
THEMIS B	19:05:24	10.60	–
THEMIS A	19:05:55	10.60	–
GOES 12	19:06:36	14.05	–
KAV - Kaktovik	19:06:00	7.97	71.11
FYU - Fort Yukon	19:06:00	8.08	67.29
PKR - Poker Flat	19:06:00	8.04	65.42
CMO - College	19:06:00	8.02	65.10
DAW - Dawson City	19:06:00	8.58	65.95
INK - Inuvik	19:06:24	8.71	71.21
ARC - Arctic Village	19:06:54	7.99	68.80
BRW - Barrow	19:07:48	7.20	70.15
T41 - Kiana	19:07:12	7.23	65.18
SuperDARN RKN	19:09:00	12.57	72.60
SBA - Scott Base	19:09:00	12.23	-79.89
MCM- McMurdo Station	19:09:00	12.23	-79.92
GOES 10	19:09:36	14.98	–
DRV - Dumont Durville	19:10:12	6.15	-80.51

highest latitude and the most dawnward MLT and the perturbation will take longer to traverse those distances.

The HFA was observed by THEMIS at 10.6 MLT. The perturbation propagation from the dawn to dusk sector is demonstrated by looking at the times in Table 7.3 for SBA, MCM, GOES 12, and GOES 10. They have 12.23, 12.23, 14.05, and 14.98 MLT respectively.

Chapter 8
Discussion and Conclusions

Hot flow anomalies can be observed throughout our solar system and can possibly occur on heliospheric scales. They were first studied in the 1980s in the data of Earth orbiting satellites. They are characterized by a significant increase in particle temperature and substantial flow deflection from the solar wind flow direction coinciding with a decrease in density.

HFAs are important to study and understand because they may play an important role in solar wind-magnetosphere coupling. They may drive magnetopause motion, boundary waves, and flux transfer events. They can excite ultra low frequency waves in the magnetosphere, drive magnetic impulse events in the ionosphere, and trigger auroral brightening or dimming. Studying HFAs will aid in the understanding of fundamental processes that operate throughout the heliosphere such as particle energization and shocks.

This dissertation presents statistical and case studies of hot flow anomalies identified in Time History of Events and Macroscale Interactions During Substorms (THEMIS) satellite data from 2007–2009. The characteristics and occurrence of HFAs, their dependence on solar wind/interplanetary magnetic field (IMF) conditions and location, and their magnetospheric-ionospheric signatures, have been investigated using in-situ spacecraft observations and ground based observations.

8.1 Statistical Analysis of Hot Flow Anomalies

This study examined plasma properties of HFAs and SHFAs observed by THEMIS from 2007-2009. This study also separated HFAs into young and mature events. The dataset included a statistically significant number of all four categories of HFAs: young SHFAs, mature SHFAs, young HFAs, and mature HFAs. The events spanned a wide range of MLTs.

After placing all events relative to a model bow shock, it was determined that HFAs and SHFAs were observed up to 6.3 R_E and 6.1 R_E upstream from the bow shock, respectively. HFA and SHFA occurrence decreases with increasing distance upstream from the bow shock. There could be a limit to how far HFAs and SHFAs can be observed upstream from the bow shock because particles reflected from the bow shock have a limited distance that they can travel sunward because of the impinging background solar wind

flow. However, many aspects such as the magnetic field orientation, the effective collision times, and instabilities that effectively generate dissipation also probably limit how far upstream HFAs can be observed. Without these instabilities, the solar wind is essentially collisionless and the particles could move very large distances upstream if they have access through an appropriate magnetic field orientation. With a quasi-perpendicular IMF, the particles will have more limited access.

Observations of both young and mature HFAs and SHFAs were made from approximately 7 to 16.5 MLT and up to 6.3 R_E upstream from the bow shock. Because we theorize that young HFAs evolve into mature HFAs [*Lucek et al.*, 2004; *Zhang et al.*, 2010], the observation suggests that HFAs form along a discontinuity that intersects the bow shock, both close to and further upstream of the bow shock. Then the process which turns a young HFA into a mature one acts along the entire length of the discontinuity. Because of THEMIS's mostly equatorial orbit from 2007–2009, observations of any HFAs and SHFAs that occurred at more polar latitudes were not able to be observed. The Cluster mission has made many non-near equatorial HFA observations. Global hybrid model simulations results from *Omidi et al.* [2014] showed that SHFAs could be generated at all cone angles and at all latitudes. The results of this dissertation also show that SHFAs were observed at all cone angles. *Facskó et al.* [2009] presented HFA locations relative to the bow shock. Their work showed HFAs up to approximately 6 R_E upstream of the bow shock and also a wide range of MLTs on both the dayside dawn and dusk flanks.

HFA location is typically expressed as being upstream from a quasi-perpendicular or quasi-parallel bow shock. In *Schwartz et al.* [2000], most HFAs have quasi-perpendicular conditions on at least one side of the HFA. For example, *Onsager et al.* [1991] discussed events at a quasi-perpendicular bow shock. From a study of 124 HFAs identified using Cluster data from 2003, 2006, and 2007, *Facskó et al.* [2009] found that approximately 66% of HFAs were found in the quasi-parallel region. For the 136 THEMIS observed HFAs in this study, approximately 44% of HFAs were in solar wind with a quasi-perpendicular orientation. *Lin* [2002] simulations discussed HFAs along quasi-parallel shocks. They suggested that structures at quasi-parallel shocks could lead to transient events in the magnetosphere.

HFA heating is not constant for all observed events. HFAs with the highest event core ion temperatures were not seen at the magnetospheric flanks. The ratio of HFA ion temperature increase to HFA electron temperature increase is highest around 12 MLT and

slightly duskward. A possible explanation is because of the curvature of the bow shock, the Mach number is always smaller at the flanks and high latitudes.

Both mature and young HFAs are slightly more prevalent when there is a more approximately radial interplanetary magnetic field. The orientation of a quasi-radial magnetic field allows the solar wind field lines to be connected to the magnetosphere for longer so that favorable HFA formation conditions can create HFAs.

No HFAs were observed when the solar wind Mach number was less than 5. This suggests that there is a minimum threshold Mach number for HFAs to form. This is in line with observations of HFAs in other studies such as *Facskó et al.* [2009].

HFAs occur most preferentially for solar wind speeds from 500–600 km/s. Faster solar wind speeds have more kinetic energy which could funnel more particles into the area favorable to HFA formation during HFA growth. For solar wind speeds faster than 600 km/s, this study observed a normalized occurrence rate that was lower than the normalized number of events with local solar wind in the 500–550 and 550–600 km/s range. This is slightly different than the *Facskó et al.* [2009] observation that HFA occurrence peaked for solar wind speeds near 650 km/s. It has been reported that the typical value of the solar wind during HFA formation is higher than the average [*Facskó et al.*, 2008, 2009]. Examining an average solar wind speed using THEMIS solar wind intervals from 2007–2009, the HFAs in this study agree with the prior results.

Density in the HFA core is lower than in the ambient solar wind. However, the amount of maximum density depression compared to its surrounding local medium, n_{HFA}/n_{sw} shows no clear trend with MLT. This ratio decreases slightly with increasing distance from the bow shock from 0 to 4 R_E for SHFAs while HFA density shows nor correlation to distance from bow shock.

Wang et al. [2013b] studied the correlation between the thermal increase and kinetic energy decrease of HFAs. They showed that a significant part of the kinetic energy of the solar wind is converted into thermal energy inside an HFA but that additional heating process(es) were also required. These processes may include particle acceleration at the bow shock or magnetic field waves. In examining both the thermal and kinetic energy of the events in this dissertation, it is hypothesized that some of the mature HFAs and SHFAs in our study are most likely events that have existed for a while before observation by THEMIS, and have therefore cooled through some mechanism such as adiabatic expansion. Continued event cooling will eventually return the HFA plasma to an equilibrium

with the solar wind. If one considers the entropy in the plasma, it is up to approximately an order of magnitude larger. Plasma expansion does not alter entropy so there are other physics occurring too. The expansion does return force balance in the structure and sets up an equilibrium. That equilibrium is different from the equilibrium of the original solar wind conditions.

Many plasma properties were examined, but SHFAs and HFAs do not show major differences in this study. This indicates that even though the HFA and SHFA drivers to create the events may be different, the observed properties once the HFA and SHFA is in existence are the same.

8.2 Spatial and Temporal Analysis of Hot Flow Anomalies

The THEMIS constellation orbit was well configured to make multi-spacecraft observations of the same HFA. This allowed for the opportunity to perform a spatial and temporal analysis of an HFA. This study focused on a hot flow anomaly observed by all five THEMIS spacecraft at approximately 21:15 UT on 10 August 2007. The orientation of three boundaries in the HFA were identified: a leading edge, tangential discontinuity, and trailing edge shock. These boundaries were observed by all THEMIS spacecraft. The calculated boundary orientations are consistent for all spacecraft.

Previous HFA studies have observed typical event boundaries as a hot core bounded by tangential discontinuities. Those TDs are then bounded by shocks (e.g. [*Schwartz et al.*, 1985; *Paschmann et al.*, 1988]). In this event, the leading edge boundary was more difficult to identify and categorize than the trailing edge TD and shock. The HFA examined did not have a strong HFA sheath on the leading edge. The boundary was chosen using a proxy for the magnetic field magnitude increase in a typical sheath. Analysis of the boundary using minimum variance did not produce a boundary where the magnetic normal was near zero for every spacecraft, as expected for a TD, so the boundary was simply called the leading edge boundary in this dissertation.

The total pressure at the center of this event was observed to be higher than that in the sheath and solar wind, as expected from prior analysis of other HFAs, and it was concluded that the HFA boundaries were expanding. The HFA expansion against the solar wind was calculated to be 283 km/s. Expanding HFA structures are typical observations (e.g. [*Thomsen et al.*, 1986; *Lucek et al.*, 2004]). Not all observed HFAs in the literature are expanding though. *Thomsen et al.* [1986] examined an event where the estimated mag-

netic tension balanced the estimated pressure gradient so the HFA cavity was probably no longer expanding. So-called stable size HFAs were also reported by *Xiao et al.* [2015]. *Xiao et al.* [2015] discussed a class of HFAs where events were contracting. Their expanding events had expansion speeds of tens to several hundred kilometers per second and the results of this dissertation fall within their observed range.

The distances between the boundaries were calculated and the HFA sheath was observed to be thicker closer to the bow shock (near THEMIS A) than at points further away (THEMIS B, C, D, and E were relatively close in location). The reason for this is most likely a combination of two mechanisms. First is that the trailing edge sheath grew thicker at THEMIS A's location than at the other spacecrafts' locations. This sheath thickened after the trailing edge passed THEMIS B–E. Second is that the HFA sheath was already thicker closer to the bow shock at the THEMIS A location when it was formed. During the time that the HFA was observed, the normals determined imply the the sheath is thicker at the bow shock. The boundary velocities determined imply the the TD is moving faster. Both factors contribute to the reason why the sheath was thicker at THEMIS A, the spacecraft closer to the bow shock.

The calculated leading edge boundary to TD distance was 4.1 R_E for THEMIS B, C, D, and E and 5.2 R_E for THEMIS A. The TD to trailing shock distance was 0.2 R_E for THEMIS B, C, D, and E and 0.6 R_E for THEMIS A. This leads to total HFA thicknesses of 4.3 R_E for THEMIS B, C, D, and E and 5.8 R_E for THEMIS A. *Schwartz et al.* [1988] reported HFA sizes of 1–3 R_E. *Facskó et al.* [2009] determined HFA sizes of up to 7.0 ± 4.3 R_E. The 4.3 and 5.8 R_E estimated sizes in this study falls within the range of HFAs in previous studies (e.g. [*Thomsen et al.*, 1986; *Facskó et al.*, 2009]) and is slightly larger than studies such as *Schwartz et al.* [1988]. Factors that influence HFA size have been studied with both simulations and satellite data analysis. It has been demonstrated that HFA size is mainly influenced by the magnetic shear and the angle between the discontinuity normal and the Sun-Earth direction [*Lin*, 2002; *Facskó et al.*, 2009].

8.3 Magnetospheric and Ground Signatures of Hot Flow Anomalies

This study examined signatures an HFA produced in the inner magnetosphere, ionosphere, and on the surface of the planet. The case study was of an HFA observed by all five THEMIS spacecraft on 22 August 2007 at approximately 19:05 UT.

The HFA is a structure in the solar wind connected to the bow shock. The lower plasma pressure inside an HFA is expected to cause a spot in the local magnetopause to bulge outwards. This is expected to cause a deformation in the magnetospheric field lines. These field lines intersect the surface of the Earth at both the northern and southern hemispheres.

Using GOES observations, a small magnetic field perturbation was observed in the magnetosphere near the time THEMIS observed an HFA upstream of the bow shock. The perturbation was largest closest to the HFA and smaller at parts of the magnetosphere further from the HFA. The perturbation observed moved from the dawnside magnetosphere to the dusk side in both spacecraft and ground magnetometer observations. Both also showed perturbation propagation along the dawn flank. It is reasonable that magnetospheric signature of the HFA first arrives at a location that is closest to the instantaneous THEMIS location because the HFA will first perturb the magnetopause at a location close to it. The magnetospheric perturbation can be expected to be a compression because the HFA sheath is a significant region of compressed region of plasma. That perturbation will then move outwards from the initial location, as observed. In simulations, *Lin* [2002] observed that the HFA bulged out into the solar wind because of enhancement of the total pressure in the hot cavity and that the local bow shock and magnetosheath could extend out into the solar wind by several Earth radii. The GOES observations do not seem to have large fluctuations due to the HFA core pressure, but only the compressed sheath.

Ground magnetometers observed a perturbation near the time that THEMIS observed the HFA. Similar to *Fillingim et al.* [2011], perturbation amplitudes of dozens of nT were measured. Magnetometers near noon MLTs observed perturbations first. Then stations at more dawnwards MLTs observed the perturbations. This is consistent with an HFA propagating tailward along the dawn flank. Using the geographical position of the magnetometers, a perturbation propagation velocity across lines of longitude was calculated as 0.32°/s and 9 km/s for the northern hemisphere and 1.27°/s and 21 km/s for the southern hemisphere. The calculated perturbation propagation velocity was faster in the magnetosphere than on the ground. The calculated azimuthal speeds could be influenced by convection or by wave propagation in the azimuthal direction. The largest perturbation amplitude was near $\pm 80^\circ$ magnetic latitude for both hemispheres. There was a very clear decrease in amplitude observed by stations at more equatorial latitudes. The largest

perturbation amplitude was near 8 MLT in the northern hemisphere and 6 MLT in the southern hemisphere. The amplitude decreased at more dawnwards MLTs.

Ground magnetometer data showed the maximum horizontal component rotates near the time that the HFA was observed. It is possible that this is a traveling convection vortex. Typical TCVs have tailwards propagation velocities between 4–6 km/s but the perturbation propagation velocity in this event was faster than this range. By identifying a peak ground magnetic field perturbation amplitude and the corresponding station magnetic latitude [*Sitar et al.*, 1998; *Fillingim et al.*, 2011], a TCV would be expected to have its center near 77° in the northern hemisphere. *Sitar et al.* [1998]; *Sibeck et al.* [1999] provided evidence linking the IMF orientation changes and HFAs to the occurrences of magnetic impulse events and traveling convection vortices. These can be driven by tailward moving field aligned currents formed from the deformation of the bow shock and magnetopause.

SuperDARN was making high latitude ionospheric observations before, during, and after the HFA interval. SuperDARN radar observations very shortly after the magnetometer perturbations showed a localized change in plasma velocity. The observations were used to create convection maps for the northern hemisphere. These maps showed a change from strongly antisunwards to low convection after the HFA was observed by THEMIS. The HFA acted like a dynamic pressure pulse on the magnetopause and therefore the shift in convection was similar to convection changes observed after pressure pulses [*Kozlovsky et al.*, 2005].

8.4 HFAs Versus Other Foreshock Transients

When first discussing the different types of foreshock transients that are found in the literature, there were properties of the transients that overlapped. There are also defining characteristics of certain phenomena that contradict other reported transients. For example, *Turner et al.* [2013] states properties of FBs: (1) HFAs formation requires an IMF discontinuity to intersect the bow shock while FB formation does not, (2) HFAs are typically a few Earth radii in width normal to the discontinuity and form at the bow shock whereas FBs can be larger than 10 R_E in width and form far upstream of the bow shock, and (3) HFAs require the electric field on one or both sides of the discontinuity to be pointed back into it but FBs do not. This dissertation discusses phenomena called spontaneous hot flow anomalies (SHFAs) which are HFAs where a IMF discontinuity is not observed and dis-

agrees with point (1). Examining point (2), we believe that differentiating HFAs and FBs is not always easy. Size differences alone do not imply that the physical mechanisms that generate HFAs and FBs are necessarily different. Size is not a qualitative difference and any distinction according to size is arbitrary. Point (3) is refuted by the HFA database of *Wang et al.* [2013b] where the inward pointing electric field is not a necessary condition to generate an HFA.

Properties of foreshock cavities and foreshock cavitons in the literature are reported as structures with strong edge compressions and with density and magnetic field depressions in the event core. For both, the bulk flow is only slightly deflected from the solar wind speed and temperature and pressure are only slightly increased inside the event. Foreshock cavitons are similar to foreshock cavities except the local solar wind has ULF waves. These properties alone are not enough to distinguish them from HFAs.

Foreshock compressional boundaries are associated with density and magnetic field decrease below solar wind levels. A bundle of IMF lines connected to the bow shock generated a convecting foreshock bounded by FCBs. [*Sibeck et al.*, 2008] suggests that the back-and-forth motion of a FCB over a spacecraft as it responds to varying IMF orientations would generate observations similar to those observed during foreshock cavities. There could be both convecting and non-convecting signatures so this alone cannot allow one to distinguish between the two FCB generation mechanisms [*Omidi et al.*, 2013a].

Due to the lack of a definitive defining observational feature for these transients, one can wonder if the observed transients are truly different types of events with different underlying physics. Simulations have shown that different generation mechanisms are operating to create these events with very similar observational features.

References

Angelopoulos, V. (2008), The THEMIS mission, *Space Sci. Rev.*, *141*, 5–34, doi:10.1007/s11214-008-9336-1.

Auster, H. U., K. H. Glassmeier, W. Magnes, O. Aydogar, W. Baumjohann, D. Constantinescu, D. Fischer, K. H. Fornacon, E. Georgescu, P. Harvey, O. Hillenmaier, R. Kroth, M. Ludlam, Y. Narita, R. Nakamura, K. Okrafka, F. Plaschke, I. Richter, H. Schwarzl, B. Stoll, A. Valavanoglou, and M. Wiedemann (2008), The THEMIS fluxgate magnetometer, *Space Sci. Rev.*, *141*, 235–264, doi:10.1007/s11214-008-9365-9.

Balogh, A., and R. A. Treumann (2013), *Physics of Collisionless Shocks*, Springer-Verlag New York, doi:10.1007/978-1-4614-6099-2.

Baumjohann, W., and R. A. Treumann (1996), *Basic Space Plasma Physics*, London: Imperial College Press.

Blanco-Cano, X., N. Omidi, and C. T. Russell (2009), Global hybrid simulations: foreshock waves and cavitons under radial interplanetary magnetic field geometry, *Journal of Geophysical Research (Space Physics)*, *114*, A01216, doi:10.1029/2008JA013406.

Calculate distance, bearing and more between Latitude/Longitude points (2017), `http://www.movable-type.co.uk/scripts/latlong.html`, online; accessed 17 June 2017.

Chiu, M. C., U. I. von-Mehlem, C. E. Willey, T. M. Betenbaugh, J. J. Maynard, J. A. Krein, R. F. Conde, W. T. Gray, J. W. Hunt, Jr., L. E. Mosher, M. G. McCullough, P. E. Panneton, J. P. Staiger, and E. H. Rodberg (1998), ACE spacecraft, *Space Sci. Rev.*, *86*, 257–284, doi:10.1023/A:1005002013459.

Chu, C., H. Zhang, D. Sibeck, A. Otto, Q. Zong, N. Omidi, J. P. McFadden, D. Fruehauff, and V. Angelopoulos (2017), THEMIS satellite observations of hot flow anomalies at Earth's bow shock, *Annales Geophysicae*, *35*, 443–451, doi:10.5194/angeo-35-443-2017.

Collinson, G., J. Halekas, J. Grebowsky, J. Connerney, D. Mitchell, J. Espley, G. DiBraccio, C. Mazelle, J.-A. Sauvaud, A. Fedorov, and B. Jakosky (2015), A hot flow anomaly at Mars, *Geophys. Res. Lett.*, *42*, 9121–9127, doi:10.1002/2015GL065079.

Collinson, G. A., D. G. Sibeck, A. Masters, N. Shane, J. A. Slavin, A. J. Coates, T. L. Zhang, M. Sarantos, S. Boardsen, T. E. Moore, and S. Barabash (2012), Hot flow anomalies at Venus, *Journal of Geophysical Research (Space Physics)*, *117*, A04204, doi: 10.1029/2011JA017277.

Collinson, G. A., D. G. Sibeck, A. Masters, N. Shane, T. L. Zhang, A. Fedorov, S. Barabash, A. J. Coates, T. E. Moore, J. A. Slavin, V. M. Uritsky, S. Boardsen, and M. Sarantos (2014), A survey of hot flow anomalies at Venus, *Journal of Geophysical Research (Space Physics)*, *119*, 978–991, doi:10.1002/2013JA018863.

Eastwood, J. P., D. G. Sibeck, V. Angelopoulos, T. D. Phan, S. D. Bale, J. P. McFadden, C. M. Cully, S. B. Mende, D. Larson, S. Frey, C. W. Carlson, K. Glassmeier, H. U. Auster, A. Roux, and O. Le Contel (2008), THEMIS observations of a hot flow anomaly: Solar wind, magnetosheath, and ground-based measurements, *Geophys. Res. Lett.*, *35*, L17S03, doi:10.1029/2008GL033475.

Eastwood, J. P., S. J. Schwartz, T. S. Horbury, C. M. Carr, K.-H. Glassmeier, I. Richter, C. Koenders, F. Plaschke, and J. A. Wild (2011), Transient Pc3 wave activity generated by a hot flow anomaly: Cluster, Rosetta, and ground-based observations, *Journal of Geophysical Research (Space Physics)*, *116*, A08224, doi:10.1029/2011JA016467.

Facskó, G., K. Kecskeméty, G. Erdős, M. Tátrallyay, P. W. Daly, and I. Dandouras (2008), A statistical study of hot flow anomalies using Cluster data, *Adv. Space Res.*, *41*, 1286–1291, doi:10.1016/j.asr.2008.02.005.

Facskó, G., J. G. Trotignon, I. Dandouras, E. A. Lucek, and P. W. Daly (2009), Study of hot flow anomalies using Cluster multi-spacecraft measurements, *Adv. Space Res.*, doi: 10.1016/j.asr.2009.08.011.

Fairfield, D. H., N. A. Tsyganenko, A. V. Usmanov, and M. V. Malkov (1994), A large magnetosphere magnetic field database, *J. Geophys. Res.*, *99*, 11,319–11,326, doi:10.1029/94JA00255.

Feldman, W. C., R. C. Anderson, S. J. Bame, J. T. Gosling, R. D. Zwickl, and E. J. Smith (1983), Electron velocity distributions near interplantary shocks, *J. Geophys. Res.*, *88*, 9949–9958, doi:10.1029/JA088iA12p09949.

Fillingim, M. O., J. P. Eastwood, G. K. Parks, V. Angelopoulos, I. R. Mann, S. B. Mende, and A. T. Weatherwax (2011), Polar UVI and THEMIS GMAG observations of the ionospheric response to a hot flow anomaly, *Journal of Atmospheric and Solar-Terrestrial Physics*, *73*, 137–145, doi:10.1016/j.jastp.2010.03.001.

Fuselier, S. A., M. F. Thomsen, J. T. Gosling, S. J. Bame, and C. T. Russell (1987), Fast shocks at the edges of hot diamagnetic cavities upstream from the earth's bow shock, *J. Geophys. Res.*, *92*, 3187–3194, doi:10.1029/JA092iA04p03187.

Giacalone, J., and D. Burgess (2010), Interaction between inclined current sheets and the heliospheric termination shock, *Geophys. Res. Lett.*, *37*, L19104, doi:10.1029/2010GL044656.

Gjerloev, J. W. (2009), A global ground-based magnetometer initiative, *EOS Transactions*, *90*, 230–231, doi:10.1029/2009EO270002.

"GOES History" (2015), `http://www.goes-r.gov/mission/history.html`, online; accessed December 2015.

Greenwald, R. A., K. B. Baker, J. R. Dudeney, M. Pinnock, T. B. Jones, E. C. Thomas, J.-P. Villain, J.-C. Cerisier, C. Senior, C. Hanuise, R. D. Hunsucker, G. Sofko, J. Koehler, E. Nielsen, R. Pellinen, A. D. M. Walker, N. Sato, and H. Yamagishi (1995), Darn/Superdarn: a global view of the dynamics of high-latitude convection, *Space Sci. Rev.*, *71*, 761–796, doi:10.1007/BF00751350.

Hasegawa, H., H. Zhang, Y. Lin, B. U. Ö. Sonnerup, S. J. Schwartz, B. Lavraud, and Q.-G. Zong (2012), Magnetic flux rope formation within a magnetosheath hot flow anomaly, *Journal of Geophysical Research (Space Physics)*, *117*, A09214.

Horbury, T. S., D. Burgess, M. Fränz, and C. J. Owen (2001), Three spacecraft observations of solar wind discontinuities, *Geophys. Res. Lett.*, *28*, 677–680, doi:10.1029/2000GL000121.

Jacobsen, K. S., T. D. Phan, J. P. Eastwood, D. G. Sibeck, J. I. Moen, V. Angelopoulos, J. P. McFadden, M. J. Engebretson, G. Provan, D. Larson, and K.-H. Fornaçon (2009), THEMIS observations of extreme magnetopause motion caused by a hot flow anomaly, *Journal of Geophysical Research (Space Physics)*, *114*, A08210, doi:10.1029/2008JA013873.

Kecskeméty, K., G. Erdős, G. Facskó, M. Tátrallyay, I. Dandouras, P. Daly, and K. Kudela (2006), Distributions of suprathermal ions near hot flow anomalies observed by RAPID aboard Cluster, *Advances in Space Research*, *38*, 1587–1594, doi:10.1016/j.asr.2005.09.027.

"Kennedy Media Gallery" (2017), `https://mediaarchive.ksc.nasa.gov/`, online; accessed 19 June 2017.

King, J. H., and N. E. Papitashvili (2005), Solar wind spatial scales in and comparisons of hourly Wind and ACE plasma and magnetic field data, *Journal of Geophysical Research (Space Physics)*, *110*, A02104, doi:10.1029/2004JA010649.

Kivelson, M. G., and C. T. Russell (Eds.) (1995), *Introduction to Space Physics*, 586 pp., Cambridge University Press, Cambridge, UK, ISBN 0521451043.

Koval, A., J. Šafránková, and Z. Němeček (2005), A study of particle flows in hot flow anomalies, *Planetary and Space Science*, *53*, 41–52, doi:10.1016/j.pss.2004.09.027.

Kozlovsky, A., V. Safargaleev, N. Østgaard, T. Turunen, A. Koustov, J. Jussila, and A. Roldugin (2005), On the motion of dayside auroras caused by a solar wind pressure pulse, *Annales Geophysicae*, *23*, 509–521, doi:10.5194/angeo-23-509-2005.

Lepping, R. P., M. H. Acũna, L. F. Burlaga, W. M. Farrell, J. A. Slavin, K. H. Schatten, F. Mariani, N. F. Ness, F. M. Neubauer, Y. C. Whang, J. B. Byrnes, R. S. Kennon, P. V. Panetta, J. Scheifele, and E. M. Worley (1995), The wind magnetic field investigation, *Space Sci. Rev.*, *71*, 207–229, doi:10.1007/BF00751330.

Lin, R. P., K. A. Anderson, S. Ashford, C. Carlson, D. Curtis, R. Ergun, D. Larson, J. McFadden, M. McCarthy, G. K. Parks, H. Rême, J. M. Bosqued, J. Coutelier, F. Cotin, C. D'Uston, K.-P. Wenzel, T. R. Sanderson, J. Henrion, J. C. Ronnet, and G. Paschmann (1995), A three-dimensional plasma and energetic particle investigation for the wind spacecraft, *Space Sci. Rev.*, *71*, 125–153, doi:10.1007/BF00751328.

Lin, Y. (2002), Global hybrid simulation of hot flow anomalies near the bow shock and in the magnetosheath, *Planet. Space Sci.*, *50*, 577–591.

Liu, T. Z., D. L. Turner, V. Angelopoulos, and N. Omidi (2016), Multipoint observations of the structure and evolution of foreshock bubbles and their relation to hot flow anomalies, *Journal of Geophysical Research (Space Physics)*, *121*, 5489–5509, doi: 10.1002/2016JA022461.

Liu, Z., D. L. Turner, V. Angelopoulos, and N. Omidi (2015), THEMIS observations of tangential discontinuity-driven foreshock bubbles, *Geophys. Res. Lett.*, *42*, 7860–7866, doi:10.1002/2015GL065842.

Louarn, P., E. Budnik, J. A. Sauvaud, G. Parks, K. Meziane, J. M. Bosqued, I. Dandouras, H. Rème, U. Mall, P. Daly, M. Dunlop, A. Balogh, L. M. Kistler, and E. Amata (2003), Observation of energy-time dispersed ion structures in the magnetosheath by CLUSTER: possible signatures of transient acceleration processes at shock, *Annales Geophysicae*, *21*, 1483–1495, doi:10.5194/angeo-21-1483-2003.

Lucek, E. A., T. S. Horbury, A. Balogh, I. Dandouras, and H. Rème (2004), Cluster observations of hot flow anomalies, *J. Geophys. Res.*, *109*, A06,207, doi:10.1029/2003JA010016.

"Maintenance trip to Rankin Inlet" (2016), `http://superdarn.ca/news/item/25-maintenance-trip-to-rankin-inlet`, online; accessed 19 June 2017.

Martens, P. C. H., and D. Cauffman (Eds.) (2002), *Multi-Wavelength Observations of Coronal Structure and Dynamics*, Pergamon.

Masters, A., H. J. McAndrews, J. T. Steinberg, M. F. Thomsen, C. S. Arridge, M. K. Dougherty, L. Billingham, S. J. Schwartz, N. Sergis, G. B. Hospodarsky, and A. J. Coates (2009), Hot flow anomalies at Saturn's bow shock, *Journal of Geophysical Research (Space Physics)*, *114*, A08217, doi:10.1029/2009JA014112.

McFadden, J. P., C. W. Carlson, D. Larson, M. Ludlam, R. Abiad, B. Elliott, P. Turin, M. Marckwordt, and V. Angelopoulos (2008), The THEMIS ESA plasma instrument and in-flight calibration, *Space Sci. Rev.*, *141*, 277–302, doi:10.1007/s11214-008-9440-2.

Merka, J., A. Szabo, J. A. Slavin, and M. Peredo (2005), Three-dimensional position and shape of the bow shock and their variation with upstream Mach numbers and interplanetary magnetic field orientation, *Journal of Geophysical Research (Space Physics)*, *110*, 4202, doi:10.1029/2004JA010944.

"NASA's ACE Spacecraft" (2017), http://www.aurora-service.eu/aurora-school/nasas-ace-spacecraft/, online; accessed 19 June 2017.

Ogilvie, K. W., D. J. Chornay, R. J. Fritzenreiter, F. Hunsaker, J. Keller, J. Lobell, G. Miller, J. D. Scudder, E. C. Sittler, Jr., R. B. Torbert, D. Bodet, G. Needell, A. J. Lazarus, J. T. Steinberg, J. H. Tappan, A. Mavretic, and E. Gergin (1995), SWE, a comprehensive plasma instrument for the wind spacecraft, *Space Sci. Rev.*, *71*, 55–77, doi:10.1007/BF00751326.

Øieroset, M., D. L. Mitchell, T. D. Phan, R. P. Lin, and M. H. Acuña (2001), Hot diamagnetic cavities upstream of the Martian bow shock, *Geophys. Res. Lett.*, *28*, 887–890, doi:10.1029/2000GL012289.

Omidi, N., and D. G. Sibeck (2007), Formation of hot flow anomalies and solitary shocks, *J. Geophys. Res.*, *112*, A01,203, doi:10.1029/2006JA011663.

Omidi, N., D. G. Sibeck, and X. Blanco-Cano (2009), Foreshock compressional boundary, *Journal of Geophysical Research (Space Physics)*, *114*, A08205, doi:10.1029/2008JA013950.

Omidi, N., J. P. Eastwood, and D. G. Sibeck (2010), Foreshock bubbles and their global magnetospheric impacts, *Journal of Geophysical Research (Space Physics)*, *115*, A06204, doi:10.1029/2009JA014828.

Omidi, N., D. Sibeck, X. Blanco-Cano, D. Rojas-Castillo, D. Turner, H. Zhang, and P. Kajdič (2013a), Dynamics of the foreshock compressional boundary and its connection to foreshock cavities, *Journal of Geophysical Research (Space Physics)*, *118*, 823–831, doi:10.1002/jgra.50146.

Omidi, N., H. Zhang, D. Sibeck, and D. Turner (2013b), Spontaneous hot flow anomalies at quasi-parallel shocks: 2. Hybrid simulations, *Journal of Geophysical Research (Space Physics)*, *118*, 173–180, doi:10.1029/2012JA018099.

Omidi, N., H. Zhang, C. Chu, D. Sibeck, and D. Turner (2014), Parametric dependencies of spontaneous hot flow anomalies, *Journal of Geophysical Research: Space Physics*, *119*(12), 9823–9833, doi:10.1002/2014JA020382.

"Omni, About the Data" (2015), http://omniweb.gsfc.nasa.gov/html/ow$_$data.html, online; accessed December 2015.

"OMNI2" (2015), http://virbo.org/OMNI/OMNI2, online; accessed January 2017.

Onsager, T. G., M. F. Thomsen, J. T. Gosling, and S. J. Bame (1990), Observational test of a hot flow anomaly formation mechanism, *J. Geophys. Res.*, *95*, 11,967–11,974.

Onsager, T. G., D. Winske, and M. F. Thomsen (1991), Interaction of a finite-length ion beam with a background plasma - Reflected ions at the quasi-parallel bow shock, *J. Geophys. Res.*, *96*, 1775–1788.

Paschmann, G., G. Haerendel, N. Sckopke, E. Moebius, and H. Luehr (1988), Three-dimensional plasma structures with anomalous flow directions near the earth's bow shock, *J. Geophys. Res.*, *93*, 11,279–11,294, doi:10.1029/JA093iA10p11279.

Rojas-Castillo, D., X. Blanco-Cano, P. Kajdič, and N. Omidi (2013), Compressional Boundaries in the Earth's Foreshock, in *American Institute of Physics Conference Series*, vol. 1539, edited by G. P. Zank, J. Borovsky, R. Bruno, J. Cirtain, S. Cranmer, H. Elliott, J. Giacalone, W. Gonzalez, G. Li, E. Marsch, E. Moebius, N. Pogorelov, J. Spann, and O. Verkhoglyadova, pp. 434–437, doi:10.1063/1.4811078.

Ruohoniemi, J. M., and K. B. Baker (1998), Large-scale imaging of high-latitude convection with super dual auroral radar network hf radar observations, *Journal of Geophysical Research: Space Physics*, *103*(A9), 20,797–20,811, doi:10.1029/98JA01288.

Schwartz, S. J. (1995), Hot flow anomalies near the Earth's bow shock, *Adv. Space Res.*, *15*, 107–116, doi:10.1016/0273-1177(95)00025-A.

Schwartz, S. J. (1998), Shock and Discontinuity Normals, Mach Numbers, and Related Parameters, *ISSI Scientific Reports Series*, *1*, 249–270.

Schwartz, S. J., C. P. Chaloner, D. S. Hall, P. J. Christiansen, and A. D. Johnstones (1985), An active current sheet in the solar wind, *Nature*, *318*, 269–271, doi:10.1038/318269a0.

Schwartz, S. J., R. L. Kessel, C. C. Brown, L. J. C. Woolliscroft, and M. W. Dunlop (1988), Active current sheets near the earth's bow shock, *J. Geophys. Res.*, *93*, 11,295–11,310, doi:10.1029/JA093iA10p11295.

Schwartz, S. J., D. Burgess, and J. J. Moses (1996), Low-frequency waves in the Earthś magnetosheath: present status, *Annales Geophysicae*, *14*, 1134–1150, doi:10.1007/s00585-996-1134-z.

Schwartz, S. J., G. Paschmann, N. Sckopke, T. M. Bauer, M. Dunlop, A. N. Fazakerley, and M. F. Thomsen (2000), Conditions for the formation of hot flow anomalies at Earth's bow shock, *J. Geophys. Res.*, *105*, 12,639–12,650, doi:10.1029/1999JA000320.

Sibeck, D. G., N. L. Borodkova, S. J. Schwartz, C. J. Owen, R. Kessel, S. Kokubun, R. P. Lepping, R. Lin, K. Liou, H. Lühr, R. W. McEntire, C.-I. Meng, T. Mukai, Z. Nemecek, G. Parks, T. D. Phan, S. A. Romanov, J. Safrankova, J.-A. Sauvaud, H. J. Singer, S. I. Solovyev, A. Szabo, K. Takahashi, D. J. Williams, K. Yumoto, and G. N. Zastenker (1999), Comprehensive study of the magnetospheric response to a hot flow anomaly, *J. Geophys. Res.*, *104*, 4577–4594, doi:10.1029/1998JA900021.

Sibeck, D. G., T.-D. Phan, R. Lin, R. P. Lepping, and A. Szabo (2002), Wind observations of foreshock cavities: A case study, *Journal of Geophysical Research (Space Physics)*, *107*, 1271, doi:10.1029/2001JA007539.

Sibeck, D. G., N. Omidi, I. Dandouras, and E. Lucek (2008), On the edge of the foreshock: model-data comparisons, *Annales Geophysicae*, *26*, 1539–1544, doi:10.5194/angeo-26-1539-2008.

Singer, H., L. Matheson, R. Grubb, A. Newman, and D. Bouwer (1996), Monitoring space weather with the GOES magnetometers, in *GOES-8 and Beyond, Society of Photo-Optical Instrumentation Engineers (SPIE) Conference Series*, vol. 2812, edited by E. R. Washwell, pp. 299–308, doi:10.1117/12.254077.

Sitar, R. J., J. B. Baker, C. R. Clauer, A. J. Ridley, J. A. Cumnock, V. O. Papitashvili, J. Spann, M. J. Brittnacher, and G. K. Parks (1998), Multi-instrument analysis of the ionospheric signatures of a hot flow anomaly occurring on July 24, 1996, *J. Geophys. Res.*, *103*, 23,357–23,372, doi:10.1029/98JA01916.

Slavin, J. A., M. H. Acuña, B. J. Anderson, S. Barabash, M. Benna, S. A. Boardsen, M. Fraenz, G. Gloeckler, R. E. Gold, G. C. Ho, H. Korth, S. M. Krimigis, R. L. McNutt, J. M. Raines, M. Sarantos, S. C. Solomon, T. Zhang, and T. H. Zurbuchen (2009), MESSENGER and Venus Express observations of the solar wind interaction with Venus, *Geophysical Review Letters*, *36*, L09106, doi:10.1029/2009GL037876.

Smith, E. J., and M. E. Burton (1988), Shock analysis - Three useful new relations, *J. Geophys. Res.*, *93*, 2730–2734, doi:10.1029/JA093iA04p02730.

Sonnerup, B. U. Ö., and L. J. Cahill, Jr. (1967), Magnetopause structure and attitude from Explorer 12 observations, *J. Geophys. Res.*, *72*, 171–183.

Sonnerup, B. U. Ö., and M. Scheible (1998), Minimum and maximum variance analysis, *ISSI Scientific Reports Series*, *1*, 185–220.

Stone, E. C., A. M. Frandsen, R. A. Mewaldt, E. R. Christian, D. Margolies, J. F. Ormes, and F. Snow (1998), The Advanced Composition Explorer, *Space Sci. Rev.*, *86*, 1–22, doi:10.1023/A:1005082526237.

"The Sun's Magnetic Field" (2012), `http://helios.gsfc.nasa.gov/solarmag.html`, online; accessed March 2016.

"The WIND Spacecraft Experiment" (2011), `http://earthweb.ess.washington.edu/space/SpaceExp/WIND/`, online; accessed 19 June 2017.

"THEMIS - eoPortal Directory - Satellite Missions" (2017), `https://directory.eoportal.org/web/eoportal/satellite-missions/t/themis`, online; accessed 19 June 2017.

"THEMIS Electrostatic Analyzer" (2017), `http://themis.igpp.ucla.edu/instrument_esa.shtml`, online; accessed 19 June 2017.

Thomas, V. A. (1989), Three-dimensional simulation of diamagnetic cavity formation by a finite-size plasma beam, *J. Geophys. Res.*, *94*, 13,579–13,583, doi:10.1029/JA094iA10p13579.

Thomas, V. A., and S. H. Brecht (1988), Evolution of diamagnetic cavities in the solar wind, *J. Geophys. Res.*, *93*, 11,341–11,353, doi:10.1029/JA093iA10p11341.

Thomas, V. A., D. Winske, M. F. Thomsen, and T. G. Onsager (1991), Hybrid simulation of the formation of a hot flow anomaly, *J. Geophys. Res.*, *96*, 11,625–11,632, doi:10.1029/91JA01092.

Thomsen, M. F., J. T. Gosling, S. A. Fuselier, S. J. Bame, and C. T. Russell (1986), Hot, diamagnetic cavities upstream from the earth's bow shock, *J. Geophys. Res.*, *91*, 2961–2973, doi:10.1029/JA091iA03p02961.

Thomsen, M. F., J. T. Gosling, S. J. Bame, K. B. Quest, and C. T. Russell (1988), On the origin of hot diamagnetic cavities near the earth's bow shock, *J. Geophys. Res.*, *93*, 11,311–11,325, doi:10.1029/JA093iA10p11311.

Tsyganenko, N. A., and D. P. Stern (1996), Modeling the global magnetic field of the large-scale Birkeland current system, *J. Geophys. Res.*, *101*, 27,187–27,198.

Turner, D. L., N. Omidi, D. G. Sibeck, and V. Angelopoulos (2013), First observations of foreshock bubbles upstream of Earth's bow shock: Characteristics and comparisons to HFAs, *Journal of Geophysical Research (Space Physics)*, *118*, 1552–1570, doi:10.1002/jgra.50198.

Uritsky, V. M., J. A. Slavin, S. A. Boardsen, T. Sundberg, J. M. Raines, D. J. Gershman, G. Collinson, D. Sibeck, G. V. Khazanov, B. J. Anderson, and H. Korth (2014), Active current sheets and candidate hot flow anomalies upstream of Mercury's bow shock, *Journal of Geophysical Research (Space Physics)*, *119*, 853–876, doi:10.1002/2013JA019052.

Vaisberg, O. L., S. D. Shuvalov, A. Y. Shestakov, and Y. M. Golubeva (2016), Origin of the backstreaming ions in a young hot flow anomaly, *Planetary and Space Science*, *131*, 102–110, doi:10.1016/j.pss.2016.08.003.

Wang, S., Q. Zong, and H. Zhang (2013a), Cluster observations of hot flow anomalies with large flow deflections: 2. Bow shock geometry at HFA edges, *Journal of Geophysical Research (Space Physics)*, *118*, 418–433, doi:10.1029/2012JA018204.

Wang, S., Q. Zong, and H. Zhang (2013b), Hot flow anomaly formation and evolution: Cluster observations, *Journal of Geophysical Research (Space Physics)*, *118*, 4360–4380, doi:10.1002/jgra.50424.

Woolliscroft, L. J. C., C. C. Brown, S. J. Schwartz, C. P. Chaloner, and P. J. Christiansen (1986), AMPTE-UKS observations of current sheets in the solar wind, *Adv. Space Res.*, *6*, 89–92, doi:10.1016/0273-1177(86)90017-7.

Xiao, T., H. Zhang, Q. Q. Shi, Q.-G. Zong, S. Y. Fu, A. M. Tian, W. J. Sun, S. Wang, G. K. Parks, S. T. Yao, H. Rème, and I. Dandouras (2015), Propagation characteristics of young hot flow anomalies near the bow shock: Cluster observations, *Journal of Geophysical Research (Space Physics)*, *120*, 4142–4154, doi:10.1002/2015JA021013.

Yizengaw, E. (2017), https://www2.bc.edu/endawoke-kassie/ionosphere.html, online; accessed May 2017.

Zhang, H., D. G. Sibeck, Q.-G. Zong, S. P. Gary, J. P. McFadden, D. Larson, K.-H. Glassmeier, and V. Angelopoulos (2010), Time History of Events and Macroscale Interactions during Substorms observations of a series of hot flow anomaly events, *Journal of Geophysical Research (Space Physics)*, *115*(A14), A12235, doi:10.1029/2009JA015180.

Zhang, H., D. G. Sibeck, Q.-G. Zong, N. Omidi, D. Turner, and L. B. N. Clausen (2013), Spontaneous hot flow anomalies at quasi-parallel shocks: 1. Observations, *Journal of Geophysical Research (Space Physics)*, *118*, 3357–3363, doi:10.1002/jgra.50376.

Zhao, L. L., H. Zhang, and Q.-G. Zong (2017), A statistical study on hot flow anomaly current sheets, *Journal of Geophysical Research (Space Physics)*, *122*, 235–248, doi:10.1002/2016JA023319.